Numerical Investigation of the Settling Behavior of Non-Spherical Particles

Application of Homogenized Lattice Boltzmann Methods

zur Erlangung des akademischen Grades eines
DOKTORS DER INGENIEURWISSENSCHAFTEN (DR.-ING.)

von der KIT-Fakultät für Chemieingenieurwesen und Verfahrenstechnik des
Karlsruher Instituts für Technologie (KIT)
genehmigte

DISSERTATION

von
M. Sc. Robin Andre Trunk
aus Heilbronn

Tag der mündlichen Prüfung: 22.07.2021

Referent: Prof. Dr.-Ing. habil. Hermann Nirschl
Erster Korreferent: Dr. Mathias J. Krause
Zweite Korreferentin: PD Dr. Gudrun Thäter

Abstract

For an improvement of separation processes regarding efficiency and selectivity, extending the knowledge of particle dynamics is crucial. This especially concerns the challenging case of particle sizes in the range around 1 µm, as neither diffusion nor inertial effects are dominant. While the particle flow has to be depicted on the scale of the process machine, effects on a scale several orders of magnitude smaller, e.g., related to the particle shape, can affect the overall separation results. In this thesis the influence of the particle's shape on its flow behaviour, more specifically the experienced drag, is studied via simulations. Presented is a correlation regarding the drag coefficient and terminal settling velocity, based on various particle shape parameters, for a confined range of Reynolds numbers and shape parameters. Furthermore, a general procedure is proposed to obtain such correlations from given data, along with simulation schemes to obtain the latter.

The simulations are performed using the homogenized lattice Boltzmann method, which is extended to depict arbitrary particle shapes in this thesis. It is also improved firstly regarding accuracy by updating the schemes for the calculation of exchanged momentum and application of forces and secondly regarding computational performance. Furthermore, all implementations and simulations are embedded in the C++ package OpenLB. As it is open-source published, the implementation of the finally applied simulation method is freely available.

As a first step, the homogenized lattice Boltzmann method, which could previously only be used for the simulation of objects with available analytical descriptions of the surface, volume and moment of inertia, is extended for arbitrary shapes. Applying the automated creation of a voxel representation of the particle, these values can be calculated for any shape, e.g., utilizing the parallel axis theorem. The new capability is then demonstrated simulating the settling of 16 limestone particles with geometries obtained from computer tomography scans. Comparing to the same simulation conducted with spheres of equal volume, the former are found to settle 28.75% slower.

The computational performance of the method is further improved by parallelizing the calculation of exchanged momentum and reducing the required memory. This leads to a code which is 99.5% parallelizable according to performance studies. Considering experimental data of a settling sphere for Reynolds numbers $\mathrm{Re} = 1.5, 4.1, 11.6$ and 32.2, obtained with particle imaging velocimetry, a comparative study is performed. Various combinations of schemes applying the force to the fluid flow and calculating the momentum are investigated, also introducing a new scheme, denoted as momentum loss algorithm, for the latter. According to this study, the new approach is to favor for small Re and comparably low resolutions. Performing a convergence study as well, the overall best combination of methods is selected, yielding an average error of about 5.5% across the tested Re and grid resolutions. For additional validation, the settling of a single sphere is further investigated and compared to correlations from literature. The best accordance is found with the correlation by Schiller and Naumann yielding an average deviation of 7.78% across the range from $\mathrm{Re} = 0.24$ up to $\mathrm{Re} = 948.67$. The error is quantified regarding the maximum occurring lattice velocity, which serves as a guideline for parameter selection, also in future studies. Besides, the capability of the method to depict the tubular pinch effect is also demonstrated. Finally, the method is validated for the case of hindered settling, considering solid volume fractions between 5% and 25%. Conducting simulations for $\mathrm{Re} = 0.53, 5.29$ and 49.46, the average deviation to results in literature is found to be only 8.07%, with the largest deviation obtained for the highest Reynolds number.

The link between particle shape and settling behaviour is studied via simulations of superellipsoids. To quantify the shape, a large set of shape descriptors like the sphericity, roundness, convexity, the Corey shape factor and the Hofmann shape entropy is used. Identifying the most relevant parameters with statistical methods, correlations regarding the drag coefficient and terminal settling velocity are constructed. The approach is based on a multiple linear regression for a polynomial constructed from the identified parameters also containing interaction terms. The multicolinearity is monitored by assessing the variance inflation factor and additional measures to control it by dropping the respective terms in the polynomial. The average error of the found drag correlation is less than a sixth of the one obtained applying correlations available in literature to the current data set. Similarly, the average error regarding the terminal settling velocity is found to be less than a fifth compared to available correlations. To prevent overfitting, the data are split in a training and a test set. The presented procedure to construct the polynomial and obtain the correlation is generally applicable to other data sets and can therefore be used to derive further correlations which might be specific to a desired set of particles.

Thereby the studies presented in this thesis aid in the design of process machines, as the newly found correlations can be used in simulations on the process scale. The tools for such simulations applying an Euler–Euler approach for the particles and the volume-averaged Navier–Stokes equations are given in publications, concomitant to this thesis. The simulation methods presented in this work, together with the described procedure to obtain new correlations, additionally allow to further automate the whole process. This may lead to a process which automatically creates predictions regarding the separation efficiency, specifically tailored for a desired particle collective and process setup.

Zusammenfassung

Zur Verbesserung von Trennprozessen bezüglich der Effizienz und Selektivität ist es notwendig, das Wissen über das Verhalten von Partikeln in Strömungen zu erweitern. Dies ist insbesondere der Fall für Partikel im Größenbereich um 1 µm, da hier weder die Diffusion, noch Trägheitseffekte die Dynamik dominant bestimmen. Weiterhin sind Abläufe in der Größenordnung eines industrierelevanten Prozesses abzubilden, während Effekte, welche sich auf der um mehrere Größenordnungen kleinere Skala eines Partikeldurchmessers abspielen, die Effizienz des gesamten Verfahrens beeinflussen können. In dieser Arbeit wird die Abhängigkeit des Strömungsverhaltens der Partikel von der Form untersucht, wozu die wirkende Strömungswiderstandskraft simulativ betrachtet wird. Es werden Korrelationen bezüglich des Widerstandkoeffizienten und der terminalen Sinkgeschwindigkeit vorgestellt. Diese beschreiben die Abhängigkeit von mehreren Formparametern und der Reynoldszahl, jeweils für einen eingeschränkten Bereich. Darüber hinaus wird ein allgemeines Vorgehen zur Erstellung solcher Korrelationen basierend auf gegebenen Daten vorgestellt.

Für die Simulationen wird die homogenized lattice Boltzmann Methode verwendet, welche im Rahmen dieser Arbeit erweitert wird, um beliebig geformte Partikel abbilden zu können. Die Methode wird weiterhin hinsichtlich der benötigten Rechenleistung und Genauigkeit optimiert, wobei für letztere der Einfluss verschiedener Ansätze für die Anwendung der Kräfte und den Impulsaustausch untersucht

wird. Der erstellte Code ist in das C++-Paket OpenLB integriert, womit alle hier präsentierten Simulationen durchgeführt werden. Da es als Open-Source-Paket veröffentlicht wird, ist die Implementierung der angewandten Simulationsmethode damit frei verfügbar.

Zunächst wird die homogenized lattice Boltzman Methode, mit der bisher nur Objekte simuliert werden konnten, für die analytische Beschreibungen der Oberfläche, des Volumens und des Trägheitsmoments verfügbar sind, für beliebige Formen erweitert. Durch die automatisierte Erstellung einer Voxel-Darstellung der Partikel können diese Werte für jede beliebige Form berechnet werden, z. B. unter Verwendung des Satzes von Steiner. Die Funktionalität dieser Erweiterung wird dann anhand der Simulation der Sedimentation von 16 Kalksteinpartikeln mit Geometrien, welche aus Computertomographie-Scans erhalten wurden, demonstriert. Führt man dieselbe Simulation mit volumenäquivalenten Kugeln durch, zeigt sich, dass die Kalksteinpartikel um 28,75% langsamer absinken.

Die Rechenleistung der Methode wird weiter verbessert, indem die Berechnung des ausgetauschten Impulses parallelisiert und der benötigte Speicher reduziert wird. Dies führt zu einem Code, der laut Performancestudie zu 99,5% parallelisierbar ist. Unter Berücksichtigung von experimentellen Daten sedimentierender Kugeln für Reynoldszahlen $\mathrm{Re} = 1{,}5; 4{,}1; 11{,}6$ und $32{,}2$, welche mittels Particle Image Velocimetry erhalten wurden, wird eine Vergleichsstudie durchgeführt. Dabei werden verschiedene Kombinationen von Ansätzen zur Anwendung der Kraft auf die Fluidströmung und zur Berechnung des ausgetauschten Impulses untersucht, wobei auch ein neuer Ansatz, der momentum loss Algorithmus, vorgestellt wird. Dieser ist der Studie zufolge für kleine Re und vergleichsweise geringe Auflösungen zu bevorzugen. Anhand einer Konvergenzstudie wird die insgesamt beste Methodenkombination ausgewählt, welche über alle getesteten Re und Gitterauflösungen hinweg einen durchschnittlichen Fehler von etwa 5,5% aufweist. Zur weiteren Validierung wird das Sedimentieren einer einzelnen Kugel genauer untersucht und mit Korrelationen aus der Literatur verglichen. Die beste Übereinstimmung wird mit der Formel von Schiller und Naumann erzielt, die mittlere

Abweichung für Reynoldszahlen zwischen Re = 0,24 und Re = 948,67 beträgt dabei 7,78%. Der Fehler wird hinsichtlich der maximal auftretenden lattice velocity quantifiziert, was Richtwerte für die Parameterwahl, auch für zukünftigen Studien, liefert. Weiterhin wird die Eignung der Methode zur Untersuchung des Segré–Silberberg Effekts demonstriert. Schließlich wird die Methode für Schwarmsedimentation unter Berücksichtigung von Feststoffvolumenanteilen zwischen 5% und 25% validiert. Bei der Durchführung von Simulationen für Re = 0,53; 5,29 und 49,46 beträgt die durchschnittliche Abweichung zu Ergebnissen in der Literatur 8,07%, wobei die größte Abweichung für die höchste Reynoldszahl erhalten wird.

Der Zusammenhang zwischen Partikelform und Sinkverhalten wird anhand der Simulation von Super-Ellipsoiden untersucht. Um die Form zu quantifizieren, werden diverse Formparameter wie die Sphärizität, Rundheit, Konvexität, der Corey-Formfaktor und die Hofmann-Formentropie eingesetzt. Nach der Identifizierung der relevantesten Parameter mit statistischen Methoden werden Korrelationen bezüglich des Widerstandskoeffizienten und der terminalen Sinkgeschwindigkeit berechnet. Der Ansatz basiert auf einer multiplen linearen Regression für ein aus den ausgewählten Parametern konstruiertes Polynom, das auch Interaktionsterme enthält. Die Multikolinearität wird dabei unter Anderem über den Varianzinflationsfaktor betrachtet, um sie durch Eliminieren einzelner Terme des Polynoms zu reduzieren. Verglichen mit gängigen Modellen aus der Literatur sinkt der durchschnittliche Fehler der neuen Korrelation bezüglich des Widerstandskoeffizienten auf ein Sechstel, bei Anwendung auf den in dieser Studie verwendeten Datensatz. Bezüglich der terminalen Sinkgeschwindigkeit ist der Fehler um den Faktor Fünf kleiner im Vergleich zu bisher verfügbaren Modellen. Um overfitting zu vermeiden, werden die Daten in Trainings- und Testdaten aufgeteilt. Das vorgestellte Verfahren zur Konstruktion des Polynoms und zum Erhalt der Korrelation ist allgemein auf andere Datensätze anwendbar und kann daher verwendet werden, um weitere Korrelationen, spezifisch für ein gewünschtes Partikelkollektiv, zu erstellen.

Somit sind die in dieser Arbeit vorgestellten Untersuchungen wertvoll für die Auslegung von Prozessmaschinen, da die neu gefundenen Korrelationen in Simulationen auf der Prozessskala verwendet werden können. Die Methoden für solche Simulationen, unter Verwendung eines Euler–Euler-Ansatzes für die Partikel und der volumengemittelten Navier–Stokes-Gleichungen, werden in begleitenden Publikationen zu dieser Arbeit vorgestellt. Zusätzlich erlauben die hier vorgestellten Simulationsmethoden, zusammen mit dem beschriebenen Verfahren zur Gewinnung neuer Korrelationen, den gesamten Prozess weiter zu automatisieren. Daraus ist ein Verfahren ableitbar, welches automatisiert Vorhersagen über die Abscheideleistung erstellt, die speziell auf ein gewünschtes Partikelkollektiv und einen Prozessaufbau zugeschnitten sind.

Contents

1 Introduction 1

2 Modeling of Particles Submersed in Fluid 7

- 2.1 Fluid Models . . . 8
  - 2.1.1 Navier–Stokes Equations . . . 8
  - 2.1.2 Volume Averaged Navier–Stokes Equations . . . 9
  - 2.1.3 Boltzmann Equation . . . 12
- 2.2 Particle Models . . . 13
  - 2.2.1 Particle Motion . . . 15
  - 2.2.2 Particle Shape Description . . . 15
  - 2.2.3 Advection–Diffusion Equation . . . 19
- 2.3 Forces . . . 20
  - 2.3.1 Drag Correlations for Single Spheres . . . 23
  - 2.3.2 Drag Correlations for non-spherical Particles . . . 25
  - 2.3.3 Correlations for Particle Collectives . . . 29
- 2.4 Coupling . . . 32

3 Numerical Methods 35

- 3.1 Lattice Boltzmann Method for Fluid Flows . . . 36
  - 3.1.1 System of Units . . . 37
  - 3.1.2 Discretization of the Phase Space . . . 38

3.1.3 Discrete Equilibrium Distribution 39
3.1.4 Macroscopic Moments 40
3.1.5 Basic Algorithm 40
3.1.6 Boundary Conditions 41
3.1.7 Forcing Schemes 44
3.2 Extension for Dense Suspensions 45
3.2.1 Force Conversion 46
3.2.2 Pressure Correction Scheme 47
3.2.3 Rescaling Scheme 48
3.3 Extension to Advection–Diffusion Problems 48
3.3.1 Calculation of the Particle Velocity Field 50
3.4 Homogenized Lattice Boltzmann Method 51
3.4.1 Particle Dynamics 52
3.4.2 Momentum Exchange Algorithms 53

4 Depiction of Arbitrary Particle Shapes in Simulations 55
4.1 Introduction 56
4.2 Mathematical Modelling 57
4.3 Numerical Methods 58
4.3.1 Homogenized Lattice Boltzmann Method (HLBM) 58
4.3.2 Representation of Particle in LBM 58
4.3.3 Incorporation of Arbitrary Shape 58
4.4 Results 59
4.4.1 Calculation of Moment of Inertia 59
4.4.2 Flow Around a Cylinder 61
4.4.3 Sedimentation of a Sphere 63
4.4.4 Sedimentation of 15 Limestone Particle 63
4.5 Conclusion 64

5 Homogenized Lattice Boltzmann Method – Validation and Applications 67
5.1 Introduction 68
5.2 Modelling 71
5.2.1 Drag Force 71

5.2.2 Hindered Settling 72
5.3 Methods 73
5.3.1 Homogenized Lattice Boltzmann Method 74
5.3.2 Forcing Schemes 74
5.3.3 Methods for Momentum Exchange 75
5.4 Results and Discussion 76
5.4.1 Settling Sphere 76
5.4.2 Tubular Pinch Effect 85
5.4.3 Hindered Settling 88
5.4.4 Computational Efficiency 91
5.5 Conclusion 92

6 Correlating the Settling Behavior of Single Particles with Shape Parameters 99
6.1 Introduction 100
6.2 Mathematical Modeling 103
6.2.1 Drag Coefficient 104
6.2.2 Shape Parameter 104
6.2.3 Particle Representation 105
6.2.4 Drag Correlations for Non-Spherical Particles 106
6.3 Numerical and Statistical Methods 108
6.3.1 Particle Generation 109
6.3.2 Statistical Tools 111
6.4 Numerical Experiments 112
6.4.1 Preparation 112
6.4.2 Simulation Setup 113
6.4.3 Validation 113
6.5 Results and Discussion 116
6.5.1 Examination of Simulation Data 116
6.5.2 Regression Analysis 119
6.6 Conclusion 125

7 Conclusion and Outlook 135

Bibliography **141**

Appendix **155**
  A List of Publications 155
  B List of OpenLB Test and Application Cases 161

1 Introduction

Particle systems and flows of coupled particle-fluid systems are ubiquitous and gaining insights about their characteristics and dynamics is relevant for a broad range of industrial applications. Despite decades of research and advances, increasing the separation efficiency [46], selectivity [89], and throughput [105], remains a topic of current research in particle separation. Besides process engineering, advances in this field are also relevant for medical applications [19, 143], for advances in anaerobic digestion of by-products of wastewater treatment [26, 27] or to fight environmental pollution [146], among others. One challenge in particle separation is the minimization of the separation gap, which describes a minimum in separation efficiency in a size range where effects of diffusion and inertial forces are both present, but neither of them dominant [80]. Simple models solely based on particle size and density are insufficient and multidimensional approaches considering more particle and process properties are required [83, 110]. For the investigation of this complex dependencies machine learning is also applied [149]. One approach to improve current models and processes is not to simplify particles as spheres of equal volume or surface, but to take the actual particle's shape into account. Studies found a dependency, e.g., of the mechanical properties of silica–rubber composites [118], the efficiency of drug carriers [19] or the classification in a hydrocyclone, on the particle shape.

Numerical simulations are one important tool to gain new insights on particle behaviour, as they allow to examine a setup which might not be experimentally accessible like the aorta [55], the human nasal cavity [56] or the lungs [143]. Furthermore, simulations allow a more detailed inspection of data at all time during the process and can thereby be a less cost intensive alternative, e.g., to study the breakage of aggregates [6]. Therefore models for the simulation of discrete particles have been developed and applied for the investigation of fluidized beds [28] or pneumatic conveying [157]. Models taking the influence of the particle presence on the fluid flow into account have also been proposed and applied to the two latter processes as well as to hydrocyclones [156]. Furthermore, numerical simulations can be used for geometry identification and optimisation [66, 67]. Studies investigated, e.g., the influence of the geometry of a centrifugal air classifier on the resulting particle size distribution [64] or optimised the separation efficiency of a cyclone via computational fluid dynamics (CFD) [90]. Models developed on the basis of simulations can predict the performance of processes and thereby aid in the design of machines [37].

One challenge in the simulation of particle flows in engineering applications is the difference in scales. On one hand taking effects into account which appear on a microscopic scale like the influence of the shape on the dynamics is desirable. On the other hand the impact of this effects, e.g., in a centrifuge, is to be studied on a macroscopic scale. Thereby a very detailed depiction of the particles is required while also considering a large amount of objects in a large domain. This leads to a high computational demand. To face this issue efficient simulation algorithms have been developed [40, 98], which are capable of utilizing large CPU computing clusters [43] or are taking advantage of recent advances in GPU computing [54]. Another way to mitigate the computational load is to choose appropriate simulation approaches to depict effects on different scales and couple them in a multi-scale simulation framework [23]. For highly detailed particle simulations usually a Lagrangian representation is chosen, applying the discrete element method (DEM) [158]. This allows to assign different properties to each of the particles and track their behaviour. For simulations of a huge amount of particles or if the size of the computational domain exceeds the characteristic particle size by several orders of magnitude, it is common to switch to a continuous approach by choosing an Eulerian representation. In this case, the particles are modeled by an advection–diffusion equation [59, 138]. One advantage of this approach is that the computational demand does not scale with the number of particles, outperforming Lagrangian approaches, e.g, in cases resulting in a steady state [155]. However, information on the micro scale is lost, as it is not possible to track individual particles or assign different properties. An overview of Eulerian and Lagrangian approaches for particle simulation is given in [85].

On the microscopic scale the simplest approach is to utilize the DEM and consider the particles as a point masses with dynamics determined by the drag force, applying Newton's second law of motion. However, this model can be extended by consideration of additional forces like gravitation, buoyancy, Basset history force [135] or the added mass effect [84]. It is also possible to consider basic information regarding the shape in this framework. Drag models exist for simple geometries like cylinders [82]. Furthermore, it is possible to approximate shapes by multiple spheres [39, 73]. However, this compound approach requires a high number of spheres for a proper approximation of complex shapes, while the computational effort scales with the number of spheres describing a particle. Therefore more sophisticated methods are required. Probably the most popular one is the immersed boundary method (IBM), which represents particles by Lagrangian points describing the object's surface on an Eulerian background grid handling the fluid flow [106, 141]. These two systems are coupled by interpolation between Lagrangian and Eulerian points, which is required in every time step. In the simulation the particle domain is still filled with fluid and a no-slip condition is enforced at the object's boundary. This approach is capable of depicting any particle shape, given a sensible distribution of points on its surface is found, if the fluid grid has a sufficient resolution to properly depict interactions with the particle. Together with the interpolations, this approach might be computationally expensive. Another approach is the partially saturated cells method (PSM) [72, 109], which is built upon the lattice Boltzmann method (LBM). It considers the interior of the particle as solid and was already in many studies, e.g., on vortex-induced vibrations [50] . Since it depicts the object directly on the fluid grid, no interpolations are required. To describe the shape more accurately, cells that are only partially covered by the particle are represented by a convex combination of fluid bulk flow and no-slip condition. However, new challenges arise for this approach, e.g., since cells which change from solid to fluid during the particle motion need to be initialized [104]. Finally the homogenized lattice Boltzmann method (HLBM) [71, 137, 139] also depicts the particle on the background grid, similar to the PSM, but does not consider the interior as solid, which is a similarity to the IBM. Instead it relaxes the fluid velocity towards the particle's velocity across a small transition zone. Thereby, e.g., the problem of cell initialization is circumvented and still no interpolations are required. Since this is a semi-local algorithm, only relying on the information of neighbouring cells, it is well suited for implementation for massive parallel computing clusters.

A simulation method capable of depicting arbitrary particle shapes and correctly capturing the dynamics is only one step on the path to improve processes by incorporating geometry characteristics in current prediction models. Since shape itself can not be quantified, relevant aspects and parameters need to be identified. While in literature many classification systems are described, which often suggest several classes based on the aspect ratio [124, 159], also new parameters like the Corey shape factor are constructed [94]. Further investigations aimed at finding a minimal set of parameters describing the particle behaviour [57] or identified the ones most relevant for a desired model [7].

The particle behaviour is often described by a model for the drag force an object experiences. The simplest shape is that of a sphere, as it is independent of orientation. For low Reynolds numbers the Stokes approximation can be used [128], beyond that, especially for the intermediate regime of Reynolds numbers between

1 and 1000, many approximations have been been proposed in literature [32]. The quantity of studies on this topic, even if restricted to spheres exposes the complexity of the topic. While all of these correlations only consider single particles in an infinitely expanded medium, correlations describing the settling of collectives of spheres do also exist [8, 111, 112]. Obtaining models for shapes different from spheres is a topic of current research, with many correlations being proposed [7, 16, 41, 61, 136]. While the elongation and flatness of an object are among the most influential parameters, they are not sufficient to describe all effects, as also the density difference between particle and fluid [7] or the orientation [125] are, among other characteristics, relevant parameters for a model aiming to correctly predict the dynamics of particles in a flow. Due to the high number of complex dependencies, correlations specific to a certain type of particles [30, 34] might be superior in prediction quality than one general one, as they are better suited for the respective characteristics. To be viable, this approach requires an abundant availability of data regarding various particles' shapes and parameters, e.g., obtained from tomographic scans [35]. This is achieved via the creation of open databases [36].

Eulerian simulation approaches depict less physical characteristics of the particles and therefore rely strongly on the quality of the underlying model. This class of methods has already been applied, e.g., for the simulation of particles in magnetic chromatography [91] utilizing an advection–diffusion equation or solute transport with a fractional advection–diffusion equation [29, 133]. Since they are applied especially when a large number of entities is considered, the influence on the fluid may not be neglected, as done for dilute suspensions [85]. To integrate it, the fluid is usually modeled by the volume-averaged Navier–Stokes equations (VANS) [4]. While the approach is well established for conventional methods like the finite volume method or the finite element method [11, 48], only few studies exist regarding the LBM. However, almost none of the latter schemes account for moving objects, as they are all tested only for a constant or spatially varying porosity [12, 45, 154], except one which also accounts for temporal derivatives. It was additionally qualitatively evaluated for particle flows, coupled with an advection–diffusion equation [59, 87].

The aim of this work is to provide the tools and description of a procedure for the detailed investigation of particle settling behaviour and creation of models for the drag coefficient and terminal settling velocity, based on LBM simulations. Furthermore the feasibility of the presented approach is demonstrated using a set of 200 superellipsoids. The derived correlations can be applied to improve the quality of large scale simulations and help in the design of processes by providing better estimates. Combining these tools with a large database of particle data, a mostly automated process for the compilation of new specialized models could be established.

The main part of this thesis is structured as follows: first the underlying model is discussed in Chapter 2 along with existing drag correlations from literature, which are used for comparison and validation. In Chapter 3 the methods applied from literature are given and new ones like the momentum loss algorithm are proposed. Within the context of this work, those approaches were implemented in the open-source C++ LBM package OpenLB [70]. The extension of HLBM to 3D and arbitrary shapes is discussed in more detail in Chapter 4 and first validations are presented. The whole method is then analysed and extensively validated in Chapter 5. Finally an application is shown along with a proposed proceeding to obtain new correlations in Chapter 6 and an outlook is given in Chapter 7.

2 Modeling of Particles Submersed in Fluid

Mathematical models are a depiction of a confined part of reality. They usually aim to give a forecast utilizing mathematical formulations based on observations [69]. Heinrich Hertz formulated three requirements for a model in the introduction to his book "Prinzipien der Mechanik": sufficiency, correctness and expediency [58]. The first one means that a model may not contain any contradictions within itself or the framework it is embedded in. Regarding the second point, a model should depict all relevant relations and therefore not vary widely from observations. As correctness can only be claimed based on current knowledge and available observations, this needs to be checked recurrently upon new insights [69]. Lastly the expediency favors the easiest model if several are equivalent regarding the other two points. A principle also known as Occam's razor.

In this chapter the models on which the later discussed simulations are based are described. They are parted in two categories, namely models regarding the fluid (Section 2.1) and models regarding the particles (Section 2.2). The interactions between these are described via the acting forces in Section 2.3 and coupling approaches in Section 2.4.

2.1 Fluid Models

In the context of this work only Newtonian fluids forming a continuum are considered, which are at least approximately incompressible. Therefore the commonly used incompressible Navier–Stokes equations are discussed, as well as a version modified by volume-averaging. The latter is valuable in the depiction of multiple phases or components [148].

For both models describing fluid flows, the Reynolds number is an important characteristic parameter to indicate similarities in the flow pattern. As the ratio of inertial to viscous forces it is given by

$$\mathrm{Re} = \frac{UL}{\nu} \ . \tag{2.1}$$

The parameter U and L denote a characteristic flow speed and length, respectively. The kinematic viscosity ν is related via the fluid's density to the dynamic viscosity $\mu = \nu\rho_\mathrm{f}$.

2.1.1 Navier–Stokes Equations

To describe the dynamics of fluids usually the Navier–Stokes equations are applied, which are based on the principles of mass and momentum conservation. Denoting the domain filled with fluid by $\Omega_\mathrm{f}(t)$, the first one is equal to the integral of the fluid density not changing over time. Applying the material derivative [86], this can be written as

$$\frac{\partial \rho_\mathrm{f}}{\partial t} + \nabla \cdot (\rho_\mathrm{f} \boldsymbol{u}_\mathrm{f}) = 0 \ , \tag{2.2}$$

with the fluid's velocity $\boldsymbol{u}_\mathrm{f} \colon \Omega_\mathrm{f} \times I \to \mathbb{R}^3$ for a time interval I. For the conservation of momentum, first the forces in Euler's first law of motion [93] are parted in volume and surface forces. The latter are given via the Cauchy stress tensor $\boldsymbol{\sigma}$

[86]. Applying the divergence theorem to the surface integral and again taking the material derivative leads to

$$\frac{\partial \rho_{\mathrm{f}} \boldsymbol{u}_{\mathrm{f}}}{\partial t} + \rho_{\mathrm{f}}(\boldsymbol{u}_{\mathrm{f}} \cdot \nabla)\boldsymbol{u}_{\mathrm{f}} = \nabla \cdot \boldsymbol{\sigma} + \boldsymbol{F} \; . \tag{2.3}$$

The volume forces $\boldsymbol{F} : \Omega_{\mathrm{f}} \times I \rightarrow \mathbb{R}^3$ are, e.g., comprised of gravity. Assuming an incompressible and viscous fluid, Equation (2.2) simplifies to $\nabla \cdot \boldsymbol{u}_{\mathrm{f}} = 0$. Moreover assuming the fluid to be Stokesian [86] and requiring a linear dependency of the stress tensor on the deformation tensor, the expression

$$\boldsymbol{\sigma} = -p\boldsymbol{I} + \mu\left(\nabla \boldsymbol{u}_{\mathrm{f}} + (\nabla \boldsymbol{u}_{\mathrm{f}})^t\right) \; , \tag{2.4}$$

is obtained for the pressure $p : \Omega_{\mathrm{f}} \times I \rightarrow \mathbb{R}$ and unit tensor $\boldsymbol{I}$. With the uniform density and viscosity of the fluid, combining the above equations leads to the incompressible Navier–Stokes equations

$$\begin{aligned} \nabla \cdot \boldsymbol{u}_{\mathrm{f}} &= 0 \; , \\ \frac{\partial \boldsymbol{u}_{\mathrm{f}}}{\partial t} + (\boldsymbol{u}_{\mathrm{f}} \cdot \nabla)\boldsymbol{u}_{\mathrm{f}} &= -\frac{1}{\rho_{\mathrm{f}}}\nabla p + \nu \Delta \boldsymbol{u}_{\mathrm{f}} + \frac{1}{\rho_{\mathrm{f}}}\boldsymbol{F} \; . \end{aligned} \tag{2.5}$$

2.1.2 Volume Averaged Navier–Stokes Equations

In some cases the interface between two phases or components can not be resolved, or it is for practical reasons not feasible to do so, e.g., for a large amount of small distributed particles. However, if a considerable solid volume fraction is to be depicted, the influence of the particles' presence on the fluid is to be taken into account. Therefore averaging techniques are required. Since there are differences in literature, the notation in this section follows the one given by Whitaker

[148]. First an operator $\langle\cdot\rangle$ yielding the superficial average and one yielding the intrinsic average $\langle\cdot\rangle_{\mathrm{f}}$ for a quantity a in the fluid domain are given by

$$\begin{aligned} \langle a\rangle &= \frac{1}{|V_{\mathrm{c}}|}\int\limits_{V_{\mathrm{c}}\cap\Omega_{\mathrm{f}}} a \; d\Omega_{\mathrm{f}} \,, \quad \text{and} \\ \langle a\rangle_{\mathrm{f}} &= \frac{1}{|V_{\mathrm{c}}\cap\Omega_{\mathrm{f}}|}\int\limits_{V_{\mathrm{c}}\cap\Omega_{\mathrm{f}}} a \; d\Omega_{\mathrm{f}} \,, \end{aligned} \tag{2.6}$$

for a control volume $V_{\mathrm{c}} \subset \Omega$. Regarding the fluid's velocity the first one yields a value as if no second phase or component were present, while the second average is considered to be closer to measurable values. Denoting the ratio of fluid volume to the total volume in a given domain with ϵ_{f}, also called void fraction, it is apparent that $\langle a\rangle = \epsilon_{\mathrm{f}}\langle a\rangle_{\mathrm{f}}$.

The averaging can now be applied to the Navier–Stokes equations shown in Equation (2.5). However, in contrast to the superficial average velocity the vector field of the intrinsic velocity looses the property of solenoidality during the process [148]. Starting with

$$\begin{aligned} \langle\frac{\partial\rho_{\mathrm{f}}}{\partial t}\rangle + \langle\nabla\cdot(\rho_{\mathrm{f}}\boldsymbol{u}_{\mathrm{f}})\rangle &= 0 \,, \\ \langle\frac{\partial\rho_{\mathrm{f}}\boldsymbol{u}_{\mathrm{f}}}{\partial t}\rangle + \langle\rho_{\mathrm{f}}(\boldsymbol{u}_{\mathrm{f}}\cdot\nabla)\boldsymbol{u}_{\mathrm{f}}\rangle &= -\langle\nabla p\rangle + \langle\mu\Delta\boldsymbol{u}_{\mathrm{f}}\rangle + \langle\boldsymbol{F}\rangle \,, \end{aligned} \tag{2.7}$$

the equations can be simplified following Jackson [63] by implying a no-slip condition at the boundary between fluid and solid object, and utilizing the relation between superficial and intrinsic averaging. This leads to

$$\begin{aligned} \rho_{\mathrm{f}}\frac{\partial\epsilon_{\mathrm{f}}}{\partial t} + \rho_{\mathrm{f}}\nabla\cdot(\epsilon_{\mathrm{f}}\langle\boldsymbol{u}_{\mathrm{f}}\rangle_{\mathrm{f}}) &= 0 \,, \\ \rho_{\mathrm{f}}\frac{\partial\epsilon_{\mathrm{f}}\langle\boldsymbol{u}_{\mathrm{f}}\rangle_{\mathrm{f}}}{\partial t} + \rho_{\mathrm{f}}\nabla\cdot(\epsilon_{\mathrm{f}}\langle\boldsymbol{u}_{\mathrm{f}}\boldsymbol{u}_{\mathrm{f}}^{t}\rangle_{\mathrm{f}}) &= -\epsilon_{\mathrm{f}}\langle\nabla p\rangle_{\mathrm{f}} + \mu\epsilon_{\mathrm{f}}\langle\Delta\boldsymbol{u}_{\mathrm{f}}\rangle_{\mathrm{f}} + \epsilon_{\mathrm{f}}\langle\boldsymbol{F}\rangle_{\mathrm{f}} \,. \end{aligned} \tag{2.8}$$

It should be noted that $(\boldsymbol{u}_{\mathrm{f}}\cdot\nabla)\boldsymbol{u}_{\mathrm{f}} = \nabla\cdot(\boldsymbol{u}_{\mathrm{f}}\boldsymbol{u}_{\mathrm{f}}^{t})$ only holds if $\nabla\cdot\boldsymbol{u}_{\mathrm{f}} = 0$, i.e., for solenoidal vector fields, and therefore has to be applied before switching to the intrinsic averaging operator.

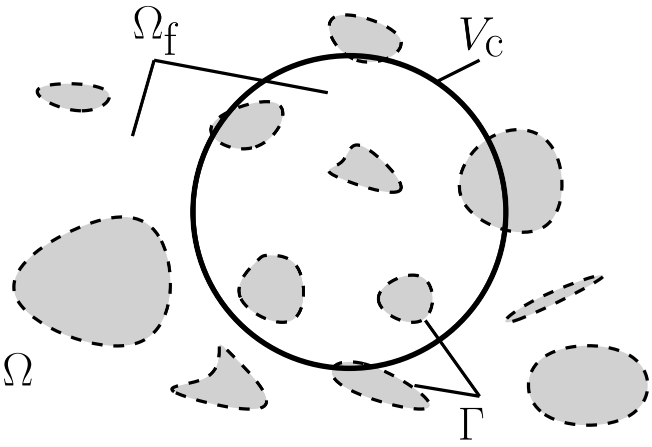

Figure 2.1: *Schematic representation of the fluid and solid domain with a control volume. (Source: Own representation based on Whitaker [148], Figure 4.2)*

With the chain rule and the divergence theorem the pressure and viscous terms can be rewritten according to Jackson [63] by

$$-\epsilon_f \langle \nabla p \rangle_f + \mu \epsilon_f \langle \Delta \boldsymbol{u}_f \rangle_f = -\nabla(\epsilon_f \langle p \rangle_f) + \mu \Delta(\epsilon_f \langle \boldsymbol{u}_f \rangle_f) - \frac{1}{|\Omega|} \int\limits_{\Gamma \cap V_c} \boldsymbol{\sigma n} \, d\Gamma \, . \tag{2.9}$$

The interface between fluid and rigid bodies is denoted by Γ, as depicted in Figure 2.1, and $\boldsymbol{n}$ represents the surface normal vector. The last term containing the integral represents the momentum exchanged between fluid and solid components and is denoted by $\boldsymbol{M}$ in the following.

The remaining term for closer consideration is the one, non-linear in velocity. Enwald et al. [38] applied a procedure similar to Reynolds decomposition from turbulence theory to split the averaged product, by splitting the velocity in an averaged value and the deviation from that. This yields

$$\rho_f \langle \boldsymbol{u}_f \boldsymbol{u}_f \rangle_f = \rho_f \langle \boldsymbol{u}_f \rangle_f \langle \boldsymbol{u}_f \rangle_f - \sigma_{SG} \, , \tag{2.10}$$

with a new subgrid stress term σ_{SG}, obtained similar as for the Reynolds-averaged Navier–Stokes equations. Finally inserting Equations (2.9) and (2.10) in Equation (2.8) yields the set denoted as volume-averaged Navier–Stokes equations in this thesis

$$\begin{aligned} \rho_{\mathrm{f}}\frac{\partial \epsilon_{\mathrm{f}}}{\partial t} + \rho_{\mathrm{f}}\nabla\cdot(\epsilon_{\mathrm{f}}\langle \boldsymbol{u}_{\mathrm{f}}\rangle_{\mathrm{f}}) = 0\ , \\ \rho_{\mathrm{f}}\frac{\partial \epsilon_{\mathrm{f}}\langle \boldsymbol{u}_{\mathrm{f}}\rangle_{\mathrm{f}}}{\partial t} + \rho_{\mathrm{f}}\nabla\cdot(\epsilon_{\mathrm{f}}\langle \boldsymbol{u}_{\mathrm{f}}\rangle_{\mathrm{f}}\langle \boldsymbol{u}_{\mathrm{f}}\rangle_{\mathrm{f}}) = -\nabla(\epsilon_{\mathrm{f}}\langle p\rangle_{\mathrm{f}}) + \mu\Delta(\epsilon_{\mathrm{f}}\langle \boldsymbol{u}_{\mathrm{f}}\rangle_{\mathrm{f}}) + \epsilon_{\mathrm{f}}\langle \boldsymbol{F}\rangle_{\mathrm{f}} \\ -\boldsymbol{M} + \nabla\cdot\sigma_{\mathrm{SG}}\ . \end{aligned} \tag{2.11}$$

2.1.3 Boltzmann Equation

Developed by Ludwig Boltzmann in 1872 [18], the Boltzmann equation is used to describe the statistical behaviour of systems in a non-equilibrium state. Considering a particle distribution function $f : \Omega_{\mathrm{f}} \times \mathbb{R}^3 \times I \to \mathbb{R}$ defined on a six-dimensional phase space, yielding the density of particles with a given velocity at a given location and time, the equation models the change of this quantity due to collisions of said particles. It should be noted that 'particles' refers in this context to the molecules of an ideal gas and should not be confused with the macroscopic particles whose behaviour is studied in this work and are described in Section 2.2. Taking the total derivative with respect to the time, the equation is given by [72]

$$\frac{\partial f}{\partial t} + \xi\cdot\nabla f + \frac{\boldsymbol{F}}{\rho}\frac{\partial f}{\partial \xi} = \left(\frac{\partial f}{\partial t}\right)_{\mathrm{coll}}\ , \tag{2.12}$$

for a particle velocity ξ, the density of a particle ρ and the right hand side representing the change due to collisions. More specifically the term Boltzmann equation refers to the form of the equation expressing the collision term by a rather unwieldy integral over the phase space, which Boltzmann found applying the 'stosszahlansatz' [18]. For the latter he considered all possible collision for a mono-atomic ideal gas. Despite this assumption, the application of the Boltzmann equation was later extended to various transport problems, like that of neutrons, radiative transfer [18] and also quantum mechanics [130].

Since the calculation of the collision integral might be challenging, simplifications have been proposed in literature. Most commonly applied is the one by Bhatnagar, Gross and Krook [10], in the following referred to as BGK collision term. Their assumption was that the collisions force the system towards an equilibrium state, which can be described by the Maxwell–Boltzmann distribution, given by [72]

$$f^{\mathrm{eq}}(\xi) = \rho \left(\frac{1}{2\pi k_{\mathrm{B}} T} \right)^{3/2} e^{-|\xi - \boldsymbol{u}|^2/(2k_{\mathrm{B}}T)} , \tag{2.13}$$

with $k_{\mathrm{B}} \approx 1.38 \times 10^{-23}\,\mathrm{m}^2\,\mathrm{kg}/(\mathrm{s}^2\,\mathrm{K})$ denoting the Boltzmann constant and for a temperature T. In this formula $\boldsymbol{u}$ refers to the local mean velocity. Together with a relaxation time τ this leads to the BGK collision term

$$\left(\frac{\partial f}{\partial t} \right)_{\mathrm{coll}} = -\frac{1}{\tau} (f - f^{\mathrm{eq}}) . \tag{2.14}$$

It was proven by many studies based on this simplification, including this work, that it produces correct results comparing it to measurements. As it also contains no contradictions, it is thereby the preferable model regarding the principle of expediency by Hertz [58].

2.2 Particle Models

To describe the dynamics of particles, further characteristic numbers are required. The first one is the particle Reynolds number Re_{p}, which is important for correlations describing the drag force affecting an object as discussed in Section 2.3. It is defined similar to the fluid, now adapted for particles, by

$$\mathrm{Re}_{\mathrm{p}} = \frac{d_{\mathrm{eq}} |\boldsymbol{u}_{\mathrm{f}} - \boldsymbol{u}_{\mathrm{p}}|}{\nu} , \tag{2.15}$$

with the diameter of the volume equivalent sphere d_{eq}, usually chosen as the characteristic length. For the characteristic speed the absolute of the particle's velocity $\boldsymbol{u}_{\mathrm{p}}$ relative to the fluid is used.

The Stokes number St, defined as the ratio of the characteristic response time of the particle to the characteristic response time of the flow, is used to describe the particle's behavior. While for values well below 1 the particle follows the streamlines closely, it will detach thereof due to inertia for larger values. The characteristic number is defined as

$$\mathrm{St} = \frac{\rho_\mathrm{p} d_\mathrm{p} |\boldsymbol{u}_\mathrm{f}|}{18\mu} , \tag{2.16}$$

with the particle's density ρ_p and diameter d_p. The latter can be replaced by the diameter of the volume equivalent sphere in the case of a non-spherical particle.

Approaches considering the particle component as continuum, as discussed later, usually also include diffusion in the model. It is therefore sensible to also consider the Péclet number

$$\mathrm{Pe} = \frac{LU}{D} , \tag{2.17}$$

defined as ratio of convective to diffusive transport, with the diffusion coefficient D. It will be useful to chose appropriate discretization schemes in Chapter 3, considering the transportiveness property, i.e., a discretization scheme's direction of influence should respect the flow direction [144].

As already mentioned in the introduction, there are two approaches for the modeling of particle dynamics. The first one is the Lagrangian, which is discussed in Section 2.2.1. It describes the motion from the point of view of an observer moving with the particle. Since in this case each object is tracked separately, it offers more possibilities for a detailed modeling. Therefore systems and parameters to quantify the representation of particle shape are introduced in Section 2.2.2. Instead describing the motion for a location fixed in space, i.e., particles entering and leaving the said location, leads to the Eulerian approach, depicting the particle collective as a continuum. It is discussed in Section 2.2.3. Both approaches are linked by the material derivative already introduced in Section 2.1.1. It was furthermore found in studies that for an increasing number of particles, the results of the Lagrangian approach converge towards the ones of Eulerian simulations [115], with a good agreement if at least 10^5 particles are considered.

2.2.1 Particle Motion

A first description of the dynamics of objects is given by Newton's laws of motion. Those have been extended from point particles to rigid bodies by Euler, his first and second law of motion are given by

$$\boldsymbol{F}_{\mathrm{p}} = m_{\mathrm{p}} \frac{\partial \boldsymbol{v}_{\mathrm{cm}}}{\partial t} \quad \text{and} \quad \boldsymbol{T}_{\mathrm{p}} = \boldsymbol{J}_{\mathrm{p}} \frac{\partial \boldsymbol{\omega}_{\mathrm{cm}}}{\partial t} \,, \tag{2.18}$$

for a torque $\boldsymbol{T}_{\mathrm{p}}$ acting on the object with angular velocity $\boldsymbol{\omega}_{\mathrm{p}}$ and moment of inertia $\boldsymbol{J}_{\mathrm{p}}$ [93]. Denoting the velocity of the center of mass of a particle with $\boldsymbol{v}_{\mathrm{cm}}$, this allows to calculate the position of the center of mass $\boldsymbol{x}_{\mathrm{cm}} = \partial \boldsymbol{v}_{\mathrm{cm}} / \partial t$ and angle $\boldsymbol{\theta} = \partial \boldsymbol{\omega}_{\mathrm{cm}} / \partial t$ of the object. The forces acting on the particle can be divided in surface forces $\boldsymbol{F}_{\mathrm{p,S}}$ like drag force, and volume forces $\boldsymbol{F}_{\mathrm{p,V}}$ like gravitation, whereby the latter often vanish considering the torque, since a homogeneous density distribution within a particle is considered in this work. The surface forces can furthermore be described by using the stress tensor [86], which leads to

$$\begin{aligned} \boldsymbol{F}_{\mathrm{p}} &= \boldsymbol{F}_{\mathrm{p,V}} + \boldsymbol{F}_{\mathrm{p,S}} = \boldsymbol{F}_{\mathrm{p,V}} + \int_{\Gamma} \boldsymbol{\sigma} \cdot \boldsymbol{n} \, d\Gamma \,, \\ \boldsymbol{T}_{\mathrm{p}} &= \int_{\Gamma} (\boldsymbol{r} \times \boldsymbol{\sigma}) \cdot \boldsymbol{n} \, d\Gamma \,, \end{aligned} \tag{2.19}$$

with Γ being the particle surface and $\boldsymbol{r}$ denoting the distance vector between a surface point and the object's center of mass. More details on the acting forces and their modeling is given in Section 2.3.

2.2.2 Particle Shape Description

Since Euler's laws of motion hold not only for point masses, but also for particles with distributed mass and arbitrary shape, the influence of the latter on the motion can be studied. To be able to formulate correlations which depend on the particle shape, it needs to be quantified. As found in discussions [7], this is a complex task and a single parameter is not sufficient to capture all relevant aspects. However, for some applications, like the analysis of gravel, classification systems are established. They are usually based on the main axis lengths of the particle, here denoted by a_L, a_I and a_S for the longest, intermediate and shortest axis, respectively. Such systems have been proposed by Sneed and Folk [124] or Zingg [159]. Later Blott and Pye [13] introduced two separate, more sophisticated systems with more classes, differentiating between rounded and non-rounded particles.

This section deals with the introduction of parameters, which allow some kind of quantification, and is oriented on [136]. A first approach are measures regarding the size. Notable are the minimum and maximum Feret diameter, given by the minimal and maximal distance between two parallel planes, which are tangential to the particle's surface. Furthermore the diameter of the smallest sphere containing the particle d_ext and the the one of the largest sphere still fitting inside the particle d_int are of interest. Considering the volume of the particle V_p, also the diameter of a sphere with equal volume can be defined

$$d_\mathrm{eq} = \left(\frac{6}{\pi} V_\mathrm{p} \right)^{1/3} . \tag{2.20}$$

Together with the particle's surface A_p these parameters can be combined to obtain more sophisticated ones. As the most common example to be mentioned here, the aspect ratio is frequently calculated in various studies. The definitions may vary, though. It is often found as the ratio of maximum to minimum Feret diameter [108]. In a more detailed view, the elongation and flatness given by

$$E = a_\mathrm{I}/a_\mathrm{L} \,, \quad F = a_\mathrm{S}/a_\mathrm{I} \,, \tag{2.21}$$

can be considered, allowing to differentiate between rod-like and plate-like particles. Thereby it is also possible to define the aspect ratio via these measures as

$AR = 0.5(E + F)$ [129]. Another common parameter regarding the compactness is the convexity

$$\kappa_{\mathrm{con}} = \frac{V_{\mathrm{p}}}{V_{\mathrm{p,conv}}} \,, \tag{2.22}$$

with $V_{\mathrm{p,conv}}$ being the volume of the convex hull. The latter is defined as the volume of the smallest convex object fully containing the particle. Analogously the solidity can be defined as ratio of the particle's surface to the one of its convex hull. The sphericity [145] is also concerned with the compactness of an object and is given by

$$\psi = \frac{1}{A_{\mathrm{p}}} \sqrt[3]{\pi \left(6V_{\mathrm{p}}\right)^2} \,. \tag{2.23}$$

It can be further specialized by division into crosswise sphericity $\psi_\perp$, i.e., considering the surface in direction of motion, and lengthwise sphericity $\psi_\parallel$, i.e., considering the surface parallel to the direction of motion. Depending on the considered particle type and application, additional parameters, which are more specific to some aspects can be of interest. One example is the roundness [52] describing the curvature of the particle's corners and edges by

$$\kappa_{\mathrm{rnd}} = \frac{V_{\mathrm{p}}}{A_{\mathrm{p}} \left(8 a_{\mathrm{L}} a_{\mathrm{I}} a_{\mathrm{S}}\right)^{1/3}} \,, \tag{2.24}$$

or the circularity

$$\kappa_{\mathrm{circ}} = \frac{A_{\mathrm{p,max}}}{0.25 \pi d_{\mathrm{eq}}^2} \,, \tag{2.25}$$

with $A_{\mathrm{p,max}}$ being the maximum projected area of the particle. If friction or surface reactions are to be considered, the texture of the surface becomes important. A first approach in its description is the irregularity parameter [108]

$$\kappa_{\mathrm{irreg}} = \frac{d_{\mathrm{int}}}{d_{\mathrm{ext}}} \,. \tag{2.26}$$

Another more detailed, but also more complex description of the surface is obtainable via Fourier analysis of the surface texture [153]. If an angle-dependent investigation of the particle geometry is possible, additional parameters regarding the angularity can be defined [108, 129].

As some sophisticated parameters might be unwieldy and complex to calculate, their utilization is often restricted to specialized applications. To be generally applicable and useful in practice the parameters need to be accessible via current measurement devices [7]. A common procedure is image analysis, whereby only the 2D equivalent of some parameters can be retrieved. It was found in studies, however, that the 2D parameters are correlated to their 3D counterpart [129]. Nevertheless complex parameters can be formulated in two dimensions, e.g., by considering the similarity to various shapes. Let C_0 be the number of characteristic corners and H_1, H_2 and H_3 be the ratio of the measured area to the one of a square, circular and triangular shape, defined by the minimum Feret diameter and the one perpendicular to it. Together with the elongation the parameter

$$\kappa_{\mathrm{sd}} = C_0 + \det \begin{bmatrix} E & H_1 \\ H_2 & H_3 \end{bmatrix} , \tag{2.27}$$

can be defined [107]. While this parameter is capable of differentiating various particle shapes, it fails to capture the roundness or irregularity of particles with few characteristic corners. Also basic operations in image processing like erosion can be used to define a mesoscopic set of shape parameters [108].

To describe rather characteristics of the flow behaviour of the particles than of their shape, more abstract parameters were obtained through the combination of the basic ones given at the beginning of this section. The one most frequently discussed is the Corey shape factor [33, 94], which is related to the flatness of the object and given by

$$\kappa_{\mathrm{CSF}} = \frac{a_{\mathrm{S}}}{\sqrt{a_{\mathrm{I}} a_{\mathrm{L}}}} . \tag{2.28}$$

Applying principles from communication theory, an entropy-like parameter denoted as Hofmann shape entropy [60] can be defined as

$$\kappa_{\mathrm{H}} = -\frac{\tilde{a}_{\mathrm{S}} \ln(\tilde{a}_{\mathrm{S}}) + \tilde{a}_{\mathrm{I}} \ln(\tilde{a}_{\mathrm{I}}) + \tilde{a}_{\mathrm{L}} \ln(\tilde{a}_{\mathrm{L}})}{\ln(3)} , \tag{2.29}$$

with the normalized axis lengths $\tilde{a}_i = a_i/(a_{\mathrm{S}} + a_{\mathrm{I}} + a_{\mathrm{L}})$ for $i \in \{S, I, L\}$. It proved to be useful in the description of settling ellipsoids [113]. Finally Bagheri and

Bonadonna [7] introduced two parameters in their investigation of the settling behavior of arbitrarily shaped particles, given by

$$\begin{aligned} \kappa_{\mathrm{BB,S}} &= FE^{1.3}\left(\frac{d_{\mathrm{eq}}^3}{a_{\mathrm{L}}a_{\mathrm{I}}a_{\mathrm{S}}}\right) , \\ \kappa_{\mathrm{BB,N}} &= F^2E\left(\frac{d_{\mathrm{eq}}^3}{a_{\mathrm{L}}a_{\mathrm{I}}a_{\mathrm{S}}}\right) . \end{aligned} \tag{2.30}$$

With the first one related to the Stokes regime (i.e., $\mathrm{Re_p} < 1$) and the second one to the Newton regime (i.e., $1000 < \mathrm{Re_p} < 10^5$), these parameters were found to be useful in the description of the drag force acting on the single settling particle. Furthermore this parameters are comparably easy to obtain as only information about the volume and major axis lengths are required.

2.2.3 Advection–Diffusion Equation

Depicting the particles as a continuum by their concentration c, the conservation of mass has to be satisfied, which was stated for a system free of sources or sinks in Equation (2.2). Now allowing for particles to enter and leave the domain, this leads to

$$\frac{\partial c}{\partial t} + \nabla \cdot \boldsymbol{j} = s , \tag{2.31}$$

with a source / sink term s and the total flux of particles denoted by $\boldsymbol{j}$. While the first term of the equation describes the change of concentration over time, the flux is given as the sum of advective and diffusive flux. The latter can be approximated by $-D\nabla c$ with the diffusivity D, according to Fick's first law. Applying this to the equation of mass conservation leads to the advection–diffusion equation

$$\frac{\partial c}{\partial t} + \boldsymbol{u}_{\mathrm{p}} \cdot \nabla c - D\Delta c = s , \tag{2.32}$$

assuming that the vector field $\boldsymbol{u}_{\mathrm{p}}$ is solenoidal. The diffusivity for a given solute and solvent can be looked up in literature or determined experimentally. With some restrictions it can also be calculated, e.g., using the Stokes–Einstein equation [25] given by

$$D = \frac{k_\mathrm{B} T}{6\pi\mu R} \,. \tag{2.33}$$

It assumes the solute as a rigid sphere with radius R submersed in a continuous solvent, which thereby forms an infinitely diluted solution. This view on the topic requires the radius of a solute object to be at least five times the one of a solvent molecule to obtain a prediction with a reasonable error [25]. Many extensions to this equation exist, e.g., for non-dilute suspensions. Typical values for the diffusion coefficient are in the range of 10^{-6} to $10^{-4}\,\mathrm{m}^2/\mathrm{s}$ for a gaseous solvent and 10^{-10} to $10^{-9}\,\mathrm{m}^2/\mathrm{s}$ for a liquid solvent [25].

Finally it should be noted that different interpretations for this equation exist, as it simply describes the transport of a scalar quantity c, which does not necessarily need to be seen as a particle concentration. It can also represent a temperature, in this case the parameter D is to be interpreted as thermal diffusivity, i.e., the thermal conductivity divided by density.

2.3 Forces

In this section forces relevant for a model describing the dynamics of particles submersed in a fluid are recapitulated. Special attention is given to the drag force, as it is the force mainly defining the behavior of a settling particle and is fairly complex to model, wherefore the details of existing models are discussed in following subsections.

A falling object usually experiences an acceleration due to a gravitational force. Since it not only depends on the mass of two objects, but also on their distance, the acceleration a particle experiences depends on its altitude. On the earth's surface the acceleration is usually approximated as $|\boldsymbol{g}| = 9.81\,\mathrm{m}/\mathrm{s}^2$. This force is opposed by buoyancy. Since the pressure in a fluid increases with depth, a submersed object experiences a pressure difference between its top and bottom. The magnitude of the force is proportional to the displaced fluid, assuming the particle is not floating on the surface or only partially submersed, the forces are given by

$$\boldsymbol{F}_{\mathrm{bg}} = m_{\mathrm{p}}\boldsymbol{g} - \rho_{\mathrm{f}} V_{\mathrm{p}} \boldsymbol{g} = m_{\mathrm{p}} \left(1 - \frac{\rho_{\mathrm{f}}}{\rho_{\mathrm{p}}}\right) \boldsymbol{g} \ . \tag{2.34}$$

While gravity and buoyancy cover the relevant external forces required in this work, the hydrodynamic force remains. In the transient case it is composed of three parts with the first one being the steady state part, described by the drag force [96]. The others are expressed by the Basset history force and the added mass force. Therefore the hydrodynamic force is given by

$$\boldsymbol{F}_{\mathrm{h}} = \boldsymbol{F}_{\mathrm{D}} + \boldsymbol{F}_{\mathrm{am}} + \boldsymbol{F}_{\mathrm{B}} \ . \tag{2.35}$$

The added mass force is caused by the fact that an object moving through a surrounding fluid has to displace the volume in its way. For a sphere and an inviscid fluid it is given by

$$\boldsymbol{F}_{\mathrm{am}} = \frac{\rho_{\mathrm{f}} V_{\mathrm{p}}}{2} \frac{d\left(\boldsymbol{u}_{\mathrm{f}} - \boldsymbol{u}_{\mathrm{p}}\right)}{dt} \ . \tag{2.36}$$

The reason for the denotation of this force becomes apparent, inserting this force in the momentum equation of Euler's first law (see Equation (2.18)) and rearranging it, since it effectively adds half of the displaced fluid mass to the particle mass.

The Basset history force [9] originates from unsteadiness and is related to decaying vorticity [96]. It is thereby a memory term due to a delayed adaption of the fluid movement in the boundary layer and is given by

$$\boldsymbol{F}_{\mathrm{B}} = \frac{3}{2} d_{\mathrm{p}}^2 \sqrt{\pi \rho_{\mathrm{f}} \mu} \int_0^t \frac{1}{\sqrt{t - t'}} \frac{d\left(\boldsymbol{u}_{\mathrm{f}} - \boldsymbol{u}_{\mathrm{p}}\right)}{dt} \, dt' \ . \tag{2.37}$$

Finally the drag is the major force acting on the particle, besides the external forces, in the setups considered in this work. By nature it is directed opposite to the direction of motion and can be divided in two parts, namely the form and friction drag [96]. The first depends on the size and shape of the particle, since it arises from a pressure difference between front and back of the particle, with front and back defined according to the direction of motion. The latter is related to friction and originates from interactions of the fluid boundary layer with the particle's surface. It therefore depends on the particle's shape and surface texture. Overall the drag is given by

$$\boldsymbol{F}_{\mathrm{D}} = \frac{1}{2}\rho_{\mathrm{f}}(\boldsymbol{u}_{\mathrm{p}} - \boldsymbol{u}_{\mathrm{f}})^2 C_{\mathrm{D}} A_{\mathrm{p}} \,, \tag{2.38}$$

for a drag coefficient C_{D}, which is to be determined. Simple approximations exist for the special case of a settling sphere in an infinitely extended fluid domain. For particle Reynolds numbers well below 1, the coefficient can be approximated according to Stokes [128] by $C_{\mathrm{D}} = 24/\mathrm{Re}_{\mathrm{p}}$. For the range of $6000 < \mathrm{Re}_{\mathrm{p}} < 10^5$ Newton found the drag coefficient to be $C_{\mathrm{D}} \approx 0.44$ [96]. For higher particle Reynolds numbers, it enters the super-critical regime. For the intermediate regime between the approximations by Stokes and Newton various correlations have been proposed in literature, with the one by Schiller and Naumann [116] being depicted in Figure 2.2.

In the following correlations regarding the drag coefficient for various cases are discussed. First the intermediate regime for a sphere is studied more closely, with the assumption of a spherical particle, being dropped afterwards to discuss correlations for arbitrary particle shapes. Since in applications usually a large amount of particles is considered and not single ones, this section closes with the discussion of drag correlations for particle collectives.

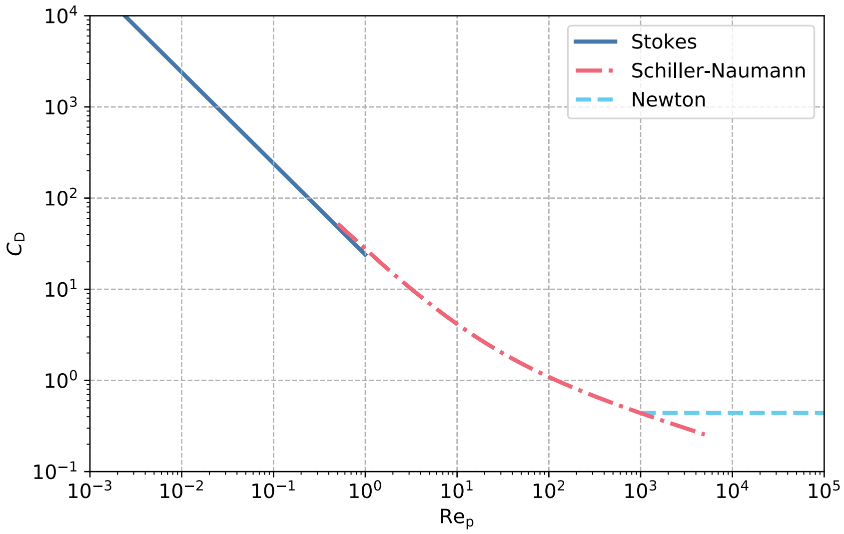

Figure 2.2: *Drag coefficient of a single settling sphere plotted against the particle Reynolds number. Depicted are the approximations by Stokes, Schiller and Naumann, and Newton around their region of applicability. (Source: Own representation)*

2.3.1 Drag Correlations for Single Spheres

A comprehensive overview of drag correlations for a single sphere in the intermediate regime is given by Dey et al. [32] and divides the correlations in those obtained by theoretical studies and those obtained empirically. Some of them are recapitulated here.

Oseen [102] extended Stokes' correlation by taking inertia into account and linearized the term quadratic in velocity of the Navier–Stokes equation. This finally leads to

$$C_\mathrm{D} = \frac{24}{\mathrm{Re_p}}\left(1 + \frac{3}{16}\mathrm{Re_p}\right) , \quad \text{for } \mathrm{Re_p} < 2 \, . \tag{2.39}$$

Starting with a dimensional analysis, Abraham [1] took advantage of the boundary layer theory assuming this region to be laminar. While effects of friction can be neglected elsewhere, they are important close to the considered object. Therefore in his model Abraham depicted a body comprised of the particle and its boundary layer. This new body allowed to derive a formulation for the drag independent of the viscosity for Reynolds numbers large enough to differentiate between a boundary layer and the remaining fluid domain. Using estimates by McDonald [92] for a remaining empirical parameter finally leads to

$$C_\mathrm{D} = \left(0.5407 + \sqrt{\frac{24}{\mathrm{Re}_\mathrm{p}}}\right)^2 , \quad \text{for } 0 < \mathrm{Re}_\mathrm{p} < 5000 . \tag{2.40}$$

While these approaches were mainly obtained by theoretical considerations, others obtained from a series of observations are also available. The first of these empirical formulas mentioned by Dey et al. [32] was obtained by Ruby [114]. However, no empirical coefficients were used or necessary in the original paper. Instead of focusing on the drag coefficient the terminal settling velocity was calculated from a force balance considering viscous forces according to Stokes's law and the momentum of the surrounding fluid on the particle, thereby bridging the gap between the Stokes and Newton regime while approximating these solutions in the limit. This type of correlations gained in complexity starting from the simple approach by Schiller and Naumann [116]

$$C_\mathrm{D} = \frac{24}{\mathrm{Re}_\mathrm{p}}\left(1 + 0.15\mathrm{Re}_\mathrm{p}^{0.687}\right) , \quad \text{for } \mathrm{Re}_\mathrm{p} < 1000 . \tag{2.41}$$

Based on 37 data points compiled from literature by Lapple and Shepherd [77], the correlation

$$C_\mathrm{D} = 0.284153\left(1 + \frac{9.04}{\mathrm{Re}_\mathrm{p}^{0.5}}\right)^2 P , \tag{2.42}$$

was proposed by Concha and Barrientos [24] with P being a polynomial of fifth order. They found an error to the experimental data of about 2.11%, claiming a good fit for particle Reynolds numbers up to 3×10^5. However, the data-set for a non-linear regression with five parameters is comparably small regarding today's opportunities, and the possibility of overfitting was not discussed. A larger data base was given, e.g., by Brown and Lawler [17], who compiled data from literature, finally leading to 480 points after revision regarding outliers and applicability, and correcting for wall influences. Based on this data Cheng [22] proposed

$$C_\mathrm{D} = \frac{24}{\mathrm{Re_p}}\left(1+0.27\mathrm{Re_p}\right)^{0.43} + 0.47\left(1-e^{-0.04\mathrm{Re_p^{0.38}}}\right) , \tag{2.43}$$

yielding an average relative error to the experimental data of 2.469%. Their study also found, in comparison to seven other correlations from literature, that independent of complexity every evaluated formula led to an averaged relative error below 5% regarding the drag coefficient. This also holds for intricate formulas like the one proposed by Almedeij [3], which is a combination of four functions with each comprised of several terms. Thereby it can be assumed that the description of the drag coefficient of a single settling sphere is well covered by literature and can thereby serve as a benchmark for methods in more complex investigations.

2.3.2 Drag Correlations for non-spherical Particles

Besides the drag coefficient sometimes explicit correlations regarding the terminal settling velocity are proposed. For spheres this was done, e.g., by Almedeij [3], Brown and Lawler [17] or Cheng [22]. While the errors are still below 5% they tend to be higher for such explicit estimations. Dropping the assumption of a spherical particle shape, only few correlations regarding the terminal settling velocity u_ts are available, e.g., by Haider and Levenspiel [47]

$$\begin{aligned} u_\mathrm{ts} &= \left(\frac{g\,\nu(\rho_\mathrm{p}-\rho_\mathrm{f})}{\rho_\mathrm{f}}\right)^{1/3}\left(\frac{18}{d_*^2}+\frac{2.335-1.744\psi}{\sqrt{d_*}}\right)^{-1} , \quad \text{with} \\ d_* &= d_{eq}\left(\frac{g(\rho_\mathrm{p}-\rho_\mathrm{f})}{\nu^2\rho_\mathrm{f}}\right)^{1/3} , \end{aligned} \tag{2.44}$$

limited to a sphericity between 0.5 and 1 for isometric particles. Nevertheless, changing the particle class can lead to errors above 25% [136], even if the given range of applicability is respected. Therefore it might be sensible to formulate correlations for a very specific class of particles, like Dellino et al. [30], who considered pumice particles of volcanic origin, leading to

$$u_{\mathrm{ts}} = \frac{1.2065\,\nu}{d_{\mathrm{eq}}} \left(\frac{d_{\mathrm{eq}}^3 g(\rho_{\mathrm{p}} - \rho_{\mathrm{f}})(\psi/\kappa_{\mathrm{circ}})^{1.6}}{\nu^2 \rho_{\mathrm{f}}} \right)^{0.5206} . \tag{2.45}$$

Drag correlations considering a preferably arbitrary shape of particles have to contain multiple shape parameters to cover a large range of possible shapes. Therefore correlations tend to be complex and require the groundwork of identifying the most influential parameters [57]. Ganser [41] proposed a correlation in 1993 taking only the sphericity into account as an additional parameter

$$\begin{aligned} C_{\mathrm{D}} &= \frac{24K_{\mathrm{S}}}{\mathrm{Re}_{\mathrm{p}}} \left(1 + 0.1118 \left(\frac{\mathrm{Re}_{\mathrm{p}} K_{\mathrm{N}}}{K_{\mathrm{S}}} \right)^{0.6567} \right) + \frac{0.4305 K_{\mathrm{N}}}{1 + 3305 K_{\mathrm{S}}/(\mathrm{Re}_{\mathrm{p}} K_{\mathrm{N}})} , \quad \text{with} \\ K_{\mathrm{S}} &= \frac{1}{3} + \frac{2}{3}\sqrt{\psi} , \\ K_{\mathrm{N}} &= 10^{1.8148(-\log\psi)^{0.5743}} . \end{aligned} \tag{2.46}$$

In this formula limited to isometric objects and based on a data set of 731 points compiled from literature, two coefficients regarding the behaviour in the Stokes and Newton regime were introduced. Later this was also adopted by Bagheri and Bonadonna [7] as stated in Section 2.2.2. These values can also be interpreted as drag correction factors, describing the deviation of the drag acting on the particle to the one which would be exerted on a volume equivalent sphere. For the Stokes regime correction factors were proposed by Leith [81]

$$K_{\mathrm{S}} = \frac{1}{3}\sqrt{\psi_{\perp}} + \frac{2}{3}\sqrt{\psi} , \tag{2.47}$$

who split it into contributions from form and friction drag, and Loth [84]

$$K_{\mathrm{S}} = \left(\frac{a_{\mathrm{L}} a_{\mathrm{I}}}{a_{\mathrm{S}}^2} \right)^{0.09} = \left(\frac{1}{\kappa_{\mathrm{CSF}}^2} \right)^{0.09} . \tag{2.48}$$

While Leith's original formula was based on sphere diameters of equal surface or projected area, later defined as (crosswise) sphericity, Loth based the formulation on the length of the main axes. Both found a discrepancy to experimental data and thereby the requirement for additional parameters, for which the orientation of the particle is often relevant though.

Based on the structure of previously defined correlations [140], Haider and Levenspiel [47] used a least squares method to fit the four coefficients to their experimental data points (408 spherical particles, 419 isometric particles, 87 discs). They presented the coefficients for correlations regarding nine different values for the sphericity, thereby demonstrating the possibility to derive several specialized correlations, and finally concluded with the general correlation

$$\begin{aligned} C_\mathrm{D} = \frac{24}{\mathrm{Re_p}}(1 + c_1 \mathrm{Re_p}^{c_2}) + \frac{c_3}{1 + c_4/\mathrm{Re_p}} \,, \quad & \text{with} \\ c_1 = e^{2.329 - 6.458\psi + 2.449\psi^2} \,, & \\ c_2 = 0.096 + 0.557\psi \,, & \\ c_3 = e^{4.905 - 13.894\psi + 18.422\psi^2 - 10.260\psi^3} \,, & \\ c_4 = e^{1.468 + 12.258\psi - 20.732\psi^2 + 15.886\psi^3} \,. & \end{aligned} \tag{2.49}$$

The measured deviations of general correlations to experimental data further reflected the high occurrence of different particle types in data. The most promising correlations regarding evaluation on different data-sets [7, 136] proposed in the last two decades are given by Bagheri and Bonadonna [7] by

$$
\begin{aligned}
C_\mathrm{D} &= \frac{24K_\mathrm{S}}{\mathrm{Re}_\mathrm{p}}\left(1+0.125\left(\frac{\mathrm{Re}_\mathrm{p}K_\mathrm{N}}{K_\mathrm{S}}\right)^{2/3}\right)+\frac{0.46K_\mathrm{N}}{1+5330/(\mathrm{Re}_\mathrm{p}K_\mathrm{N}/K_\mathrm{S})}\,, \quad \text{with}\\
K_\mathrm{S} &= 0.5\left(F_\mathrm{S}^{1/3}+F_\mathrm{S}^{-1/3}\right)\,,\\
K_\mathrm{N} &= 10^{c_1(-\log F_\mathrm{N})^{c_2}}\,,\\
c_1 &= 0.45+\frac{10}{e^{2.5\log\rho'}+30}\,,\\
c_2 &= 1-\frac{37}{e^{3\log\rho'}+100}\,,\\
F_\mathrm{S} &= FE^{1.3}\frac{d_{eq}^3}{a_\mathrm{S}a_\mathrm{I}a_\mathrm{L}}\,,\\
F_\mathrm{N} &= F^2E\frac{d_{eq}^3}{a_\mathrm{S}a_\mathrm{I}a_\mathrm{L}}\,.
\end{aligned}
\tag{2.50}
$$

and by Hölzer and Sommerfeld [61]

$$
C_\mathrm{D} = \frac{8}{\mathrm{Re}_\mathrm{p}\sqrt{\psi_\parallel}}+\frac{16}{\mathrm{Re}_\mathrm{p}\sqrt{\psi}}+\frac{3}{\sqrt{\mathrm{Re}_\mathrm{p}}\psi^{3/4}}+0.421^{0.4(-\log\psi)^{0.2}}\frac{1}{\psi_\perp}\,. \tag{2.51}
$$

The first of these correlations also respects the density ratio ρ' between fluid and particle. Both correlations provide significantly better results compared to preceding ones, especially for shapes strongly deviating from that of a sphere. In both studies this is achieved by a large number of better balanced data points. Hölzer and Sommerfeld [61] compiled information about 683 spherical particles, 337 cubical and cylindrical particles, 665 isometric particles and 386 discs and plates from literature, totaling in 2061 data points. Bagheri and Bonadonna [7] added own experimental data to a set compiled from literature to 2166 data points spread across the Stokes, intermediate and Newton regime. They further considered analytical solutions for 10^4 ellipsoids in the Stokes regime. Despite the improvements some effects are still not captured by currently available models, reflected in a spread visible in the data [7]. Therefore more parameters need to be considered and the development of a general process for the generation of such correlations becomes sensible. This allows to face the complexity of the shape dependency with easily obtainable correlations, given an appropriate available data set.

2.3.3 Correlations for Particle Collectives

Having discussed the deviation of the drag force from that of spherical particles due to shape in the previous section, in this one the assumption of the particle being solitary in an infinitely expanded medium is dropped. Correlations found in literature usually describe the average settling velocity of the upper front to the clear water zone for a suspension settling under gravity. Based on a terminal settling velocity, most often according to Stokes [128] (referred to as u_S), the formulations depend on the solid volume fraction ϕ. The correlations are given by

$$\begin{aligned}
u_\mathrm{Steinour}(\phi) &= u_\mathrm{S}(1-\phi)^2 e^{-4.19\phi}\ , && \text{(2.52a)}\\
u_\mathrm{Hawksley}(\phi) &= u_\mathrm{S}(1-\phi)^2 e^{-2.5(1-\phi)/(1-0.609\phi)}\ , && \text{(2.52b)}\\
u_\mathrm{RZ}(\phi) &= u_\mathrm{S}(1-\phi)^n\ , && \text{(2.52c)}\\
u_\mathrm{Oliver}(\phi) &= u_\mathrm{S}\left(1-0.75\phi^{\frac{1}{3}}\right)(1-2.15\phi)\ , && \text{(2.52d)}\\
u_\mathrm{BM}(\phi) &= u_\mathrm{ts}\frac{1-\phi}{(1+\phi^{\frac{1}{3}})e^{\frac{5\phi}{3(1-\phi)}}}\ . && \text{(2.52e)}
\end{aligned}$$

Further details on the correlations are given in Table 2.1. While most of the investigations are based on experimental data, Hawksley [51] based the formula on theoretical reasoning using the effective relative viscosity of a suspension given by Vand [142]. His results were found to be in good agreement with experiments for a solid volume fraction up to 35% [101]. One of the most frequently applied correlations regarding hindered settling is the one given by Richardson and Zaki, who investigated the topic not merely from a theoretical perspective [112] but also experimentally [111], considering not only the case of settling glass spheres, but also the fluidization of glass particles and other materials, e.g., steel, or shapes, e.g., cylinders. They concluded with a formula containing an exponent, which is chosen according to the particle Reynolds number and is given by

$$n = \begin{cases} 4.65\,, & \text{for } \ \mathrm{Re_p} < 0.2 \\ 4.35\mathrm{Re_p}^{-0.03}\,, & \text{for } \ 0.2 < \mathrm{Re_p} < 1 \\ 4.45\mathrm{Re_p}^{-0.1}\,, & \text{for } \ 1 < \mathrm{Re_p} < 500 \\ 2.39\,, & \text{for } \ 500 < \mathrm{Re_p} \end{cases} . \tag{2.53}$$

Later Garside and Al-Dibouni [42] proposed logistic curves describing the drag coefficient regarding their experimental data. Deriving an exponent for the equation of Richardson and Zaki from their results yielded

$$n = \frac{5.1 + 0.27\mathrm{Re_p}^{0.9}}{1 + 0.1\mathrm{Re_p}^{0.9}}\,, \tag{2.54}$$

finding this formulation similar in accuracy to their curves, however with significant deviations for low solid volume fractions ($\phi < 0.1$). Barnea and Mizrahi [8] compiled their data from several sources in literature and deduced a formulation for the creeping flow range. They state, however, that the correlation can be extended using drag correlations for single particles beyond the Stokes regime as reference value, as discussed in Section 2.3.1.

Table 2.1: *Information on the range of applicability for various correlations regarding the hindered settling of suspensions. Data aggregated from the respective publications.*

author	year	Equation	$\mathrm{Re_p}$	ϕ	material
Steinour [127]	1944	(2.52a)	0.0025–0.0026	$< 49,8\%$	tapioca, glass
Hawksley [51]	1951	(2.52b)	–	$< 35\%$	theoretical
Richardson and Zaki [111, 112]	1954	(2.52c)	< 7000	$< 66\%$	glass
Oliver [101]	1961	(2.52d)	< 0.39	$< 35\%$	Kallodoc
Barnea and Mizrahi [8]	1973	(2.52e)	< 1	$< 60\%$	various
Garside and Al-Dibouni[42]	1977	(2.54)	3.84–1180	$< 50\%$	glass

The comparability of the given correlations is limited [8], as definitions of relevant parameters, like the Reynolds number, differ and the results are related to different parameters, i.e., different velocities for the settling of a single sphere. Besides for the drag coefficient, also correlations regarding the force have been proposed, e.g., by Tenneti et al. [134]. Their investigation was based on IBM simulations and they split the absolute of the drag force again in form and friction drag, normalizing the term with the drag force according to Stokes. With the assumption of the normalized form drag being linearly dependent on the Reynolds number Re_m, defined via the mean flow velocity, and the friction drag being independent of it, they concluded with

$$
\begin{aligned}
F_\mathrm{D} &= \frac{F_\mathrm{D,single}}{(1-\phi)^3} + \mathrm{Re}_\mathrm{m} F_\mathrm{form} + F_\mathrm{friction}\,, \quad \text{with} \\
F_\mathrm{form} &= \phi^3 \left(0.95 + \frac{0.61\phi^3}{(1-\phi)^2} \right)\,, \\
F_\mathrm{friction} &= \frac{5.81\phi}{(1-\phi)^3} + 0.48 \frac{\phi^{1/3}}{(1-\phi)^4}\,.
\end{aligned}
\tag{2.55}
$$

For the drag force experienced by a single settling sphere $F_\mathrm{D,single}$ they applied the one given by Schiller and Naumann [116].

In a final step for a full correlation describing the settling of particle collectives of various shapes, the correlations presented in this section need to be combined with the ones in the previous section. This was done by He et al. [53], who tested various combinations considering a solid volume fraction between 0.1 and 0.35 in IBM simulations with $10 \leq \mathrm{Re}_\mathrm{p} \leq 200$. The best agreement was found using the correlation by Tenneti et al. [134] to depict the influence of the solid volume fraction and combining it with the correlation by Hölzer and Sommerfeld [61], describing the influence of particle shape. However, the orientation of the particles has to be taken into account.

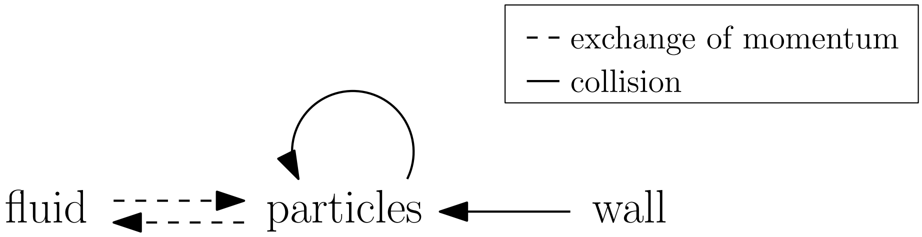

Figure 2.3: *Schematic of coupling between fluid, particles and the wall of the domain. (Source: Own representation)*

2.4 Coupling

In systems consisting of multiple components, the coupling between each of them is important to depict all relevant physical effects. Omitting additional effects like magnetic forces, all relevant remaining interactions are depicted in Figure 2.3. The easiest approach is to consider only the influence of the fluid on the particles, which is usually labeled as one-way-coupling and achieved via the forces discussed in Section 2.3. They are applied, e.g., in the calculation of the particle velocity $\boldsymbol{u}_\mathrm{p}$ applied in the advection–diffusion equation, discussed in Section 2.2.3. This of course is only justified if the impact of the particles' presence is negligible and the solution is diluted.

Multiple models exist for dense suspensions. If a Lagrangian approach is used for the particles, the multi-phase particle-in-cell method [5] can be applied, converting macroscopic parameters like the velocity of the flow field to Lagrangian points and aggregating information like the particle concentration within a cell. Alternatively the concentration can be depicted directly using the advection–diffusion equation. Having this Eulerian view on the particles, the VANS equations can be used for the fluid to represent the presence of the solid objects. Another approach would be to use interface tracking techniques considering the particles as a continuum, i.e., a suspension [100]. For this purpose also multi-component methods like the free energy method [119] can be used, allowing for a blurred interface and miscibility. Yamamoto et al. [151] compared the results of interface tracking and Lagrangian approaches to experimental data. For a surface-resolved representation of the particles, the exchanged momentum is calculated directly at the particles' surface [109] and the surrounding fluid is displaced. Since for these approaches the fluid and the particles influence each other, they are labeled as two-way-coupling.

Finally also taking particle–particle and particle–wall collisions into account, one achieves a four-way-coupling. For Lagrangian approaches each collision has to be modeled [95] and for implementations the topics of contact detection and contact treatment need to be covered. While the particles are depicted with an advection–diffusion equation, the collisions are represented on a macroscopic level via the diffusion.

3

Numerical Methods

Having the model set, the equations need to be solved. Since in many cases like for the Navier–Stokes equations, it is only possible to obtain analytical solutions for very specialized cases [88, 121], thereby with significant restrictions, numerical methods have to be applied to approximate the correct solution [86]. To solve the partial differential equations associated with the topic of particles settling in a fluid, often the classical methods like finite differences are applied. More sophisticated approaches are the finite volume method [99], considering the volume leaving and entering a cell, and the finite element method [122]. The latter considers macroscopic quantities via cell average values and can also be applied to solid mechanics. However, it is also possible not to solve for this macroscopic quantities directly but to describe the problem on a mesoscopic level via a statistical view on the molecular behaviour. This is what the Boltzmann equation is applied for, leading to the LBM when discretized [131].

The method has been developed from the lattice gas cellular automata in the late 80s with the aim of eradicating statistical noise [130], as the predecessor relied on Boolean representations. During the past three decades the approach was extended for various applications like multi-phase flows and made its way into mainstream. Not least due to its simplicity and good fitting for current distributed computing architecture the method has become popular, as the major part of the calculations is at least semi-local, i.e., requiring only information of directly neighbouring nodes [130]. Therefore the memory bandwidth is often the limiting factor for LBM computing performance. On the downside the LBM is from its basis formulated as time dependent and therefore usually inefficient in finding steady-state solutions compared to classical methods, for which, e.g., the Navier–Stokes equations can be formulated independent of time, directly calculating the steady-state solution. Since in this work dynamic cases are of interest, this drawback can be ignored. A more comprehensive list of advantages and disadvantages of the LBM with further literature references was aggregated by Krüger et al. [72].

3.1 Lattice Boltzmann Method for Fluid Flows

In this section the most common version of LBM is introduced, which is based on the BGK collision operator, discussed in Section 2.1.3, with one single relaxation time. Many sources in literature give a comprehensive overview, also discussing schemes with multiple relaxations times, boundary conditions, forcing schemes and various extensions to the method [2, 21, 72]. The method applied for the simulations is based on the lattice Boltzmann equation and is obtained by the end of this section. A Chapman–Enskog analysis [20] can be applied to ensure, that it matches the model, i.e., the Navier–Stokes equations, on a macroscopic level. Alternative approaches for the recovery of the macroscopic equations exist and are discussed by Krüger et al. [72].

To formulate the discrete algorithm, non-dimensionalization and recovery of macroscopic moments is necessary as well as the discretization of the domain, i.e., the phase space, the Maxwell–Boltzmann distribution, and the Boltzmann equation with BGK collision operator. These points will be discussed in the following subsections.

3.1.1 System of Units

For ease of use and to simplify the calculations, all relevant parameters and variables are non-dimensionalized by the discretization parameters, therefore yielding a spatial and time step size of one. To ensure that this scaling does not affect the solution, the condition is that similarity numbers like the Reynolds number remain unchanged. Denoting non-dimensionalized values with the superscript $^{\mathrm{L}}$ for *lattice system* and introducing the spatial and temporal discretization parameters δx and δt and finally using the fluid density as characteristic value yields

$$l^{\mathrm{L}} = \frac{l}{\delta x} , \quad t_{\mathrm{s}}^{\mathrm{L}} = \frac{t_{\mathrm{s}}}{\delta t} , \quad \rho^{\mathrm{L}} = \frac{\rho}{\rho_{\mathrm{f}}} , \tag{3.1}$$

for a length l, time span t_{s} and density ρ. From this three basic parameters more complex values like the velocity $\boldsymbol{u}$, force $\boldsymbol{F}$, viscosity ν, mass m and pressure p can be non-dimensionalized by

$$\begin{aligned} \boldsymbol{u}^{\mathrm{L}} &= \boldsymbol{u}\frac{\delta t}{\delta x} , \quad \boldsymbol{F}^{\mathrm{L}} = \boldsymbol{F}\frac{\delta t^2}{\rho_{\mathrm{f}}\delta x^4} , \quad \nu^{\mathrm{L}} = \nu\frac{\delta t}{\delta x^2} , \\ m^{\mathrm{L}} &= m\frac{1}{\rho_{\mathrm{f}}\delta x^3} , \quad p^{\mathrm{L}} = p\frac{\delta t^2}{\rho_{\mathrm{f}}\delta x^2} . \end{aligned} \tag{3.2}$$

Recalling the definition of characteristic numbers like the Reynolds, Stokes or Péclet number, their values remain unaffected by this operation and of course the step sizes in lattice units are given by $\delta x^{\mathrm{L}} = \delta t^{\mathrm{L}} = 1$.

By changing the discretization parameters the accuracy can be increased, however, errors of different sources need to be balanced [72]. While the discretization errors scale with δx^2 and δt^2, a compressibility error scaling with the squared Mach number has to be factored in [123]. This number is defined as the ratio of fluid velocity to the speed of sound. Since the latter error scales by $\delta t^2/\delta x^2$, the method is ensured to be second order accurate in space and first order accurate in time, establishing the relation $\delta t \sim \delta x^2$, denoted as *diffusive scaling* [72].

3.1.2 Discretization of the Phase Space

One pillar of the LBM in its basic form is the approximation of the computational domain by a structured uniform grid with step size δx, albeit approaches for non-uniform meshes exist, too [117]. It remains to find a discrete set replacing the continuous velocity space. Applying a Gauß–Hermite quadrature such sets of q velocities can be found as nodes $\boldsymbol{c}_i^{\mathrm{L}}$ of the quadrature rule with according weights w_i [72], with $i = 0, \dots, q-1$. Since the Navier–Stokes equations are to be approximated some conditions have to be met besides mass and momentum conservation. The moments, with the j-th moment given by

$$\sum_{i=0}^{q-1} w_i \left(\boldsymbol{c}_i^{\mathrm{L}}\right)^j , \tag{3.3}$$

have to obey conditions regarding isotropy up to the fifth moment [150]. Since all weights also need to be non-negative, a sufficiently large set is required [72]. Furthermore the lattice speed of sound depends on the chosen discretization. For most relevant sets in this thesis, it is given by $c_{\mathrm{s}}^{\mathrm{L}} = 1/\sqrt{3}$ [150].

A found discretization of the phase space is by convention denoted as DdQq, for a spatial dimension d and the number of discrete velocities q. For the Navier–Stokes equations, typical sets are D2Q9 and D3Q19, while for simpler cases like the advection–diffusion equation, the requirements regarding the isotropy are lower and thereby allow for smaller velocity sets like D2Q5 and D3Q7 [72]. For the latter a different lattice speed of sound is obtained, it is given by $c_{\mathrm{s}}^{\mathrm{L}} = 1/2$ [31]. The velocities and weights for the most common sets are given in Table 3.1.

Table 3.1: *Discrete lattice velocities and weights according to different discretizations of the velocity space. Data taken from Krüger et al. [72], and Deville and Gatsky [31].*

discretization	$\boldsymbol{c}_i^{\mathrm{L}}$	number	$\lvert\boldsymbol{c}_i^{\mathrm{L}}\rvert$	w_i
D2Q5	$(0,0)$	1	0	1/3
	$(\pm1,0),\ (0,\pm1)$	4	1	1/6
D2Q9	$(0,0)$	1	0	4/9
	$(\pm1,0),\ (0,\pm1)$	4	1	1/9
	$(\pm1,\pm1)$	4	$\sqrt{2}$	1/36
D3Q7	$(0,0,0)$	1	0	1/4
	$(\pm1,0,0),\ (0,\pm1,0),\ (0,0,\pm1)$	6	1	1/8
D3Q19	$(0,0,0)$	1	0	1/3
	$(\pm1,0,0),\ (0,\pm1,0),\ (0,0,\pm1)$	6	1	1/18
	$(\pm1,\pm1,0),\ (\pm1,0,\pm1),\ (0,\pm1,\pm1)$	12	$\sqrt{2}$	1/36

3.1.3 Discrete Equilibrium Distribution

To derive a discrete version of the Maxwell–Boltzmann distribution given by Equation (2.13), the assumption of everything being isothermal is made. Krüger et al. [72] presented a derivation via an Hermite series expansion, while Hänel [49] approaches the topic by expanding the term in the exponential function and applying a low Mach number expansion. Cutting off the expansion after a finite number of terms, a discretization error dependent on the Mach number is introduced. Both approaches lead to the same result, given by

$$f_i^{\mathrm{eq}}(\rho^{\mathrm{L}},\boldsymbol{u}^{\mathrm{L}}) = \rho^{\mathrm{L}} w_i \left(1 + \frac{\boldsymbol{c}_i \cdot \boldsymbol{u}^{\mathrm{L}}}{c_{\mathrm{s}}^2} - \frac{|\boldsymbol{u}^{\mathrm{L}}|^2}{2c_{\mathrm{s}}^2} + \frac{(\boldsymbol{c}_i \cdot \boldsymbol{u}^{\mathrm{L}})^2}{2c_{\mathrm{s}}^4}\right), \tag{3.4}$$

for the local density $\rho^{\mathrm{L}} = \rho^{\mathrm{L}}(\boldsymbol{x},t)$ and local velocity $\boldsymbol{u}^{\mathrm{L}} = \boldsymbol{u}^{\mathrm{L}}(\boldsymbol{x},t)$, which can be computed from the moments, as discussed in Section 3.1.4. For reasons of readability $f^{\mathrm{eq}}(\boldsymbol{c}_i,\rho^{\mathrm{L}},\boldsymbol{u}^{\mathrm{L}})$ is identified with $f_i^{\mathrm{eq}}(\rho^{\mathrm{L}},\boldsymbol{u}^{\mathrm{L}})$ and the superscript $^{\mathrm{L}}$ is dropped for the equilibrium distribution function, the lattice speed of sound and the discrete velocities, as from this point on these quantities are always given in lattice units. The discrete f_i are obtained in a similar way, also using Gauß–Hermite Polynomials and including the weights in the definition [72].

3.1.4 Macroscopic Moments

Macroscopic quantities can be computed from the particle distribution function f_i via the moments, as frequently presented in literature [49, 72, 150]. Similar to the equilibrium distribution function, the superscript $^{\mathrm{L}}$ is also dropped for the discrete particle distribution function obtained likewise as the discrete equilibrium distribution function, since from now on it is always considered to be in lattice units. Furthermore identifying $f(\boldsymbol{x}, \mathbf{c}_i, t)$ with $f_i(\boldsymbol{x}, t)$ the moments are obtained by

$$\begin{aligned} \sum_{i=0}^{q-1} f_i(\boldsymbol{x}, t) &= \rho^{\mathrm{L}}(\boldsymbol{x}, t) \, , \\ \sum_{i=0}^{q-1} \mathbf{c}_i f_i(\boldsymbol{x}, t) &= \rho^{\mathrm{L}}(\boldsymbol{x}, t) \boldsymbol{u}^{\mathrm{L}}(\boldsymbol{x}, t) \, , \\ \sum_{i=0}^{q-1} \mathbf{c}_i \boldsymbol{c}_i^t f_i(\boldsymbol{x}, t) &= \mathbf{\Pi}^{\mathrm{L}}(\boldsymbol{x}, t) \, , \end{aligned} \tag{3.5}$$

with $\mathbf{\Pi}^{\mathrm{L}}$ being the stress tensor. In the context of the lattice Boltzmann equation, the isothermal equation of state is given by

$$p^{\mathrm{L}}(\boldsymbol{x}, t) = c_{\mathrm{s}}^2 \rho^{\mathrm{L}}(\boldsymbol{x}, t) \, . \tag{3.6}$$

While the quantities f_i, ρ^{L}, $\boldsymbol{u}^{\mathrm{L}}$, $\boldsymbol{F}^{\mathrm{L}}$, p^{L}, $\mathbf{\Pi}^{\mathrm{L}}$ and their alterations are defined for a point $\boldsymbol{x}$ in the discrete fluid domain $\Omega_{\mathrm{f}}^{\mathrm{L}}$ and point t in the discrete time interval I^{L}, the arguments will be omitted in the following if not necessary for the understanding for reasons of readability.

3.1.5 Basic Algorithm

With everything discretized and recalling the BGK collision operator, finally the lattice Boltzmann equation reads

$$f_i(\boldsymbol{x} + \mathbf{c}_i \delta t^{\mathrm{L}}, t + \delta t^{\mathrm{L}}) - f_i(\boldsymbol{x}, t) = -\frac{\delta t^{\mathrm{L}}}{\tau} \left(f_i(\boldsymbol{x}, t) - f_i^{\mathrm{eq}}(\rho^{\mathrm{L}}, \boldsymbol{u}^{\mathrm{L}}) \right) \, , \tag{3.7}$$

with the relaxation time $\tau = \nu^{\mathrm{L}}/c_{\mathrm{s}}^2 + 0.5$. Introducing a post-collision particle distribution function denoted by $f_i^*(\boldsymbol{x},t)$, allows to divide the equation in a collision step

$$f_i^*(\boldsymbol{x},t) = f_i(\boldsymbol{x},t) - \frac{\delta t^{\mathrm{L}}}{\tau}\left(f_i(\boldsymbol{x},t) - f_i^{\mathrm{eq}}(\rho^{\mathrm{L}},\boldsymbol{u}^{\mathrm{L}})\right) , \tag{3.8}$$

and a streaming step

$$f_i(\boldsymbol{x} + \boldsymbol{c}_i\delta t^{\mathrm{L}}, t + \delta t^{\mathrm{L}}) = f_i^*(\boldsymbol{x},t) . \tag{3.9}$$

Physically this can be interpreted as the particles relaxing towards a thermodynamic equilibrium with relaxation time τ during the collision step, while the behaviour of the particles between two collisions is described in the streaming step. Due to the latter $|\boldsymbol{c}_i|\delta x$ can be interpreted as mean free path length which, divided by a characteristic length of the flow, yields the Knudsen number. Since it is desired to approximate the incompressible Navier–Stokes equations, the Knudsen number should be small. In fact this is an assumption in the process of recovering the macroscopic equations [72] and thereby leads to the requirement of a high spatial resolution for a good approximation.

3.1.6 Boundary Conditions

The formulation of boundary conditions in terms of the LBM is often equivalent with reconstructing the unknown parts of a particle distribution function. Compared to classical methods for which a pressure, velocity or even their rate of change can be prescribed, the conditions need to be formulated on a mesoscopic level. Considering the particle distribution function, the number of degrees of freedom that is to be dealt with is higher, which can be challenging or enable the formulation of more detailed, sophisticated conditions [72]. The discussions in this section will be regarding a D2Q9 lattice, the application to other discretizations works analogously.

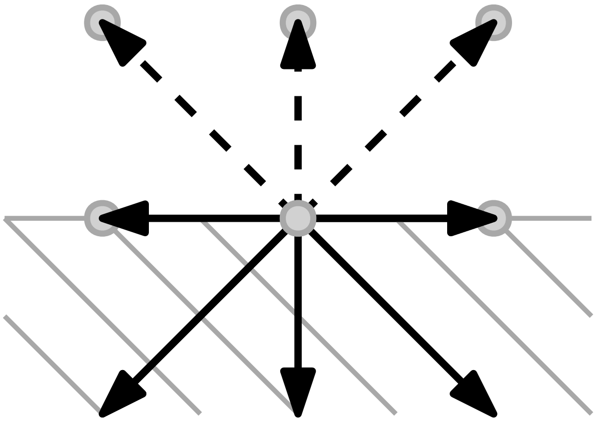

Figure 3.1: *Particle distribution functions for a boundary node in a D2Q9 setup. (Source: Own representation based on Krüger et al. [72], Figure 5.21)*

A boundary node is depicted in Figure 3.1, along with the post-streaming particle distribution functions indicated by arrows. While the solid arrows indicate known f_i, the dashed ones indicate unknown f_i, as they originate from outside the domain. A first approach can be to identify these incoming distributions with the ones outgoing on the opposite side of the domain, leading to a periodic boundary condition [72]. Yet, this does not always fit the physical setup which is to be considered. Conditions regarding the velocity to simulate an inflow boundary and a no-slip condition for the walls are required.

To recover missing f_i, many approaches and classifications of these exist, which are discussed in literature [72, 79]. For conditions regarding velocity and pressure, the regularized approach proposed by Latt [78] is applied for the simulations in this work. It replaces all particle distributions on the boundary by the sum of the equilibrium distribution and the off-equilibrium parts recovered via the stress tensor

$$f_i = f_i^{\mathrm{eq}}(\rho^{\mathrm{L}}, \boldsymbol{u}^{\mathrm{L}}) + \frac{w_i}{2}\left(\frac{\mathbf{c}_i\mathbf{c}_i}{c_\mathrm{s}^4} - \frac{I}{c_\mathrm{s}^2}\right) : \mathbf{\Pi}^{\mathrm{L},(1)} \; . \tag{3.10}$$

The colon operator denotes a tensor contraction and $\mathbf{\Pi}^{\mathrm{L},(1)}$ is computed similar as in Equation (3.5), but basing the computation on the second term of a series expansion of f_i regarding a small value instead of f_i. For these computations ρ^{L} or

$\boldsymbol{u}^{\mathrm{L}}$ need to be recovered first, as the other one is chosen according to the desired boundary condition. For a point in space $\boldsymbol{x}$ and in time t, it is apparent that $\rho^{\mathrm{L}} = f_{-} + f_{+} + f_{\|}$ if all f_i were known. Herein $f_{\|}$ identifies the sum of the particle distribution functions tangential to the boundary, including f_0, while f_{-} denotes the sum of the unknown ones and f_{+} the sum of the remaining. It is found from Equation (3.5) and symmetry conditions that the density can be calculated by

$$\rho^{\mathrm{L}} = \frac{2f_{+} + f_{\|}}{1 + u_{\perp}} , \tag{3.11}$$

with $u_{\perp}$ being the projected velocity normal to the boundary [79]. The inflow speed at the boundary can be computed similarly from a given density or pressure [160] by

$$u_{\mathrm{in}} = 1 - \frac{f_{\|} + 2f_{+}}{\rho^{\mathrm{L}}} . \tag{3.12}$$

Finally the off-equilibrium parts of the f_i are required for the calculation of the off-equilibrium stress tensor $\boldsymbol{\Pi}^{\mathrm{L},(1)}$ as stated before. They are obtained by a bounce-back assumption for the off-equilibrium parts. Let $\bar{i}$ be the index of the discrete velocity and particle distribution function for which $\boldsymbol{c}_{\bar{i}} = -\boldsymbol{c}_i$ applies. Then the stress tensor can be computed using $f_i^{(1)} = f_{\bar{i}} - f_{\bar{i}}^{\mathrm{eq}}(\rho^{\mathrm{L}}, \boldsymbol{u}^{\mathrm{L}})$ [79]. These temporary values are sufficient for the recovery of the off-equilibrium stress tensor, but can not completely fulfill the boundary condition on their own [79]. Additionally an error is introduced since the series expansion is cut off after the second term.

Lastly a no-slip condition is required to describe the walls. Due to its simplicity most frequently the bounce-back method is applied, which was discussed in detail by Krüger et al. [72]. There are two approaches for implementation, the first one is denoted as *halfway bounce-back* and reflects the particle distribution during the streaming step by

$$f_i(\boldsymbol{x}, t + \delta t^{\mathrm{L}}) = f_{\bar{i}}^{*}(\boldsymbol{x}, t) , \tag{3.13}$$

while the other one, denoted as *fullway bounce-back*, takes care of that during a collision step in the simulation by

$$f_i^{*}(\boldsymbol{x} + \boldsymbol{c}_{\bar{i}}\delta t^{\mathrm{L}}, t) = f_{\bar{i}}(\boldsymbol{x} + \boldsymbol{c}_{\bar{i}}\delta t^{\mathrm{L}}, t) , \tag{3.14}$$

for an unknown f_i. In this work the latter approach is applied.

3.1.7 Forcing Schemes

To incorporate external forces in the LBM, multiple schemes exist in literature, three of which are presented here. They all share a common framework, first the calculation of the first moment (see Equation (3.5)), yielding the momentum and thereby the velocity, is modified. In the presence of a force $\boldsymbol{F}^{\mathrm{L}}\colon \Omega_{\mathrm{f}}^{\mathrm{L}} \times I^{\mathrm{L}} \to \mathbb{R}^3$ the velocity is calculated by

$$\boldsymbol{u}^{\mathrm{L}} = \frac{1}{\rho^{\mathrm{L}}} \sum_{i=0}^{q-1} \boldsymbol{c}_i f_i + \frac{\boldsymbol{F}^{\mathrm{L}} \delta t^{\mathrm{L}}}{2\rho^{\mathrm{L}}} \,, \tag{3.15}$$

to maintain accuracy of the LBM [72]. Also the collision step is updated to

$$f_i^* = f_i - \frac{\delta t^{\mathrm{L}}}{\tau} \left(f_i - f_i^{\mathrm{eq}}(\rho^{\mathrm{L}}, \boldsymbol{u}^{\mathrm{L}} + A \frac{\boldsymbol{F}^{\mathrm{L}} \delta t^{\mathrm{L}}}{\rho^{\mathrm{L}}}) \right) + \delta t^{\mathrm{L}} S_i \,, \tag{3.16}$$

modifying the velocity argument in the equilibrium distribution function depending on a factor A and adding a source term $S_i\colon \Omega_{\mathrm{f}}^{\mathrm{L}} \times I^{\mathrm{L}} \to \mathbb{R}$. The models discussed in the following only differ by the definition of A and S_i.

Shan and Chen [120] proposed a scheme referred to as *velocity shift method* by choosing

$$A = \frac{\tau}{\delta t^{\mathrm{L}}} \quad \text{and} \quad S_i = 0 \,, \tag{3.17}$$

for single- and multi-phase flows. For this approach the force is equivalent to a velocity difference in the equilibrium distribution. Another simple forcing approach was published by Kupershtokh et al. [74], now only changing the source term, it is given by

$$A = 0 \quad \text{and} \quad S_i = f_i^{\mathrm{eq}}(\rho^{\mathrm{L}}, \boldsymbol{u}^{\mathrm{L}} + \delta \boldsymbol{u}^{\mathrm{L}}) - f_i^{\mathrm{eq}}(\rho^{\mathrm{L}}, \boldsymbol{u}^{\mathrm{L}}) \,, \tag{3.18}$$

with $\delta \boldsymbol{u}^{\mathrm{L}} = \boldsymbol{F}^{\mathrm{L}} \delta t^{\mathrm{L}} / \rho^{\mathrm{L}}$ being the change of mass velocity. It is to be noted that in this scheme the unmodified version of $\boldsymbol{u}^{\mathrm{L}}$ according to Equation (3.5) is applied in the equilibrium distribution. This method was derived directly from the Boltzmann equation and is referred to as *exact difference method*. For the last method Guo et al. [44] adapted both the velocity and the source term to

$$\begin{aligned} A &= \frac{1}{2}\,, \\ S_i &= \left(1 - \frac{\delta t^{\mathrm{L}}}{2\tau}\right) w_i \left(\frac{\boldsymbol{c}_i - \boldsymbol{u}^{\mathrm{L}}}{c_{\mathrm{s}}^2} + \frac{(\boldsymbol{c}_i \cdot \boldsymbol{u}^{\mathrm{L}})\boldsymbol{c}_i}{c_{\mathrm{s}}^4}\right) \cdot \boldsymbol{F}^{\mathrm{L}}\,. \end{aligned} \tag{3.19}$$

While all these formulations correctly recover the forced Navier–Stokes equations [72], they differ in complexity and accuracy. The latter is investigated in Chapter 5.

3.2 Extension for Dense Suspensions

Multiple approaches for the simulation of fluid flows containing a dense suspension have been proposed in literature, e.g., from the perspective of flow through a porous medium [45] or multi-phase flows [126]. This section is concerned with methods approximating the volume-averaged Navier–Stokes equations discussed in Section 2.1.2, based on the LBM. The approaches given in literature [12, 59, 154] mostly differ by the implementation of force, momentum exchange and additional source terms. Recovering the macroscopic equations via a Chapman–Enskog [20] analysis, differences in the pressure term are found [59], revealing that some methods are not well suited for dynamic cases like the simulation of a moving suspension [12].

For all approaches however, the moments are redefined regarding the void fraction $\epsilon_\mathrm{f}\colon \Omega_\mathrm{f}^\mathrm{L} \times I^\mathrm{L} \to \mathbb{R}$ [59] to

$$\begin{aligned} \epsilon_\mathrm{f}\rho^\mathrm{L} &= \sum_{i=0}^{q-1} f_i \,, \\ \epsilon_\mathrm{f}\rho^\mathrm{L}\langle \boldsymbol{u}^\mathrm{L}\rangle_\mathrm{f} &= \sum_{i=0}^{q-1} \boldsymbol{c}_i f_i \,, \end{aligned} \tag{3.20}$$

also omitting the arguments of ϵ_f, if not necessary for understanding. From this point, already the first simple approach labelled as *direct forcing* can be made. The physical behaviour is approximated, considering Newton's third law and thus applying the negative of the hydrodynamic forces acting on the particles to the fluid and using a forcing scheme as discussed in Section 3.1.7.

3.2.1 Force Conversion

Since the particles are underresolved in the simulations, the momentum exchange term and subgrid stress in the volume-averaged Navier–Stokes equations (2.11) need to be modeled. This is usually done by including the hydrodynamic force, discussed in Section 2.3, which in turn is often simplified to be only comprised of the drag force. Since all formulations regarding the drag force are given for a single particle and not accumulated forces of the whole collective in a considered cell, they need to be transformed.

Typically forces are considered as force densities, i.e., divided by the volume they act upon, in fluid dynamics and the LBM. Considering Euler's laws of motion and denoting quantities regarding a single particle with the index $_\mathrm{p,1}$ and quantities regarding the entirety of particles in a unit volume with the index $_\mathrm{p,coll}$, one finds

$$\frac{\boldsymbol{F}_\mathrm{p,coll}}{\rho_\mathrm{p,coll}} = \frac{\boldsymbol{F}_\mathrm{p,1}}{m_\mathrm{p,1}} \,, \tag{3.21}$$

which finally leads to

$$\boldsymbol{F}_{\mathrm{p,coll}} = (1-\epsilon_{\mathrm{f}})\frac{\boldsymbol{F}_{\mathrm{p,1}}}{V_{\mathrm{p,1}}} \ . \tag{3.22}$$

Converting $\boldsymbol{F}_{\mathrm{p,coll}}$ to lattice units finally gives the force which can be used in the discussed schemes.

Another challenge is due to the drag force. As the recovery of the fluid's velocity is now dependent on the force as defined in Equation (3.15) and the drag force in turn depends on the relative and therefore the fluid's velocity, the method becomes implicit. This can be solved either by using the velocity of the previous time step in the calculation of the force, introducing a time dependent error, or by the introduction of an auxiliary variable as shown by Höcker et al. [59]. In their publication they also describe the incorporation of non-linear drag schemes, according to Guo and Zhao [45].

3.2.2 Pressure Correction Scheme

Zhang et al. [154] compared the Navier–Stokes equations to their volume-averaged version and modified the equilibrium distribution function for reasons of similarity to

$$\widetilde{f_i^{\mathrm{eq}}}(\rho^{\mathrm{L}}, \boldsymbol{u}^{\mathrm{L}}) = \epsilon_{\mathrm{f}} f_i^{\mathrm{eq}}(\rho^{\mathrm{L}}, \boldsymbol{u}^{\mathrm{L}}) \ . \tag{3.23}$$

Recovering the macroscopic equations regarding this change via a Chapman–Enskog [20] analysis revealed differences to the actual volume-averaged equations. Therefore Zhang et al. [154] introduced an additional force term with

$$\boldsymbol{F}_{\mathrm{pc}}^{\mathrm{L}} = c_{\mathrm{s}}^2 \langle \rho^{\mathrm{L}} \rangle \nabla \epsilon_{\mathrm{f}} = \langle p^{\mathrm{L}} \rangle \nabla \epsilon_{\mathrm{f}} \ , \tag{3.24}$$

utilizing the forcing approach by Guo et al. [44]. The change in the equilibrium distribution function along with the additional force term are labelled as *pressure correction scheme*. However, Blais et al. [12] found the scheme to be still insufficient, as for non-constant void fractions wrong solutions of the velocity field were obtained and the simulations were found to be unstable.

3.2.3 Rescaling Scheme

Höcker et al. [59] proposed the *rescaling scheme* from which the volume-averaged Navier–Stokes equations can be properly recovered. Unlike other schemes it aims at updating the streaming step. First splitting the particle distribution function by

$$\pi_i = w_i \sum_{j=0}^{q-1} f_j \ , \quad \text{and} \quad \zeta_i = f_i - \pi_i \ , \tag{3.25}$$

allows to scale only the more pressure related part π_i by the local void fraction before and after streaming. Finally the scheme can be summed by the streaming step being defined as

$$\begin{aligned} f_i(\boldsymbol{x} + \mathbf{c}_i \delta t, t + \delta t) &= \epsilon_\mathrm{f}(\boldsymbol{x} + \mathbf{c}_i \delta t, t + \delta t) \frac{\pi_i(\boldsymbol{x}, t)}{\epsilon_\mathrm{f}(\boldsymbol{x}, t)} + \zeta_i(\boldsymbol{x}, t) \\ &= f_i(\boldsymbol{x}, t) + \pi_i(\boldsymbol{x}, t) \frac{\epsilon_\mathrm{f}(\boldsymbol{x} + \mathbf{c}_i \delta t, t + \delta t) - \epsilon_\mathrm{f}(\boldsymbol{x}, t)}{\epsilon_\mathrm{f}(\boldsymbol{x}, t)} \ . \end{aligned} \tag{3.26}$$

3.3 Extension to Advection–Diffusion Problems

The LBM can also be applied to solve the advection–diffusion equation. With the quantity of interest being the particle concentration c, only minor changes are required to the basic LBM scheme [97]. First the lattice relaxation time is defined as $\tau = D/c_\mathrm{s}^2 + 0.5$ using the diffusion coefficient. Labelling the particle distribution functions regarding the advection–diffusion equation by g_i for better discriminability, the simplest equilibrium distribution function, for which the desired macroscopic equations are recovered, is linear in velocity and given by

$$g_i^\mathrm{eq}(c^\mathrm{L}, \boldsymbol{u}_\mathrm{p}^\mathrm{L}) = c^\mathrm{L} w_i \left(1 + \frac{\mathbf{c}_i \cdot \boldsymbol{u}_\mathrm{p}^\mathrm{L}}{c_\mathrm{s}^2} \right) \ . \tag{3.27}$$

However, it is also possible to use equilibrium distributions of higher order. For this system only the concentration, calculated by

$$c^{\mathrm{L}} = \sum_{i=0}^{q-1} g_i \,, \tag{3.28}$$

is conserved, not its momentum [72]. At this point the velocity $\boldsymbol{u}_{\mathrm{p}}^{\mathrm{L}}$ is assumed to be given, its calculation is discussed in Section 3.3.1. Overall the scheme's accuracy is found to be only of first order, however, Latt [78] proposed an extension to achieve a second order accuracy.

The last difference concerning the Navier–Stokes equations in the LBM are the reduced requirements regarding the moments, wherefore a simpler discretization of the velocity space is adequate [97]. A square lattice configuration, i.e., D2Q5 or D3Q7, is sufficient [62]. It is even possible to drop the zero velocity, which describes the resting particles, leading to D2Q4. Considering the Courant number

$$C = \frac{\|\boldsymbol{u}_{\mathrm{p}}\|_2 \delta t}{\delta x} \,, \tag{3.29}$$

Suga [132] investigated the stability and accuracy of the LBM for advection–diffusion problems regarding different discretizations. He found the stability region to be

$$\begin{aligned} \mathrm{C} &\le \frac{1}{2}\,, \quad && \text{for D2Q4}\,,\\ \mathrm{C} &\le \frac{2}{5}\,, \quad && \text{for D2Q5}\,,\\ \mathrm{C} &\le \frac{1}{3}\,, \quad && \text{for D2Q9}\,, \end{aligned} \tag{3.30}$$

decreasing with an increasing number of discrete velocities. Furthermore the Péclet number is to be considered for stability. For a finite differences approach, it is required that Pe < 2, otherwise stability and accuracy can not be ensured [144]. This is due to the advective transport becoming the dominant part in the equation, which has to be taken account for by the applied discretization scheme, e.g., a *streamline upwind scheme* can be applied [144]. Suga's investigations [132] showed that the LBM approach is less restrictive regarding the Péclet number if

D2Q9 is used. While the different discretizations produce results with a similar accuracy for Pe ≤ 1 and C ≤ 0.2, no restrictions regarding Pe were found for D2Q9 with C ≤ 0.1, testing for Péclet numbers up to 1000.

3.3.1 Calculation of the Particle Velocity Field

The particle velocity field is obtained from a finite difference scheme, solving

$$m_{\mathrm{p}}^{\mathrm{L}} \frac{d\boldsymbol{u}_{\mathrm{p}}^{\mathrm{L}}}{dt} = \boldsymbol{F}_{\mathrm{D}}^{\mathrm{L}} \,. \tag{3.31}$$

For the right hand side, a drag correlation from Section 2.3 can be used and even completed to the full hydrodynamic force, adding the added mass force and the Basset history force. The differential on the left hand side is the material derivative, wherefore the equation takes the form

$$\frac{\partial \boldsymbol{u}_{\mathrm{p}}^{\mathrm{L}}}{\partial t} + \boldsymbol{u}_{\mathrm{p}}^{\mathrm{L}} \nabla \cdot \boldsymbol{u}_{\mathrm{p}}^{\mathrm{L}} = \frac{\boldsymbol{F}_{\mathrm{D}}^{\mathrm{L}}}{m_{\mathrm{p}}^{\mathrm{L}}} \,, \tag{3.32}$$

leading to a convection-dominated problem. In this case the results are not necessarily bounded applying a central difference scheme [144], which can lead to unphysical results. To solve this issue, an *upwind scheme* is employed, for which the spatial derivative is given as

$$\frac{d\alpha(x)}{dx} = \begin{cases} \frac{\alpha(x)-\alpha(x-\delta x)}{\delta x}\,, & \text{for } \beta > 0 \\ \frac{\alpha(x+\delta x)-\alpha(x)}{\delta x}\,, & \text{for } \beta < 0 \end{cases} , \tag{3.33}$$

for a quantity $\alpha \in \mathbb{R}$ advected by $\beta \in \mathbb{R}$. This also respects the transportiveness of the flow. Regarding the stability, the Courant–Friedrich–Lewy condition $\mathrm{C} < 1$ has to be satisfied. Due to this biased difference quotient, the scheme introduces an error in the form of added artificial diffusion [144]. An application of the complete one-way coupled systems of particles submersed in a fluid was presented by Trunk et al. [138], showing a case-dependent approach to handle the artificial diffusion.

3.4 Homogenized Lattice Boltzmann Method

In the HLBM, the particles are depicted as surface-resolved objects. This allows for a direct computation of the hydrodynamic force at the surface, thereby dropping the requirement to model the drag. It can be segmented into the following parts:

- particle representation
- coupling fluid → particles
- coupling particles → fluid
- particle dynamics

The particle geometries can be drawn from analytical expressions, e.g., for spheres, cuboids or superellipsoids, or from geometry data obtained by computer tomography. From the chosen model, a voxel representation of the object is generated, which does not necessarily have the same resolution as the grid, used for the simulation [139]. The relevant particle parameters like the volume or the moment of inertia can also be computed from this, using the parallel axis theorem. For this a homogeneous density is assumed. This data can be used to depict the particle on the simulation grid, i.e., relating each node with the volume fraction covered by a particle $\gamma\colon \Omega_{\mathrm{f}}^{\mathrm{L}} \times I^{\mathrm{L}} \rightarrow \mathbb{R}$, which can also be reformulated to be interpreted as porosity [71]. It is also possible to use γ to formulate a smooth transition between particle and fluid cells. This is required, e.g, for the application of shape optimisation schemes [65].

The coupling of the fluid on the particles is achieved by calculating the exchanged momentum. Since in contrast to other methods, no solid boundary is applied to depict the particle surface, methods found in literature may need to be adapted. An overview on available methods is given in Section 3.4.2 and they are evaluated regarding accuracy in Section 5.4.1.

The presence of the particles is represented by a shift in velocity. Similarly to the immersed boundary method, the fluid is forced to obey the particle velocity in the covered regions. To achieve this and maintain the transition between fluid and particles, the convex combination

$$\bar{\boldsymbol{u}}^{\mathrm{L}} = (1-\gamma)\boldsymbol{u}_{\mathrm{f}}^{\mathrm{L}} + \gamma \boldsymbol{u}_{\mathrm{p}}^{\mathrm{L}} , \tag{3.34}$$

is introduced. A velocity difference is then obtained by $\delta \boldsymbol{u} = \bar{\boldsymbol{u}}^{\mathrm{L}} - \boldsymbol{u}_{\mathrm{f}}^{\mathrm{L}}$, which in the LBM framework can be converted to a force, as seen in Section 3.1.7. A comparative study regarding the forcing schemes is given in Section 5.4.1, finding the exact difference method [74] and the forcing scheme given by Guo et al. [44] to be similar in accuracy, while both are superior to the approach by Shan and Chen [120]. The HLBM, originally proposed with the latter forcing approach, is then updated accordingly.

The particle dynamics mainly follow Euler's laws of motion, discussed in Section 2.2.1. The equations are solved utilizing a velocity Verlet algorithm to update the particle velocity and position of the center of mass.

3.4.1 Particle Dynamics

Considering the center of mass' position and velocity, as well as angle and angular velocity, they can be updated by

$$\begin{aligned} \boldsymbol{x}_{\mathrm{cm}}(t+\delta t) &= \boldsymbol{x}_{\mathrm{cm}}(t) + \boldsymbol{v}_{\mathrm{cm}}(t)\delta t + \frac{1}{2}\boldsymbol{a}_{\mathrm{cm}}(t)\delta t^2 , \\ \boldsymbol{v}_{\mathrm{cm}}(t+\delta t) &= \boldsymbol{v}_{\mathrm{cm}}(t) + \frac{\delta t}{2}(\boldsymbol{a}_{\mathrm{cm}}(t+\delta t) + \boldsymbol{a}_{\mathrm{cm}}(t)) , \\ \boldsymbol{\theta}(t+\delta t) &= \boldsymbol{\theta}(t) + \boldsymbol{\omega}_{\mathrm{cm}}(t)\delta t + \frac{1}{2}\boldsymbol{\alpha}_{\mathrm{cm}}(t)\delta t^2 , \\ \boldsymbol{\omega}_{\mathrm{cm}}(t+\delta t) &= \boldsymbol{\omega}_{\mathrm{cm}}(t) + \frac{\delta t}{2}(\boldsymbol{\alpha}_{\mathrm{cm}}(t+\delta t) + \boldsymbol{\alpha}_{\mathrm{cm}}(t)) , \end{aligned} \tag{3.35}$$

using a velocity Verlet algorithm with the acceleration $\boldsymbol{a}_{\mathrm{cm}}$ and angular acceleration $\boldsymbol{\alpha}_{\mathrm{cm}}$ of the center of mass. The accelerations are obtained from the force, as stated in Equations (2.18) and (2.19). The final particle velocity field, relevant for the coupling with the fluid is then obtained by

$$\boldsymbol{u}_{\mathrm{p}}(\boldsymbol{x},t)=\begin{cases}\boldsymbol{v}_{\mathrm{cm}}(t)+\boldsymbol{\omega}_{\mathrm{cm}}(t)\times(\boldsymbol{x}-\boldsymbol{x}_{\mathrm{cm}}(t))\,, & \text{for } \boldsymbol{x}\in\Omega_{\mathrm{p}}(t)\\ 0\,, & \text{else}\end{cases}\,, \tag{3.36}$$

with $\Omega_{\mathrm{p}}(t)$ denoting the volume covered by particles at a point in time t.

3.4.2 Momentum Exchange Algorithms

The first momentum exchange algorithm was proposed by Ladd [75, 76] and a modified version of it was applied by Krause et al. [71] for simulations with the HLBM. It is given by

$$\boldsymbol{F}_{\mathrm{h}}^{\mathrm{L}}(t)=\sum_{\boldsymbol{x}\in\Omega_{\mathrm{p}}(t)}\sum_{i=1}^{q-1}\boldsymbol{c}_i\left(f_i(\boldsymbol{x}+\boldsymbol{c}_i\delta t,t)+f_{\bar{i}}(\boldsymbol{x},t)\right)\,, \tag{3.37}$$

dropping the additional term regarding a moving no-slip boundary. Another approach was proposed by Wen et al. [147], incorporating the particle velocity not in an extra boundary term, but in the node-wise calculations, given by

$$\boldsymbol{F}_{\mathrm{h}}^{\mathrm{L}}(t)=\sum_{\boldsymbol{x}\in\Omega_{\mathrm{p}}(t)}\sum_{i=1}^{q-1}\Big(\boldsymbol{c}_i-\boldsymbol{u}_{\mathrm{p}}^{\mathrm{L}}(\boldsymbol{x},t)\Big)f_i(\boldsymbol{x}+\boldsymbol{c}_i\delta t,t)+\Big(\boldsymbol{c}_{\bar{i}}+\boldsymbol{u}_{\mathrm{p}}^{\mathrm{L}}(\boldsymbol{x},t)\Big)f_{\bar{i}}(\boldsymbol{x},t)\,, \tag{3.38}$$

thus achieving improvements regarding the Galilean invariance. Alternatively the momentum lost by the fluid in the previous time-step can be applied. Recalling the convex combination of velocity stated in Equation (3.34) and, e.g., applying the exact difference method, the exchanged momentum is given by

$$\boldsymbol{F}_{\mathrm{h}}^{\mathrm{L}}(t)=\sum_{\boldsymbol{x}\in\Omega_{\mathrm{p}}(t)}\sum_{i=1}^{q-1}\boldsymbol{c}_i\left(f_i^{\mathrm{eq}}(\rho^{\mathrm{L}},\bar{\boldsymbol{u}}^{\mathrm{L}})-f_i^{\mathrm{eq}}(\rho^{\mathrm{L}},\boldsymbol{u}_{\mathrm{f}}^{\mathrm{L}})\right)\,. \tag{3.39}$$

This approach as well as the other momentum exchange approaches are further discussed in Section 5.3.3 and are evaluated within the HLBM framework in Section 5.4.1.

4 Depiction of Arbitrary Particle Shapes in Simulations

This chapter was published in the following article:

R. Trunk, J. Marquardt, G. Thäter, H. Nirschl and M. J. Krause
Towards the simulation of arbitrarily shaped 3D particles using a homogenised lattice Boltzmann method
Computers and Fluids, 172 (2018)
https://doi.org/10.1016/j.compfluid.2018.02.027

Own contribution according to the contributor roles taxonomy CRediT [14]:

- conceptualization
- data curation
- formal Analysis
- investigation
- methodology
- project administration
- software
- validation
- visualization
- writing – original draft
- writing – review & editing

Computers and Fluids 172 (2018) 621–631

Contents lists available at ScienceDirect

Computers and Fluids

journal homepage: www.elsevier.com/locate/compfluid

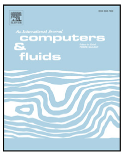

Towards the simulation of arbitrarily shaped 3D particles using a homogenised lattice Boltzmann method

Robin Trunk[a,b,c,*], Jan Marquardt[a], Gudrun Thäter[b], Hermann Nirschl[a], Mathias J. Krause[a,b,c]

[a] *Institute for Mechanical Process Engineering and Mechanics, Karlsruhe Institute of Technology, Karlsruhe. Germany*
[b] *Institute for Applied and Numerical Mathematics,Karlsruhe Institute of Technology, Karlsruhe, Germany*
[c] *Lattice Boltzmann Research Group, Karlsruhe Institute of Technology, Karlsruhe, Germany*

ARTICLE INFO

Article history:
Received 30 October 2017
Revised 22 February 2018
Accepted 23 February 2018
Available online 24 February 2018

MSC:
00-01
99-00

Keywords:
Lattice Boltzmann method
Arbitrarily shaped particle
Sedimentation
Homogenised Lattice Boltzmann method
OpenLB

ABSTRACT

The homogenised lattice Boltzmann method (HLBM), previously published by Krause et al. is extended for 3D simulations. The presented approach facilitates the simulation of arbitrarily shaped particles, which are automatically constructed from a geometry file, describing the surface. The proposed method relies on a discrete representation of the particle on a homogeneous grid rather than an approximation by a shape which can be described by a simple analytical equation or a combination of such. Results of numerical experiments are presented, validating the construction of the discrete particle representation, the particle dynamics as well as the acting forces. Moreover, an application of the method for the simulation of limestone particles based on geometry data generated from computer tomography scans is showcased.

1. Introduction

Applications in a multitude of fields such as drug delivery in medicine or solid-liquid separation in process engineering rely on the physical laws of particulate flows [1,2]. Often a raw approximation suffices for the design of facilities, however, a more in-depth understanding of the dynamics and impact of the acting forces is crucial in the process of improvement [3]. Especially the separation efficiency and selectivity can be enhanced by taking the shape of particles into account for simulations [4]. This is relevant in separation processes, where a sharp particle size distribution is the desired result. In industrial production, the margins of error for such processes can be low, e.g. in the production of slurry for chemical-mechanical planarisation for the production of wafer [5]. To achieve such a high level of selectivity, the real shape of the particles has to be taken into account. Since the described processes are not or only partly accessible for measurement devices, numerical simulations are required. The applied methods have to be capable of simulating a large amount of suspended particles, to capture effects relevant on the process scale, as well as depicting a high degree of detail to further extend the knowledge of the dynamics relevant e.g. for separation processes.

Among existing methods, lattice Boltzmann methods (LBM) proved to excel in simple and efficient parallel processing, fitting current multi- and many-core computing architecture [6–9]. Therefore, they provide a reasonable base for simulations of a large amount of particles, which is computational expensive. Due to advances in computing architecture and algorithms in recent years, it is possible to simulate a large amount of single particles [10]. Such Euler–Lagrange approaches have become a feasible approach since they can be based on simple differential equations and therefore allow fast computations for a reduced complexity. In such discrete element methods (DEM) the particles can be approximated as spheres in a first step, which yields good accuracy for a lot of applications [11,12]. However, to increase the quality of results for highly specialised fields of application, more factors have to be considered [13], including the shape of the particles, as shown by Wachs et al. [14]. For DEM simulations this can be achieved e.g. by considering compound particles as described by Favier et al. [15] and applied to industrial applications e.g. by Just et al. [16]. On

---

[*] Corresponding author at: Institute for Mechanical Process Engineering and Mechanics, Karlsruhe Institute of Technology, Karlsruhe. Germany
E-mail address: robin.trunk@kit.edu (R. Trunk).

https://doi.org/10.1016/j.compfluid.2018.02.027
0045-7930/

the one hand, the DEM has been improved by such expansions, e.g. by considering the influence of the particles' presence on the fluid [17], on the other hand, new methods like the immersed boundary method (IB) [18,19] emerged to meet the challenge. For the latter, a particle is represented by its boundary, consisting of several points moving independently of the Eulerian grid for the fluid. The coupling between particle and fluid is achieved by interpolation of hydrodynamic forces between the grid nodes of the fluid and the Lagrangian points of the particle. This however increases the demand on computational resources to simulate a certain amount of objects compared to basic DEM approaches. IB has already been applied to many applications, also due to its capability of considering deformable objects like filaments [20,21] or flapping wings [22], as well as rigid bodies [23]. For such shape-resolved methods the complexity of contact detection and treatment rises if arbitrary shapes are to be considered and efficient schemes may come with limitations, e.g. to convex shapes [24]. The challenge of particle contact is topic of current research, e.g. a contact treatment scheme for non-convex particles has been proposed by Rakotonirina et al. [25], which considers the objects to be a compound of convex particles. DEM and IB schemes for particle simulation are independent of the schemes applied for the fluid, as long as an underlying fluid velocity field exists, and have also been coupled with LBM fluid solvers [26,27].

Based on LBM, particles are also often expressed by a no-slip boundary condition. Various types of such interpolated bounce-back schemes are applicable for this purpose, as the one proposed by Bouzidi et al. [28] or the multireflection boundary described by Ginzburg and d'Humières [29]. An overview and comparison of this conditions is given in Peng et al. [30]. Combined with a momentum exchange algorithm (MEA) described by Ladd [31,32], such boundaries lead to an efficient scheme which takes advantage of the good parallel scalability of the method [33,34]. Another approach in particle simulations is given by Noble and Torczynski [35] in their partially saturated cells method, where the LBM collision is redefined dependant on the solid volume fraction, yielding a bounce-back boundary in the limit of pure solid.

An alternative has recently been published by Krause et al. [36], namely the homogenised lattice Boltzmann method (HLBM), which applies the MEA by Ladd but coupled with a porous media approach, incorporating a smooth transition zone between fluid and solid instead of a Bouzidi boundary. Compared to IB it does not require any interpolations, since the particle resides on the fluid grid instead of an independent representation by Lagrangian points. An overview of methods for particle simulations, regarding the scopes of flow and size can be found in [37].

The methods presented in this paper aim at giving a tool for simulations which yield results relevant on the process-scale and yet use a detailed representation of the particle.

Furthermore, the aim is to obtain a method relying on less assumptions and restrictions (e.g. restriction of applicability to convex objects) regarding the particle shape.

Furthermore, the long-time goal is to obtain a method relying on less assumptions and restrictions (e.g. restriction of applicability to convex objects) regarding the particle shape. As step towards this, an objective is the development of a processing strategy for real particle geometries generated from computer tomography scans. The challenge of contact treatment will be addressed in future works.

Therefore, an additional objective is the development of a processing strategy for real particle geometries generated from computer tomography scans.

Therefore, an extension to HLBM, proposed by Krause et al. [36], to 3D is presented. The proposed method preserves the parallel scalability of LBM and therefore qualifies for large scale simulations. Furthermore, a processing scheme of arbitrary geometries for the simulation of particles is described, which relies on the construction of a grid-like discrete representation of the particle. To the knowledge of the authors, such extensions for HLBM, like the fully automated treatment of arbitrarily shaped particles from STL-files, have not been investigated yet. To show the capability of the described method, the sedimentation of 3D limestone particles is examined. For this case the collision like behaviour already observed in Krause et al. [36] again occurs indicating an momentum exchange between the particle intrinsic to the proposed method. To ensure physical correctness this however needs further investigations.

In this paper, the equations as well as the underlying physical model are briefly described in Section 2. Afterwards, the applied methods are described in Section 3, which is divided in one section for HLBM in 3D, one characterizing the particle dynamics and one for the realisation of the scheme of the arbitrarily shaped particles and implementation. In Section 4, the results of numerical experiments are presented including a validation case for the computation of physical particle parameter, such as the moment of inertia. Moreover, convergence studies have been performed to validate the particle dynamics, considering a settling sphere, as well as the hydrodynamic forces, examining the flow around a cylinder. Finally, an application case is given, to demonstrate the capabilities of the proposed scheme.

2. Mathematical modelling

The equations covering the required physics for the model are related to fluid and rigid body dynamics. The flow of the fluid surrounding a particle and the flow induced by its motion is described by the incompressible Navier–Stokes equations, given by

$$\frac{\partial \boldsymbol{u}_\mathrm{f}}{\partial t} + (\boldsymbol{u}_\mathrm{f}\cdot\nabla)\boldsymbol{u}_\mathrm{f} - \nu\Delta\boldsymbol{u}_\mathrm{f} + \frac{1}{\rho_\mathrm{f}}\nabla p = \boldsymbol{F}_\mathrm{f} \qquad \text{in } \Omega\times(t_0,t_1),$$

$$\nabla\cdot\boldsymbol{u}_\mathrm{f} = 0 \qquad \text{in } \Omega\times(t_0,t_1). \tag{1}$$

The equations are defined on a domain $\Omega\in\mathbb{R}^d$ and time interval $I=[t_0,t_1]\subseteq\mathbb{R}$ for a spatial dimension $d\in\{2,3\}$. Here $\boldsymbol{u}_\mathrm{f}:\Omega\times I\to\mathbb{R}^d$ gives the fluids velocity and $p:\Omega\times I\to\mathbb{R}$ the pressure, whereas the kinematic viscosity $\nu\in\mathbb{R}_{>0}$ and density $\rho_\mathrm{f}\in\mathbb{R}_{>0}$ are characteristic parameter of the considered fluid. The last variable $\boldsymbol{F}_\mathrm{f}$ represents external forces acting on the fluid. To fully describe the fluid dynamics, problem dependent boundary and initial conditions need to be added, this will be discussed in Section 3 and 4.

The motion of the particle is governed by the equations of rigid body dynamics, based on Newton's second law of motion. Let Ω_p denote the domain covered by particles, which are considered to have a Dirichlet boundary regarding their velocity in order to represent the surface. Since the particles are in motion, the particle domain is time-dependent $\Omega_\mathrm{p}=\Omega_\mathrm{p}(t)$, accordingly the Navier–Stokes equation are considered to be defined on $\Omega_\mathrm{f}(t)=\Omega\setminus\Omega_\mathrm{p}(t)$ from now on. For a particle p with mass m_p and moment of inertia $\boldsymbol{J}_\mathrm{p}$, this leads to the equations

$$m_\mathrm{p}\frac{\partial \boldsymbol{u}_\mathrm{p}(t)}{\partial t} = \boldsymbol{F}_\mathrm{p}(t),$$

$$\boldsymbol{J}_\mathrm{p}\frac{\partial \boldsymbol{\omega}_\mathrm{p}(t)}{\partial t} = \boldsymbol{T}_\mathrm{p}(t),$$

where $\boldsymbol{u}_\mathrm{p}:I\to\mathbb{R}^d$ and $\boldsymbol{\omega}_\mathrm{p}:I\to\mathbb{R}^d$ denote the particle's translational and angular velocity, with $\boldsymbol{F}_\mathrm{p}$ and $\boldsymbol{T}_\mathrm{p}$ being the force and torque acting on the particle. The hydrodynamic forces acting on the particle are denoted by $\boldsymbol{F}^H$. Since the model depicts the volume and surface of the particle, a combined hydrodynamic force can be computed from a momentum exchange discussed in Section 3.2. Also, the gravitational force, given by $\boldsymbol{F}^G=(0,0,m_\mathrm{p}g)$ with gravitational acceleration g, is taken into account. Finally, the fluid and solid component are coupled by the application of these forces

$$\boldsymbol{F}_\mathrm{f} = \boldsymbol{F}^H \ , \quad \boldsymbol{F}_\mathrm{p} = \boldsymbol{F}^H + \boldsymbol{F}^G \ , \quad \boldsymbol{T}_\mathrm{p} = \boldsymbol{r} \times \boldsymbol{F}^H \ ,$$

for a position vector $\boldsymbol{r}$ for the point of application of the force.

3. Numerical methods

3.1. Homogenised lattice Boltzmann method (HLBM)

In LBM, the fluid is characterised by the distribution of fluid particles in the phase space, described by a function f, solving a discretised Boltzmann equation. A short overview of the discretisation is given below, however, since the basic LBM scheme is not the focus of this paper, the authors refer to existing literature for further information [38–40].

The spatial domain is approximated by a uniform grid Ω_h with spacing $h \in \mathbb{R}_{>0}$, while the discrete velocity space is described by a set of q velocities. The resulting phase space is denoted by DdQq. A common choice is D3Q19 for a 3 dimensional domain with a set of 19 velocities $\boldsymbol{c}_i \in \mathbb{R}^3$ $(i = 0, \dots, 18)$ [41], given by

$$\boldsymbol{c}_i = \begin{cases} (0,0,0), & i = 0, \\ (\pm\frac{1}{h},0,0), (0,\pm\frac{1}{h},0), (0,0,\pm\frac{1}{h}), & i = 1,2,\dots,6, \\ (\pm\frac{1}{h},\pm\frac{1}{h},0), (\pm\frac{1}{h},0\pm\frac{1}{h}), (0,\pm\frac{1}{h},\pm\frac{1}{h}) & i = 7,8,\dots,18. \end{cases}$$

Furthermore, the collision term of the Boltzmann equation is replaced with a simple approximation proposed by Bhatnagar, Gross and Krook, called BGK collision operator [42].

The lattice Boltzmann equation then is given by

$$f_i(\boldsymbol{x} + \boldsymbol{c}_i\delta t, t + \delta t) - f_i(\boldsymbol{x}, t) = -\frac{1}{\tau}\left(f_i(\boldsymbol{x}, t) - f_i^{\mathrm{eq}}(\rho, \bar{\boldsymbol{u}})\right) \ , \tag{2}$$

for a grid node $\boldsymbol{x} \in \Omega_h$ and $t \in I_h$, with the temporal space I_h resulting from the chosen discretisation of space and velocity.

The temporal spacing is given by $\delta t \in \mathcal{O}(|h|^2)$.

Furthermore, $f_i : \Omega_h \times I_h \to \mathbb{R}^+, i = 0, \dots, q-1$ represents the fluid particle density at location $\boldsymbol{x}$ moving with velocity $\boldsymbol{c}_i$. The velocity $\bar{\boldsymbol{u}}$ applied here is given in Eq. (3) and will be discussed later. It is possible to recover macroscopic quantities for $(\boldsymbol{x}, t) \in \Omega_h \times I_h$ by considering the momenta of the particle distribution function, yielding

$$\begin{aligned} \rho(\boldsymbol{x}, t) &= \sum_{i=0}^{q} f_i(\boldsymbol{x}, t), \\ \boldsymbol{u}_\mathrm{f}(\boldsymbol{x}, t) &= \frac{1}{\rho(\boldsymbol{x}, t)} \sum_{i=0}^{q} f_i(\boldsymbol{x}, t)\boldsymbol{c}_i. \end{aligned}$$

The lattice Boltzmann equation can be decomposed into two steps, namely:

1) Collision: A relaxation of the probability functions f_i on each lattice node towards the local equilibrium distribution f_i^{eq}: $\tilde{f}_i(\boldsymbol{x}, t) = f_i(\boldsymbol{x}, t) - \frac{1}{\tau}\left(f_i(\boldsymbol{x}, t) - f_i^{eq}(\rho, \bar{\boldsymbol{u}})(\boldsymbol{x}, t)\right)$.
2) Streaming: The distribution functions f_i spreads in the direction of the assigned lattice vector $\boldsymbol{c}_i$ to the next lattice node: $f_i(\boldsymbol{x} + \delta t\boldsymbol{c}_i, t + \delta t) = \tilde{f}_i(\boldsymbol{x}, t)$.

Here $\tau \in \mathbb{R}_{>0}$ is a characteristic relaxation time, depending on the fluid's kinematic viscosity and the chosen discretisation parameter. Furthermore, a discrete Maxwell–Boltzmann distribution f_i^{eq}, which depends on the fluids' density and velocity, is used to describe the thermodynamic equilibrium.

To incorporate the presence of moving porous media [43], the velocity has been replaced by a convex combination

$$\bar{\boldsymbol{u}}(\boldsymbol{x}, t) = \boldsymbol{u}_\mathrm{f}(\boldsymbol{x}, t) + d(\boldsymbol{x}, t)(\boldsymbol{u}_\mathrm{B}(\boldsymbol{x}, t) - \boldsymbol{u}_\mathrm{f}(\boldsymbol{x}, t)) \ . \tag{3}$$

For d: $\Omega_h \times I_h \to [0,\ 1]$ this yields a stationary porous medium if $\boldsymbol{u}_\mathrm{B} = 0$, see Spaid and Phelan [43], or a moving porous medium which can be considered as a particle for $\boldsymbol{u}_\mathrm{B} = \boldsymbol{u}_\mathrm{p}$, see Krause et al. [36].

3.2. Representation of particle in HLBM

The velocity $\boldsymbol{u}_\mathrm{p}$ is considered to be the translational velocity of the particle applied to its centre of mass. As can be seen in Eq. 3, nodes with $d(\boldsymbol{x}, t) = 0$ act like fluid, whereas $d(\boldsymbol{x}, t) = 1$ results in movement of the fluid according to the rigid body motion. In order to keep a continuous transition from the fluid to the solid component a ϵ-boundary is added. Here $\epsilon_h = \epsilon h \in \mathbb{R}_{>0}$ is the smoothing parameter, describing the size of the transition zone for a particle. For further information on this smoothened boundary, see Krause et al. [36]. The interaction of the particle with the fluid is described as an external force. More precisely, the influence on the fluid is expressed by the velocity $\bar{\boldsymbol{u}}$ (see Eq. (3)), which is included in the Maxwell–Boltzmann distribution function f_i^{eq}. Given that a porous particle is included into the lattice Boltzmann equation through a change of velocity, this alteration of velocity leads to a loss of momentum, which can be interpreted as a balancing force acting on the particle's boundary. As a result of the given conditions, the MEA proposed by Ladd [31,32] is utilised to approximate the acting force on the boundary. Between a lattice node $\boldsymbol{x}$ and its neighbouring node $\boldsymbol{x} + \boldsymbol{c}_i\delta t$ the momentum exchange is calculated by

$$\boldsymbol{g}_i(\boldsymbol{x}, t) = \boldsymbol{c}_i f_i(\boldsymbol{x}, t) + \boldsymbol{c}_{i^*} f_{i^*}(\boldsymbol{x}, t + \boldsymbol{c}_i\delta t),$$

where $\boldsymbol{c}_{i^*} = -\boldsymbol{c}_i$ and f_{i^*} is the momentum distribution function according to $\boldsymbol{c}_{i^*}$. Krause et al. [36] extended this method for HLBM, which considers porous particles. As a result of the smooth porosity transition, momentum transfer takes place at the whole transition zone, not only at the boundary. Thereby the hydrodynamic force $\boldsymbol{F}^H$ and torque $\boldsymbol{T}^H$ acting on the particle are calculated by

$$\begin{aligned} \boldsymbol{F}^H(\boldsymbol{x}, t) &= \sum_{\boldsymbol{x} \in \mathrm{p}_h} s(\boldsymbol{x}, t) \sum_i \boldsymbol{g}_i(\boldsymbol{x}, t) \ , \\ \boldsymbol{T}^H(\boldsymbol{x}, t) &= \sum_{\boldsymbol{x} \in \mathrm{p}_h} s(\boldsymbol{x}, t)(\boldsymbol{x} - \boldsymbol{X}_\mathrm{p}(t)) \sum_i \boldsymbol{g}_i(\boldsymbol{x}, t) \ , \end{aligned}$$

with the particle's centre of mass $\boldsymbol{X}_\mathrm{p}(t)$, the set of nodes inside the particle boundary p_h and the support of the function $d(\boldsymbol{x},\ t)$

$$s(\boldsymbol{x}, t) = \begin{cases} 1, & \text{for } d(\boldsymbol{x}, t) > 0 \\ 0, & \text{for } d(\boldsymbol{x}, t) = 0. \end{cases}$$

3.3. Incorporation of arbitrary shapes

Describing physical quantities, like the moment of inertia, of an arbitrarily shaped body is challenging, since there is no generic analytical way to calculate these. In order to simplify this problem, the representation of the particle on an uniform grid in HLBM, by the porosity parameter d residing on the grid nodes, is considered. However, for the discrete representation of the particle, a second grid is applied, which is not necessarily constructed with the same spacing parameter h as the fluid grid. This allows for higher resolutions and more accurate solutions, while barely affecting the required computational effort. With this grid-approach, e.g. the volume V of a particle, described by n blocks with the volume $V_\mathrm{B} = h_\mathrm{p}^3$, is obtained by $V = nV_\mathrm{B}$ using the grid spacing parameter h_p for the particle's grid. While a variation in density can easily be incorporated, a homogeneous mass distribution is assumed for now. Thereby, the mass of a particle is given by $m_\mathrm{p} = \rho_\mathrm{p} V$. Moreover, the centre of mass $\boldsymbol{X}_\mathrm{p}$ is given by

$$\boldsymbol{X}_\mathrm{p} = \frac{\sum_{\mathrm{B} \in \mathrm{p}} \boldsymbol{X}_\mathrm{B} m_\mathrm{B}}{m_\mathrm{p}} = \frac{\sum_j \boldsymbol{X}_\mathrm{B}}{n} \ , \tag{4}$$

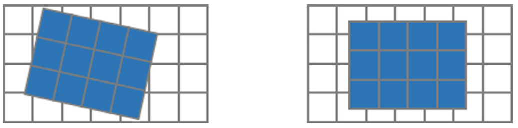

Fig. 1. Offset of the particle grid to the fluid lattice caused by rotation (left) and translation (right).

where $\boldsymbol{X}_\mathrm{B}$ is the centre of mass of block B belonging to the particle p and m_B its mass.

Since the rotation is described around the main axes by euler angles, the moment of inertia $\boldsymbol{J}_\mathrm{p} \in \mathbb{R}^3$ has to be computed accordingly. A single block's moment of inertia is computed by $\boldsymbol{J}_\mathrm{B} = \frac{2m_\mathrm{B}}{12} h_\mathrm{p}^2$. Utilizing the parallel axis theorem, the centre of mass of the particle p is moved into the origin of the coordinate system. A summation of the moment of inertia of each block finally yields

$$\boldsymbol{J}_\mathrm{p} = \sum_{\mathrm{B}\in\mathrm{p}} \boldsymbol{J}_\mathrm{B} = \sum_{\mathrm{B}\in\mathrm{p}} m_\mathrm{B} \left(\frac{h_\mathrm{p}^2}{6} + \boldsymbol{D}_\mathrm{B} \right) , \tag{5}$$

with $\boldsymbol{D}_\mathrm{B}$ being the vector of distances to the rotation axes.

As the particle moves, it can not be guaranteed that the nodes of the particle grid match the ones of the fluid lattice (see Fig. 1). Therefore it is checked whether a node of the fluid lattice is occupied by a particle by applying the discrete representation as a stencil.

To achieve this, the physical coordinates of the fluid node are translated and rotated into particle coordinate system in which the particle center of mass matches the origin and the Euler angles of the particle are zero. For a given set of Euler angles (θ_1, θ_2, θ_3) with the rotation matrix

$$R_\theta = \begin{pmatrix} \cos\theta_2 \cos\theta_3 & \cos\theta_2 \sin\theta_3 & -\sin\theta_2 \\ \cos\theta_1 (\sin\theta_2 \cos\theta_3 - \cos\theta_3) & \sin\theta_1 \sin\theta_2 \sin\theta_3 + \cos\theta_1 \cos\theta_3 & \sin\theta_1 \cos\theta_2 \\ \cos\theta_1 (\sin\theta_2 \cos\theta_3 + \cos\theta_3) & \cos\theta_1 \sin\theta_2 \sin\theta_3 - \sin\theta_1 \cos\theta_3 & \cos\theta_1 \cos\theta_2 \end{pmatrix}.$$

the described transformation of a coordinate in the fluid system $\boldsymbol{Y}$ is given by

$$\boldsymbol{Y}^* = R_\theta (\boldsymbol{Y} - \boldsymbol{X}_\mathrm{p}(t)) - \boldsymbol{X}_\mathrm{p} \ .$$

Here $\boldsymbol{Y}^* \in \Omega_h$ are the physical coordinates of a fluid node in the particle system. From this point the coordinates are mapped to the closest node of the particle grid by a nearest neighbour approximation.

To reduce cost of the described coordinate transformation only fluid nodes within a circumradius of the particle's centre of mass are checked and stored values of the rotation matrix, which is precomputed each time step for each particle, are used. This procedure does not require updating the discrete particle representation on the particle grid, whereby STL-data are not required for the simulation. To allow for fast checks whether a node is occupied by a particle, the data are stored in an octree structure.

Since all this operations as well as the computations required for the momentum exchange are strictly local regarding the fluid lattice, the calculations can easily be parallelised along with LBM by domain decomposition methods. However, the scale-up depends heavily on the solid volume fraction and its distribution in the considered application case.

Describing the smoothing ϵ region is more challenging in 3D, especially when arbitrary shapes are to be considered. As universal approach Gaussian smoothing is applied to the edges. The porosity of a certain point is calculated considering the surrounding porosity in the continuous, non-smoothed representation (e.g. a STL-file). Through utilisation of the Gaussian distribution function in 3D

$$f(x_1, x_2, x_3) = \Pi_{i=1}^3 \frac{1}{\sigma_i \sqrt{2\pi}} \exp\left(-\frac{(x_i - \mu_i)^2}{2\sigma_i^2} \right),$$

with the standard deviations $\sigma_i = 1$ and mean values $\mu_i = 0$ weights for the porosities around the considered node at $x_i = 0$ are obtained. The new calculated porosity at that node is then given by the sum of all weighted porosities for $x_i \in \{-\epsilon_h, 0, \epsilon_h\}$.

3.4. Rigid body dynamics

Updates to the position and velocity are accomplished by the Verlet algorithm, given by

$$\boldsymbol{X}_\mathrm{p}(t + \delta t) = \boldsymbol{X}_\mathrm{p}(t) + \boldsymbol{u}_\mathrm{p}(t)\delta t + \frac{1}{m_\mathrm{p}} \boldsymbol{F}^T(t) h^4,$$

$$\boldsymbol{u}_\mathrm{p}(t + \delta t) = \boldsymbol{u}_\mathrm{p}(t) + \frac{\boldsymbol{F}^T(t) + \boldsymbol{F}^T(t + \delta t)}{2m_\mathrm{p}} \delta t,$$

with the total force $\boldsymbol{F}^T$ acting on the particle. This force is a sum of all acting forces, the hydrodynamic force $\boldsymbol{F}^H$ and the gravitational force $\boldsymbol{F}^G = (0, 0, -m_\mathrm{p} g)$. The angles θ as well as angular velocity $\boldsymbol{\omega}_\mathrm{p}$ are computed analogously.

4. Results

The presented method is validated in three steps, which correspond to the Section 4.1, 4.2 and 4.3. First, the parameter computation strategy is validated by considering an ellipsoid as well as a particle geometry obtained from CT-scans, for which the volume and moment of inertia are computed. As a second step, the computation of hydrodynamic forces is reviewed for the example of a flow around a cylinder. The resulting drag and lift coefficients are compared to literature as well as to computations with a cylinder represented by a fixed no-slip boundary. The third step in validation addresses the particle dynamics, considering a falling sphere, for which the resulting settling velocity is compared to literature. Finally, in Section 4.4 the application case of sedimenting limestone particles is given.

4.1. Calculation of moment of inertia

At first, the generation of parameters, i.e. the volume and moments of inertia, is validated. Therefore, an ellipsoid with half-axes $a = 0.0692$, $b = 0.08$ and $c = 0.098$ (see Fig. 2), which is approximated by a grid, is studied. The values computed from this discrete representation are compared to the ones given by analytical formulas. Since an ellipsoid has curved boundaries with varying curvature, it is ensured that its borders won't be grid-compliant. For a spacing parameter $h_\mathrm{p} = \frac{1}{900} m$ the volume is recovered up to 0.75% accuracy, the moment of inertia is computed according to (5) for the main axes. Here the grid spacing is varied according to $h_\mathrm{p} = \frac{0.01}{N} m$ for a scaling parameter $N \in \mathbb{R}_{>0}$. The results an be seen in Fig. 3–5.

The analytical solutions for the respective rotation axes are given by $J_x^{an} = 0.00758 kg \cdot m^2$, $J_y^{an} = 0.00682 \mathrm{kg} \cdot \mathrm{m}^2$ and $J_z^{an} = 0.0053 kg \cdot m^2$, let the computed solutions further be denoted by J_x, J_y and J_z. The deviation form the analytical solution is then given in Table 1 and shows convergence to the correct solution. Since arbitrary shapes are to be considered, the method is also

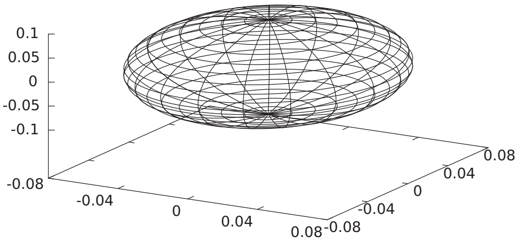

Fig. 2. Studied ellipsoid with half-axes $a = 0.0692m$, $b = 0.08m$ and $c = 0.098m$.

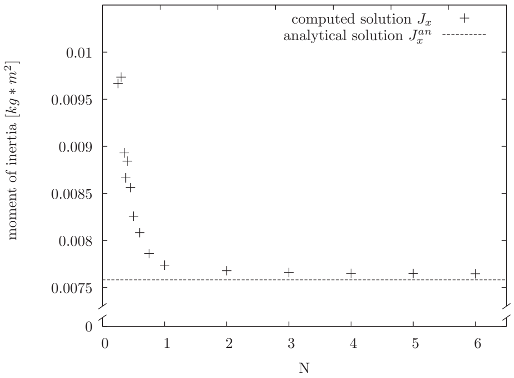

Fig. 3. Moment of inertia for rotation around the x-axis for an ellipsoid with half-axes $a = 0.0692m$, $b = 0.08m$ and $c = 0.098m$.

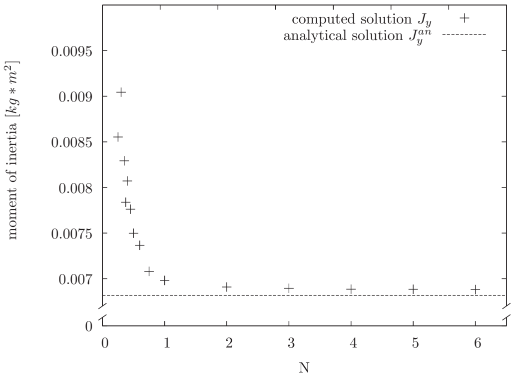

Fig. 4. Moment of inertia for rotation around the y-axis for an ellipsoid with half-axes $a = 0.0692m$, $b = 0.08m$ and $c = 0.098m$.

Table 1
Percental deviation of the moments of inertia of the main axes of an ellipsoid with half-axes $a = 0.0692m$, $b = 0.08m$ and $c = 0.098m$ regarding the grid spacing h_p.

h_p	J_x	J_y	J_z
0.025	16.65	18.4	20.2
0.01	2.06	2.39	3.37
0.0025	0.9	0.99	1.09
0.00125	0.83	0.92	0.98

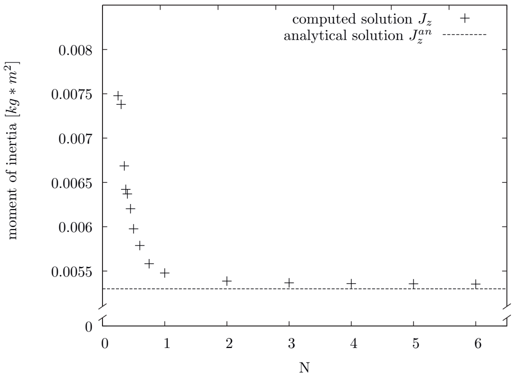

Fig. 5. Moment of inertia for rotation around the z-axis for an ellipsoid with half-axes $a = 0.0692m$, $b = 0.08m$ and $c = 0.098m$.

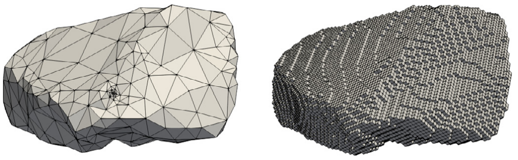

Fig. 6. Geometry representation of a limestone particle generated from a CT-scan (left) and a representation of the same particle approximated by 74781 blocks (right).

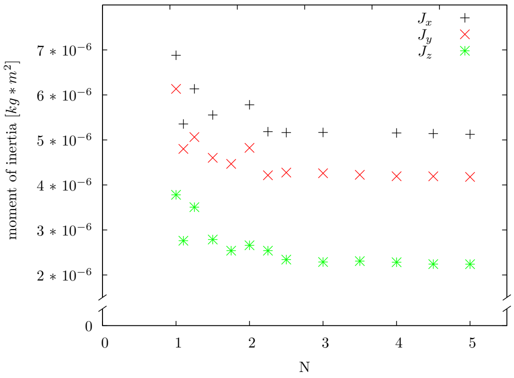

Fig. 7. Moments of inertia of the limestone particle.

applied to the geometry of a limestone particle, which is depicted together with the approximation on a grid with 74781 blocks in Fig. 6. The volume of the particle with dimension $0.02295m \times 0.03745m \times 0.052m$ is approximated to $1.6152 \cdot 10^{-5} m^3$ for the spacing parameter $h_p = 0.0006m$. Furthermore, the components of the moment of inertia are calculated and converge, as can be seen in Fig. 7, towards a fixed value. For the mentioned grid spacing ($N = 16.6\bar{6}$) they are computed to be $J_x = 5.08 \cdot 10^{-6} kg \cdot m^2$, $J_y = 4.12 \cdot 10^{-6}\mathrm{kg} \cdot \mathrm{m}^2$ and $J_z = 2.17 \cdot 10^{-6}\mathrm{kg} \cdot \mathrm{m}^2$.

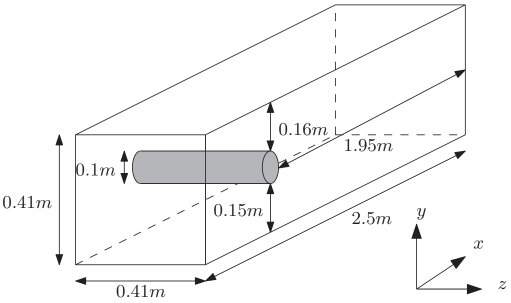

Fig. 8. Setup for the simulation of a flow around a cylinder [44].

Table 2
Computed drag coefficients c_D for the flow around a cylinder.

c_D	$N = 1$	$N = 2$	$N = 3$	$N = 4$	$N = 5$
$\epsilon = 2$	9.83	7.57	7.05	6.81	6.68
$\epsilon = 1$	8.15	6.90	6.63	6.51	6.43
$\epsilon = 0.5$	6.93	6.44	6.35	6.30	6.27
$\epsilon = 0$	6.90	6.38	6.24	6.22	6.19
Bouzidi	6.35	6.22	6.20	6.19	6.18
Schäfer et al. [44]			6.05–6.25		

Table 3
Computed lift coefficients c_L for the flow around a cylinder.

c_L $(\times 10^{-2})$	$N = 1$	$N = 2$	$N = 3$	$N = 4$	$N = 5$
$\epsilon = 2$	0.00	1.04	1.11	1.11	1.09
$\epsilon = 1$	0.00	0.66	0.81	0.87	0.90
$\epsilon = 0.5$	0.00	0.77	0.88	0.91	0.92
$\epsilon = 0$	0.00	0.53	0.66	0.73	0.76
Bouzidi	13.20	2.50	0.45	1.25	0.63
Schäfer et al. [44]			0.80–1.00		

4.2. Flow around a cylinder

For verification of the hydrodynamic forces of the presented method the benchmark case of a flow around a cylinder according to Schäfer et al. [44] is considered. The geometry used for the simulation can be seen in Fig. 8. In our case the cylinder is represented by a spatial fixed HLBM object. While the walls have a bounce-back boundary as no-slip condition, the outflow at $x = 2.5m$ is treated by a regularized pressure boundary, while the inflow at $x = 0m$ is treated by a regularized velocity boundary, both described in [45]. The velocity profile is given according to Schäfer et al. [44] by

$$\boldsymbol{u}_\mathrm{f}(0, y, z) = 7.2yz\frac{(0.41 - y)(0.41 - z)}{0.41^4} \ .$$

For reasons of comparability the kinematic viscosity and fluid density are set to $\nu = 10^{-3}m^2/s$ and $\rho_\mathrm{f} = 1000kg/m^3$ respectively. The drag and lift coefficients, denoted by c_D and c_L, computed by

$$c_D = \frac{2F_x^H}{0.041\rho_\mathrm{f}\tilde{u}^2} \ , \quad c_L = \frac{2F_y^H}{0.041\rho_\mathrm{f}\tilde{u}^2} \ ,$$

with the average inflow velocity $\tilde{u}$, are compared to the ones presented by Schäfer et al. [44] and to a reference solution computed with the cylinder represented by a Bouzidi boundary condition. For a given grid spacing parameter $h = \frac{0.01}{N}m$, the grid-independence has been investigated, the results can be seen in Table 2 and 3. For the drag coefficient the results computed with HLBM are in good agreement with the ones obtained with a Bouzidi boundary condition and are also within the interval given by Schäfer et al. beginning with $N = 3$. The approach with a static Bouzidi boundary yields similar results requiring less cells compared to HLBM and therefore performs better in the stationary case. However, considering moving objects a Bouzidi boundary requires computational expensive distance calculations in each time step.

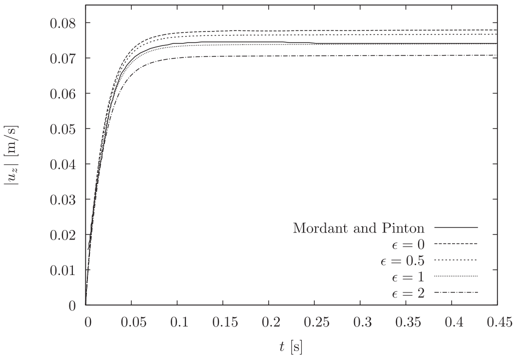

Fig. 9. Magnitude of velocity of the sphere in z-direction for different ϵ with $N = 3$ compared to the experimental results of Mordant and Pinton [46].

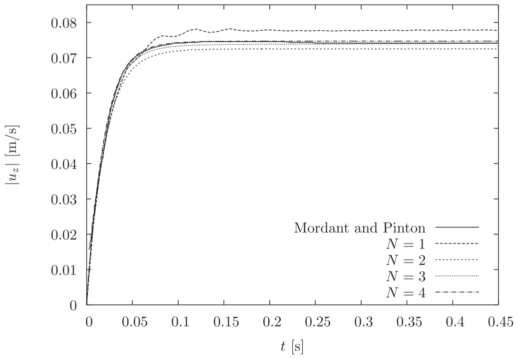

Fig. 10. Magnitude of velocity of the sphere in z-direction for different resolutions with $\epsilon = 1$ compared to the experimental results of Mordant and Pinton [46].

The computed lift coefficient on the other hand closely resembles the interval given by Schäfer et al. however, fluctuations around this interval can be observed, for HLBM as well as for the computations performed with a Bouzidi boundary. For HLBM and $N = 1$ the lift coefficient is of the order of magnitude of computational accuracy and therefore neglected. For this setup the size of a grid cell is $0.01m$. Therefore the deviation in y-direction of the cylinder from the centre of the channel falls below this value with $0.005m$. Since the flow field is symmetric, the lift force originates from this deviation which may not be depicted correctly dependent on the implementation and discretisation for $N = 1$ as the problem is under-resolved.

Furthermore the results show a dependency of the computed coefficients on the parameter ϵ, since it influences the simulated size of the object. However, the applied ϵ_h depends on the grid spacing and the deviation between the solutions for different ϵ decreases for higher grid resolutions as can be seen in Table 2 and 3.

To show grid independence, the experimental order of convergence (EOC), given by

$$EOC(j, k) = \frac{\log(err(j)) - \log(err(k))}{\log(j) - \log(k)} \ , \tag{6}$$

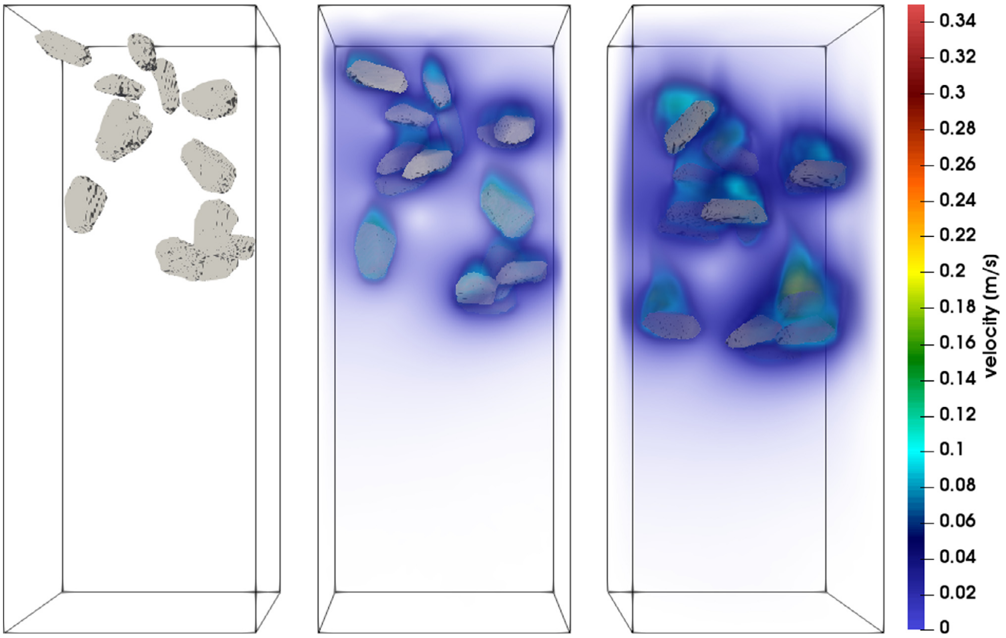

Fig. 11. Velocity magnitude of 15 sedimenting limestone particles at $t = 0s$ (left), $t = 0.576s$ (mid) and $t = 1.152s$ (right).

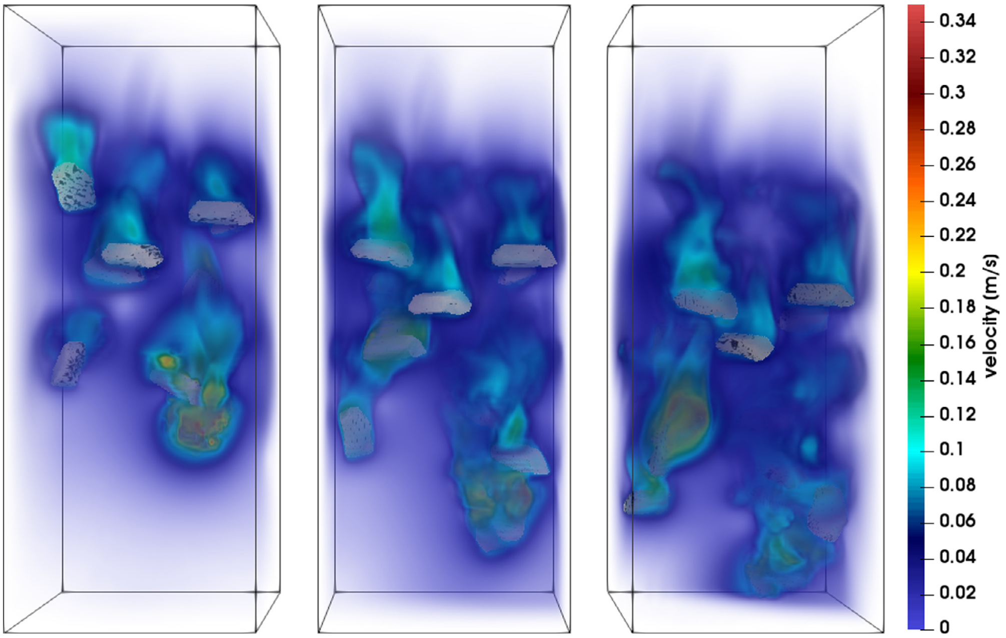

Fig. 12. Velocity magnitude of 15 sedimenting limestone particles at $t = 1.656s$ (left), $t = 2.232s$ (mid) and $t = 2.736s$ (right).

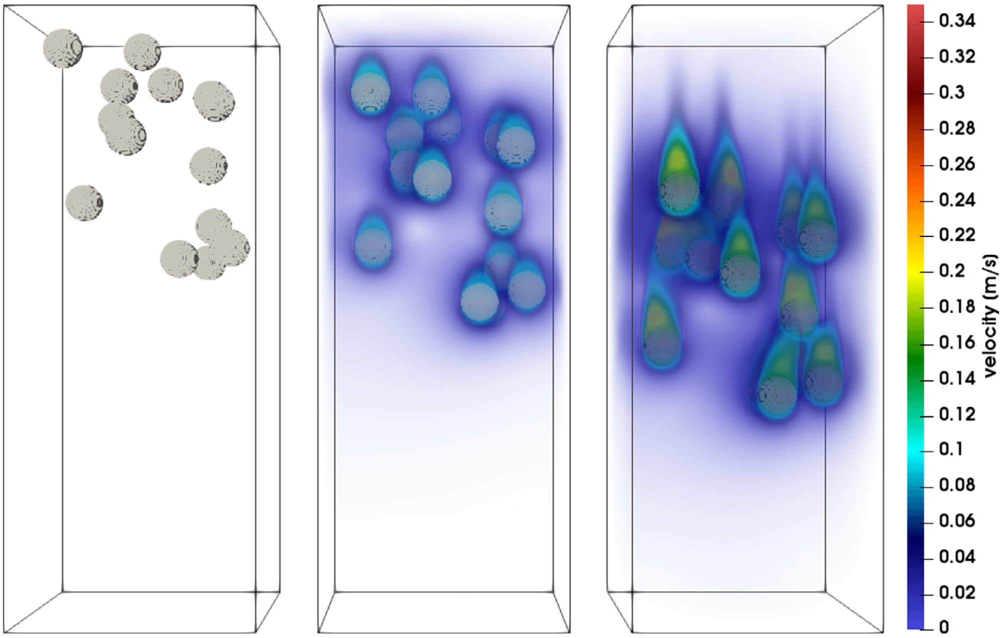

Fig. 13. Velocity magnitude of 15 sedimenting spheres at $t = 0s$ (left), $t = 0.576s$ (mid) and $t = 1.152s$ (right).

Table 4
Computed lift coefficients c_L for the flow around a cylinder.

	$EOC(1, 2)$	$EOC(2, 3)$	$EOC(3, 4)$	average EOC
$\epsilon = 2$	1.83	2.16	3.52	2.50
$\epsilon = 1$	1.87	2.10	3.30	2.42
$\epsilon = 0.5$	1.97	1.80	3.74	2.50
$\epsilon = 0$	1.91	3.30	1.18	2.13
Bouzidi	2.07	3.12	3.77	2.99

is computed. Here $err(j) = \|c_D^{N=j} - c_D^{N=5}\|$ denotes the deviation from the respective solution for $N = 5$. The results are depicted along with the averaged EOC in Table 4, showing a quadratic convergence.

4.3. Sedimentation of a sphere

To investigate the settling velocity of a spherical particle, it is placed at $(0.0025m, 0.0025m, 0.0049m)$ in a domain of the size $0.005m \times 0.005m \times 0.05m$ with periodic boundaries. The parameter are chosen according to the case # 1 of the experiments conducted by Mordant and Pinton [46] who measured the velocity of settling spheres. This setup has also been considered for numerical simulations by Uhlmann [19], applying an immersed boundary method. The kinematic viscosity is given by $\nu = 0.89 \cdot 10^{-6} \frac{m^2}{s}$, the radius of the sphere by $r_s = 0.00025m$ and the density of the sphere by $\rho_p = 2560kg/m^3$, which corresponds to glass. The surrounding fluid in the experiments is water, assuming room temperature, the density is chosen to be $\rho_f = 998kg/m^3$.

To compare the results, the particle Reynolds number Re_p is computed by

$$Re_p = \frac{2r_s\|u_z\|_\infty}{\nu} \ .$$

Table 5
Particle Reynolds number Re_p of a settling sphere ($N = 4$ and $\epsilon = 1$) in comparison to Uhlmann (simulation) and Mordant and Pinton (experiment).

	Re_p
present	41.97
Uhlmann [19]	41.12
Mordant and Pinton [46]	41.17

Here $\|u_z\|_\infty$ is the maximum velocity according to amount of the sphere in z-direction measured during the simulation. The grid spacing parameter is given by $h = \frac{0.00008}{N}m$ for $N \in \{1, 2, 3, 4\}$. Thereby the sphere is resolved by at least 6 cells along the diameter. For the temporal discretisation $\delta t = \frac{0.000075}{N^2}$ is applied. The temporal evolution of the velocity in the conducted simulations is depicted in Fig. 10 and Fig. 9. Applying a smooth transition zone, described in Section 3.1, it is found that $\epsilon = 1$ yields the best results, as $\epsilon = 2$ leads a strong deviation since the sphere appears enlarged by the smooth transition zone. Studying the grid independence in Fig. 9, the results show a convergent behaviour, as $h \to 0$ and thereby $\epsilon_h \to 0$. While for $N = 1$ oscillations, probably due to a discretisation error, can be observed they vanish for higher resolutions. Considering the resolution $N = 4$ and choosing $\epsilon = 1$ the maximal occurring particle Reynolds number is given by $Re_p = 41.97$. This overestimates the results of Uhlmann by 2.1% and the meassurements of Mordant and Pinton by 1.9% (see Table 5).

4.4. Simulation of 15 limestone particle

The limestone particle discussed in Section 4.1 is placed 15 times in a fluid domain with a size of $0.2m \times 0.2m \times 0.5m$. The particles are randomly distributed in the top 40% of the domain with different angles, as depicted in Fig. 11 (left). The particles sediment

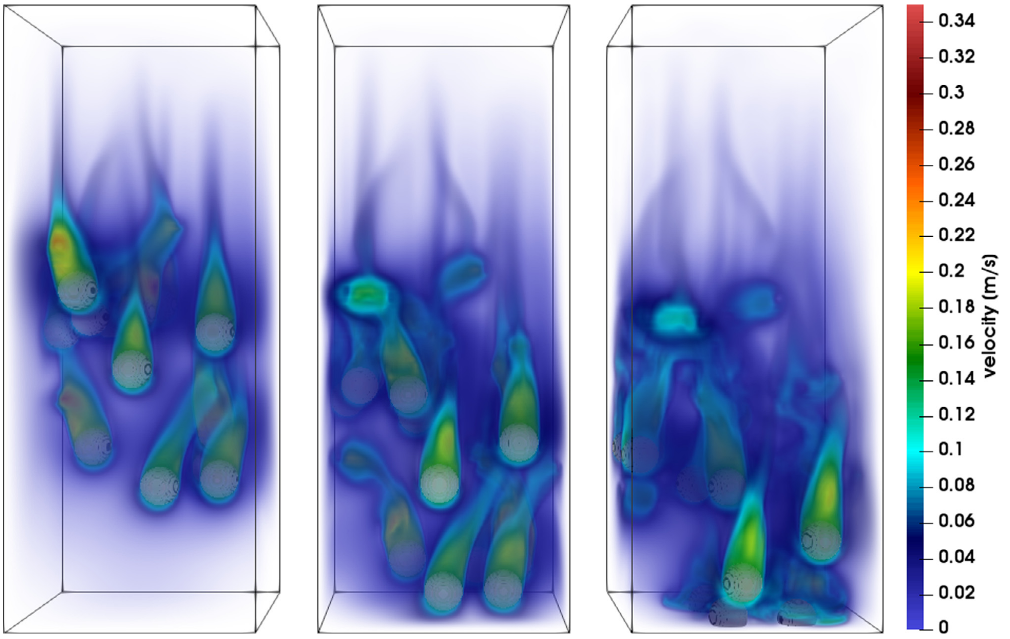

Fig. 14. Velocity magnitude of 15 sedimenting spheres at $t = 1.656s$ (left), $t = 2.232s$ (mid) and $t = 2.736s$ (right).

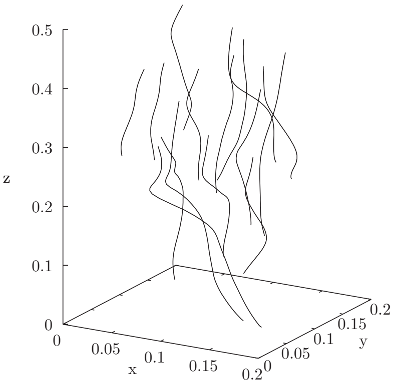

Fig. 15. Pathlines of the limestone particle up to $t = 2.66s$.

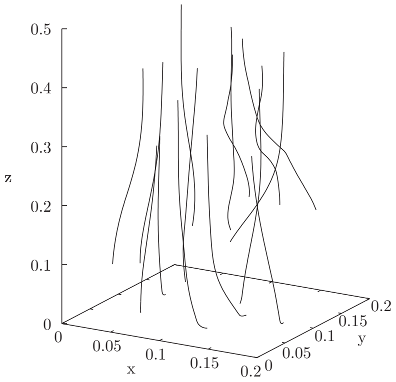

Fig. 16. Pathlines of the spherical particle up to $t = 2.66s$.

under the influence of gravity, inducing a fluid flow, that is shown in Fig. 11 and 12 for different points in time. For further studies the same experiment has been conducted with spheres (see Fig. 13 and 14) with the same mass as the limestone particle and the same starting points. The equivalent radius has been computed to be $0.01568m$. The pathlines of the centres of mass of the particle can be seen in Fig. 15 and Fig. 16. As expected the paths of the spheres are smoother, which is reflected by the mean settling velocity, which is computed to $\bar{u}_l = 0.0865 \frac{m}{s}$ for limestone particle and to $\bar{u}_s = 0.1214 \frac{m}{s}$ for spheres. For the calculations, velocities from the start of the simulations up the time when the first particle reaches the bottom of the domain are considered. This demonstrates the influence of the particle shape on the settling behaviour. In the conducted experiments a momentum exchange between the particles has been observed, leading to a collision-like behaviour. This is probably caused by the relaxation towards the particle velocity of the fluid in combination with the smooth transition region. However, it yet has to be verified that this correctly depicts the underlying physics.

5. Conclusion

An extension of HLBM to 3D is presented along with a strategy for the treatment of arbitrary particle shapes. The generation of physical parameters like the moment of inertia and the volume from a surface representation of the particle is validated by the consideration of an ellipsoid, for which analytical solutions exist, as well as for a complex geometry. The dynamics and computations of hydrodynamic forces are verified by investigating a settling sphere and a flow around a cylinder as benchmark. The results for both cases show good agreement with existing literature. Furthermore, a grid independence study yields a quadratic convergence for the drag coefficient.

For further works a closer investigation of observed repulsive effects acting similar to the treatment of particle collisions is required. Therefore the applied momentum exchange algorithm needs to be examined for approaching particles regarding underlying physical effects like lubrication forces or compressibility effects. In this context also investigations regarding an ideal smoothing parameter ϵ are required. The here presented 3D implementation provides the foundation for this investigations. Furthermore a study of the limits and influence regarding the Reynolds number is of interest.

In the application case the settling of 15 limestone particles is investigated and compared to an analogue case utilising spheres instead. The finding is a difference in the average settling velocity of the bodies, which gives proof to the influence of particle shape on the macroscopic flow behaviour of a suspension, thereby, implying the relevance, e.g. for solid-liquid separation processes.

Acknowledgment

This work was performed on the computational resource For HLR II funded by the Ministry of Science, Research and the Arts Baden-Württemberg and DFG (“Deutsche Forschungsgemeinschaft”).

References

[1] Wang B, Chu KW, Yu AB. Numerical study of particle–fluid flow in a hydrocyclone. Industr Eng Chem Res 2007;46(13):4695–705. doi:10.1021/ie061625u.

[2] de Vasconcelos T, Sapoval B, Andrade Jr J, Grotberg J, Hu Y, Filoche M. Particle capture into the lung made simple? J Appl Physiol 2011;110(6):1664–73. doi:10.1152/japplphysiol.00866.2010.

[3] Lecrivain G, Rayan R, Hurtado A, Hampel U. Using quasi-DNS to investigate the deposition of elongated aerosol particles in a wavy channel flow. Comput Fluids 2016;124:78–85. doi:10.1016/j.compfluid.2015.10.012.

[4] Champion JA, Katare YK, Mitragotri S. Particle shape: a new design parameter for micro- and nanoscale drug delivery carriers. J Controlled Release 2007;121(1–2):3–9. doi:10.1016/j.jconrel.2007.03.022.

[5] Luo J, Dornfeld DA. Effects of abrasive size distribution in chemical mechanical planarization: modeling and verification. IEEE Trans Semicond Manuf 2003;16(3):469–76. doi:10.1109/TSM.2003.815199.

[6] Feichtinger C, Habich J, Köstler H, Hager G, Rüde U, Wellein G. A flexible patch-based lattice Boltzmann parallelization approach for heterogeneous gpu–cpu clusters. Parallel Comput 2011;37(9):536–49. doi:10.1016/j.parco.2011.03.005.

[7] Körner C, Pohl T, Rüde U, Thürey N, Zeiser T. Parallel lattice boltzmann methods for CFD applications. Berlin, Heidelberg: Springer Berlin Heidelberg; 2006. p. 439–66. doi:10.1007/3-540-31619-1_13.

[8] Heuveline V, Krause M, Latt J. Towards a hybrid parallelization of lattice Boltzmann methods. Comput Math Appl 2009;58(5):1071–80. doi:10.1016/j.camwa.2009.04.001.

[9] Krause MJ, Gengenbach T, Heuveline V. Hybrid parallel simulations of fluid flows in complex geometries: application to the human lungs. In: Guarracino M, Vivien F, Traeff J, Cannatoro M, Danelutto M, Hast A, et al., editors. Euro-Par 2010 Parallel Processing Workshops. Lecture Notes in Computer Science, 6586. Springer Berlin / Heidelberg; 2011. p. 209–16.

[10] Vié A, Pouransari H, Zamansky R, Mani A. Particle-laden flows forced by the disperse phase: comparison between Lagrangian and Eulerian simulations. Int J Multiphase Flow 2016;79:144–58. doi:10.1016/j.ijmultiphaseflow.2015.10.010.

[11] Henn T, Thäter G, Dörfler W, Nirschl H, Krause M. Parallel dilute particulate flow simulations in the human nasal cavity. Comput Fluids 2016;124:197–207. doi:10.1016/j.compfluid.2015.08.002.

[12] Chiesa M, Mathiesen V, Melheim JA, Halvorsen B. Numerical simulation of particulate flow by the Eulerian–Lagrangian and the Eulerian–Eulerian approach with application to a fluidized bed. Comput Chem Eng 2005;29(2):291–304. doi:10.1016/j.compchemeng.2004.09.002.

[13] Schäfer B, Harting J, Hecht M, Nirschl H. Agglomeration and filtration of colloidal suspensions with DLVO interactions in simulation and experiment. J Colloid Interface Sci 2010;349:186.

[14] Wachs A, Girolami L, Vinay G, Ferrer G. Grains3d, a flexible dem approach for particles of arbitrary convex shape-part i: numerical model and validations. Powder Technol 2012;224(Supplement C):374–89.

[15] Favier J, Abbaspour-Fard M, Kremmer M, Raji A. Shape representation of axi-symmetrical, non-spherical particles in discrete element simulation using multi-element model particles. Eng Comput (Swansea) 1999;16(4):467–80. doi:10.1108/02644409910271894.

[16] Just S, Toschkoff G, Funke A, Djuric D, Scharrer G, Khinast J, et al. Experimental analysis of tablet properties for discrete element modeling of an active coating process. Am Assoc Pharmaceutical Scientists 2013;14(1):402–11. doi:10.1208/s12249-013-9925-5.

[17] Maier M-L, Henn T, Thaeter G, Nirschl H, Krause MJ. Multiscale simulation with a two-way coupled lattice Boltzmann method and discrete element method. Chemical Engineering & Technology 2017;40(9):1591–8. doi:10.1002/ceat.201600547.

[18] Peskin CS. The immersed boundary method. Acta numerica 2002;11:479–517.

[19] Uhlmann M. An immersed boundary method with direct forcing for the simulation of particulate flows. J Comput Phys 2005;209(2):448–76. doi:10.1016/j.jcp.2005.03.017.

[20] Zhu L, Peskin CS. Simulation of a flapping flexible filament in a flowing soap film by the immersed boundary method. J Comput Phys 2002;179(2):452–68. doi:10.1006/jcph.2002.7066.

[21] Stockie JM, Green SI. Simulating the motion of flexible pulp fibres using the immersed boundary method. J Comput Phys 1998;147(1):147–65. doi:10.1006/jcph.1998.6086.

[22] Rosis AD, Falcucci G, Ubertini S, Ubertini F. Aeroelastic study of flexible flapping wings by a coupled lattice boltzmann-finite element approach with immersed boundary method. J Fluids Struct 2014;49(Supplement C):516–33. doi:10.1016/j.jfluidstructs.2014.05.010.

[23] Wang Z, Fan J, Luo K. Combined multi-direct forcing and immersed boundary method for simulating flows with moving particles. Int J Multiphase Flow 2008;34(3):283–302. doi:10.1016/j.ijmultiphaseflow.2007.10.004.

[24] Boon CW, Houlsby GT, Utili S. A new algorithm for contact detection between convex polygonal and polyhedral particles in the discrete element method. Comput Geotech 2012;44:73–82.

[25] Rakotonirina AD, Delenne J-Y, Wachs A. A parallel discrete element method to model collisions between non-convex particles. EPJ Web Conf 2017;140:06004.

[26] Feng Z-G, Michaelides EE. The immersed boundary-lattice Boltzmann method for solving fluid-particles interaction problems. J Comput Phys 2004;195(2):602–28.

[27] Krüger T, Varnik F, Raabe D. Efficient and accurate simulations of deformable particles immersed in a fluid using a combined immersed boundary lattice boltzmann finite element method. Comput Math Appl 2011;61(12):3485–505. doi:10.1016/j.camwa.2010.03.057.

[28] Bouzidi M, Firdaouss M, Lallemand P. Momentum transfer of a Boltzmann-lattice fluid with boundaries. Phys Fluids 2001;13(11):3452–9. doi:10.1063/1.1399290.

[29] Ginzburg I, d’Humieres D. Multireflection boundary conditions for Lattice Boltzmann models. Phys Rev E 2003;68:066614. doi:10.1103/PhysRevE.68.066614.

[30] Peng C, Teng Y, Hwang B, Guo Z, Wang L-P. Implementation issues and benchmarking of Lattice Boltzmann method for moving rigid particle simulations in a viscous flow. Comput Math Appl 2016;72(2):349–74. doi:10.1016/j.camwa.2015.08.027.

[31] Ladd AJC. Numerical simulations of particulate suspensions via a discretized boltzmann equation. part 1. theoretical foundation. J Fluid Mech 1994;271:285–309. doi:10.1017/S0022112094001771.

[32] Ladd AJC. Numerical simulations of particulate suspensions via a discretized Boltzmann equation. Part 2. numerical results. J Fluid Mech 1994;271:311–39. doi:10.1017/S0022112094001783.

[33] Ladd AJC, Verberg R. Lattice-Boltzmann simulations of particle-fluid suspensions. J Stat Phys 2001;104(5):1191–251. doi:10.1023/A:1010414013942.

[34] Feng YT, Han K, Owen DRJ. Coupled lattice Boltzmann method and discrete element modelling of particle transport in turbulent fluid flows: Computational issues. Int J Numer Methods Eng 2007;72(9):1111–34. doi:10.1002/nme.2114.

[35] Noble DR, Torczynski JR. A Lattice-Boltzmann method for partially saturated computational cells. Int.J. Modern Phys. C 1998;09(08):1189–201. doi:10.1142/S0129183198001084.

[36] Krause MJ, Klemens F, Henn T, Trunk R, Nirschl H. Particle flow simulations with homogenised lattice Boltzmann methods. Particuology 2017;34(Supplement C):1–13. doi:10.1016/j.partic.2016.11.001.

[37] van der Sman RGM. Simulations of confined suspension flow at multiple length scales. Soft Matter 2009;5:4376–87. doi:10.1039/B915749M.

[38] Chen S, Doolen G. Lattice Boltzmann method for fluid flows. Annu Rev Fluid Mech 1998;30:329–64. doi:10.1146/annurev.fluid.30.1.329.

[39] Aidun C, Clausen J. Lattice-Boltzmann method for complex flows. Annu Rev Fluid Mech 2010;42:439–72. doi:10.1146/annurev-fluid-121108-145519.

[40] Krüger T, Kusumaatmaja H, Kuzmin A, Shardt O, Silva G, Viggen E. The Lattice Boltzmann method: principles and practice. Graduate Texts in Physics. Springer; 2016. ISBN 978-3-319-44647-9.

[41] d'Humières D, Ginzburg I, Krafczyk M, Lallemand P, Luo LS. Multiple–relaxation–time lattice Boltzmann models in three dimensions. Philosophical Transactions of the Royal Society of London A: Mathematical, Physical and Engineering Sciences 2002;360:437–51.

[42] Bhatnagar PL, Gross EP, Krook M. A model for collision processes in gases. i. small amplitude processes in charged and neutral one-component systems. Phys Review 1954;94(3):511–25. doi:10.1103/PhysRev.94.511.

[43] Spaid MA, Phelan J, F R. Lattice Boltzmann methods for modeling microscale flow in fibrous porous media. Phys Fluids 1997;9(9):2468–74.

[44] Schäfer M, Turek S, Durst F, Krause E, Rannacher R. Benchmark computations of laminar flow around a cylinder. Flow simulation with high-performance computers. Bd. 2. Hrsg.: E.H. Hirschel. - Braunschweig (u.a.): Vieweg, 1996 – Notes on numerical fluid mechanics; 52. S. 547–566. Braunschweig: Vieweg; 1996.

[45] Latt J, Chopard B, Malaspinas O, Deville M, Michler A. Straight velocity boundaries in the lattice boltzmann method. Phys Rev E 2008;77:056703. doi:10.1103/PhysRevE.77.056703.

[46] Mordant N, Pinton J-F. Velocity measurement of a settling sphere. Eur Phys J B 2000;18(2):343–52. doi:10.1007/PL00011074.

5 Homogenized Lattice Boltzmann Method – Validation and Applications

This chapter was published in the following article:

R. Trunk, T. Weckerle, N. Hafen, G. Thäter, H. Nirschl and M. J. Krause
Revisiting the Homogenized Lattice Boltzmann Method with Applications on Particulate Flows
Computation, 9.11 (2021)
https://doi.org/10.3390/computation9020011

Own contribution according to the contributor roles taxonomy CRediT [14]:

- conceptualization
- data curation
- formal Analysis
- funding acquisition
- investigation
- methodology
- project administration
- software
- validation
- visualization
- writing – original draft
- writing – review & editing

computation MDPI

Article

Revisiting the Homogenized Lattice Boltzmann Method with Applications on Particulate Flows

Robin Trunk [1,2,*], Timo Weckerle [1,2], Nicolas Hafen [1,2], Gudrun Thäter [1,3], Hermann Nirschl [2] and Mathias J. Krause [1,3]

[1] Lattice Boltzmann Research Group, Karlsruhe Institute of Technology, Straße am Forum 8, 76131 Karlsruhe, Germany; timo.weckerle@student.kit.edu (T.W.); nicolas.hafen@kit.edu (N.H.); gudrun.thaeter@kit.edu (G.T.); mathias.krause@kit.edu (M.J.K.)
[2] Institute for Mechanical Process Engineering and Mechanics, Karlsruhe Institute of Technology, Straße am Forum 8, 76131 Karlsruhe, Germany; hermann.nirschl@kit.edu
[3] Institute for Applied and Numerical Mathematics, Karlsruhe Institute of Technology, Englerstraße 2, 76131 Karlsruhe, Germany
* Correspondence: robin.trunk@kit.edu

Abstract: The simulation of surface resolved particles is a valuable tool to gain more insights in the behaviour of particulate flows in engineering processes. In this work the homogenized lattice Boltzmann method as one approach for such direct numerical simulations is revisited and validated for different scenarios. Those include a 3D case of a settling sphere for various Reynolds numbers. On the basis of this dynamic case, different algorithms for the calculation of the momentum exchange between fluid and particle are evaluated along with different forcing schemes. The result is an updated version of the method, which is in good agreement with the benchmark values based on simulations and experiments. The method is then applied for the investigation of the tubular pinch effect discovered by Segré and Silberberg and the simulation of hindered settling. For the latter, the computational domain is equipped with periodic boundaries for both fluid and particles. The results are compared to the model by Richardson and Zaki and are found to be in good agreement. As no explicit contact treatment is applied, this leads to the assumption of sufficient momentum transfer between particles via the surrounding fluid. The implementations are based on the open-source C++ lattice Boltzmann library OpenLB.

Keywords: homogenized lattice Boltzmann method; hindered settling; OpenLB; particle simulation; momentum exchange algorithm; tubular pinch effect

check for updates

Citation: Trunk, R.; Weckerle, T.; Hafen, N.; Thäter, G.; Nirschl, H.; Krause, M.J. Revisiting the Homogenized Lattice Boltzmann Method with Applications on Particulate Flows. *Computation* **2021**, *9*, 11. https://doi.org/10.3390/computation9020011

Received: 22 December 2020
Accepted: 20 January 2021
Published: 27 January 2021

1. Introduction

The simulation of particulate flows finds application in many fields as it permits a detailed examination of an engineering process. It allows access to data on particle behaviour, for which experimental measuring is complex or costly. It was already applied for the simulation of solid separation processes by Viduka et al. [1], testing different pulsation profiles of a jigging device, or by Li et al. [2] regarding the separation of soybeans from mustard seeds. The work presented here is the validation and improvement of a method for direct numerical simulation, also depicting the particle's shape. The industrial relevance of this topic has been shown, e.g., by Champion et al. [3] who showed that particle shape significantly influences the performance of drug carriers. A discussion on the industrial relevance of particle shape for products and processes is also given by Davies [4], who references, e.g., the relevance for the production of rubber, as also stated by Scotti et al. [5]. On the most coarse level, particles can be depicted as a continuum by considering distributions with Euler–Euler approaches utilising an advection–diffusion equation [6–8]. Approaches which treat each particle as separate entity yield more details. With the discrete element method (DEM), e.g., separation processes in a cyclone can be studied [9] considering the particles as solid spheres. Furthermore, adsorption processes in a static mixer [10] or packing characteristics of powder [11] are of interest. The DEM can be used together with various approaches and models for the simulation and representation of the fluid. The coupling of DEM particles with a model for a non-Newtonian turbulent fluid is for example relevant in the simulation of anaerobic digestion [12]. A review of applications for DEM simulations is given by Zhu et al. [13].

For more sophisticated studies, hydrodynamic forces on a particle and its shape can be resolved by direct numerical simulations (DNS) [14]. This enables, e.g., the calculation of drag correlations [15]. Focusing on the shape, the investigation of the interaction between particles and a rough surface is possible [16]. At this point, however, proper collision treatment becomes important. For the absence of a significant influence of a fluid, the framework Grains3D [17,18] has been presented to investigate arbitrarily shaped convex particles under the influence of gravity and contact forces applying the Gilbert–Johnson–Keerthi algorithm for contact detection and distance calculation. The framework has later been extended to concave shapes by representing them as glued convex shapes [19]. Considering particles submersed in fluid, a simple approach is the one of glued spheres [20] to approximate various particle shapes and get more information on the distribution of acting forces. For this approximation, however, the accuracy is limited as the required number of spheres increases drastically for better approximations of a shape. To circumvent this problem, the object can be described by several Lagrange points on the surface, at which the hydrodynamic forces are calculated. This points can be independent of the underlying grid, which represents the fluid. This allows for a high accuracy in depiction of the shape, but requires frequent interpolation between fluid and particle points. This common approach is called immersed boundary method (IBM) [21]. One of its advantages is that it can be coupled with various approaches to solve the fluid system like the finite element method, the finite volume method or the lattice Boltzmann method (LBM) [22,23].

The coupled IBM–LBM has been frequently applied for the investigation of fluid structure interaction problems [24]. While many studies of, e.g., vortex induced vibrations [22,25] or the flow around a torus by Wu and Shu [26] only consider simpler geometries with analytical representations, mappings for more complex polygons exist, as discussed by Owen et al. [27]. Nevertheless, more complex structures can be simulated as well as described by Beny and Latt [28], who simulated multiple propellers on a GPU system. In IBM–LBM, it is possible to also consider simple strings as shown by Tian et al [22] who simulated filaments in a flow. A comparative study of IBM approaches was performed by Kang and Hassan [29], who investigated the flow past a cylinder and decaying Taylor–Green vortices.

The homogenized lattice Boltzmann method (HLBM) used in this work, in turn, has very few restrictions regarding the shape, since a voxel representation of almost any object can be chosen for simulations, as shown in [30]. Very thin objects, however, remain problematic, as they may not be captured by the lattice resolution. The main difference between IBM and HLBM is the way the objects are represented. The former employs Lagrangian points, which allows thin structures but requires interpolations and the creation of a distribution of those points on the surface of the object. The latter directly uses points on the fluid grid. The correct depiction of a structure, in this case, mainly depends on the grid resolution.

The LBM proved to be easy to parallelize due to the fact that most calculations are carried out in a strictly local collision step. This has been investigated for the use on computing clusters with GPU systems [31] as well as mixed CPU–GPU systems [32]. For LBM, additional approaches for the simulation of arbitrarily shaped particles are available, which are specific to their method. The most common one is the partially saturated cells method (PSM), in its original version proposed by Noble and Torczynski [33]. It depicts the object on the fluid grid by assigning a linear combination of a no-slip condition and bulk flow to a grid cell depending on its distance to the actual physical particle boundary. This is possible as LBM operates on a mesoscopic level considering the fluid by distributions of fluid-particles in a phase space. There are several aspects to this approach if moving objects are considered, e.g., the refilling of cells that were previously covered by a particle or the chosen no-slip condition. This has been investigated by Peng et al. [34].

Another topic is the way the hydrodynamic force is calculated. The stress integration method, e.g., described in [35,36], is also applicable for other simulation approaches and not specific to LBM but proved to be inefficient [37,38]. An alternative is the momentum exchange algorithm (MEA) [39,40], which calculates differences in the momentum via the mentioned particle distributions in the phase space. For this method, various formulations and improvements have been proposed [41–44] and are subject to current investigations [34].

In this study three applications are presented. For the first case of a settling sphere, the results are validated against ten Cate et al. [45], who performed simulations of a single sphere for different Reynolds numbers and compared the data to particle imaging velocimetry experiments. In addition, the results are compared to various drag correlations discussed in Section 2.1.

The second case simulates the tubular pinch effect first described by Segré and Silberberg [46]. They found that a neutrally buoyant particle in a tube flow equilibrates at a position between the tube's center and its wall and that the results for single particles can be extended to mixtures by linear combination [47]. Later, Tachibana et al. [48] found that the equilibrium position depends on the ratio of sphere diameter to tube diameter, which should be larger than 0.2 for the effect to be clearly visible. Karnis et al. [49] studied further the influence of the Reynolds number and the distance between two spheres on this effect.

The case of hindered settling is also relevant in many applications of process engineering as usually collectives of particles are processed. This is reflected in many studies simulating this case [50–53]. The results are usually compared to an empirical correlation found by Richardson and Zaki [54]. However, more correlations exist as discussed in Section 2.2. The results in this study are compared to different correlations to give a better overview.

In this work, the HLBM proposed by Krause et al. [30,55] is applied. Contrary to other approaches for moving objects, HLBM does not represent objects by a sharp no-slip boundary but rather with interior fluid utilising a forcing scheme and a transition region to mimic such a condition. This is a similarity to the IBM and leads to the need for further research as existing MEA approaches are developed for no-slip boundaries in the first place. Therefore, a novel momentum loss algorithm (MLA) is tested in this study. The semi-locality (depending on the chosen approach for the calculation of hydrodynamic forces) of the HLBM allows for an easy and efficient implementation on parallel systems without the need of costly interpolations. On the other hand, no refilling of cells is required as in PSM approaches. Besides the new MLA the HLBM is revisited and for the first time evaluated for different forcing schemes and methods for the calculation of hydrodynamic forces. To the knowledge of the authors such a comparative study for HLBM has not been performed before. This finally leads to a new improved scheme, which is validated for the simple case of a settling sphere but also tested for the application in hindered settling simulations and the tubular pinch effect. The results are compared to common experimentally determined correlations and reference simulations. This shows the range of applicability of the presented method, e.g., regarding the Reynolds number. Such tests are currently not found in literature for HLBM, however, this information is of interest when choosing a proper simulation approach depending on an application. Therefore, additionally different cases are examined for the first time with HLBM, which is important as, e.g., the tubular pinch effect can't be reproduced by all approaches for DNS particle simulations as stated by Li et al. [35] and Peng et al. [34]. Additionally, considering the case of hindered settling the investigation of particle interactions, first mentioned by Krause et al [55], is continued, which was not found in other publications. To the knowledge of the authors, the investigations and findings for HLBM presented in this work have not been shown before.

The remainder of this paper is organized as follows: in Section 2 the physical background and correlations found in the literature are discussed. Then, in Section 3 the methods used for the simulations are discussed along with various forcing and MEA schemes to be tested. Finally, in Section 4 the results of the numerical investigation are presented and the conclusion is drawn in Section 5. All simulations presented are performed with the open-source lattice Boltzmann C++ framework OpenLB [56].

2. Modelling

This study focuses on two component systems of rigid particles submersed in a water-like fluid. The latter is described by the incompressible Navier–Stokes equations, given by

$$\begin{aligned} \frac{\partial \boldsymbol{u}_\mathrm{f}}{\partial t} + (\boldsymbol{u}_\mathrm{f} \cdot \nabla)\boldsymbol{u}_\mathrm{f} - \nu \Delta \boldsymbol{u}_\mathrm{f} + \frac{1}{\rho_\mathrm{f}} \nabla p = \boldsymbol{F}_\mathrm{f} \quad & \text{in } \Omega \times I\,, \\ \nabla \cdot \boldsymbol{u}_\mathrm{f} = 0 \quad & \text{in } \Omega \times I\,. \end{aligned} \tag{1}$$

The equations are defined on a spatial domain $\Omega \in \mathbb{R}^d$ of dimension $d \in 2,3$ and a time interval $I \subseteq \mathbb{R}$. The fluid velocity is denoted by $\boldsymbol{u}_\mathrm{f} : \Omega \times I \to \mathbb{R}^d$, while $p : \Omega \times I \to \mathbb{R}$ describes the pressure, $\rho_\mathrm{f} \in \mathbb{R}_{>0}$ the fluid's density and $\nu \in \mathbb{R}_{>0}$ its kinematic viscosity. $\boldsymbol{F}_\mathrm{f} : \Omega \times I \to \mathbb{R}^d$ represents the total of external forces acting on the fluid.

The dynamics of the second component, the rigid particles, are governed by the equations based on Newton's second law of motion

$$m_\mathrm{p} \frac{\partial \boldsymbol{u}_\mathrm{p}}{\partial t} = \boldsymbol{F}_\mathrm{p} \quad \text{and} \quad \boldsymbol{J}_\mathrm{p} \frac{\partial \boldsymbol{\omega}_\mathrm{p}}{\partial t} = \boldsymbol{T}_\mathrm{p}\,. \tag{2}$$

With the particle mass $m_\mathrm{p} \in \mathbb{R}_{>0}$, the particle velocity $\boldsymbol{u}_\mathrm{p} : \Omega \times I \to \mathbb{R}^d$ and the force acting on the particle $\boldsymbol{F}_\mathrm{p} : \Omega \times I \to \mathbb{R}^d$, the trajectory of motion can be calculated. The rotational behaviour is modelled analogously with the moment of inertia $\boldsymbol{J}_\mathrm{p} \in \mathbb{R}^{\hat{d}}$, the angular velocity $\boldsymbol{\omega}_\mathrm{p} : \Omega \times I \to \mathbb{R}^{\hat{d}}$ and the torque $\boldsymbol{T}_\mathrm{p} : \Omega \times I \to \mathbb{R}^{\hat{d}}$. Here $\hat{d} = 1$ for $d = 2$ and $\hat{d} = 3$ for $d = 3$.

In this study, only the gravitational and buoyancy forces are considered as external forces. They are given by $\boldsymbol{F}^\mathrm{G} = (0, 0, m_\mathrm{p} g)$ and $\boldsymbol{F}^\mathrm{B} = (0, 0, -m_\mathrm{p} \frac{\rho_\mathrm{f}}{\rho_\mathrm{p}} g)$ for $d = 3$ ($\boldsymbol{F}^\mathrm{G} = (0, m_\mathrm{p} g)$ and $\boldsymbol{F}^\mathrm{B} = (0, -m_\mathrm{p} \frac{\rho_\mathrm{f}}{\rho_\mathrm{p}} g)$ for $d = 2$) for a gravitational acceleration of g. This means, forces regarding particle-particle and particle-wall contact are neglected in this study and momentum between particles is only transferred via the fluid. As most cases consider only single particles with no relevant wall contact this is reasonable. The only exception is the investigation of hindered settling in Section 4.3. Here the system is discretized with a decent resolution to allow for sufficient momentum transfer via the fluid. Along with the hydrodynamic force $\boldsymbol{F}^\mathrm{H} : \Omega \times I \to \mathbb{R}^d$ accounting for the momentum transfer between fluid and particles, the combined forces are given by

$$\boldsymbol{F}_\mathrm{f} = \boldsymbol{F}^\mathrm{H}\,, \quad \boldsymbol{F}_\mathrm{p} = \boldsymbol{F}^\mathrm{G} - \boldsymbol{F}^\mathrm{B} - \boldsymbol{F}^\mathrm{H} \quad \text{and} \quad \boldsymbol{T}_\mathrm{p} = \boldsymbol{r} \times \left(-\boldsymbol{F}^\mathrm{H}\right), \tag{3}$$

for a vector $\boldsymbol{r} \in \mathbb{R}^d$ denoting the distance to the center of mass of a particle.

2.1. Drag Force

While in this study a DNS approach is chosen, for methods considering the particles as single points the hydrodynamic force has to be modelled. This is done via a drag force, accounting for the resistance an object experiences when moving relative to a surrounding fluid. It is defined by

$$\boldsymbol{F}^\mathrm{D} = \frac{1}{2} \rho_\mathrm{f} (\boldsymbol{u}_\mathrm{p} - \boldsymbol{u}_\mathrm{f})^2 C_D A\,, \tag{4}$$

with $A \in \mathbb{R}_{>0}$ being the area of the projection of the object in flow direction. While the determination of the drag coefficient $C_D \in \mathbb{R}$ for various shapes is subject to current research [57,58], for spheres many correlations depending on the Reynolds number Re have been given. The latter is defined as

$$\mathrm{Re} = \frac{d_{\mathrm{P}} \|\boldsymbol{u}_{\mathrm{P}}\|}{\nu} \,, \tag{5}$$

for the cases considered in this work, with a particle's diameter $d_{\mathrm{P}} \in \mathbb{R}_{>0}$. For small Reynolds numbers the drag coefficient is described by Stokes' law [59]

$$C_D = \frac{24}{\mathrm{Re}} \,, \quad \text{for } \mathrm{Re} < 1 \,. \tag{6}$$

While in the Newton regime between $\mathrm{Re} = 10^3$ and $\mathrm{Re} = 10^5$ the coefficient is defined by $C_D = 0.44$, many correlations exist for the transition region of Reynolds numbers between 1 and 10^3. Notable here is among others the contribution by Abraham [60], who took the boundary layer into account for a theoretical derivation, leading to

$$C_D = \left(0.5407 + \sqrt{\frac{24}{\mathrm{Re}}}\right)^2 \,, \quad \text{for } 0 < \mathrm{Re} < 5000 \,. \tag{7}$$

Schiller and Naumann [61] used an empirical approach to obtain the commonly used approximation of

$$C_D = \frac{24}{\mathrm{Re}}\left(1 + 0.15\mathrm{Re}^{0.687}\right) \,, \quad \text{for } \mathrm{Re} < 800 \tag{8}$$

for the drag coefficient. As many more correlations can be found, the authors refer to Dey et al. [62] for a comprehensive overview.

2.2. Hindered Settling

The above mentioned drag correlations consider the case of free settling, more precisely the settling of a single sphere in an infinitely extended medium. In practical applications, collectives of particles are more common, which leads to the case of hindered settling caused by interactions between particles. The empirical correlations developed in many past studies proved to be sensible approaches in modeling such behaviour.

The oldest recapitulated here is the one by Steinour [63], who investigated spheres consisting of tapioca and glass, for a solid volume fraction ϕ of up to 49.8%. The experimental conditions correspond to $\mathrm{Re} = 0.0025$ and $\mathrm{Re} = 0.0026$, leading to

$$u_{\mathrm{Steinour}}(\phi) = u_{\mathrm{S}}(1-\phi)^2 e^{-4.19\phi} \,. \tag{9}$$

The hindered settling velocity is here expressed relative to the terminal settling velocity according to Stokes' u_{S}, obtained by inserting Equation (6) in Equation (4).

Another correlation was found by Oliver [64]. In the experiments with Kallodoc particles, Reynolds numbers up to 0.39 were reached with solid volume fractions up to 35%. The results are reflected in the formula for the hindered settling velocity given by

$$u_{\mathrm{O}}(\phi) = u_{\mathrm{S}}\left(1 - 0.75\phi^{\frac{1}{3}}\right)(1 - 2.15\phi) \,. \tag{10}$$

One of the most commonly used expressions was found in investigations performed by Richardson and Zaki, who approached the topic from both, an analytical [54] and an experimental [65] perspective. Their formulation was subject to many adaptions regarding accuracy, convenience and extension of applicability [66–69]. In the original form it is given by $u_{\mathrm{RZ}}(\phi) = u_{\mathrm{S}}(1-\phi)^n$, with

$$n = \begin{cases} 4.65 & \text{for } \mathrm{Re} < 0.2 \\ 4.35\mathrm{Re}^{-0.03} & \text{for } 0.2 < \mathrm{Re} < 1 \\ 4.45\mathrm{Re}^{-0.1} & \text{for } 1 < \mathrm{Re} < 500 \\ 2.39 & \text{for } 500 < \mathrm{Re} \end{cases} . \tag{11}$$

In a more comprehensive study taking also the results of other authors into account along with their findings, Barnea and Mizrahi [70] concluded with the general correlation

$$u_{\mathrm{BM}}(\phi) = u_{\mathrm{S}} \frac{1-\phi}{(1+\phi^{\frac{1}{3}})e^{\frac{5\phi}{3(1-\phi)}}} , \tag{12}$$

which is independent of the Reynolds number. While this is the finding for the creeping flow regime (Re $\ll$ 1), Barnea and Mizrahi suggest the application of drag correlations beyond Stokes' law. Therefore in contrast to other publications, for higher Re the hindered settling velocity is not based on u_{S} anymore, but on a terminal settling velocity determined, e.g., by Equation (8).

3. Methods

For the simulations, the lattice Boltzmann method was applied, which operates on a uniform cubical grid Ω_{h} approximating the computational domain. This structure is, together with the discrete phase space, spanned by the d spatial dimensions and a discrete set of q velocities $\boldsymbol{c}_i \in \mathbb{R}^d$, $i = 0, \ldots, q-1$, denoted as lattice. The latter is usually labeled as DdQq. Choosing commonly used sets, the simulations in this study were performed on a D2Q9 and a D3Q19 lattice. As usual, the computations were conducted in lattice units meaning all values were scaled such that the grid spacing and time step size became $\delta x^{\mathrm{L}} = 1$ and $\delta t^{\mathrm{L}} = 1$, respectively. The superscript $^{\mathrm{L}}$ indicates that a value is given in lattice units. For reasons of readability, all values in this section were assumed to be in lattice units if not stated otherwise omitting the superscript.

The propagation of particle distributions $f_i : \Omega_{\mathrm{h}} \times I_{\mathrm{h}} \to \mathbb{R}$, $i = 0, \ldots, q-1$, for a discretized time interval I_{h}, on the given lattice is described by the lattice Boltzmann equation. Together with the Bhatnagar—Gross—Krook (BGK) collision operator [71] it reads

$$f_i(\boldsymbol{x}+\boldsymbol{c}_i, t+1) - f_i(\boldsymbol{x}, t) = -\frac{1}{\tau}\Big(f_i(\boldsymbol{x}, t) - f_i^{\mathrm{eq}}(\rho, \boldsymbol{u})\Big) , \quad \text{for } \boldsymbol{x} \in \Omega_{\mathrm{h}},\ t \in I_{\mathrm{h}},\ i = 0, \ldots, q-1 . \tag{13}$$

The lattice relaxation time τ is related to the lattice kinematic viscosity by

$$\nu = c_{\mathrm{s}}^2\left(\tau - \frac{1}{2}\right) . \tag{14}$$

Beside a streaming of particle distributions, Equation (13) describes the relaxation of a system towards an equilibrium state given by the discrete Maxwell–Boltzmann distribution

$$f_i^{\mathrm{eq}}(\rho, \boldsymbol{u}) = w_i \rho \left(1 + \frac{\boldsymbol{c}_i \cdot \boldsymbol{u}}{c_{\mathrm{s}}^2} + \frac{(\boldsymbol{c}_i \cdot \boldsymbol{u})^2}{2c_{\mathrm{s}}^4} + \frac{\boldsymbol{u}^2}{2c_{\mathrm{s}}^2}\right) , \quad \text{for } i = 0, \ldots, q-1 . \tag{15}$$

Here, w_i are weights originating from a Gauss–Hermite quadrature rule and $c_{\mathrm{s}} = \frac{1}{\sqrt{3}}$ is the lattice speed of sound, valid for both lattice configurations used in this work. The density and velocity on a grid point can be calculated by moments of the discrete distributions

$$\rho(\boldsymbol{x}, t) = \sum_{i=0}^{q-1} f_i(\boldsymbol{x}, t) \quad \text{and} \quad \boldsymbol{u}(\boldsymbol{x}, t) = \frac{1}{\rho}\sum_{i=0}^{q-1} \boldsymbol{c}_i f_i(\boldsymbol{x}, t) , \quad \text{for } \boldsymbol{x} \in \Omega_{\mathrm{h}},\ t \in I_{\mathrm{h}} , \tag{16}$$

respectively. Furthermore, the pressure p is related to the density ρ in LBM by $p(\boldsymbol{x},t) = \rho(\boldsymbol{x},t)c_s^2$. In the rest of this section, the arguments for density and velocity are omitted for better comprehensibility. For a more comprehensive overview on this simulation approach, the authors refer to [23].

3.1. Homogenized Lattice Boltzmann Method

The DNS simulations in this study were performed utilizing the HLBM, which was first published by Krause et al. [55] and was extended to 3D by Trunk et al. [30]. The extensions of the method to the standard LBM with BGK collision could be divided into three parts. Namely, the representation of an object on the lattice, the forcing scheme applied to the fluid to account for the particles' presence and a method to calculate the exchanged momentum between an object and fluid for the calculation of forces acting on the object. From this point, the trajectory of a particle is calculated according to Equation (2) in combination with a velocity-Verlet algorithm [72,73].

Object Representation. The depiction of arbitrary shapes within the HLBM is described in detail by Trunk et al. [30]. Here, only a brief overview is given. From a voxel representation of the object, which did not necessarily have the same spatial resolution as the lattice, parameters like the moment of inertia and the mass were calculated. For a smooth transition between fluid and particle domain, a Gaussian filter was applied. If an analytical representation of the shape was given, a smooth transition could also be defined utilizing trigonometric functions as described by Krause et al. [55]. This led to a mapping function $d_\mathrm{B} : \Omega \times I \to [0,1]$, which took on the value of 0 in the fluid domain and 1 in the area covered by the object. In the transition region it yielded values in between. Along with the current position of the object $\boldsymbol{x}_\mathrm{p} \in \Omega$ this defined a domain $B(t) = \{\boldsymbol{x} \in \Omega : d_\mathrm{B}(\boldsymbol{x},t) \neq 0\}$ which was covered by the body. To account for the presence of particles, the velocity used in the equilibrium distribution Equation (15) was replaced by the convex combination

$$\tilde{\boldsymbol{u}}(\boldsymbol{x},t) = \boldsymbol{u}(\boldsymbol{x},t) + d_\mathrm{B}(\boldsymbol{x},t)\big(\boldsymbol{u}_\mathrm{p}(\boldsymbol{x},t) - \boldsymbol{u}(\boldsymbol{x},t)\big) \quad \text{for } \boldsymbol{x} \in B(t),\ t \in I_\mathrm{h}\,. \tag{17}$$

The velocity difference $\Delta\boldsymbol{u} = \tilde{\boldsymbol{u}} - \boldsymbol{u}$ could be used in forcing schemes as stated in the next Section.

Forcing Schemes. As the effect on the fluid is given via a velocity difference, in previous publications a forcing scheme according to Shan and Chen [74] has been chosen, which only modifies the velocity inserted in the Maxwell–Boltzmann distribution. In this study, several forcing schemes (proposed by Shan and Chen [74], Guo et al. [75] and Kupershtokh et al. [76]) were considered (see Section 3.2) and then tested in Section 4.1.

Momentum Exchange. Various methods to calculate the exchanged momentum are given in Section 3.3 and are applied in Section 4.1. They were evaluated regarding the accuracy of the velocity profile of a falling sphere. In previous publications [30,55] an adapted version of the momentum exchange according to Ladd [39,40] was used.

3.2. Forcing Schemes

To incorporate a force in LBM, the definition of the velocity handed to the Maxwell–Boltzmann distribution, from now on labeled $\boldsymbol{u}^\mathrm{eq}$, was modified and/or a source term S_i was added to the right hand side of Equation (13). In all cases, the fluid velocity given in Equation (16) was redefined in the presence of a force $\boldsymbol{F}$ to

$$\boldsymbol{u} = \frac{1}{\rho}\sum_{i=0}^{q-1} \boldsymbol{c}_i f_i(\boldsymbol{x},t) + \frac{\boldsymbol{F}\delta t}{2\rho}\,, \quad \text{for } \boldsymbol{x} \in \Omega_\mathrm{h},\ t \in I_\mathrm{h}\,. \tag{18}$$

For a more comprehensive discussion on forcing schemes the authors again refer to Krüger et al. [23], however, the three forcing schemes used in this study are briefly summarized here.

The approach of Shan and Chen [74] only modifies the equilibrium velocity to

$$\boldsymbol{u}^{\mathrm{eq}} = \frac{1}{\rho}\sum_{i=0}^{q-1} \boldsymbol{c}_i f_i(\boldsymbol{x},t) + \tau\frac{\boldsymbol{F}}{\rho}\,, \quad \text{for } \boldsymbol{x} \in \Omega_{\mathrm{h}},\ t \in I_{\mathrm{h}}\,. \tag{19}$$

This scheme originates from methods for multi-component and multi-phase flows, but is also applicable to single-component systems. It is frequently used due to its simplicity and performance advantage, however, a dependency of the results on τ is found, e.g., by Huang et al. [77] examining various forcing schemes for multi-phase LBM. Along with this scheme, a velocity shift method is proposed by Shan and Chen [74], which states $\boldsymbol{F} = \frac{\rho}{\tau}\Delta\boldsymbol{u}$. Guo et al. [75] proposed a scheme modifying both the velocity and the source term to

$$\boldsymbol{u}^{\mathrm{eq}} = \frac{1}{\rho}\sum_{i=0}^{q-1} \boldsymbol{c}_i f_i(\boldsymbol{x},t) + \frac{\boldsymbol{F}\delta t}{2\rho}\,, \quad \text{for } \boldsymbol{x} \in \Omega_{\mathrm{h}},\ t \in I_{\mathrm{h}}\,, \tag{20}$$

$$S_i(\boldsymbol{x},t) = \left(1 - \frac{\delta t}{2\tau}\right) w_i \left(\frac{\boldsymbol{c}_i - \boldsymbol{u}}{c_{\mathrm{s}}^2} + \frac{(\boldsymbol{c}_i \cdot \boldsymbol{u})\boldsymbol{c}_i}{c_{\mathrm{s}}^4}\right) \cdot \boldsymbol{F}\,, \quad \text{for } \boldsymbol{x} \in \Omega_{\mathrm{h}},\ t \in I_{\mathrm{h}}\,. \tag{21}$$

At last, the exact difference method (EDM) by Kupershtokh et al. [76] only introduces a source term $S_i(\boldsymbol{x},t) = f_i^{\mathrm{eq}}(\rho, \boldsymbol{u} + \Delta\boldsymbol{u}) - f_i^{\mathrm{eq}}(\rho, \boldsymbol{u})$ to the system. The velocity difference $\Delta\boldsymbol{u}$ it is based upon is calculated by $\Delta\boldsymbol{u} = \boldsymbol{F}\delta t/\rho$, since $\delta t = \delta x = 1$ in lattice units as stated before. In this approach the velocity $\boldsymbol{u}$ remains just as defined in Equation (16).

3.3. Methods for Momentum Exchange

In this study, different schemes for the momentum exchange between fluid and particle are also discussed. The first is an adaptation of the MEA by Ladd [39,40] which has been applied in [30,55]. As shown in [37,38], it can be written as

$$\boldsymbol{F}^{\mathrm{H}}(t) = \sum_{\boldsymbol{x} \in B(t)} \sum_{i=1}^{q-1} \boldsymbol{c}_i \left(f_i(\boldsymbol{x} + \boldsymbol{c}_i, t) + f_{\bar{i}}(\boldsymbol{x}, t)\right)\,, \quad \text{for } t \in I_{\mathrm{h}}\,. \tag{22}$$

Here $f_{\bar{i}}$ is defined as distribution function according to the velocity $\boldsymbol{c}_{\bar{i}}$, which is opposite to $\boldsymbol{c}_i$, i.e., $\boldsymbol{c}_{\bar{i}} = -\boldsymbol{c}_i$. Various Improvements have been suggested [41,78], as this approach fails, e.g., in the simulation of the tubular pinch effect described by Segré and Silberberg [46,47], as stated by Peng et al. [34]. In their study, they compared different MEA approaches and tested them along with other aspects of moving boundary implementations. One of the most common approaches is the one by Wen et al. [42]

$$\boldsymbol{F}^{\mathrm{H}}(t) = \sum_{\boldsymbol{x} \in B(t)} \sum_{i=1}^{q-1} (\boldsymbol{c}_i - \boldsymbol{u}_{\mathrm{p}}) f_i(\boldsymbol{x} + \boldsymbol{c}_i, t) + (\boldsymbol{c}_i + \boldsymbol{u}_{\mathrm{p}}) f_{\bar{i}}(\boldsymbol{x}, t)\,, \quad \text{for } t \in I_{\mathrm{h}}\,. \tag{23}$$

It incorporates the particle velocity for higher accuracy and in order to achieve Galilean invariance.

Lastly, a new approach is proposed by the authors denoted as momentum loss algorithm. As in the HLBM objects are depicted with interior fluid rather than with a sharp no-slip boundary, the investigation for alternative approaches to calculate exchanged momentum is of interest. Examined in this work is the method of computing the momentum directly from the introduced forcing for the approaches by Kupershtokh et al. [76] and Shan and Chen [74]. For the latter this means

$$\boldsymbol{F}^{\mathrm{H}}(t) = \frac{1}{\tau} \sum_{\boldsymbol{x} \in B(t)} \sum_{i=1}^{q-1} \boldsymbol{c}_i \left(f_i^{\mathrm{eq}}(\rho, \tilde{\boldsymbol{u}}) - f_i^{\mathrm{eq}}(\rho, \boldsymbol{u})\right)\,, \quad \text{for } t \in I_{\mathrm{h}}\,, \tag{24}$$

while for the EDM it is slightly different namely,

$$\boldsymbol{F}^{\mathrm{H}}(t) = \sum_{\boldsymbol{x}\in B(t)} \sum_{i=1}^{q-1} \boldsymbol{c}_i \left(f_i^{\mathrm{eq}}(\rho,\tilde{\boldsymbol{u}}) - f_i^{\mathrm{eq}}(\rho,\boldsymbol{u}) \right) , \quad \text{for } t \in I_{\mathrm{h}} . \tag{25}$$

The forcing schemes and methods for momentum exchange discussed in this section allow for a comparative study. The previously used HLBM approach is based on the forcing introduced by Shan and Chen [74] and the momentum exchange by Ladd [39,40]. According to literature [34], there are methods available which yield a higher accuracy. This will be investigated in Section 4.1 leading to an updated version of HLBM which is expected to yield higher accuracy.

4. Results and Discussion of Numerical Experiments

In this Section, various schemes for forcing and momentum exchange are tested along with the remaining HLBM implementation. In Section 4.1 first, the approaches are compared regarding the settling velocity of a sphere and the best performing combination is selected for further validation against existing drag correlations for spheres. Afterwards, the implementation is applied to the cases of a neutrally buoyant particle in a pipe in Section 4.2 and hindered settling in Section 4.3, respectively.

4.1. Settling Sphere

In this section, simulation results are first compared to experimental data by ten Cate et al. [45] for evaluation and validation of the chosen methods and subsequently against empirical correlations discussed in Section 2.1.

4.1.1. Simulation Setup—Comparison to Literature

The settling of a single sphere has been investigated by ten Cate et al. [45] both, experimentally and numerically. Therefore a sphere of diameter $d_{\mathrm{p}} = 0.015\,\mathrm{m}$ with density $\rho_{\mathrm{p}} = 1120\,\mathrm{kg\,m^{-3}}$ was placed 0.12 m from the bottom in a container of height 0.16 m and a width and depth of 0.1 m, as shown in Figure 1. This setup was used to examine the settling for different Reynolds numbers by varying the fluid density ρ_{f} and dynamic viscosity μ_{f}. The same setup was chosen for the simulations with different discretization parameters for each case. The values were given along with the simulation results of ten Cate et al. [45] for a resolution of four cells per particle radius in Table 1. The Reynolds number was given in this case according to the values in the table by $\mathrm{Re} = d_{\mathrm{p}} u_{\infty} \rho_{\mathrm{f}} / \mu_{\mathrm{f}}$. For the boundaries, a no-slip halfway bounce-back condition [79] was chosen.

Table 1. Values of the setup of the four cases for a settling sphere investigated by ten Cate et al. [45] along with the deviation of their results to the maximum settling velocity u_{∞} predicted with the drag correlation by Abraham [60].

Case	ρ_{f} in $\mathrm{kg\,m^{-3}}$	μ_{f} in $\mathrm{kg\,m^{-1}s^{-1}}$	Re	δx in m	δt in s	u_{∞} in $\mathrm{m\,s^{-1}}$ (Abraham [60])	Error in %
1	970	0.373	1.5	1.671×10^{-3}	3.891×10^{-4}	0.038	10.6
2	965	0.212	4.1	1.645×10^{-3}	2.41×10^{-4}	0.06	5.0
3	962	0.113	11.6	1.61×10^{-3}	1.526×10^{-4}	0.091	4.5
4	960	0.058	31.9	1.559×10^{-3}	1.01×10^{-4}	0.128	5.3

In this study, the given setup is investigated for different combinations of forcing and momentum exchange schemes described in Sections 3.2 and 3.3. Additionally, a convergence study is performed.

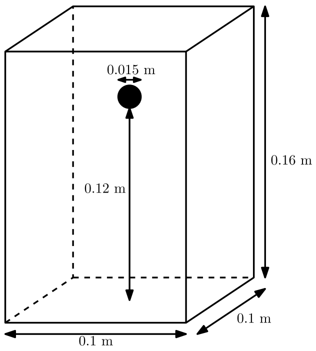

Figure 1. Setup of the simulation according to ten Cate at al. [45].

4.1.2. Results and Discussion—Comparison to Literature

For reasons of readability, further abbreviations are introduced. Here, GUO and SCF refer to the respective forcing schemes by Guo et al. [75] and Shan and Chen [74] (see Section 3.2). Additionally, MEA-L and MEA-W refer to the momentum exchange algorithms by Ladd [39,40] and Wen et al. [42]. As different resolutions are studied a factor N is introduced to scale the effective grid spacing to $\delta x/N$.

From the simulations, the root mean squared error (RMSE) relative to the maximum absolute velocity of the respective case and the deviation of the maximum settling velocity compared to the one calculated according to the drag correlation by Abraham [60] are given in Table 2 for $N = 1$ and in Table 3 for $N = 8$. To further compare the whole curves, similarity measures were calculated [80], i.e., a partial curve mapping (PCM) [81] and the area between curves according to Jekel et al. [80]. The latter was less influenced by noisy data or outliers. As reference solution in this calculation, the experimental data of ten Cate et al. [45] were used and approximated by a polynomial fit of 18-th order. The RMSE of the fit for case 1 to 4 was given by 0.01447, 0.01481, 0.01838, and 0.02093. The values were rounded to six decimal places to demonstrate that some differences (e.g., between MEA-L and MEA-W) were on a negligible level for this case.

For better comprehensibility, the values in Tables 2 and 3 are averaged over the four cases for each setup in Table 4. The mean error regarding the maximum settling velocity in the reference was given by 6.35%. For the same grid spacing, the combinations EDM and MEA-W, EDM and MEA-L and GUO and MEA-W performed best (about 5.5%) with the first one yielding slightly better results. The same holds for the area between the curves, PCM and RMSE. While for smaller grid spacing the results were predominantly better, the same conclusions could be drawn as for $N = 1$, with the combination of EDM and MEA-W performing better or equal to all other combinations. Only for PCM, the combination of EDM and MLA yielded the best results while it performed worst in all other cases. Looking only at the results for the cases with lower Reynolds numbers however, this setup yielded the highest accuracy in all values except in the prediction of the maximum settling velocity. This might also be due to the fact that the latter was not calculated from experimental values, but from a given correlation.

A possible reason for this behaviour is that forcing terms for points in the interior of the particle domain did not cancel out in contrast to MEA approaches. While for static objects no difference in the results was observed for the MLA, the error increased with the Reynolds number. This can also be seen in Figure 2. Since the objects did not have strict no-slip boundaries, simply omitting contributions to the force of points beyond the physical boundary was no solution. The transition region between the cells relevant and the ones not relevant for the hydrodynamic force within the particle domain seemed to be dependent on both the discretization parameters and the velocity. Further research in the future is required at this point. In empirical studies the influence of different parameters like grid spacing and the velocity or Reynolds number need to be quantified to deduce further steps in improving the proposed MLA.

Some configurations are plotted in Figure 2 for $N = 8$, along with the experimental results by ten Cate et al. [45]. At this point, it can be concluded that all combinations tested in this study yielded reasonable results with the RMSE being the same order of magnitude as the RMSE for the utilized fit. While the application of EDM and MLA should be restricted to low Reynolds numbers only, where it performed best among the considered schemes. The combination of SCF and MEA-L, which was used in previous publications of HLBM [30,55] was among the worst, therefore the overall best performing configuration of EDM and MEA-W was chosen for the remaining calculations.

To further validate the implementation, a convergence study was performed. The experimental order of convergence (EOC) given by

$$EOC(N, \hat{N}) = \frac{\log(\mathrm{err}(\mathrm{N})) - \log(\mathrm{err}(\hat{\mathrm{N}}))}{\log(N) - \log(\hat{N})}\,, \tag{26}$$

was calculated for two different grid spacings $\delta x/N$ and $\delta x/\hat{N}$ with $N < \hat{N}$. The function $\mathrm{err} : [1, 2, 4, 8] \to \mathbb{R}$ gives the difference of a chosen error or similarity measure for a given N to the value in the same setup but with a grid spacing according to $N = 8$. This way, for each case and setup, two values, i.e., $EOC(1, 2)$ and $EOC(2, 4)$ were obtained. Averaging all values for the experimental order of convergence of a given combination of schemes for a measure leads to Table 5.

Table 2. Different error measures [80] for the four cases described by ten Cate et al. [45] for various combinations of momentum exchange and forcing schemes. The error in terminal velocity is given relative to the analytical values according to Abraham [60]. The results in the table refer to $N = 1$.

Case	Forcing	Momentum Exchange	RMSE	PCM	Area between Curves	Error in % Maximum Velocity
1	EDM	MEA-W	0.04191	3.63347	0.00386	4.69880
1	EDM	MLA	0.02722	2.17069	0.00292	4.91581
1	EDM	MEA-L	0.04187	3.61223	0.00386	4.71524
1	GUO	MEA-W	0.04190	3.63317	0.00386	4.69881
1	SCF	MEA-W	0.02616	3.86421	0.00323	6.73646
1	SCF	MEA-L	0.02618	3.87909	0.00323	6.73834
2	EDM	MEA-W	0.07019	1.96464	0.00703	6.08454
2	EDM	MLA	0.11885	4.41254	0.01115	6.71691
2	EDM	MEA-L	0.07028	1.96609	0.00704	6.08627
2	GUO	MEA-W	0.07019	1.96473	0.00703	6.08455
2	SCF	MEA-W	0.10945	3.48661	0.01082	7.83986
2	SCF	MEA-L	0.10952	3.49102	0.01082	7.85094
3	EDM	MEA-W	0.04287	1.50668	0.00409	6.23779
3	EDM	MLA	0.08819	2.58684	0.01000	8.01712
3	EDM	MEA-L	0.04289	1.50718	0.00409	6.23545
3	GUO	MEA-W	0.04287	1.50659	0.00409	6.23780
3	SCF	MEA-W	0.05442	2.00959	0.00585	7.27864
3	SCF	MEA-L	0.05443	2.00904	0.00585	7.28794
4	EDM	MEA-W	0.02578	0.50550	0.00271	4.88694
4	EDM	MLA	0.10395	2.71061	0.01302	9.27789
4	EDM	MEA-L	0.02580	0.50635	0.00271	4.89684
4	GUO	MEA-W	0.02578	0.50551	0.00271	4.88695
4	SCF	MEA-W	0.03347	0.86398	0.00401	5.84097
4	SCF	MEA-L	0.03349	0.86637	0.00402	5.84066

Table 3. Different error measures [80] for the four cases described by ten Cate et al. [45] for various combinations of momentum exchange and forcing schemes. The error in terminal velocity is given relative to the analytical values according to Abraham [60]. The results in the table refer to $N = 8$.

Case	Forcing	Momentum Exchange	RMSE	PCM	Area between Curves	Error in % Maximum Velocity
1	EDM	MEA-W	0.03241	4.35586	0.00422	8.24923
1	EDM	MLA	0.03399	2.84034	0.00448	8.27399
1	EDM	MEA-L	0.03241	4.35589	0.00422	8.24930
1	GUO	MEA-W	0.03241	4.35586	0.00422	8.24923
1	SCF	MEA-W	0.03442	4.41524	0.00457	8.49026
1	SCF	MEA-L	0.03442	4.41527	0.00457	8.49039
2	EDM	MEA-W	0.03224	1.11747	0.00347	4.32345
2	EDM	MLA	0.05467	1.03172	0.00550	4.44263
2	EDM	MEA-L	0.03224	1.11747	0.00347	4.32358
2	GUO	MEA-W	0.03224	1.11748	0.00347	4.32345
2	SCF	MEA-W	0.03326	1.10431	0.00359	4.59350
2	SCF	MEA-L	0.03326	1.10431	0.00359	4.59360
3	EDM	MEA-W	0.02349	0.64709	0.00162	4.43872
3	EDM	MLA	0.06483	1.49952	0.00563	4.83740
3	EDM	MEA-L	0.02349	0.64703	0.00162	4.43877
3	GUO	MEA-W	0.02349	0.64709	0.00162	4.43872
3	SCF	MEA-W	0.02079	0.76920	0.00152	4.67580
3	SCF	MEA-L	0.02079	0.76898	0.00152	4.67593
4	EDM	MEA-W	0.08260	1.06138	0.00223	4.96350
4	EDM	MLA	0.08638	1.67762	0.00927	6.09874
4	EDM	MEA-L	0.08259	1.06147	0.00223	4.96360
4	GUO	MEA-W	0.08260	1.06139	0.00223	4.96350
4	SCF	MEA-W	0.08877	1.03403	0.00251	5.16140
4	SCF	MEA-L	0.08875	1.03418	0.00251	5.16147

Table 4. Mean values of the results presented in Tables 2 and 3. The averages are taken over the four application cases.

N	Forcing	Momentum Exchange	RMSE (Mean)	PCM (Mean)	Area between Curves (Mean)	Error in % Maximum Velocity (Mean)
1	EDM	MEA-W	0.04519	1.90257	0.00442	5.47702
1	EDM	MLA	0.08455	2.97017	0.00927	7.23193
1	EDM	MEA-L	0.04521	1.89796	0.00443	5.48345
1	GUO	MEA-W	0.04519	1.90250	0.00442	5.47703
1	SCF	MEA-W	0.05588	2.55610	0.00598	6.92398
1	SCF	MEA-L	0.05590	2.56138	0.00598	6.92947
8	EDM	MEA-W	0.04268	1.79545	0.00288	5.49373
8	EDM	MLA	0.05997	1.76230	0.00622	5.91319
8	EDM	MEA-L	0.04268	1.79546	0.00288	5.49381
8	GUO	MEA-W	0.04268	1.79545	0.00288	5.49373
8	SCF	MEA-W	0.04431	1.83069	0.00305	5.73024
8	SCF	MEA-L	0.04430	1.83069	0.00305	5.73035

Table 5. Mean experimental order of convergence (EOC) for different error and similarity measures regarding $N = 8$. Results are averaged over all values for a given combination of forcing and momentum exchange scheme as well as all cases.

Forcing	**Momentum Exchange**	**EOC (RMSE)**	**EOC (PCM)**	**EOC (Area between Curves)**	**EOC (Error in % Maximum Velocity)**
EDM	MEA-W	1.79	1.81	2.06	1.39
EDM	MLA	1.37	2.00	1.49	1.66
EDM	MEA-L	1.79	1.81	2.05	1.36
GUO	MEA-W	1.79	1.81	2.06	1.39
SCF	MEA-W	1.57	1.03	1.72	1.55
SCF	MEA-L	1.57	1.03	1.72	1.55

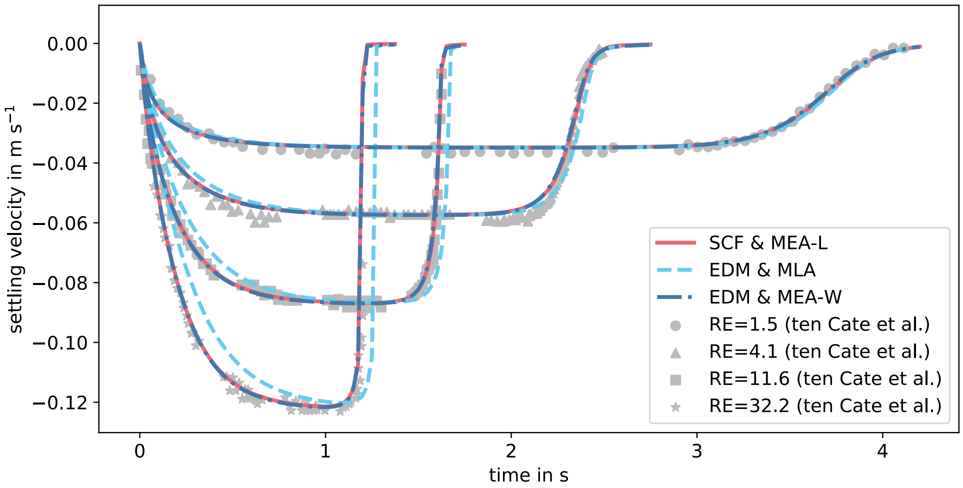

Figure 2. Settling velocity in the four defined cases for different combinations of forcing and momentum exchange schemes along with the experimental results by ten Cate et al. [45].

The mean EOC values were between 1 and 2 for all schemes, thereby superlinear convergence can be assumed. Similar to the results in previous tables, combinations of EDM or GUO with MEA-W or MEA-L performed best while combinations with SCF were falling behind. The MLA yielded the highest convergence rate for PCM and the maximum settling velocity while it also yielded the worst for the other measures. The results for $\mathrm{Re} = 11.6$ with EDM and MEA-W are depicted for different grid spacings according to the parameter N in Figure 3.

The combination of EDM and MEA-W was chosen for all further computations, as it proved best in overall performance. The applicability of the MLA, however, seemed to be limited to some low Reynolds number cases.

Thereby the HLBM was updated, while in previous publications a combination of SCF and MEA-L was used for the calculations the new approach consisting of EDM and MEA-W yielded better results and a higher accuracy.

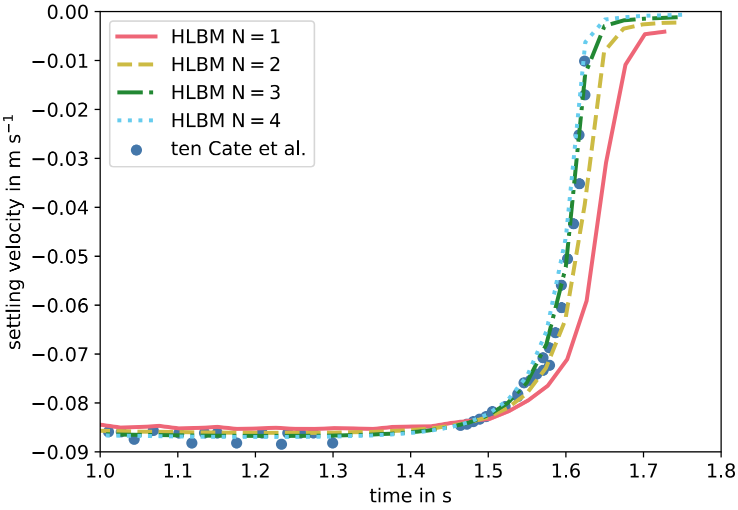

Figure 3. Extract of the results for the case of Re = 11.6 with exact difference method (EDM) and momentum exchange algorithm (MEA)-W for different grid spacings along with the experimental data by ten Cate et al. [45].

4.1.3. Simulation Setup—Comparison to Correlations

To check if the drag correlations presented in Section 2.1 can be reproduced by the HLBM, again the setup of a single settling sphere was chosen. It was placed with the center 0.021 m above the bottom of a domain of size 0.0055 m × 0.0055 m × 0.022 m. The top and bottom of the domain were equipped with no-slip boundaries again, but in contrast to the previous case the sides were chosen to be periodic. The densities of the fluid and the sphere were $\rho_\mathrm{f} = 1000\,\mathrm{kg\,m^{-3}}$ and $\rho_\mathrm{p} = 2500\,\mathrm{kg\,m^{-3}}$, respectively. The dynamic viscosity was varied to change the Reynolds number, the sphere had a diameter of $d_\mathrm{p} = 0.0005\,\mathrm{m}$ and the gravitational acceleration was given by $g = 9.81\,\mathrm{m\,s^{-2}}$. In this subsection Re is defined via the given ρ_f and d_p, while u_∞ is defined by the used drag correlation and μ_f as shown in Table 6.

The grid spacing was given by $\delta x = 3.125 \times 10^{-5}\,\mathrm{m}$, this means the particle diameter was equivalent to 8 grid cells. As stated by ten Cate et al. [45], DNS methods experience a non-physical dependency of the drag force on the kinematic viscosity. This has also been investigated by Rohde et al. [82] for a boundary taking the actual, non-voxelized, surface. This effect is described to be less significant for Re $\gg$ 1 and a scaling procedure is proposed to estimate the hydrodynamic radius for the simulation. In this study, the radius and grid spacing were kept fixed, only the temporal discretization was adapted. LBM simulations required the maximum occurring velocity in lattice units to be much smaller than c_s to ensure incompressible flow conditions and stability. Estimating the maximum velocity u_∞ by the drag correlation in Equation (8) and choosing the discretization such that this velocity was equivalent to 0.01 in lattice units finally led to

$$\delta t = \frac{0.01}{u_\infty}\delta x\,. \tag{27}$$

Table 6. Deviation of of the drag coefficients calculated by homogenized lattice Boltzmann method (HLBM) simulations to different drag correlations.

μ_f	C_D	Stokes		Abraham		Schiller and Naumann	
in kg $\mathrm{m}^{-1}\mathrm{s}^{-1}$	(Simulated)	Re	Error in %	Re	Error in %	Re	Error in %
2.0×10^{-2}	86.6942	0.26	−7.72	0.23	−24.93	0.24	−17.33
1.5×10^{-2}	56.7155	0.45	7.33	0.40	−17.98	0.42	−8.42
1.0×10^{-2}	29.6648	1.02	26.31	0.84	−14.14	0.90	−2.68
5.0×10^{-3}	10.5937	4.09	80.42	2.90	−9.38	3.08	2.74
2.5×10^{-3}	4.5797	16.35	212.00	9.18	−1.61	9.57	6.94
1.25×10^{-3}	2.2965	65.40	525.82	26.57	3.29	26.83	5.34
6.25×10^{-4}	1.2539	261.60	1266.86	70.48	−0.79	69.50	−3.52
3.125×10^{-4}	0.7339	1046.40	3100.03	173.68	−11.84	170.80	−14.74
1.5625×10^{-4}	0.5213	4185.60	8992.70	404.05	−15.27	406.40	−14.28
7.8125×10^{-5}	0.4543	16,742.40	31,595.60	900.47	−8.31	948.67	1.76

4.1.4. Results and Discussion—Comparison to Correlations

In all simulations, the sphere reached a stable settling velocity, which was used to calculate the drag coefficient using Equation (4) with the fluid velocity assumed to be zero. The results are presented in Table 6 along with Reynolds numbers according to the terminal velocity of the drag correlations by Stokes, Abraham and Schiller and Naumann, discussed in Section 2.1. Additionally, the deviation in % from the analytical value of the respective correlation is given.

Here, the closest correlation was the one by Schiller and Naumann with an average error of 7.78% calculated from the absolute values of the ones given in Table 6. The results yielded a slightly worse error of 10.75% comparing to Abraham. Additionally, as expected for $\mathrm{Re} < 1$ the results were closer to the prediction using Stokes drag.

On the other hand, deviations in this region might also be due to the stronger viscosity dependency for low Re discussed in Section 4.1.3. Another reason for deviations might be the lattice relaxation time entering the region of under-relaxation [23] for $\mathrm{Re} < 1$ and approaching the value of 0.5 for the high Re considered here. For a stable simulation $\tau > 0.5$ is required [23]. This, however, is related to the chosen discretization. For reasons of comparability between the data points δx was kept constant, however, adapting it to achieve a reasonable τ can presumably improve the results. Increasing the grid resolution and also the gravitational acceleration, Reynolds numbers up to 1591 were reached in tests. At this point, a further increase was limited by available computational resources, as not only did δx need to be lowered, but also the domain size had to be increased to allow the particle to reach its terminal velocity. Overall, the results are in good agreement with the discussed correlations, this can be seen in Figure 4, where the Reynolds number was defined via the maximum settling velocity in the simulation.

For further analysis, δt was varied by choosing a different lattice velocity to be equivalent to the one calculated by Schiller and Naumann in Equation (27). These results can be used in further simulations for an a-priori estimate of the error regarding the temporal resolution, for cases that allow an estimation of the maximum occurring velocity.

The results in Table 7 show that u^L should be at least smaller or equal to 0.04 as this gave a 7.5% deviation from the finest tested temporal resolution. A value of $u^\mathrm{L} = 0.01$ would be most desirable since from this point on the deviation was smaller than most errors measured in this work. Then again, this meant the computational cost quadruple compared to the just found minimum requirement regarding the lattice velocity, since u^L was directly proportional to δt. Using $u^\mathrm{L} = 0.0025$ as a reference was justified as halving $u^\mathrm{L} = 0.005$ only led to a change below 1% regarding the maximum settling velocity. Overall, almost perfect linear convergence was observed considering the average $EOC = 0.97$ regarding the maximum settling velocity. The results are also depicted in Figure 5, where a convergence towards a value in between the predictions by Abraham [60] and Schiller and Naumann [61] is shown.

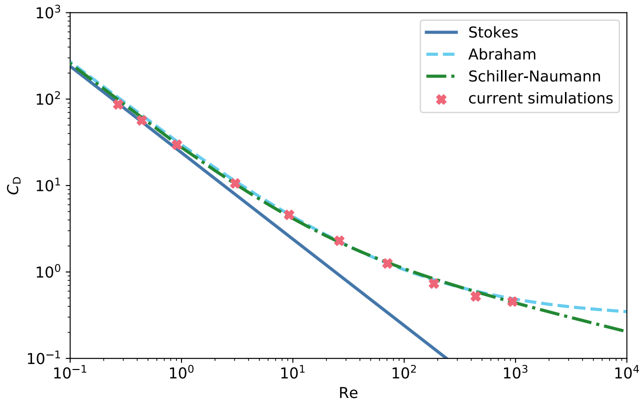

Figure 4. Drag coefficient of correlations discussed in Section 2.1 along with the simulation results plotted against the Reynolds number, computed using the maximum settling velocity measured in the simulation.

Table 7. Maximum settling velocity for $\mu_\mathrm{f} = 0.005\,\mathrm{kg\,m^{-1}\,s^{-1}}$ for a chosen lattice velocity u^L (see Equation (27)). Additionally, given is the deviation to the velocity obtained with $u^\mathrm{L} = 0.0025$ and the change of maximum velocity to the value obtained with the next smaller u^L.

u^L	**0.0025**	**0.005**	**0.01**	**0.02**	**0.04**	**0.08**	**0.16**
u_∞ in $\mathrm{m\,s^{-1}}$	0.02975	0.03002	0.03042	0.03102	0.031981	0.03375	0.03768
Deviation in %	0	0.89	2.24	4.25	7.50	13.45	26.64
Change in %	-	0.89	1.33	1.97	3.11	5.54	11.6

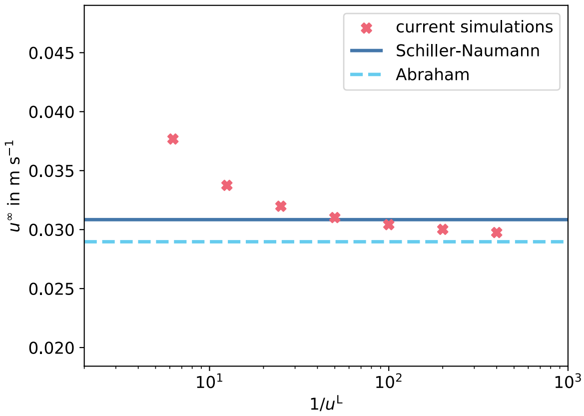

Figure 5. Maximum settling velocity for $\mu_\mathrm{f} = 0.005\,\mathrm{kg\,m^{-1}\,s^{-1}}$ over the chosen lattice velocity u^L (see Equation (27)).

4.1.5. Further Discussion—Onset of Unsteadiness

Spheres settling under the influence of gravity experience a range of regimes of motion, depending on the density ratio between the spheres and the fluid as well as the Reynolds or Galileo number. This has been shown and experimentally investigated by Horowitz and Williamson [83]. Later, Rahmani and Wachs [84] investigated the same behaviour via simulations. Following their definition of the Galileo number as

$$\mathrm{Ga} = \frac{\sqrt{|1-\rho_\mathrm{P}/\rho_\mathrm{f}|gd_\mathrm{P}^3}}{\nu}, \tag{28}$$

the simulations presented in Section 4.1.4 cover a range of $\mathrm{Ga} = 2.14$ up to $\mathrm{Ga} = 548.97$. For this discussion, the size of the domain has been extended to 0.0375 m in z-direction. In this context, it is notable that the unsteadiness observed in experiments can only be reproduced in simulations if the setup is not perfectly symmetrical, i.e., if the sphere does not perfectly align with the grid for a domain free of disturbance. Therefore, the sphere is moved $0.3\delta x$ from the center of the domain in x- and y-direction respectively. It can be observed that for $\mathrm{Ga} = 137.24$, a sphere follows a slightly oblique path, while all spheres with lower Ga settle vertically straight, as depicted in Figure 6. This fits the results by Jenny et al. [85], who found the onset of oblique motion at about $\mathrm{Ga} = 150$, and Rahmani and Wachs [84].

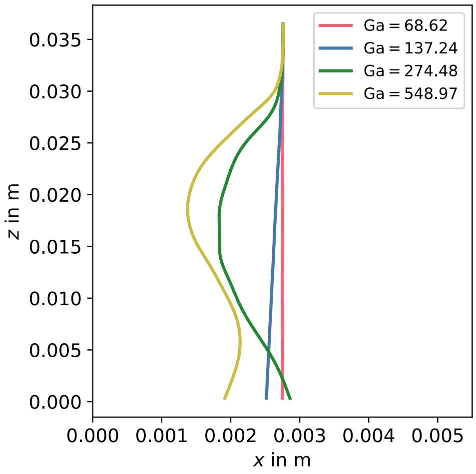

Figure 6. Path in the x-z-plane for spheres with different Ga.

For higher Galileo numbers, the motion seems to be characterized by an oblique oscillation. However, to ensure this classification, a closer evaluation with a longer settling path is required, especially since Rahmani and Wachs [84] as well as Jenny et al. [85] predicted a chaotic motion for this parameters. The vortex structure shown in Figure 7 also seems to be rather chaotic. A thorough investigation of the different settling regimes including the vortex shedding, which was found as depicted in Figure 7, however, exceeds the scope of the present work at this point.

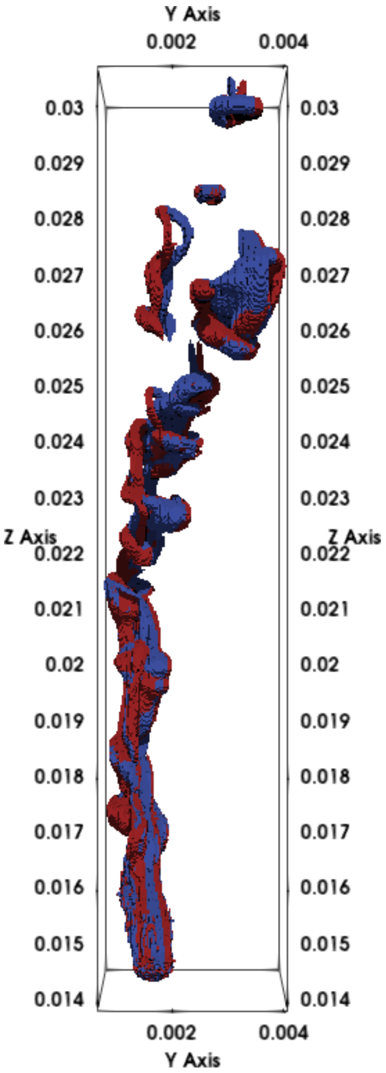

Figure 7. Contours of the stream-wise vorticity for a sphere with $\mathrm{Ga} = 548.97$ at $t = 0.19$ s.

4.2. Tubular Pinch Effect

In this section, 2D simulations regarding the tubular pinch effect are presented. It was first discovered [46] and then further investigated [47] by Segré and Silberberg. The effect describes the motion of neutrally buoyant particles in a tube flow towards an equilibrium position between the tube's center and its wall. As reference simulation, results by Li et al. [35] and Inamuro et al. [36] are considered.

4.2.1. Simulation Setup

For all considered cases, the base setup depicted in Figure 8 was the same, only the parameters change. The tube with diameter D and length L was equipped with pressure boundary conditions at front and back. A flow was induced by a pressure difference

Δp^{L}, considering the relation between pressure and density this was equivalent to setting $\rho^{\mathrm{L}} = 1 \pm p^{\mathrm{L}}/6$, for an initial density of $\rho^{\mathrm{L}} = 1$ across the domain. For the particle, a periodic boundary was chosen. As contact with the given boundary implementation distorted the particle movement, the particle was always kept one particle diameter d_{p} away. While pressure boundaries were applied to the fluid domain, the particle experienced the periodic boundary before the actual end of the domain and got cut off one particle diameter before the pressure outlet. The part of the particle having left the domain via this boundary entered the domain also one particle diameter from the pressure inlet. This is done similarly by Li et al. [35] while Inamuro et al. [36] present a boundary condition capable of handling particles passing through it. To account for this difference, the domain was enlarged by $2d_{\mathrm{p}}$ in flow direction so that the domain length stayed the same from perspective of the circle. The top and bottom of the domain had a no-slip condition for the fluid as well as the submersed object. The periodicity for the particles was required to reduce computational load since, as depicted in Figure 9, the domain would require between 15 and 60 times the size, depending on the case. It also allowed us to study the influence of the distance between spheres by varying the domain length as presented by Inamuro et al. [36]. The application of periodicity as described by Li et al. [35] was required as the improved periodic particle boundary presented in Inamuro et al. [36] was formulated for particles represented by a bounce-back boundary and could therefore not be applied straightforward for HLBM.

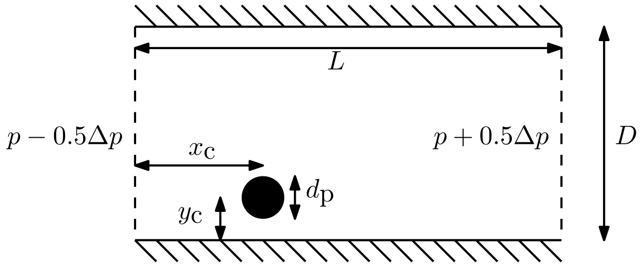

Figure 8. Computational domain for the investigation of the tubular pinch effect.

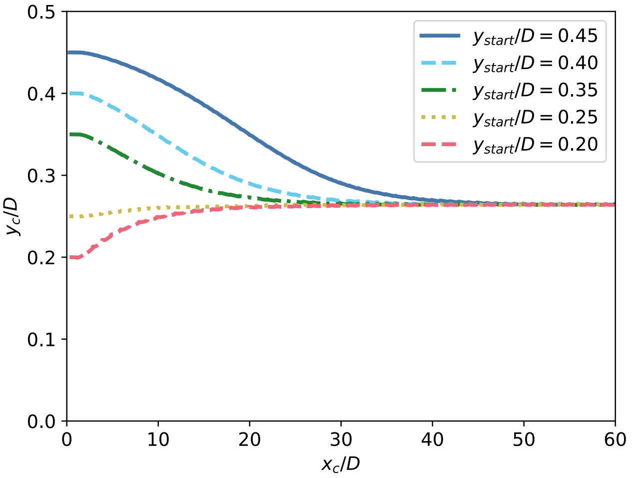

Figure 9. Results of various starting positions of the circle according to case 2 of Inamuro et al. [36].

The calculations in the reference literature were performed in lattice units, therefore the discretization parameters were chosen accordingly. Additionally, all values in this subsection and the one regarding the results of this case are therefore non-dimensionalized by those discretization parameters, just like shown in the references. As no value was affiliated with a unit, the superscript $^{\mathrm{L}}$, indicating lattice units, is also dropped in this section for reasons of readability. The viscosity is defined by Equation (14) for a given τ. Since, as also stated by Inamuro et al. [36], the error was proportional to the maximum occuring lattice velocity squared, it was monitored for the presented cases.

The trajectory of the submersed circle is described by the coordinates of its center $(x_{\mathrm{c}}, y_{\mathrm{c}})$. All simulations are run for 6×10^5 time steps to ensure convergence according the the results shown in Figure 9.

4.2.2. Results and Discussion

The results of the simulations are printed in Table 8 for different cases with the respective parameters. For each case, the simulations were run for different starting points $y_{\mathrm{start}}/D \in \{0.2, 0.250.35, 0.4, 0.45\}$ of the circle and the simulations showed a convergence towards a single position for each case as depicted in Figure 9. The resulting y_{c}/D was averaged over the last $20,000$ time steps of each simulation and over the results of all starting points.

Table 8. Parameters of the simulations investigating the tubular pinch effect along with the results for multiple cases according to Inamuro et al. [36] and the one described by Li et al. [35].

Case	τ	Δp	D	L	d_{p}/D	y_{c}/D	Error in %
Inamuro et al. case 2	1.4	8.167×10^{-4}	200	200	0.25	0.2642	−3.33%
Inamuro et al. case 6	0.757	2.337×10^{-4}	200	200	0.25	0.2548	−5.83%
Inamuro et al. case 11	1.4	1.633×10^{-3}	200	400	0.25	0.2726	−4.35%
Inamuro et al. case 14	0.95	3.207×10^{-3}	100	400	0.5	0.3590	−5.48%
Li et al.	0.75	2.670×10^{-4}	100	400	0.25	0.2756	−4.10%

Inamuro et al. [36] investigated the influence of various parameter like Re, d_{p}/D and the distance between two circles, which is reflected in the area covered by particles. They found the same relations as Karnis et al. in their experiments [49], namely that the equilibrium position of the circle gets closer to the wall for higher Re, but closer to the center for more distance between two objects and also gets closer to the center for increasing d_{p}/D. Inamuro et al. [36] defined the Reynolds number for this case as the ratio of time- and space-averaged velocity times the distance between the walls to the kinematic viscosity. The values were chosen to approximately achieve a maximum lattice velocity of $u^{\mathrm{L}} = 0.04$, this was also found in the current simulations with $u^{\mathrm{L}} \approx 0.041$ across all runs. With an average absolute error of 4.75% across the cases the results showed good agreement to the ones obtained by Inamuro et al. [36]. The most probable source of the deviation was the difference in boundary conditions at the in- and outflow.

With an error of −4.1%, the last case is also in good agreement with Li et al. [35], however, they also stated an error of 5.16% comparing with case 2 of Inamuro et al. [36]. As the parameter did not fully match any of those reference cases, a comparison between the two reference publications is complicated, especially since for the last case in Table 8, a maximum lattice velocity of $u^{\mathrm{L}} \approx 0.096$ was measured.

Additionally, the applicability of the MEA-L was tested for HLBM in this case. As already stated by Li et al. [35] and Peng et al. [34], it was found that the MEA according to Ladd [39,40] is not able to reproduce the tubular pinch effect. In all cases, the circle reached its final position in the middle of the tube.

4.3. Hindered Settling

In this section, the phenomenon of hindered settling is simulated with HLBM. Although there was no explicit collision model implemented, the particles affected each other by momentum transfer via the fluid. This, of course, was only sufficient if the spatial and temporal resolution was chosen fine enough that the transferred momentum prevented an overlapping of particles by several cells. This effect has been observed in previous publications regarding HLBM, e.g., by Krause et al. [55], but has up to now only been described qualitatively. Therefore, the study of hindered settling was used to investigate the occurring error regarding the velocity and solid volume fraction. This case aimed at testing the quality of results without collision model and if the effect could be reproduced at all. Therefore, the simulations were compared to various correlations presented in Section 2.2.

4.3.1. Simulation Setup

For this simulations, random distributions of spheres were created in the bottom half of a domain of size 0.00625 m × 0.00625 m × 0.025 m. The latter was equipped with no-slip boundary conditions at the bottom and top and was periodic for fluid and particles at the sides. The considered solid volume fractions in the bottom half are 5%, 10%, 15%, 20% and 25%, which required 373, 746, 1119, 1492 and 1865 spheres, respectively. The starting setup for the solid volume fraction $\phi = 0.2$ is depicted in Figure 10.

The spheres had a diameter of $d_\mathrm{p} = 0.0005\,\mathrm{m}$ and a density of $\rho_\mathrm{p} = 2500\,\mathrm{kg\,m^{-3}}$, while the physical parameters of the fluid were given by $\rho_\mathrm{f} = 1000\,\mathrm{kg\,m^{-3}}$ and $\nu = 10^{-6}\,\mathrm{m^2\,s^{-1}}$. To study the effect regarding different Reynolds numbers the gravitational acceleration was varied. For an a-priori estimation of Re, the terminal settling velocity u_∞ of a sphere according to Schiller and Naumann was used (see Section 2.1). Investigated are the cases of $\mathrm{Re} = 0.53$ ($g = 0.056\,\mathrm{m\,s^{-2}}$), $\mathrm{Re} = 5.29$ ($g = 0.748\,\mathrm{m\,s^{-2}}$) and $\mathrm{Re} = 49.64$ ($g = 15.22\,\mathrm{m\,s^{-2}}$).

For spatial discretization $\delta x = 2.27 \times 10^{-5}\,\mathrm{m}$ was chosen, thereby the diameter of a sphere was equivalent to 11 grid cells. Furthermore

$$\delta t = \frac{u_\infty}{u^\mathrm{L}} \delta x \tag{29}$$

was chosen to ensure a sufficient temporal resolution, with $u^\mathrm{L} = 0.005$, for all cases.

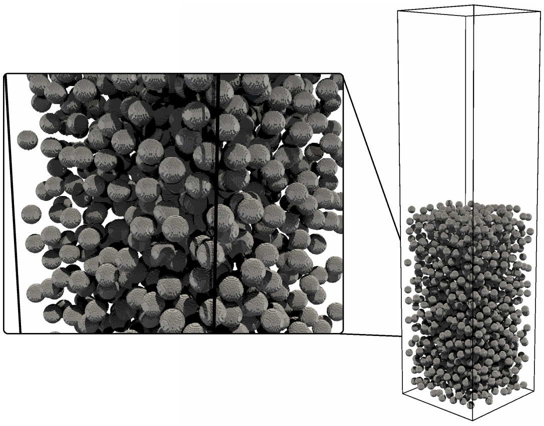

Figure 10. Random distribution of spheres in the computational domain for the hindered settling simulations with a solid volume fraction of 20%.

4.3.2. Results and Discussion

The hindered settling velocity of the particle collective was calculated by tracking the upper front to the clear water zone. Therefore, the settling velocity in direction of gravitation was averaged over the highest 5% of particles. The velocity field during the process is visualized in Figure 11.

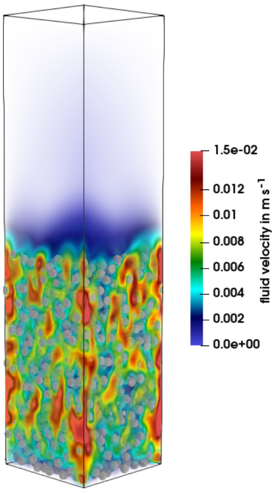

Figure 11. Velocity field around the sphere at $t = 0.23$ s for the case of $\mathrm{Re} = 5.29$ with a solid volume fraction of $\phi = 0.2$.

Since the number of simulated particles was low compared to an experimental setup, especially for low solid volume fractions, the calculated velocity is prone to oscillations. Therefore, it was further averaged over time, beginning with the first point, for which the absolute of the averaged velocity decreases. The endpoint was defined by the the time the first particle of the considered 5% reached the bottom 15% of the domain. The results of the averaging over the particles for $\mathrm{Re} = 49.64$ are depicted in Figure 12 along with the part used for temporal averaging, represented by the dashed line. In the following, this latter average will be denoted as simulated hindered settling velocity u_{sim}.

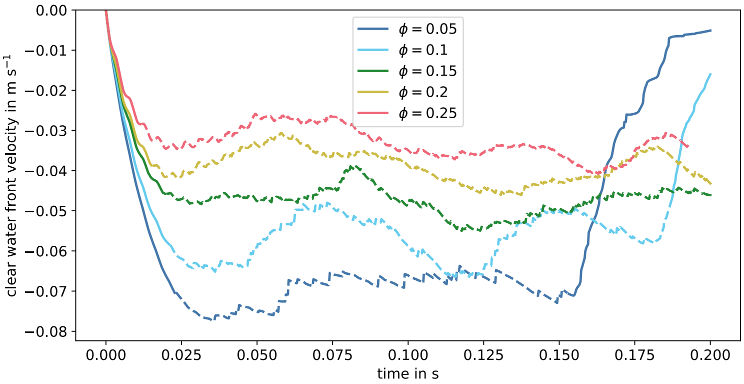

Figure 12. Averages over the settling velocity of the top 5% of particles for various ϕ and $\mathrm{Re} = 49.64$. The part used for temporal averaging is depicted as dashed line.

While a comparison to Steinour [63] resulted in throughout large errors, the deviations to different other correlations based on a single particle settling velocity according to Stokes [59] and to Schiller and Naumann [61] (here denoted by $u_{\text{S-N}}$) are given in Table 9. The best agreement was achieved with the results by Barnea and Mizrahi [70] in combination with the drag correlation by Schiller and Naumann with an average error of 8.07%. This was expectable since they already stated to use drag correlations beyond Stokes with their formula for higher Reynolds numbers. For the case of $\text{Re} = 0.53$ the used drag correlation had negligible influence as it yielded 4.77% deviation to the results with Stokes and 4.82% to the results in combination with $u_{\text{S-N}}$. Except for the correlation of Oliver built upon Schiller and Naumann yielding an average error of 7.05%, mainly the case of $\text{Re} = 49.46$ contributed to the error. This was to be expected since the discretization remained the same, but the spheres moved faster, increasing the possibility of large particle volumes overlapping and thereby making further momentum transfer via the fluid impossible. Additionally, high solid volume fractions seemed to have a negative effect on the results, this is shown in the last column of Table 9. Similar as for the high Reynolds number cases the error likely originated from the missing explicit contact model. For this comparably large number of spheres the occurrence of multiple contacts in a short time was possible, which pushed spheres to overlap each other. Despite these errors it was shown that hindered setting could be simulated with this approach however, with limitations to the solid volume fraction and velocity in combination with spatial and temporal discretization.

Table 9. Simulated hindered settling velocity regarding different Re and ϕ in comparison to different correlations.

Re	$\boldsymbol{\phi}$	u_{sim} **in** $\mathbf{m\,s^{-1}}$	**Error in %** (u_{RZ}, u_S)	**Error in %** (u_O, u_S)	**Error in %** (u_{BM}, u_S)	**Error in %** (u_{RZ}, $u_{S\text{-}N}$)	**Error in %** (u_O, $u_{S\text{-}N}$)	**Error in %** (u_{BM}, $u_{S\text{-}N}$)
0.53	0.05	−0.00071	−23.38	−10.17	−3.97	−15.90	−1.46	5.35
0.53	0.1	−0.00055	−24.69	−16.87	−7.46	−17.28	−8.81	1.51
0.53	0.15	−0.00045	−20.36	−19.03	−6.15	−12.46	−11.18	2.95
0.53	0.2	−0.00037	−15.63	−21.35	−5.47	−7.19	−13.73	3.70
0.53	0.25	−0.00031	−5.06	−18.20	0.80	4.52	−10.27	10.57
5.29	0.05	−0.00691	−46.58	−34.75	−30.24	−20.82	−4.00	2.63
5.29	0.1	−0.00551	−48.15	−37.75	−30.71	−22.56	−8.41	1.95
5.29	0.15	−0.00444	−48.68	−40.61	−31.16	−22.72	−12.61	1.29
5.29	0.2	−0.00367	−47.08	−41.07	−29.17	−19.62	−13.29	4.22
5.29	0.25	−0.00295	−46.26	−41.77	−28.24	−17.62	−14.32	5.58
49.46	0.05	−0.06962	−74.81	−67.71	−65.47	−18.17	3.13	10.26
49.46	0.1	−0.05656	−76.34	−68.63	−65.08	−21.76	0.19	11.53
49.46	0.15	−0.04757	−76.80	−68.71	−63.73	−21.83	−0.06	15.84
49.46	0.2	−0.03889	−77.69	−69.34	−63.14	−23.30	−2.07	17.71
49.46	0.25	−0.03300	−77.49	−68.01	−60.58	−20.96	2.17	25.90

In this setup the only boundary conditions applied were periodic boundaries and a bounce-back no-slip condition, which are both mass conserving. Since the collision step executed a standard BGK collision with forcing, which was also mass conserving [23], this was also true for the whole scheme. Additionally, during the simulations no notable accumulation or dilution of mass within the areas covered by particles were observed.

Independent of the used drag formula, the correlation according to Richardson and Zaki [54] yielded the worst results among the more precisely studied ones. The average error was 47.27% for the combination with u_{S}, intended by the originators. However, it dropped to 17.78% using $u_{\text{S-N}}$. The varying deviations to the drag correlations and obviously also between those correlations show the complexity of this application case.

Many reasons for errors and deviations can be found for this application case. Besides the possible influence of the starting distribution of the spheres, it can also be deduced from Figure 12 that a larger domain with more particles was required for more reliable results. Since the clear water front was not necessarily sharp and easy to track, a broader domain with more particles would smooth oscillations in this chaotic top region. Lowering the percentage of tracked particles e.g., to 2%, improved the results in comparison to the correlations, however, it also increased the oscillations. Using the top 5% was a compromise between reliable results and a precise tracking of the front by only considering the uppermost particles. A broader domain and clear water front would therefore be beneficial. The extend of the simulation, however, was limited for DNS approaches due to high computational costs.

Furthermore, the probable main point is that no explicit particle-particle collision model is applied and the momentum is solely exchanged via the fluid. This, of course, can be a main source of error, especially if the particles start to overlap by several cells. The latter is caused by a resolution chosen too coarse in comparison to the velocity of the spheres, so that the repelling effect of momentum exchange via the fluid is diminished. The good agreement, e.g., with the results by Barnea and Mizrahi and the obvious dependency of the simulated hindered settling velocity on ϕ however, show that it is possible to sufficiently depict the effect of hindered settling with the chosen setup. While capable of properly simulating the settling phase, the presented method is not suitable for the study of bed formation, as particles start to overlap once sedimented due to the absence of an explicit collision model. No influence of this nonphysical behaviour back on the settling process was observed.

4.4. Computational Efficiency

The performance of the algorithm has been recently investigated by Bretl et al. [86]. In their study, also based on OpenLB [56], they investigated the speedup S, which was defined as ratio of execution times using a single process T_1 to using n_p processes. Comparing to the theoretical value for a code which is 99.5% parallelizable given by

$$S = \frac{T_1}{T_1(0.005 + 0.995/n_\mathrm{p})}\,, \tag{30}$$

they found the results to be in good agreement. These, however, are results for the algorithm in the case of a single settling particle. Considering the case of hindered settling presented in Section 4.3, the dependency of the performance on the number of simulated objects was studied. As measure, the amount of million lattice site updates per second and core (MLUPps) was used. The cases for $\mathrm{Re} = 49.64$ were evaluated with the simulations run on a system equipped with Intel Xeon E5-2660 v3 processors.

Each simulation used a lattice with 83,717,424 cells and took 176,000 time-steps utilizing 80 cores. The results are depicted in Figure 13 together with a fit to a rational function f with

$$f(\phi) = \frac{a_1\phi + a_2}{a_3\phi + a_4}\,, \tag{31}$$

and fitting parameters $a_1, a_2, a_3, a_4 \in \mathbb{R}$. The function yielded 0.45 MLUPps for $\phi = 1$ and approached 0.35 MLUPps asymptotically as $\phi \to \infty$. Despite the questionable physicality regarding such a solid volume fraction for a set of spherical particles, those numbers were useful to estimate the lower bounds of single core performance for this method. The decrease in MLUPps was to be expected, since for each cell covered by a particle, additional computations regarding the hydrodynamic force were required (see e.g., Equation (23)). The influence of the number of particles on the performance, however, did not only depend on the solid volume fraction, but also on the distribution of the objects. Since for the parallelization MPI was used, each particle was treated by the process responsible for the domain it resided in. As in this simulation the particles accumulated at the bottom of the domain, a small number of processors had to take care of the calculation of hydrodynamic forces for all particles. A discussion on distribution strategies of computational load among the processors (load optimal strategy vs. communication optimal strategy) is given by Henn et al. [87].

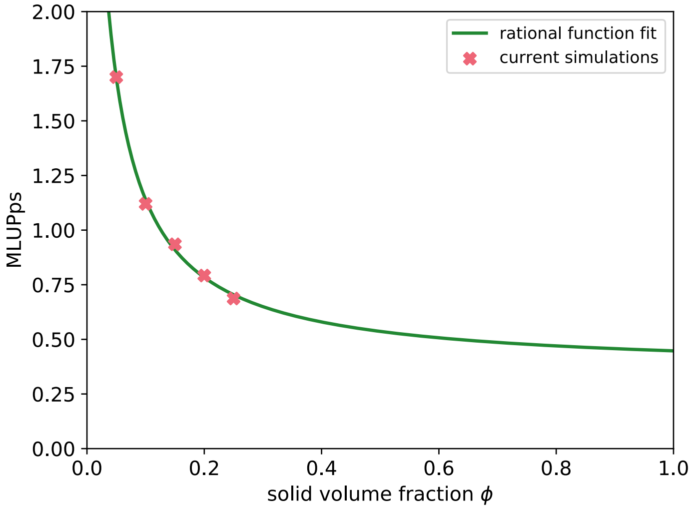

Figure 13. Performance data as million lattice updates per second and core, regarding the number of simulated particles.

5. Conclusions

The homogenized lattice Boltzmann method has been revisited and various forcing schemes and approaches to calculate exchanged momentum have been evaluated. Among the latter is a new proposed algorithm based on the momentum loss on a cell. However, it showed substandard accuracy except in the case of low Reynolds numbers. It is assumed that the hydrodynamic force is overestimated due to effects correlated to the interior fluid. The amount of force contributed by the latter is hardly distinguishable from the amount related to momentum exchanged with the bulk fluid. As most MEAs are constructed for a sharp solid boundary, further research at this point should be considered in the future. Since issues related to the interior fluid also exist for the immersed boundary method, it might be possible to adapt improvements.

Besides this a combination of Kupershtokh forcing and the MEA by Wen et al. [38] gave the overall best results. This finally leads to an updated version of HLBM, for which the results are in good agreement to literature (e.g., regarding the velocity profile of a settling sphere).

Furthermore, the reproducibility of drag correlations was tested yielding an error of 7.78% compared to the one by Schiller and Naumann in the range from $\mathrm{Re} = 0.24$ up to $\mathrm{Re} = 948.67$. Therefore, the applicability of HLBM for Reynolds numbers up to the Newton regime is shown.

In the next application case, the tubular pinch effect was investigated in 2 dimensions. Here, the error to reference simulations in the literature regarding the influence of the Reynolds number, the ratio of circle to tube diameter and the distance between the circles, never exceeded 5.83%.

The authors furthermore showed that the cases of hindered settling can be investigated with HLBM for a sufficient resolution, even without an explicit collision model. With a deviation of 8.07% to the correlation by Barnea and Mizrahi, the results are in excellent agreement, especially considering the error regarding a single settling particle. For more reliable computations regarding hindered settling, particularly for higher Reynolds numbers, and for bed formation processes an additional collision model is mandatory. The implementation of such is planned for future research, especially to evaluate the actual improvement in the quality of results as an effect of the addition of an explicit contact model.

Overall, the updated version of HLBM performed well across all application cases with good agreement to existing literature regarding experimental and theoretical results.

Author Contributions: Conceptualization, R.T.; methodology, R.T.; software, R.T., N.H., T.W., M.J.K.; validation, R.T.; formal analysis, R.T., T.W.; investigation, R.T.; resources, M.J.K., H.N.; data curation, R.T.; writing—original draft preparation, R.T.; writing—review and editing, R.T., N.H., G.T., M.J.K.; visualization, R.T.; supervision, M.J.K., H.N.; project administration, M.J.K., R.T.; funding acquisition, M.J.K., R.T. All authors have read and agreed to the published version of the manuscript.

Funding: This research was funded by the Deutsche Forschungsgemeinschaft (DFG) [grant KR 4259/8-2] within the priority program SPP2045 MehrDimPart "Highly specific and multidimensional fractionation of fine particle systems with technical relevance". The authors also acknowledge support by the Open Access Publishing Fund of the Karlsruhe Institute of Technology (KIT).

Institutional Review Board Statement: Not applicable.

Informed Consent Statement: Not applicable.

Data Availability Statement: Data is contained within the article.

Acknowledgments: The authors gratefully acknowledge the Steinbuch Centre for Computing at KIT for providing access to their high performance computer ForHLR II, where most computations were carried out as part of the CPE project. The authors also acknowledge DUG Technology for providing high-performance computing resources and expertise to support this research.

Conflicts of Interest: The authors declare no conflict of interest.

Abbreviations

The following abbreviations are used in this manuscript:

BGK	Bhatnagar–Gross–Krook
DNS	direct numerical simulation
EDM	exact difference method
EOC	experimental order of convergence
GUO	Guo forcing
HLBM	homogenised lattice Boltzmann method
LBM	lattice Boltzmann method
MEA	momentum exchange algorithm
MEA-L	momentum exchange algorithm according to Ladd [39,40]
MEA-W	momentum exchange algorithm according to Wen et al. [42]
MLA	momentum loss algorithm
MLUPps	million lattice site updates per second and per processor
PCM	partial curve mapping
RMSE	root mean squared error
SCF	Shan–Chen forcing scheme
Roman	
A	projected area of an object in flow direction
B	domain covered by a particle
C_D	drag coefficient
$\boldsymbol{c}_i$	i-th discrete lattice velocity
c_s	lattice speed of sound
$d, \hat{d}$	spatial dimension
d_B	mapping function of an object on the lattice
d_p	particle diameter
D	tube diameter
f_i	particle distribution function in the phase space according to the i-th lattice velocity
f_i^eq	Maxwell–Boltzmann distribution function according to the i-th lattice velocity

$\boldsymbol{F}$	force
$\boldsymbol{F}_{\mathrm{f}}$	force acting on the fluid
$\boldsymbol{F}_{\mathrm{p}}$	force acting on the particle
$\boldsymbol{F}^{\mathrm{B}}$	Buoyancy force
$\boldsymbol{F}^{\mathrm{D}}$	drag force
$\boldsymbol{F}^{\mathrm{G}}$	gravitational force
$\boldsymbol{F}^{\mathrm{H}}$	hydrodynamic force
g	gravitational acceleration
I	time interval
I_{h}	discrete time interval
J_{p}	moment of inertia
L	tube length
m_{p}	particle mass
$N, \hat{N}$	resolution parameter
n_{p}	number of processes
p	pressure
p^{L}	pressure in lattice units
q	dimension of the velocity space of a lattice
$\boldsymbol{r}$	distance to the center of mass of an object
Re	Reynolds number
S	speedup
S_i	source term in the LBM collision step according to the i-th lattice velocity
t	time
T_{p}	torque
$\boldsymbol{u}$	velocity
$\tilde{\boldsymbol{u}}$	redefined velocity in the presence of a particle
u_{BM}	hindered settling velocity according to Barnea and Mizrahi
$\boldsymbol{u}^{\mathrm{eq}}$	velocity used in the Maxwell–Boltzmann distribution
$\boldsymbol{u}_{\mathrm{f}}$	fluid velocity
u_{O}	hindered settling velocity according to Oliver
$\boldsymbol{u}_{\mathrm{p}}$	particle velocity
u_{RZ}	hindered settling velocity according to Richardson and Zaki
u_{S}	terminal settling velocity according to Stokes
$u_{\mathrm{S-N}}$	terminal settling velocity according to Schiller and Naumann
u_{sim}	simulated hindered settling velocity
u_{Steinour}	hindered settling velocity according to Steinour
u_{∞}	maximum settling velocity
u^{L}	velocity in lattice units
w_i	weighting function according to the i-th lattice velocity
$\boldsymbol{x}$	coordinates of a lattice point
x_{c}	x-coordinate of particle center
y_{c}	y-coordinate of particle center
y_{start}	initial y-coordinate of particle center
Greek	
δt	time step size in SI units
δx	grid spacing in SI units
δt^{L}	time step size in lattice units
δx^{L}	grid spacing in lattice units
$\Delta\boldsymbol{u}$	difference between fluid velocity and the velocity in presence of an object
μ_{f}	dynamic viscosity
ν	kinematic viscosity
ρ	density in lattice units
ρ_{f}	fluid density
ρ_{p}	particle density
τ	lattice relaxation time

ϕ solid volume fraction
ω angular velocity
Ω spatial domain
Ω_h discrete approximation of the spatial domain Ω

References

1. Viduka, S.M.; Feng, Y.Q.; Hapgood, K.; Schwarz, M. Discrete particle simulation of solid separation in a jigging device. *Int. J. Miner. Process.* **2013**, *123*, 108–119. [CrossRef]
2. Li, J.; Webb, C.; Pandiella, S.; Campbell, G. A Numerical Simulation of Separation of Crop Seeds by Screening—Effect of Particle Bed Depth. *Food Bioprod. Process.* **2002**, *80*, 109–117. [CrossRef]
3. Champion, J.A.; Katare, Y.K.; Mitragotri, S. Particle shape: A new design parameter for micro- and nanoscale drug delivery carriers. *J. Control. Release* **2007**, *121*, 3–9. [CrossRef] [PubMed]
4. Davies, R. A simple feature-space representation of particle shape. *Powder Technol.* **1975**, *12*, 111–124. [CrossRef]
5. Scotti, R.; Wahba, L.; Crippa, M.; D'Arienzo, M.; Donetti, R.; Santo, N.; Morazzoni, F. Rubber-silica nanocomposites obtained by in situ sol–gel method: particle shape influence on the filler-filler and filler-rubber interactions. *Soft Matter* **2012**, *8*, 2131. [CrossRef]
6. Trunk, R.; Henn, T.; Dörfler, W.; Nirschl, H.; Krause, M.J. Inertial dilute particulate fluid flow simulations with an Euler–Euler lattice Boltzmann method. *J. Comput. Sci.* **2016**, *17*, 438–445. [CrossRef]
7. Höcker, S.B.; Trunk, R.; Dörfler, W.; Krause, M.J. Towards the simulations of inertial dense particulate flows with a volume-averaged lattice Boltzmann method. *Comput. Fluids* **2018**, *166*, 152–162. [CrossRef]
8. Li, Z.; Yazdani, A.; Tartakovsky, A.; Karniadakis, G.E. Transport dissipative particle dynamics model for mesoscopic advection-diffusion-reaction problems. *J. Chem. Phys.* **2015**, *143*, 014101. [CrossRef]
9. Chu, K.; Wang, B.; Yu, A.; Vince, A. CFD-DEM modelling of multiphase flow in dense medium cyclones. *Powder Technol.* **2009**, *193*, 235–247. [CrossRef]
10. Maier, M.L.; Milles, S.; Schuhmann, S.; Guthausen, G.; Nirschl, H.; Krause, M.J. Fluid flow simulations verified by measurements to investigate adsorption processes in a static mixer. *Comput. Math. Appl.* **2018**, *76*, 2744–2757. [CrossRef]
11. Parteli, E.J.R.; Pöschel, T. Particle-based simulation of powder application in additive manufacturing. *Powder Technol.* **2016**, *288*, 96–102. [CrossRef]
12. Dapelo, D.; Trunk, R.; Krause, M.J.; Bridgeman, J. Towards Lattice-Boltzmann modelling of unconfined gas mixing in anaerobic digestion. *Comput. Fluids* **2019**, *180*, 11–21. [CrossRef]
13. Zhu, H.; Zhou, Z.; Yang, R.; Yu, A. Discrete particle simulation of particulate systems: A review of major applications and findings. *Chem. Eng. Sci.* **2008**, *63*, 5728–5770. [CrossRef]
14. Shardt, O.; Derksen, J. Direct simulations of dense suspensions of non-spherical particles. *Int. J. Multiph. Flow* **2012**, *47*, 25–36. [CrossRef]
15. Kravets, B.; Rosemann, T.; Reinecke, S.; Kruggel-Emden, H. A new drag force and heat transfer correlation derived from direct numerical LBM-simulations of flown through particle packings. *Powder Technol.* **2019**, *345*, 438–456. [CrossRef]
16. Dolanský, J.; Chára, Z.; Vlasák, P.; Kysela, B. Lattice Boltzmann method used to simulate particle motion in a conduit. *J. Hydrol. Hydromechanics* **2017**, *65*, 105–113. [CrossRef]
17. Wachs, A.; Girolami, L.; Vinay, G.; Ferrer, G. Grains3D, a flexible DEM approach for particles of arbitrary convex shape—Part I: Numerical model and validations. *Powder Technol.* **2012**, *224*, 374–389. [CrossRef]
18. Rakotonirina, A.D.; Wachs, A. Grains3D, a flexible DEM approach for particles of arbitrary convex shape—Part II: Parallel implementation and scalable performance. *Powder Technol.* **2018**, *324*, 18–35. [CrossRef]
19. Rakotonirina, A.D.; Delenne, J.Y.; Radjai, F.; Wachs, A. Grains3D, a flexible DEM approach for particles of arbitrary convex shape—Part III: extension to non-convex particles modelled as glued convex particles. *Comput. Part. Mech.* **2019**, *6*, 55–84. [CrossRef]
20. Nolan, G.; Kavanagh, P. Random packing of nonspherical particles. *Powder Technol.* **1995**, *84*, 199–205. [CrossRef]
21. Uhlmann, M. An immersed boundary method with direct forcing for the simulation of particulate flows. *J. Comput. Phys.* **2005**, *209*, 448–476. [CrossRef]
22. Tian, F.B.; Luo, H.; Zhu, L.; Liao, J.C.; Lu, X.Y. An efficient immersed boundary-lattice Boltzmann method for the hydrodynamic interaction of elastic filaments. *J. Comput. Phys.* **2011**, *230*, 7266–7283. [CrossRef]
23. Krüger, T.; Kusumaatmaja, H.; Kuzmin, A.; Shardt, O.; Silva, G.; Viggen, E.M. *The Lattice Boltzmann Method*; Graduate Texts in Physics; Springer International Publishing: Cham, Switzerland, 2017.
24. Feng, Z.G.; Michaelides, E.E. The immersed boundary-lattice Boltzmann method for solving fluid–particles interaction problems. *J. Comput. Phys.* **2004**, *195*, 602–628. [CrossRef]
25. Wu, J.; Wu, J.; Zhan, J.; Zhao, N.; Wang, T. A Robust Immersed Boundary-Lattice Boltzmann Method for Simulation of Fluid-Structure Interaction Problems. *Commun. Comput. Phys.* **2016**, *20*, 156–178. [CrossRef]

26. Wu, J.; Shu, C. An improved immersed boundary-lattice Boltzmann method for simulating three-dimensional incompressible flows. *J. Comput. Phys.* **2010**, *229*, 5022–5042. [CrossRef]
27. Owen, D.R.J.; Leonardi, C.R.; Feng, Y.T. An efficient framework for fluid-structure interaction using the lattice Boltzmann method and immersed moving boundaries. *Int. J. Numer. Methods Eng.* **2011**, *87*, 66–95. [CrossRef]
28. Beny, J.; Latt, J. Efficient LBM on GPUs for dense moving objects using immersed boundary condition. *arXiv* **2019**, arXiv:1904.02108.
29. Kang, S.K.; Hassan, Y.A. A comparative study of direct-forcing immersed boundary-lattice Boltzmann methods for stationary complex boundaries. *Int. J. Numer. Methods Fluids* **2011**, *66*, 1132–1158. [CrossRef]
30. Trunk, R.; Marquardt, J.; Thäter, G.; Nirschl, H.; Krause, M.J. Towards the simulation of arbitrarily shaped 3D particles using a homogenised lattice Boltzmann method. *Comput. Fluids* **2018**, *172*, 621–631. [CrossRef]
31. Kuznik, F.; Obrecht, C.; Rusaouen, G.; Roux, J.J. LBM based flow simulation using GPU computing processor. *Comput. Math. Appl.* **2010**, *59*, 2380–2392. [CrossRef]
32. Feichtinger, C.; Habich, J.; Köstler, H.; Rüde, U.; Aoki, T. Performance modeling and analysis of heterogeneous lattice Boltzmann simulations on CPU–GPU clusters. *Parallel Comput.* **2015**, *46*, 1–13. [CrossRef]
33. Noble, D.R.; Torczynski, J.R. A Lattice-Boltzmann Method for Partially Saturated Computational Cells. *Int. J. Mod. Phys. C* **1998**, *9*, 1189–1201. [CrossRef]
34. Peng, C.; Teng, Y.; Hwang, B.; Guo, Z.; Wang, L.P. Implementation issues and benchmarking of lattice Boltzmann method for moving rigid particle simulations in a viscous flow. *Comput. Math. Appl.* **2016**, *72*, 349–374. [CrossRef]
35. Li, H.; Lu, X.; Fang, H.; Qian, Y. Force evaluations in lattice Boltzmann simulations with moving boundaries in two dimensions. *Phys. Rev. E* **2004**, *70*. [CrossRef]
36. Inamuro, T.; Maeba, K.; Ogino, F. Flow between parallel walls containing the lines of neutrally buoyant circular cylinders. *Int. J. Multiph. Flow* **2000**, *26*, 1981–2004. [CrossRef]
37. Mei, R.; Yu, D.; Shyy, W.; Luo, L.S. Force evaluation in the lattice Boltzmann method involving curved geometry. *Phys. Rev. E* **2002**, *65*. [CrossRef]
38. Wen, B.; Li, H.; Zhang, C.; Fang, H. Lattice-type-dependent momentum-exchange method for moving boundaries. *Phys. Rev. E* **2012**, *85*. [CrossRef]
39. Ladd, A.J.C. Numerical simulations of particulate suspensions via a discretized Boltzmann equation. Part 1. Theoretical foundation. *J. Fluid Mech.* **1994**, *271*, 285–309. [CrossRef]
40. Ladd, A.J.C. Numerical simulations of particulate suspensions via a discretized Boltzmann equation. Part 2. Numerical results. *J. Fluid Mech.* **1994**, *271*, 311–339. [CrossRef]
41. Clausen, J.R.; Aidun, C.K. Galilean invariance in the lattice-Boltzmann method and its effect on the calculation of rheological properties in suspensions. *Int. J. Multiph. Flow* **2009**, *35*, 307–311. [CrossRef]
42. Wen, B.; Zhang, C.; Tu, Y.; Wang, C.; Fang, H. Galilean invariant fluid-solid interfacial dynamics in lattice Boltzmann simulations. *J. Comput. Phys.* **2014**, *266*, 161–170. [CrossRef]
43. Chen, Y.; Cai, Q.; Xia, Z.; Wang, M.; Chen, S. Momentum-exchange method in lattice Boltzmann simulations of particle-fluid interactions. *Phys. Rev. E* **2013**, *88*. [CrossRef] [PubMed]
44. Lorenz, E.; Caiazzo, A.; Hoekstra, A.G. Corrected momentum exchange method for lattice Boltzmann simulations of suspension flow. *Phys. Rev. E* **2009**, *79*. [CrossRef] [PubMed]
45. Ten Cate, A.; Nieuwstad, C.H.; Derksen, J.J.; Van den Akker, H.E.A. Particle imaging velocimetry experiments and lattice-Boltzmann simulations on a single sphere settling under gravity. *Phys. Fluids* **2002**, *14*, 4012–4025. [CrossRef]
46. Segré, G.; Silberberg, A. Radial Particle Displacements in Poiseuille Flow of Suspensions. *Nature* **1961**, *189*, 209–210. [CrossRef]
47. Segré, G.; Silberberg, A. Behaviour of macroscopic rigid spheres in Poiseuille flow Part 2. Experimental results and interpretation. *J. Fluid Mech.* **1962**, *14*, 136–157. [CrossRef]
48. Tachibana, M. On the behaviour of a sphere in the laminar tube flows. *Rheol. Acta* **1973**, *12*, 58–69. [CrossRef]
49. Karnis, A.; Goldsmith, H.L.; Mason, S.G. The flow of suspensions through tubes: V. Inertial effects. *Can. J. Chem. Eng.* **1966**, *44*, 181–193. [CrossRef]
50. Baldock, T.; Tomkins, M.; Nielsen, P.; Hughes, M. Settling velocity of sediments at high concentrations. *Coast. Eng.* **2004**, *51*, 91–100. [CrossRef]
51. Derksen, J.J. Eulerian-Lagrangian simulations of settling and agitated dense solid-liquid suspensions-achieving grid convergence. *AIChE J.* **2018**, *64*, 1147–1158. [CrossRef]
52. Deshpande, R.; Antonyuk, S.; Iliev, O. DEM-CFD study of the filter cake formation process due to non-spherical particles. *Particuology* **2020**. [CrossRef]
53. Zaidi, A.A.; Tsuji, T.; Tanaka, T. Hindered Settling Velocity & Structure Formation during Particle Settling by Direct Numerical Simulation. *Procedia Eng.* **2015**, *102*, 1656–1666. [CrossRef]
54. Richardson, J.; Zaki, W. The sedimentation of a suspension of uniform spheres under conditions of viscous flow. *Chem. Eng. Sci.* **1954**, *3*, 65–73. [CrossRef]
55. Krause, M.J.; Klemens, F.; Henn, T.; Trunk, R.; Nirschl, H. Particle flow simulations with homogenised lattice Boltzmann methods. *Particuology* **2017**, *34*, 1–13. [CrossRef]

56. Krause, M.J.; Kummerländer, A.; Avis, S.J.; Kusumaatmaja, H.; Dapelo, D.; Klemens, F.; Gaedtke, M.; Hafen, N.; Mink, A.; Trunk, R.; et al. OpenLB—Open source lattice Boltzmann code. *Comput. Math. Appl.* **2020**. [CrossRef]
57. Hölzer, A.; Sommerfeld, M. New simple correlation formula for the drag coefficient of non-spherical particles. *Powder Technol.* **2008**, *184*, 361–365. [CrossRef]
58. Bagheri, G.; Bonadonna, C. On the drag of freely falling non-spherical particles. *Powder Technol.* **2016**, *301*, 526–544. [CrossRef]
59. Stokes, G.G. On the Effect of Internal Friction of Fluids on the Motion of Pendulums. *Trans. Camb. Philos. Soc.* **1851**, *9*, 8–106. [CrossRef]
60. Abraham, F.F. Functional Dependence of Drag Coefficient of a Sphere on Reynolds Number. *Phys. Fluids* **1970**, *13*, 2194. [CrossRef]
61. Schiller, L.; Naumann, A. Über die grundlegenden Berechnungen bei der Schwerkraftaufbereitung. *Z. Des Vereines Dtsch. Ingenieure* **1933**, *77*, 318–320.
62. Dey, S.; Ali, S.Z.; Padhi, E. Terminal fall velocity: the legacy of Stokes from the perspective of fluvial hydraulics. *Proc. R. Soc. Math. Phys. Eng. Sci.* **2019**, *475*, 20190277. [CrossRef] [PubMed]
63. Steinour, H.H. Rate of sedimentation.Nonflocculated Suspensions of Uniform Spheres. *Ind. Eng. Chem.* **1944**, *36*, 618–624. [CrossRef]
64. Oliver, D. The sedimentation of suspensions of closely-sized spherical particles. *Chem. Eng. Sci.* **1961**, *15*, 230–242. [CrossRef]
65. Richardson, J.; Zaki, W. Sedimentation and fluidisation: Part I. *Chem. Eng. Res. Des.* **1954**, *75*, S82–S100. [CrossRef]
66. Rowe, P.N. A convenient empirical equation for estimation of the Richardson-Zaki exponent. *Chem. Eng. Sci.* **1987**, *42*, 2795–2796. [CrossRef]
67. Di Felice, R.; Gibilaro, L.G.; Foscolo, P.U. On the hindered settling velocity of spheres in the inertial flow regime. *Chem. Eng. Sci.* **1995**, *50*, 3005–3006. [CrossRef]
68. Di Felice, R. The sedimentation velocity of dilute suspensions of nearly monosized spheres. *Int. J. Multiph. Flow* **1999**, *25*, 559–574. [CrossRef]
69. Lu, Y.; Wei, L.; Wei, J. A numerical study of bed expansion in supercritical water fluidized bed with a non-spherical particle drag model. *Chem. Eng. Res. Des.* **2015**, *104*, 164–173. [CrossRef]
70. Barnea, E.; Mizrahi, J. A generalized approach to the fluid dynamics of particulate systems. *Chem. Eng. J.* **1973**, *5*, 171–189. [CrossRef]
71. Bhatnagar, P.L.; Gross, E.P.; Krook, M. A Model for Collision Processes in Gases. I. Small Amplitude Processes in Charged and Neutral One-Component Systems. *Phys. Rev.* **1954**, *94*, 511–525. [CrossRef]
72. Verlet, L. Computer 'Experiments' on Classical Fluids. I. Thermodynamical Properties of Lennard-Jones Molecules. *Phys. Rev.* **1967**, *159*, 98–103. [CrossRef]
73. Swope, W.C.; Andersen, H.C.; Berens, P.H.; Wilson, K.R. A computer simulation method for the calculation of equilibrium constants for the formation of physical clusters of molecules: Application to small water clusters. *J. Chem. Phys.* **1982**, *76*, 637–649. [CrossRef]
74. Shan, X.; Chen, H. Lattice Boltzmann model for simulating flows with multiple phases and components. *Phys. Rev. E* **1993**, *47*, 1815–1819. [CrossRef]
75. Guo, Z.; Zheng, C.; Shi, B. Discrete lattice effects on the forcing term in the lattice Boltzmann method. *Phys. Rev. E* **2002**, *65*. [CrossRef] [PubMed]
76. Kupershtokh, A.; Medvedev, D.; Karpov, D. On equations of state in a lattice Boltzmann method. *Comput. Math. Appl.* **2009**, *58*, 965–974. [CrossRef]
77. Huang, H.; Krafczyk, M.; Lu, X. Forcing term in single-phase and Shan-Chen-type multiphase lattice Boltzmann models. *Phys. Rev. E* **2011**, *84*. [CrossRef]
78. Caiazzo, A.; Junk, M. Boundary forces in lattice Boltzmann: Analysis of Momentum Exchange algorithm. *Comput. Math. Appl.* **2008**, *55*, 1415–1423. [CrossRef]
79. Sukop, M.C.; Thorne, D.T. *Lattice Boltzmann Modeling*; Springer: Berlin/Heidelberg, Germany, 2006.
80. Jekel, C.F.; Venter, G.; Venter, M.P.; Stander, N.; Haftka, R.T. Similarity measures for identifying material parameters from hysteresis loops using inverse analysis. *Int. J. Mater. Form.* **2019**, *12*, 355–378. [CrossRef]
81. Witowski, K.; Stander, N. Parameter Identification of Hysteretic Models Using Partial Curve Mapping. In Proceedings of the 12th AIAA Aviation Technology, Integration, and Operations (ATIO) Conference and 14th AIAA/ISSMO Multidisciplinary Analysis and Optimization Conference, Indianapolis, IN, USA, 17–19 September 2012.
82. Rohde, M.; Derksen, J.J.; Van den Akker, H.E.A. Volumetric method for calculating the flow around moving objects in lattice-Boltzmann schemes. *Phys. Rev. E* **2002**, *65*. [CrossRef]
83. Horowitz, M.; Williamson, C.H.K. The effect of Reynolds number on the dynamics and wakes of freely rising and falling spheres. *J. Fluid Mech.* **2010**, *651*, 251–294. [CrossRef]
84. Rahmani, M.; Wachs, A. Free falling and rising of spherical and angular particles. *Phys. Fluids* **2014**, *26*, 083301. [CrossRef]
85. Jenny, M.; Dušek, J.; Bouchet, G. Instabilities and transition of a sphere falling or ascending freely in a Newtonian fluid. *J. Fluid Mech.* **2004**, *508*, 201–239. [CrossRef]

86. Bretl, C.; Trunk, R.; Nirschl, H.; Thäter, G.; Dorn, M.; Krause, M.J. Preliminary study of particle settling behaviour by shape parameters via lattice Boltzmann simulations. In *High Performance Computing in Science and Engineering '20*; Nagel, W., Kröner, D., Resch, M., Eds.; Springer: New York, NY, USA, 2020.
87. Henn, T.; Thäter, G.; Dörfler, W.; Nirschl, H.; Krause, M.J. Parallel dilute particulate flow simulations in the human nasal cavity. *Comput. Fluids* **2016**, *124*, 197–207. [CrossRef]

6

Correlating the Settling Behavior of Single Particles with Shape Parameters

This chapter was published in the following article:

R. Trunk, C. Bretl, G. Thäter, H. Nirschl, M.Dorn and M. J. Krause
A Study on Shape-Dependent Settling of Single Particles with Equal Volume Using Surface Resolved Simulations
Computation, 9.40 (2021)
https://doi.org/10.3390/computation9040040

Own contribution according to the contributor roles taxonomy CRediT [14]:

- conceptualization
- data curation
- formal Analysis
- funding acquisition
- investigation
- methodology
- project administration
- software
- validation
- visualization
- writing – original draft
- writing – review & editing

computation

MDPI

Article

A Study on Shape-Dependent Settling of Single Particles with Equal Volume Using Surface Resolved Simulations

Robin Trunk [1,2,*], Colin Bretl [1,2], Gudrun Thäter [1,3], Hermann Nirschl [2], Márcio Dorn [4] and Mathias J. Krause [1,2,3]

[1] Lattice Boltzmann Research Group, Karlsruhe Institute of Technology, Straße am Forum 8, 76131 Karlsruhe, Germany; colin.bretl@student.kit.edu (C.B.); gudrun.thaeter@kit.edu (G.T.); mathias.krause@kit.edu (M.J.K.)
[2] Institute for Mechanical Process Engineering and Mechanics, Karlsruhe Institute of Technology, Straße am Forum 8, 76131 Karlsruhe, Germany; hermann.nirschl@kit.edu
[3] Institute for Applied and Numerical Mathematics, Karlsruhe Institute of Technology, Englerstraße 2, 76131 Karlsruhe, Germany
[4] Institute of Informatics, Federal University of Rio Grande do Sul, Av. Bento Goncalves 9500, Porto Alegre 91501-970, Brazil; marcio.dorn@inf.ufrgs.br
* Correspondence: robin.trunk@kit.edu

Abstract: A detailed knowledge of the influence of a particle's shape on its settling behavior is useful for the prediction and design of separation processes. Models in the available literature usually fit a given function to experimental data. In this work, a constructive and data-driven approach is presented to obtain new drag correlations. To date, the only considered shape parameters are derivatives of the axis lengths and the sphericity. This does not cover all relevant effects, since the process of settling for arbitrarily shaped particles is highly complex. This work extends the list of considered parameters by, e.g., convexity and roundness and evaluates the relevance of each. The aim is to find models describing the drag coefficient and settling velocity, based on this extended set of shape parameters. The data for the investigations are obtained by surface resolved simulations of superellipsoids, applying the homogenized lattice Boltzmann method. To closely study the influence of shape, the particles considered are equal in volume, and therefore cover a range of Reynolds numbers, limited to [9.64, 22.86]. Logistic and polynomial regressions are performed and the quality of the models is investigated with further statistical methods. In addition to the usually studied relation between drag coefficient and Reynolds number, the dependency of the terminal settling velocity on the shape parameters is also investigated. The found models are, with an adjusted coefficient of determination of 0.96 and 0.86, in good agreement with the data, yielding a mean deviation below 5.5% on the training and test dataset.

Keywords: single particle settling; non-spherical; particle shape; OpenLB; lattice Boltzmann method; homogenised lattice Boltzmann method

check for updates

Citation: Trunk, R.; Bretl, C.; Thäter, G.; Nirschl, H.; Dorn, M.; Krause, M.J. A Study on Shape-Dependent Settling of Single Particles with Equal Volume Using Surface Resolved Simulations. *Computation* **2021**, *9*, 40. https://doi.org/10.3390/computation9040040

Academic Editor: Philipp Neumann

Received: 15 February 2021
Accepted: 22 March 2021
Published: 25 March 2021

1. Introduction

Describing the settling of particles of various shapes is relevant for a wide range of applications. Fu et al. [1] found, e.g., that modifying the shape of lactose powder can be an efficient way to change its flow properties. Furthermore, the particle shape is related to the efficiency of classification processes in hydro cyclones [2]. It is also relevant for medical applications: Champion et al. [3] identified the shape as being critical to the performance of drug carriers. More recently, Waldschläger and Schüttrumpf [4] investigated the velocities of micro-plastic settling and rising—among other things—for different shapes, such as fragments, pellets, and fibers. They found that shapes make a big difference.

A challenge is the classification of the different shapes. A first approach is categorization in classes. Based on elongation and flatness (defined via main axis lengths), Zingg [5] introduced four different classes (blade, disc, rod and sphere). Sneed and Folk [6] distinguish ten classes, including, in particular, compactness. This, however, does not cover all aspects of shape and further parameters are required. The need for a uniform definition is also reflected in the existence of a specific international standard ISO 9276-6 [7]. Due to the interdependence of many parameters, the construction of a set covering most aspects of shape while also ensuring pairwise independence is complicated. Therefore, Hentschel and Page [8] performed a cluster analysis to identify a minimal set, finding the aspect ratio and a form factor, describing the ruggedness as most important. Later, a more granular classification system with 25 classes was proposed by Blott and Pye [9], also taking the roundness and sphericity into account. To find a correlation applicable to a wide range of shapes, however, there should not be a sharp distinction between classes, but a smooth transition between shapes.

In addition to those parameters, the orientation of the particle is also relevant, as some correlations regarding the settling of particles depend on the crosswise sphericity, which also depends on it. This is, furthermore, of importance in the formation of sediments, as discussed by Allen [10], who stated that the orientation is mainly influenced by the Reynolds number. Sheikh et al. [11] performed simulations to study the orientation of spheroid settling under turbulent conditions. An overview of the orientation of particles for a broad range of Reynolds numbers was given by Bagheri and Bonadonna [12]; for Reynolds numbers up to 100, the particles tend to settle in an orientation which maximizes the drag [13], while many particles have no preferred orientation in the Stokes regime. However, the shape additionally affects the orientation, as shown by Shao et al. [14], who found differences in orientation not only for triangular and rectangular particles, but also for rectangular particles with different aspect ratios for the same Reynolds number.

Extending the drag correlations for spheres [15–17] to other particle shapes has been a topic of ongoing research for a long time. McNown [18] proposed a formula for ellipsoids in the Stokes regime in 1950. It is still present in current research, e.g., Sommerfeld and Qadir [19] presented a study investigating the drag and lift depending on the angle of eight particles with different sphericity via lattice Boltzmann simulations in 2018. While the correlation by Leith [20] is restricted to the Stokes regime, it is based on the differentiation between form and friction drag, which depend on the surface tangential and are normal to the settling direction. This differentiation is also visible in later works by Ganser [21], Loth [22], and Hölzer and Sommerfeld [23]. Most correlations are, therefore, based on a similar model with values fitted according to predominantly experimental, but also analytical data. The calculation of drag correction factors for the Stokes and Newton regime, used in the correlations, is common. Bagheri and Bonadonna [12] introduced the additional requirement that shape parameters need to be accessible without extensive measurement effort. They concluded with a correlation solely based on the axis lengths, volume and density ratio, thereby omitting the otherwise commonly used sphericity. Their correlation, together with the one presented by Hölzer and Sommerfeld [23], is among the best performing correlations currently available in the literature for a wide range of Reynolds numbers and shapes. However, all presented correlations mimic a similar structure, based on the assumptions by Leith [20], only modifying terms and adding parameters and further correction terms. This leads to the situation where, even for the best models, a remaining spread is visible, which is not explained by the correlation. As hinted by Bagheri and Bonadonna [12], the range of considered shape parameters needs to be extended to capture more effects; this was also found by Tran-Cong et al. [24].

Depending on the considered particles, more specific correlations are available. Dellino et al. [25] and Dioguardi and Mele [26] presented correlations for pumice particles, namely samples of material from eruptions at the Vesuvius and Camp Flegrei volcanoes. Since the topic of settling non-spherical particles proved to be complex and affected by many factors, investigations of such specific sets as well as additional effects are sensible. For the latter, Hölzer and Sommerfeld [27] investigated, among other things, the influence of the Magnus effect. Few investigations exist which do not correlate the drag coefficient with a Reynolds number, but aim to directly describe the terminal settling velocity. The correlations considered here are the ones by Haider and Levenspiel [28] and Dellino et al. [25]. Such correlations, in addition to being an easy, accessible, a-priori estimate for the terminal settling velocity, might help to improve other models. A broad range of investigations of particle behavior, e.g., in the lung [29,30] or in mixing processes [31], could benefit from such models. For such more specific applications, a tool to obtain correlations, best fit for the considered purpose and the available data, might be more beneficial than a general correlation aiming to describe all cases.

Furthermore, the quality and abundance of data are crucial for a regression analysis and model development. Experimental data might be expensive to obtain, especially in large scales, since one has to measure all relevant parameters for existing particles. This is also discussed by Bagheri and Bonadonna [12], who restricted the model to shape parameters that are easily accessible. This is handy for application, since the required data of a new particle system can be obtained comparably simply, and increases the amount of available datapoints; however, some not-captured effects might be related to more sophisticated shape parameters.

The aim of this work is to provide a tool capable of delivering drag correlations with a good fit for a given set of data, and also apply it to the results of simulations yielding correlations for the drag coefficient and terminal settling velocity. The available literature usually only addresses new correlations, based on the modification and extension of existing models, which are obtained by extending the data basis. This work takes a data-driven approach, obtaining a database not through experimental studies, but through simulations. Depending on the availability of computational resources and preexisting models and implementations, simulations of arbitrarily shaped particles [32] might be an efficient alternative, with the information regarding the settling behavior of the particles becoming more accessible. Therefore, the procedure described in this work allows for a larger database to be obtained, along with advances in available computing power and algorithmics.

Here, the particles were modeled by superellipsoids, as this allows for the depiction of a broad range of shapes. Since the particle shapes can be analytically described, a vast amount of shape parameters can be calculated, which might not be accessible to experimental measurement devices. Therefore, in this work, multiple shape parameters besides axis length, elongation, flatness and sphericity are considered,such as roundness, convexity and further constructed parameters like the Corey shape factor [18], which are displayed in Section 2.2. The considered parameters are also evaluated regarding their relevance during the investigation. As with this representation via superellipsoids, edges are usually, at least to some extent, rounded and not sharp, except for extreme values; this reflects the nature of real particle systems, since corners and edges are usually rounded due to collisions. Therefore, 200 particles, with different shapes and densities, were simulated individually in this work. The shapes were constructed to provide a dataset with preferably equally distributed shape parameters, to reduce the effect of a stronger weighting of a specific class of particles.

One aim of this study is to find a new, improved correlation in a constructive way, by applying a polynomial regression and investigating the statistical relevance of various existing shape parameters and their interactions. To the knowledge of the authors, such an investigation has not been performed before, especially also considering the multicollinearity and statistical relevance of each term by various measures. In addition, a correlation for the terminal settling velocity is proposed.

The simulations were performed applying the homogenized lattice Boltzmann method (HLBM), introduced by Krause et al. [33] and validated in a previous work by Trunk et al. [34]. It is used within the open-source C++ simulation framework OpenLB [35,36].

The remainder of this work is organised as follows. In Section 2, the model for the settling of particles is given as well as an overview of relevant existing drag correlations for spheres and non-spherical particles. The shape parameters considered in this work are defined and the depiction of particles by superellipsoids is described. Following this, in Section 3, the necessary information regarding the applied simulation method and the generation process of the particle dataset is given. In Section 3.2, the applied statistical tools, later applied in the investigation, are introduced. Finally, in Section 4, the conduction and validation of numerical experiments is discussed, and the results are presented in Section 5. The latter is divided into a general inspection of results (Section 5.1), and the regression analyses regarding the drag coefficient (Section 5.2.1) and the terminal settling velocity (Section 5.2.2). A brief overview of the findings is then given in the conclusion in Section 6.

2. Mathematical Modeling

In this work, the behavior of single settling particles in a liquid is studied. Since this is similar to previous studies, this rather general part of the section strongly follows the one given in the preceding publication by Trunk et al. [34]. The dynamic behavior of the system is defined by the motion of the particle and the fluid. The latter is governed by the incompressible Navier–Stokes equations

$$\begin{aligned} \frac{\partial \boldsymbol{u}_\mathrm{f}}{\partial t} + (\boldsymbol{u}_\mathrm{f} \cdot \nabla)\boldsymbol{u}_\mathrm{f} - \nu \Delta \boldsymbol{u}_\mathrm{f} + \frac{1}{\rho_\mathrm{f}} \nabla p = \boldsymbol{F}_\mathrm{f} \quad & \text{in } \Omega_\mathrm{f} \times I\,, \\ \nabla \cdot \boldsymbol{u}_\mathrm{f} = 0 \quad & \text{in } \Omega_\mathrm{f} \times I\,. \end{aligned} \tag{1}$$

They are defined for a time interval $I \subseteq \mathbb{R}$ on a spatial domain Ω_f which, together with the area covered by the particle Ω_p, spans the computational domain $\Omega_\mathrm{f} \cup \Omega_\mathrm{p} = \Omega \subseteq \mathbb{R}^3$. Since the considered particles are not stationary, it is $\Omega_\mathrm{f} = \Omega_\mathrm{f}(t)$ and $\Omega_\mathrm{p} = \Omega_\mathrm{p}(t)$. $\boldsymbol{u}_\mathrm{f} : \Omega_\mathrm{f} \times I \to \mathbb{R}^3$ denotes the fluid velocity, while $p : \Omega_\mathrm{f} \times I \to \mathbb{R}$ describes the pressure, $\rho_\mathrm{f} \in \mathbb{R}_{>0}$ the fluid's density and $\nu \in \mathbb{R}_{>0}$ its kinematic viscosity. The total force experienced by the fluid is denoted by $\boldsymbol{F}_\mathrm{f}$, and is solely composed of the hydrodynamic force due to the exchange of momentum with the submersed particle.

The rigid particle's motion follows Newton's second law of motion

$$m_\mathrm{p} \frac{d\boldsymbol{u}_\mathrm{p}}{dt} = \boldsymbol{F}_\mathrm{p} \quad \text{and} \quad \frac{d(\boldsymbol{J}_\mathrm{p} \boldsymbol{\omega}_\mathrm{p})}{dt} = \boldsymbol{T}_\mathrm{p}\,. \tag{2}$$

Here, $m_\mathrm{p} \in \mathbb{R}_{>0}$ is the particle's mass, $\boldsymbol{u}_\mathrm{p} : I \to \mathbb{R}^3$ the particle's velocity and $\boldsymbol{F}_\mathrm{p} : I \to \mathbb{R}^3$ the force acting on the particle. The rotation can be described in an equivalent way to the moment of inertia $\boldsymbol{J}_\mathrm{p} \in \mathbb{R}^3$, the angular velocity $\boldsymbol{\omega}_\mathrm{p} : I \to \mathbb{R}^3$ and the torque $\boldsymbol{T}_\mathrm{p} : I \to \mathbb{R}^3$. Together with an expression for the force $\boldsymbol{F}_\mathrm{p}$, this enables the calculation of a particle's trajectory.

The only external forces relevant in this work are the gravitational and buoyancy forces, given by $\boldsymbol{F}^\mathrm{BG} = (0, 0, m_\mathrm{p}(1 - \frac{\rho_\mathrm{f}}{\rho_\mathrm{p}})g)$. The gravitational acceleration of g is equal to $9.81\,\mathrm{m\,s^{-2}}$ throughout this paper. Since only a single particle is considered, contact forces are neglected. Therefore, with the hydrodynamic force $\boldsymbol{F}^\mathrm{H} : I \to \mathbb{R}^3$, responsible for the momentum transfer between fluid and particle, and the vector $\boldsymbol{r} \in \mathbb{R}^3$ yielding the distance to the center of mass for a point in the particle, the force in Equation (2) is given by

$$\begin{aligned} \boldsymbol{F}_\mathrm{p} &= \boldsymbol{F}^\mathrm{BG} + \int_S \left[-p\boldsymbol{I} + \frac{1}{\mathrm{Re}} (\nabla \boldsymbol{u}_\mathrm{f} + \nabla \boldsymbol{u}_\mathrm{f}^t) \right] \cdot \boldsymbol{n} dS\,, \\ \boldsymbol{T}_\mathrm{p} &= \int_S \boldsymbol{r} \times \left[-p\boldsymbol{I} + \frac{1}{\mathrm{Re}} (\nabla \boldsymbol{u}_\mathrm{f} + \nabla \boldsymbol{u}_\mathrm{f}^t) \right] \cdot \boldsymbol{n} dS\,, \end{aligned} \tag{3}$$

with $\boldsymbol{n}$ being the normal on the surface S of an object.

2.1. Drag Coefficient

The force mainly responsible for interaction between particle and fluid is the drag force, which depends on the relative velocity between the considered object and the surrounding fluid. In general, it is given by

$$\boldsymbol{F}^{\mathrm{D}} = \frac{1}{2}\boldsymbol{\rho}_{\mathrm{f}}(\boldsymbol{u}_{\mathrm{p}} - \boldsymbol{u}_{\mathrm{f}})^2 C_{\mathrm{D}} A \,, \tag{4}$$

with A denoting the projected surface of the considered object in the direction of the relative flow. The drag coefficient C_{D} depends on the shape of the particle [24,37], but mainly on the Reynolds number

$$\mathrm{Re} = \frac{d_{\mathrm{eq}} u_{\mathrm{ts}}}{\nu} \,, \tag{5}$$

with the terminal settling velocity u_{ts}. In this work, the diameter of the volume equivalent sphere d_{eq}, described in the next section, is used as characteristic length. This allows the calculation of Re for arbitrary shapes.

For the simple shape of a sphere, numerous correlations for C_{D} have been proposed based on experimental and analytical investigations [38]. This has already been investigated by the authors in a previous work [34]. The most common correlation is given by Stokes [15] for $\mathrm{Re} < 1$ with $C_{\mathrm{D,S}} = 24/\mathrm{Re}$. Inserting this in Equation (4), and assuming a force balance, as stated in Equation (3), this leads to the terminal settling velocity

$$u_{\mathrm{ts,S}} = \sqrt{\frac{4}{3}\frac{g d_{\mathrm{eq}}}{C_{\mathrm{D,S}}}\frac{\rho_{\mathrm{p}} - \rho_{\mathrm{f}}}{\rho_{\mathrm{f}}}} \,. \tag{6}$$

Another common drag correlation for Reynolds numbers up to 800 has been proposed by Schiller and Naumann [16]. It is given by

$$C_{\mathrm{D,SN}} = \frac{24}{\mathrm{Re}}\left(1 + 0.15\mathrm{Re}^{0.687}\right) \,, \tag{7}$$

and has been extended by Clift and Gauvin [17] for the full intermediate and Newton regime by

$$C_{\mathrm{D,CG}} = \frac{24}{\mathrm{Re}}\left(1 + 0.15\mathrm{Re}^{0.687}\right) + 0.42\left(1 + \frac{42500}{\mathrm{Re}^{1.16}}\right)^{-1} \,. \tag{8}$$

2.2. Shape Parameter

Some of the challenges in the selection of particle shape parameters are caused by the numerous ways of defining the measures and the correlation between the parameters. Additionally, since a particle's shape can be arbitrarily complex, it cannot be fully described by a small set of values, which usually are not fully independent of each other. In this section, the measures used in this work are briefly introduced.

A first approach is the definition of the diameter of a sphere with a volume equal to the one of the particle V_{p}. It is given by

$$d_{\mathrm{eq}} = \sqrt[3]{\frac{6}{\pi} V_{\mathrm{p}}} \,. \tag{9}$$

Since this parameter alone does not carry any information about the shape, additional values like the aspect ratio, defined as the ratio of minimum to maximum of the Feret diameter, are required. In previous studies by the authors [39], it was shown that this parameter is still too generic; therefore, it is split in elongation

$$E = a_{\mathrm{I}} / a_{\mathrm{L}} \,, \tag{10}$$

and flatness

$$F = a_\mathrm{S}/a_\mathrm{I}\,, \tag{11}$$

in this work. Here, a_L, a_I and a_S denote the longest, intermediate and shortest half-axis of the particle, respectively.

Another common parameter is the convexity κ_con, defined as the ratio of the particle's volume to the volume of its convex hull, taking values between 0 and 1. The sphericity ψ, as defined by Wadell [40], has already been used in many studies regarding the particle shape [19,23]. It also takes values between 0 and 1, with the latter being a perfect sphere. Defined as the ratio between the surface of a volume-equivalent sphere and the particle's surface A_p, it is given as

$$\psi = \frac{1}{A_\mathrm{p}}\sqrt[3]{\pi(6V_\mathrm{p})^2}\,. \tag{12}$$

While the sphericity describes the particle's resemblance to a sphere, the roundness κ_rnd is related to the curvature of its corners and edges. While the definition based on the measurements by Krumbein [41] or by Wadell [40] are rather inconvenient to calculate, it is defined here as

$$\kappa_\mathrm{rnd} = \frac{V_\mathrm{p}}{A_\mathrm{p}(8a_\mathrm{L}a_\mathrm{I}a_\mathrm{S})^{1/3}}\,. \tag{13}$$

This formula was proposed by Hayakawa and Oguchi [42], who found a strong correlation with the results by Krumbein [41].

Further parameters can be created, e.g., by combining the lengths of the main axes. A common parameter is the Corey shape factor λ_CSF [18,43], yielding lower values with a flatter particle. It is defined by

$$\lambda_\mathrm{CSF} = \frac{a_\mathrm{S}}{\sqrt{a_\mathrm{I}a_\mathrm{L}}}\,. \tag{14}$$

The Hofmann shape entropy λ_H [44], which was found to properly describe the dynamics of settling ellipsoids [45], is defined in a more complex way as

$$\lambda_\mathrm{H} = -\frac{\tilde{a}_\mathrm{S}\ln(\tilde{a}_\mathrm{S}) + \tilde{a}_\mathrm{I}\ln(\tilde{a}_\mathrm{I}) + \tilde{a}_\mathrm{L}\ln(\tilde{a}_\mathrm{L})}{\ln(3)}\,, \tag{15}$$

for axis lengths normalized as $\tilde{a}_i = a_i/(a_\mathrm{S} + a_\mathrm{I} + a_\mathrm{L})$ for $i \in \{S, I, L\}$. Le Roux investigated the settling of grains with a database containing (prolate and oblate) spheroids, discs, cylinders, and ellipsoids, finding correlations for the settling velocity of the particles and also performing a hydrodynamic classification regarding the shape [46]. The found parameter

$$\lambda_\mathrm{LR} = \left(1 - \frac{a_\mathrm{S}}{a_\mathrm{L}}\right)^{\sigma}\,, \tag{16}$$

depends on a value σ which is dependent of the class of shape; it is given, e.g., by $\sigma = 2.5$ for ellipsoids and $\sigma = 1.6$ for discs.

2.3. Particle Representation

For the depiction of arbitrary particle shapes, superellipsoids are chosen in this work, as they represent a compromise between a diversity of possible shapes (e.g., rectangular, spheroidal or cylindrical) and analytical manageability. Information on the modeling parameter and transformations of a superellipsoid are given, e.g., by Williams and Pentland [47] or Barr [48]. Even contact-detection algorithms exist, as presented by Wellmann et al. [49]. An extensive discussion on the geometric properties is given by Jaklič [50].

Let (X, Y, Z) be the coordinates of a point in $\mathbb{R}^3$; then, a superellipsoid is described by

$$\left(\left|\frac{X}{a}\right|^{\xi_1} + \left|\frac{Y}{b}\right|^{\xi_1}\right)^{\xi_2/\xi_1} + \left|\frac{Z}{c}\right|^{\xi_2} \leq 1\,, \tag{17}$$

for half-axis lengths a, b, c in x-, y- and z-direction, respectively. The exponents ξ_1 and ξ_2 control the roundness of the superellipsoid. Considering $a = b = c$, this geometric primitive, e.g., takes on the shape of a sphere for $\xi_1 = \xi_2 = 2$, a cube for $\xi_1, \xi_2 \to \infty$ or the the shape of a cylinder for $\xi_1 = 2$ and $\xi_2 \to \infty$. Overall, the shape is convex for $\xi_1 \geq 1$ and tends to be flatter for $\xi_2 \to 0$.

While Equation (17) allows a description of the surface, the volume and moment of inertia are also required for the simulation. They can be defined utilizing the moments given by Jaklič and Solina [51] as

$$m_{i,j,k} = \frac{2}{i+j+2} a^{i+1} b^{j+1} c^{k+1} \xi_1 \xi_2 B\left((k+1)\frac{\xi_1}{2}, (i+j+2)\frac{\xi_1}{2} + 1\right) B\left((j+1)\frac{\xi_2}{2}, (i+1)\frac{\xi_2}{2}\right), \tag{18}$$

for $i, j, k \in \mathbb{N}_0$. The beta function is given by

$$B(x, y) = \int_0^1 t^{x-1}(1-t)^{y-1} dt \qquad \text{for } x, y > 0\,, \tag{19}$$

or can alternatively be represented as combination of gamma functions. Based on Equation (18), the volume V_p and the moment of inertia $\boldsymbol{J}_\mathrm{p} = (J_{xx}, J_{yy}, J_{zz})$ are now defined as

$$V_\mathrm{p} = m_{0,0,0}\,, \tag{20}$$

$$J_{xx} = m_{0,2,0} + m_{0,0,2}\,, \tag{21}$$

$$J_{yy} = m_{2,0,0} + m_{0,0,2}\,, \tag{22}$$

$$J_{zz} = m_{2,0,0} + m_{0,2,0}\,. \tag{23}$$

2.4. Drag Correlations for Non-Spherical Particles

There have been many attempts to find and improve a drag correlation for different particle shapes and different ranges of Reynolds numbers. The oldest discussed here is derived by Leith [20] for the Stokes region. Considering the form drag originating from pressure on the particle's surface and friction drag caused by a tangential shear stress, Leith proposed a formula based on the diameter of a surface-equivalent sphere and the diameter of a sphere with the same projected area in the direction of motion. His parameters were later interpreted as sphericity ψ and crosswise sphericity $\psi_\perp$, i.e., the ratio of projected area of a volume-equivalent sphere to the projected area of the particle normal to the direction of motion, leading to the most commonly used version

$$K_\mathrm{S} = \frac{1}{3}\sqrt{\psi_\perp} + \frac{2}{3}\sqrt{\psi}\,. \tag{24}$$

Here, K_S denotes the drag correction factor for a particle in the Stokes regime regarding a volume-equivalent sphere. As Leith [20] found evaluating his results, these do not fully explain the experimental reference data; he proposed the application of a least-squares fit for additional terms regarding the axis lengths. Likely because these results are specific to the considered data basis, usually, only the formula depicted here is referenced.

Later, Haider and Levenspiel [28] performed a non-linear regression analysis on a data basis of 409 polyhedrons and 87 discs for Reynolds numbers up to 2.6×10^5. The result is the comparably complex formulation of

$$\begin{aligned} C_\mathrm{D,HL} &= \frac{24}{\mathrm{Re}}\left(1 + c_1 \mathrm{Re}^{c_2}\right) + \frac{c_3}{1 + c_4/\mathrm{Re}}\,, \quad \text{with} \\ c_1 &= e^{2.329 - 6.458\psi + 2.449\psi^2}\,, \\ c_2 &= 0.096 + 0.557\psi\,, \\ c_3 &= e^{4.905 - 13.894\psi + 18.422\psi^2 - 10.260\psi^3}\,, \\ c_4 &= e^{1.468 + 12.258\psi - 20.732\psi^2 + 15.886\psi^3}\,. \end{aligned} \tag{25}$$

The error for the disc-like particles was found to be approximately four times the one of the polyhedral particles, probably due to the unbalanced data basis. In addition, Haider and Levenspiel [28] proposed a formulation to estimate the terminal settling velocity for isometric particles with a sphericity between 0.5 and 1, by

$$\begin{aligned} u_{\mathrm{ts,HL}} &= \left(\frac{g\nu(\rho_\mathrm{p}-\rho_\mathrm{f})}{\rho_\mathrm{f}}\right)^{1/3}\left(\frac{18}{d_*^2}+\frac{2.335-1.744\psi}{\sqrt{d_*}}\right)^{-1}, \quad \text{with} \\ d_* &= d_{eq}\left(\frac{g(\rho_\mathrm{p}-\rho_\mathrm{f})}{\nu^2\rho_\mathrm{f}}\right)^{1/3}. \end{aligned} \tag{26}$$

A study by Ganser [21] considering 731 datapoints aggregated from the literature concluded with

$$\begin{aligned} C_{\mathrm{D,G}} &= \frac{24K_\mathrm{S}}{\mathrm{Re}}\left(1+0.1118\left(\frac{\mathrm{Re}K_\mathrm{N}}{K_\mathrm{S}}\right)^{0.6567}\right)+\frac{0.4305K_\mathrm{N}}{1+3305K_\mathrm{S}/(\mathrm{Re}K_\mathrm{N})}, \quad \text{with} \\ K_\mathrm{S} &= \frac{1}{3}+\frac{2}{3}\sqrt{\psi}, \\ K_\mathrm{N} &= 10^{1.8148(-\log\psi)^{0.5743}}. \end{aligned} \tag{27}$$

As well as the new correction factor for the Stokes regime, an additional one was introduced for the Newton regime, along with the assumption that these two factors are sufficient for an adequate prediction of the drag coefficient for Reynolds numbers up to $\mathrm{Re}K_\mathrm{S}K_\mathrm{N} \leq 10^5$. While the formula presented here is mainly applicable to isometric objects, alternatives for disc-like particles were also presented; however, these require knowledge of the orientation of the particle. These shape-dependent differences were found to mainly affect K_S. Ganser [21] further concluded that the introduction of a third parameter for the intermediate regime could reduce the remaining variance.

Loth [22] extended the investigations of Ganser [21] and Leith [20], also providing a more differentiated discussion on the behavior in the intermediate Reynolds number regime. Their finding was that different formulations are required regarding the circularity of the projected area of the particle in the direction of motion. This, of course, also required knowledge of orientation. Despite this, an additional correction factor for the Stokes regime

$$K_\mathrm{S} = \left(\frac{a_\mathrm{L}a_\mathrm{I}}{a_\mathrm{S}^2}\right)^{0.09} = \left(\frac{1}{\lambda_\mathrm{CSF}^2}\right)^{0.09}, \tag{28}$$

was proposed, describing irregular particles.

To incorporate the particle orientation without differentiation between shape classes, Hölzer and Sommerfeld [23] proposed taking the lengthwise sphericity $\psi_\parallel$, defined as "the ratio between the cross-sectional area of the volume equivalent sphere and the difference between half the surface area and the mean longitudinal (i.e., parallel to the direction of relative flow) projected cross-sectional area of the considered particle" [23] into account. Their correlation, which was evaluated on 2061 datapoints, is given by

$$C_{\mathrm{D,HS}} = \frac{8}{\mathrm{Re}\sqrt{\psi_\parallel}}+\frac{16}{\mathrm{Re}\sqrt{\psi}}+\frac{3}{\sqrt{\mathrm{Re}}\psi^{3/4}}+0.421^{0.4(-\log\psi)^{0.2}}\frac{1}{\psi_\perp}, \tag{29}$$

and showed a tremendous improvement in the prediction of the drag coefficient for disc-like objects. They also showed that replacing lengthwise with crosswise sphericity only leads to a drop in the mean deviation from 14.1% to 14.4% from the experimental results.

Finally, Bagheri and Bonadonna [12] compiled a large dataset of 2166 particles from the literature and their own experiments across sub-critical Reynolds numbers, paired with analytical data for 10^4 ellipsoids in the Stokes regime. Based on the assumption by Ganser [21], they concluded with a formula based on Stokes and Newton correction factors

$$
\begin{aligned}
C_{\mathrm{D,BB}} &= \frac{24K_{\mathrm{S}}}{\mathrm{Re}}\left(1+0.125\left(\frac{\mathrm{Re}K_{\mathrm{N}}}{K_{\mathrm{S}}}\right)^{2/3}\right)+\frac{0.46K_{\mathrm{N}}}{1+5330/(\mathrm{Re}K_{\mathrm{N}}/K_{\mathrm{S}})}, \quad \text{with} \\
K_{\mathrm{S}} &= 0.5\left(F_{\mathrm{S}}^{1/3}+F_{\mathrm{S}}^{-1/3}\right), \\
K_{\mathrm{N}} &= 10^{c_1(-\log F_{\mathrm{N}})^{c_2}}, \\
c_1 &= 0.45+\frac{10}{e^{2.5\log\rho'}+30}, \\
c_2 &= 1-\frac{37}{e^{3\log\rho'}+100}, \\
F_{\mathrm{S}} &= FE^{1.3}\frac{d_{eq}^3}{a_{\mathrm{S}}a_{\mathrm{I}}a_{\mathrm{L}}}, \\
F_{\mathrm{N}} &= F^2E\frac{d_{eq}^3}{a_{\mathrm{S}}a_{\mathrm{I}}a_{\mathrm{L}}}.
\end{aligned}
\tag{30}
$$

The formula here is not taken directly from the publication, but a corrected version by Bagheri and Bonadonna [52]. They further argued that the sphericity, in addition to being harder to measure, is inferior to a shape descriptor based on the axis lengths. In an extensive discussion of particle behavior in the Stokes and Newton regime, it was found that the density ratio ρ' is also relevant, especially in the Newton regime. This is supported by various studies, suggesting that the trajectory might change depending on the density ratio [53–55]. A comparison showed their formula yielded the lowest deviation across all correlations discussed up to this point, and thereby is currently among the best-performing, together with the one proposed by Hölzer and Sommerfeld [23], to the knowledge of the authors. However, a spread in results is still visible. This hints that further effects and parameters might need to be considered to further improve the formulation.

More specific to a set of pumice particles from volcanic eruptions, Dioguardi and Mele [26] proposed a correlation depending on the drag coefficient for spheres, computed according to Clift and Gauvin [17], and the ratio of sphericity to circularity ϕ. The latter is given as ratio of maximum projected area to the projected area of a volume-equivalent sphere. Their formula finally reads

$$
C_{\mathrm{D,DM}} = \frac{C_{\mathrm{D,CG}}}{\mathrm{Re}^2(\psi/\phi)^{\mathrm{Re}^{-0.23}}}\left(\frac{\mathrm{Re}}{1.1883}\right)^{1/0.4826}. \tag{31}
$$

Dellino et al. [25] used the same dataset to develop a direct correlation between the terminal settling velocity and particle parameters, also relying on the ratio between sphericity and circularity. This is given by

$$
u_{\mathrm{ts,D}} = \frac{1.2065\nu}{d_{\mathrm{eq}}}\left(\frac{d_{\mathrm{eq}}^3 g(\rho_{\mathrm{p}}-\rho_{\mathrm{f}})(\psi/\phi)^{1.6}}{\nu^2\rho_{\mathrm{f}}}\right)^{0.5206}. \tag{32}
$$

This allows for a direct estimation of the terminal settling velocity without the need for an iterative algorithm, as is required when using the correlations regarding the drag coefficient.

3. Numerical and Statistical Methods

For the numerical simulations in this paper, the homogenized lattice Boltzmann method is applied. The method and implementation have been extensively tested and validated in a previous publication by Trunk et al. [34]; therefore, only the relevant parts are summarized here.

The HLBM was first proposed by Krause et al. [33] and later updated by Trunk et al. [34]. In this work, the version used in the latter publication is used, which is based on a forcing scheme by Kupershtokh et al. [56] and the momentum exchange algorithm by Wen et al. [57]. The extension to 3D and the incorporation of arbitrary particle shapes was described by Trunk et al. [32]. A setup similar to the one used in this work was studied by Trunk et al. [34] for spheres, yielding an error of approximately 6% compared to the drag correlation by Schiller and Naumann [16] and approximately 3% to the drag correlation by Abraham [58].

Since this approach is a specialisation of the more general lattice Boltzmann method (LBM), all values are non-dimensionalized by the spatial and temporal discretization parameter δx and δt and the density ρ_f during processing. The resulting system is denoted as a "lattice system". It was found by Trunk et al. [34] that the quality of the results depends on the maximal occurring velocity in the lattice system $u^\mathrm{L}_\mathrm{max}$ for the investigation of settling processes, defined by

$$u^\mathrm{L}_\mathrm{max} = \frac{\delta t}{\delta x^2} u_\mathrm{max} \,, \tag{33}$$

with u_max as the maximum fluid velocity observed in the simulation. For a sufficiently low error, $u^\mathrm{L}_\mathrm{max}$ should be smaller than 0.04. A further condition exists regarding the lattice relaxation time

$$\tau = \nu \frac{\delta t}{\delta x} \frac{1}{c_\mathrm{s}^2} + 0.5 \,, \tag{34}$$

where c_s^2 is the lattice speed of sound [59]. For the simulation to be stable, τ may not be too close to 0.5. For further information on the LBM, the interested reader is referred to Krüger et al. [59].

3.1. Particle Generation

According to the approach described in Section 2.3, a particle is defined by 5 parameters. To create a collection, parameter ranges are defined, for which the half-axis lengths are defined via elongation and flatness, starting with $a = 0.01\,\mathrm{m}$. Varying the particle's density, the parameters

$$\begin{aligned} E &\in \{0.5, 0.6, 0.7, 0.8, 0.9, 1\} \,, \\ F &\in \{0.5, 0.6, 0.7, 0.8, 0.9, 1\} \,, \\ \xi_1 &\in \{8, 2, 1, 0.933, 0.9, 0.866, 0.833, 0.8, 0.766, 0.733, 0.7, 0.666\} \,, \\ \xi_2 &\in \{8, 2, 1\} \,, \\ \rho_\mathrm{p} &\in \{2360\,\mathrm{kg\,m^{-3}}, 2460\,\mathrm{kg\,m^{-3}}, 2560\,\mathrm{kg\,m^{-3}}, 2660\,\mathrm{kg\,m^{-3}}, 2760\,\mathrm{kg\,m^{-3}}\} \,, \end{aligned} \tag{35}$$

lead to a group of 6480 particles. For comparability, the half-axes of all generated objects are scaled equally, such that the resulting particle has a volume of $1.66742 \times 10^{-11}\,\mathrm{m}^3$. Thereby, the equivalent sphere diameter of all generated particles is $d_\mathrm{eq} = 3.1697 \times 10^{-4}\,\mathrm{m}$. During the creation process, all shape parameters given in Section 2.2 are calculated along with the volume, according to Equation (20). Furthermore, the terminal settling velocity obtained using the drag correlation by Stokes (Equation (6)) and the surface are computed. For the latter, a triangulation of the parametric representation in terms of the modified spherical coordinates of Equation (17) is used [51].

From this set of particles, 200 are selected, such that a chi-squared test [60] for an equal distribution of frequencies yields a p-value above 0.99 for all considered parameters; some of them are shown in Figure 1. The frequencies are given for a sensible choice of numbers of bins for each parameter, as shown in Table 1. For the density, 5 bins wwere used, as only this number of discrete values is considered. For reference, the data and parameters for all 200 particles are given in Appendix A.

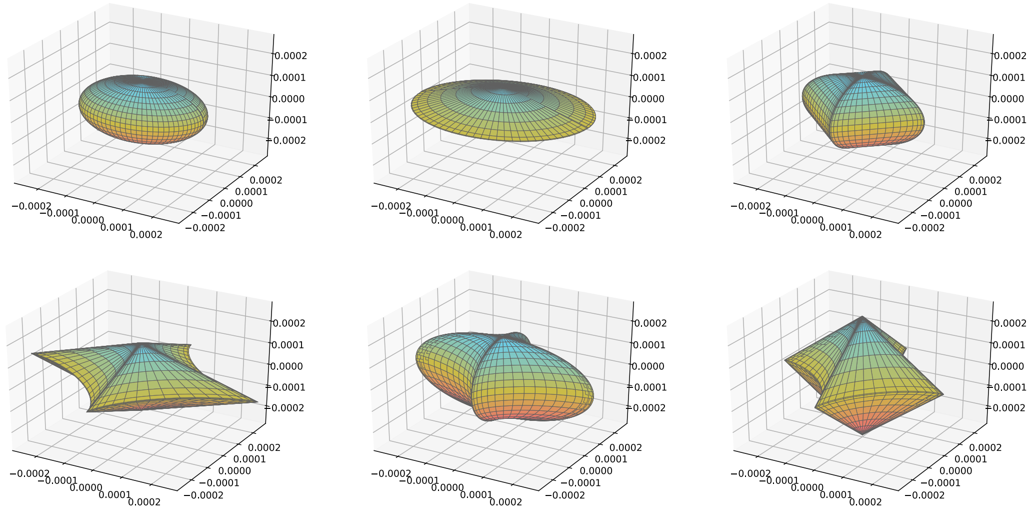

Figure 1. Some examples of particle shapes considered via superellipsoids. Depicted (from left to right and top to bottom) are the particles with ID 5, 17, 28, 143, 166 and 200, according to Appendix A.

Table 1. Results of a chi-squared test for equal distribution of frequencies of different shape parameters.

	Elongation	**Flatness**	**Convexity**	**Sphericity**	**Density**
numberof bins	6	6	6	5	5
p-value	0.998	0.995	0.999	1.000	1.000

As a first step, the Pearson correlation coefficients [60,61] for the shape parameters are calculated; their absolute values are depicted in Table 2. The results show three clusters of strong correlation. Firstly the constructed shape factors, i.e., the Corey shape factor, the Hofmann shape entropy and the Le Roux shape parameter; this is to be expected, as all of them depend on the axis lengths of the investigated objects. This also explains the second correlation between the first cluster and the elongation and flatness. The third group contains the convexity, sphericity and roundness. This suggests that adding more than one of these parameters to a model will have a weaker influence on the quality of the results. Lastly, a weaker correlation between this third cluster and the exponent ξ_1 used in the particle creation process can be observed. Furthermore, the axis lengths are correlated to almost every other parameter, except the density, as it is varied independently.

Table 2. Absolute Values of the correlation coefficients according to Pearson [61] for the considered shape parameters.

	a_L	a_I	a_S	ξ_1	ξ_2	ρ_P	E	F	κ_con	ψ	$\psi_\perp$	κ_rnd	λ_CSF	λ_H	λ_LR
a_L	1.0	0.55	0.04	0.41	0.17	0.03	0.74	0.51	0.65	0.52	0.64	0.68	0.67	0.73	0.75
a_I	0.55	1.0	0.57	0.39	0.47	0.08	0.13	0.13	0.63	0.61	0.47	0.85	0.05	0.04	0.02
a_S	0.04	0.57	1.0	0.18	0.57	0.03	0.44	0.72	0.41	0.45	0.31	0.61	0.73	0.64	0.65
ξ_1	0.41	0.39	0.18	1.0	0.02	0.08	0.19	0.15	0.47	0.44	0.31	0.57	0.18	0.21	0.21
ξ_2	0.17	0.47	0.57	0.02	1.0	0.03	0.16	0.36	0.07	0.05	0.23	0.34	0.34	0.32	0.31
ρ_P	0.03	0.08	0.03	0.08	0.03	1.0	0.02	0.1	0.03	0.05	0.04	0.05	0.08	0.02	0.03
E	0.74	0.13	0.44	0.19	0.16	0.02	1.0	0.45	0.33	0.2	0.47	0.17	0.72	0.85	0.84
F	0.51	0.13	0.72	0.15	0.36	0.1	0.45	1.0	0.07	0.01	0.0	0.01	0.94	0.79	0.83
κ_con	0.65	0.63	0.41	0.47	0.07	0.03	0.33	0.07	1.0	0.93	0.75	0.86	0.17	0.22	0.23
ψ	0.52	0.61	0.45	0.44	0.05	0.05	0.2	0.01	0.93	1.0	0.73	0.86	0.08	0.1	0.12
$\psi_\perp$	0.64	0.47	0.31	0.31	0.23	0.04	0.47	0.0	0.75	0.73	1.0	0.74	0.18	0.2	0.23
κ_rnd	0.68	0.85	0.61	0.57	0.34	0.05	0.17	0.01	0.86	0.86	0.74	1.0	0.06	0.08	0.11
λ_CSF	0.67	0.05	0.73	0.18	0.34	0.08	0.72	0.94	0.17	0.08	0.18	0.06	1.0	0.92	0.95
λ_H	0.73	0.04	0.64	0.21	0.32	0.02	0.85	0.79	0.22	0.1	0.2	0.08	0.92	1.0	0.99
λ_LR	0.75	0.02	0.65	0.21	0.31	0.03	0.84	0.83	0.23	0.12	0.23	0.11	0.95	0.99	1.0

3.2. Statistical Tools

To find the correlation between a dependent variable Y (here, e.g., the drag coefficient) and multiple independent variables X_i, $i \in \{1, \ldots, k;\ k \in \mathbb{N}\}$ (here e.g., sphericity), often, regression analysis is applied to find a model, yielding approximations of the dependent variable $\hat{Y}$. The quality of a model is evaluated by the amount of variance in the data it can describe; this is given by the coefficient of determination

$$R^2 = 1 - \frac{\sum_{j=1}^{n} r_j^2}{\sum_{j=1}^{n} (Y_j - \bar{Y})^2}\,, \quad \text{with } n \in \mathbb{N}\,, \tag{36}$$

for the residuals $r_j = Y_j - \hat{Y}_j$. Here, $\bar{Y}$ represents the mean and n is the number of datapoints. Considering multiple independent variables, the adjusted version given by

$$R_\mathrm{a}^2 = 1 - (1 - R^2)\frac{n-1}{n-k-1}\,, \tag{37}$$

is more appropriate. This further allows the definition of the variance inflation factor *VIF* as a measure of multicollinearity [62] by

$$VIF_i = \frac{1}{1 - R_i^2}\,, \tag{38}$$

with R_i^2 being the coefficient of determination of a linear regression, choosing X_i as the dependent variable. Values > 10 are considered critical since they indicate a high level of multicollinearity, which negatively affects the stability of the method chosen to calculate the regression coefficients.

To further obtain an a priori estimation regarding the dependency between two explanatory variables, the mutual information *MI* introduced by Shannon [63], defined as the difference between the sum of entropy of the two variables and the joint entropy, is calculated. Later, Kraskov et al. [64] introduced an estimate for this, using k-nearest neighbor distances, which is applied in this work. *MI* reaches its minimum of 0 for strictly independent variables. Another measure is the F-value of a linear regression, with only one explanatory variable regarding the desired dependent variable, given as

$$F_\mathrm{sample} = \frac{R^2/k}{(1 - R^2)/(n-k-1)}\,. \tag{39}$$

A high value indicates the relevance of the explanatory variable in the description of the dependent one [62]; however, this test is more suited to the detection of linear dependency.

To evaluate the significance of an explanatory variable for a performed regression, a *t*-test is performed. Here, a large t-value implies a high significance of the explanatory variable. Since the values can also be negative, the absolute has to be considered. For the variable X_i, with the associated regression coefficient β_i, the score is given as

$$T_{\text{sample}} = \left| \beta_i \left(\frac{\sqrt{(n-k-1)^{-1} \sum_{j=1}^{n} r_j^2}}{\sqrt{\sum_{j=1}^{n} (X_{i,j} - \bar{X}_i)^2}} \right)^{-1} \right| , \tag{40}$$

for the mean of an explanatory variable for all observations, $\bar{X}_i$. With the T-distribution, an additional p-value can be computed to check if a term is significant above a threshold level, usually chosen as $\alpha = 0.05$. Another measure to evaluate the significance of an explanatory variable is the permutation importance introduced by Breiman [65]. It requires a score to evaluate the quality of a model, which is here chosen asthe coefficient of determination R^2. For each considered variable, the regression is performed five times, with the values of the variable being shuffled each time over the observations, thereby destroying the correlation between feature and dependent variable. The mean R^2 across this runs is subtracted from the one obtained with not-permuted data, yielding the permutation importance PI.

Finally, the observations are evaluated regarding the regression performed to identify outliers. The first approach is to standardize the residuals: observations yielding an absolute value above three are considered to be outliers. In the following, Cook's distance

$$d_{\text{Cook}} = \frac{\sum_{j=1}^{n} (\hat{Y}_j - \hat{Y}_{j(l)})}{(n-k-1)^{-1} \sum_{j=1}^{n} r_j} , \quad l \in \{1, \dots, n\} , \tag{41}$$

is computed to evaluate the influence of an observation on the model. Here, $\hat{Y}_{j(l)}$ is the approximation of the dependent variable by a model unaware of the l-th observation. For this measure, a value above 0.5 marks an influential point, while values above 1 indicate an outlier.

4. Numerical Experiments

In this section, some preparatory calculations regarding the starting conditions are presented, as well as the simulation setup for the investigation of settling particles. For the latter, some preliminary studies validating the setup are discussed.

4.1. Preparation

Depending on the Reynolds number, the initial conditions, i.e., the orientation of the particle, should be checked. For low Re, objects tend to keep their angle; for intermediate Re, axis-symmetric particles rotate such that the maximum projected area is normal to the flow or settling direction. Using the equivalent spherical diameter for the Reynolds number and utilising the drag correlation by Schiller and Naumann [16], it can be estimated that $\text{Re} = 15.41$ with $\nu = 10^{-6}\,\text{m}^2\,\text{s}^{-1}$. The later-observed terminal settling velocities lead to Reynolds numbers between $\text{Re} = 9.64$ and $\text{Re} = 22.86$. As this is in the intermediate regime, the angle for which the projection in settling direction yields the maximum surface is calculated.

For these calculations, a voxel representation of the superellipsoid is used and the projected surface is calculated. To find the maximum, the particle is rotated in 1° steps around the x-axis and y-axis. Since superellipsoids are rotational symmetric, in this case, around the z-axis, this suffices. This additional information is required to ensure that all objects have the same starting conditions, especially for the investigation of the initial phase of the particle leveling out at its equilibrium position.

4.2. Simulation Setup

For the investigation of single particle settling, the superellipsoids are placed in a domain with 0.007 m width and depth and a height of 0.0175 m, as depicted in Figure 2. The center of mass of the object is initially located in the middle of the domain, $2a_{\max}$ from the top. The latter corresponds to the maximum half-axis length across all particles $a_{\max} = 4.777 \times 10^{-4}$ m. For the fluid $\rho_f = 998\,\mathrm{kg\,m^{-3}}$ and $\nu = 10^{-6}\,\mathrm{m^2\,s^{-1}}$ is chosen, while the gravitational acceleration is given as $g = 9.81\,\mathrm{m\,s^{-2}}$.

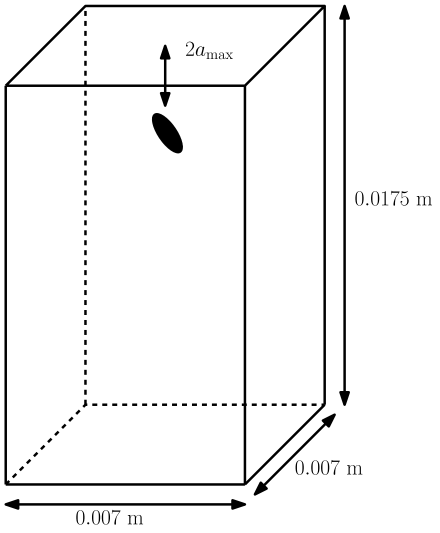

Figure 2. Initial configuration of the simulation.

The discretization is chosen such that the volume-equivalent sphere diameter is resolved by 20 cells; this represents a grid spacing of $\delta x = 1.584\,84 \times 10^{-5}$ m. The resulting domain thereby consists of 215,877,220 cells. Since it was found by Trunk et al. [34] that the maximum occurring lattice velocity should not exceed 0.04, the temporal discretization is chosen such that the maximum velocity of a volume-equivalent sphere according to Schiller and Naumann [16] equals a lattice velocity of 0.02, leading to $\delta t = 6.519\,15 \times 10^{-6}$ s. This proved to be sufficient as, in the later-performed simulation, the lattice velocity did not exceed $u^{\mathrm{L}}_{\max} = 0.0319$. Furthermore, the chosen parameters yield a lattice relaxation time of $\tau = 0.5779$ for the simulations. The top and bottom of the domain are equipped with a no-slip bounce-back boundary condition, while the sides are periodic for the fluid as well as the particle.

To observe how a particle equilibrates to its final orientation from a given initial orientation, equal starting conditions have to be ensured for comparability. Therefore, each superellipsoid is placed in the domain rotated by 45° from its assumed final orientation (according to Section 4.1) regarding the x-axis and y-axis. The rotation is performed around axes through the geometric center of the object, as the density distribution is assumed to be homogeneous. Each simulation runs until the center of the considered superellipsoid is $1.1a_{\max}$ above the ground.

4.3. Validation

While the method itself has been extensively validated by Trunk et al. [34], this subsection deals with the validation of the chosen setup, i.e., the chosen domain size and resolution of the computational grid.

As previously found by Rahmani and Wachs [55], grid convergence can be complicated in DNS simulations of settling particles. Some turbulent effects are influenced by the resolution, and slight deviations in the shape can lead to a different settling path.

Grid convergence can be complicated in DNS simulations of settling particles with complex shapes. Slight deviations in the representation of the object's shape in the simulation, depending on the resolution, might lead to deviations in some of the tracked parameters, such as the path or the angle.

In this way, convergence might not be observed in a quantitative way, comparing two paths, but rather a qualitative way. While the amplitude and exact positions of maxima and minima, e.g., in settling velocity, may vary, other aspects, such as the frequency of oscillation and settling regime, can be compared, as described in [55]. To achieve high-quality results, the resolution should be high enough to depict all relevant features, while also being as low as possible to allow for a large domain and, therefore, a long settling path. To find the lowest required resolution, the particle with ID 96 is selected for resolution tests, since it has the smallest half-axis (9.1×10^{-5} m). For the tests, the setup described in Section 4.2 is used and the number of cells N per equivalent sphere diameter is varied. The voxel representation of the particle for $N = 20$ is depicted in Figure 3.

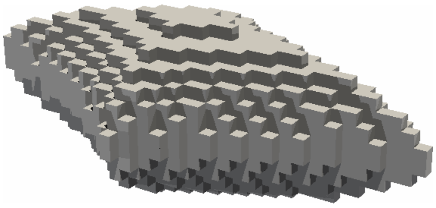

Figure 3. Voxel representation of the particle with the shortest half-axis length of 9.1×10^{-5} m for $N = 20$.

While the lowest tested resolution of $N = 8$ yields a terminal settling velocity of $0.049\,\mathrm{m\,s^{-1}}$, all other resolutions lead to a velocity of $0.047\,\mathrm{m\,s^{-1}}$, with a deviation of less than 1%. Therefore, a resolution of at least $N = 12$ is required to correctly depict the terminal settling velocity. The results regarding the settling velocity are depicted in Figure 4. The fluctuations in the angle around the y-axis depicted in Figure 5 are below 10° and seem to oscillate around $\theta^y = 0°$. The differences in deflection in the y-direction were of size $0.05 d_{\mathrm{eq}}$, and therefore small. To ensure a sufficiently high resolution, $N = 20$ is chosen for all further simulations.

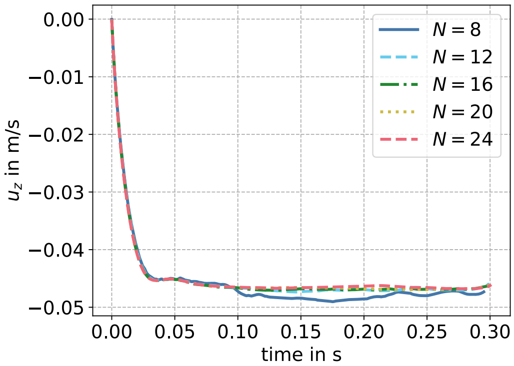

Figure 4. Coordinates of the center of mass of the particle, projected on a plane normal to the settling direction. Results printed for different grid spacings, for the particle with the shortest half-axis.

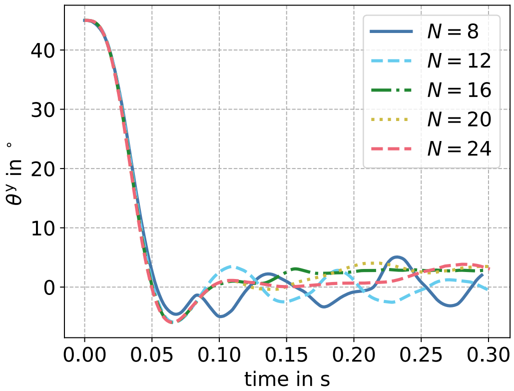

Figure 5. Plot of the angle for rotation around the y-axis over time during the settling. Results printed for different grid spacings, for the particle with the shortest half-axis.

To study the influence of the domain size on the particle settling, the setup described in Section 4.2 was used, now with the particle (ID 138) with the longest half-axis of 4.78×10^{-4} m. The size of the domain in the directions normal to the settling direction was varied between 0.003 m and 0.011 m. Here, the influence on the terminal settling velocity was completely negligible, as, for all cases, the deviation from the average of $0.035\,\mathrm{m\,s^{-1}}$ was below 1%. The differences regarding the path were also quite low, as depicted in Figures 6 and 7. Since the settling regime, e.g., described by Horowitz and Williamson [66] for spheres, is significantly influenced by perturbations, as described by Bagheri et al. [12], the chosen domain should still not be the smallest one possible, to allow for settling paths with more deflection from the midst. To ensure a domain large enough for particles with an oblique settling path to sediment without perturbation via the periodic boundary, the domain size was chosen as 0.007 m in all further computations.

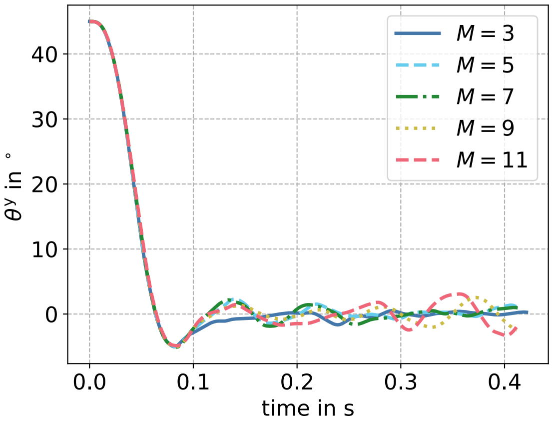

Figure 6. Plot of the angle for rotation around the y-axis over time during the settling. Results printed for different grid spacings, for the particle with the longest half-axis.

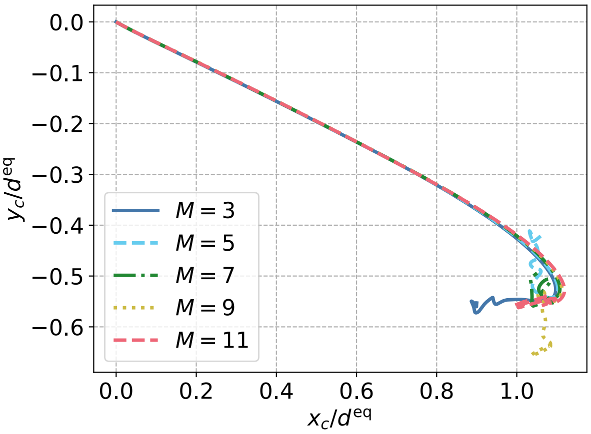

Figure 7. Coordinates of the center of mass of the particle projected, on a plane normal to the settling direction. Results printed for different grid spacings, for the particle with the longest half-axis.

5. Results and Discussion

The results are presented in two sections. First, in Section 5.1, an overview of the data processing and performance of a shape classification is given. Furthermore, a first impression of the dependency of the drag coefficient on the shape parameters is given. Then, in Section 5.2, two regression analyses are presented, one regarding the drag coefficient and one regarding the terminal settling velocity.

5.1. Examination of Simulation Data

In this section, the processing of the simulation data is described, e.g., the calculation of relevant parameters like the terminal settling velocity in Section 5.1.1. Furthermore, the particle shape is classified and the influence of some shape parameters is investigated. Finally, in Section 5.1.3, some exceptions, like particles which did not reach a stable terminal settling velocity, are analysed.

5.1.1. Data Processing

Each of the 200 particles was tracked during the simulations described in Section 4.2. The terminal settling velocity was calculated by averaging the velocity in a settling direction between 0.15 s and 0.23 s, as, during this time, all particles have reached a stable velocity and the influence of the bottom wall was not noticeable. An exception were 11 particles (with IDs 60–64, 80, 96 and 100–103), which did not reach a stable velocity, as still a slow but continuous increase in velocity was observed up to the bottom of the domain, where the influences of the bottom wall were also noticeable. These shapes need to be investigated in a domain allowing for a longer settling path. For all others, the maximum deviation to the calculated average in the given time interval was below 1.35%. The range of terminal settling velocities observed across all simulations spans from $0.030\,\mathrm{m\,s^{-1}}$ to $0.072\,\mathrm{m\,s^{-1}}$, leading to Reynolds numbers between $\mathrm{Re} = 9.64$ and $\mathrm{Re} = 22.86$.

Similar to the terminal settling velocity, the force was calculated by averaging over the same time interval, to calculate the drag coefficient via Equation (4). Using the drag correlation by Schiller and Naumann [16] for a volume-equivalent sphere, a drag correction factor can be calculated, which was found to be between 0.92 and 2.32 for the particles considered in this work.

Regarding the orientation of the particles, the angle around each of the three rotation axes was considered separately for the last 30% of the settling duration. The orientation was considered to be stable if, for each angle, the deviation from the average over the given time interval did not exceed two degrees and the angle did not increase or decrease monotonically over time. The latter was considered to be the case if the time derivative was positive or negative for more than 95% of the time steps in the considered interval. By this reasoning, 25 particles were found to be not stable in orientation, i.e., the ones with IDs 12, 29, 30–32, 48–50, 60–64, 70, 79, 84, 100–103, 175, 185, 186, 199 and 200. For all other particles, the final angles were calculated by averaging over the given time interval. This allows for the calculation of the crosswise sphericity, as described in Section 2.4.

5.1.2. Shape Classes and Influence of Shape Parameters

Investigating the particle behavior regarding the shape parameter, the influence of elongation and flatness is clearly visible, as depicted in Figure 8. Bagheri and Bonadea [12] found a similar dependency for the Stokes and Newton regime.

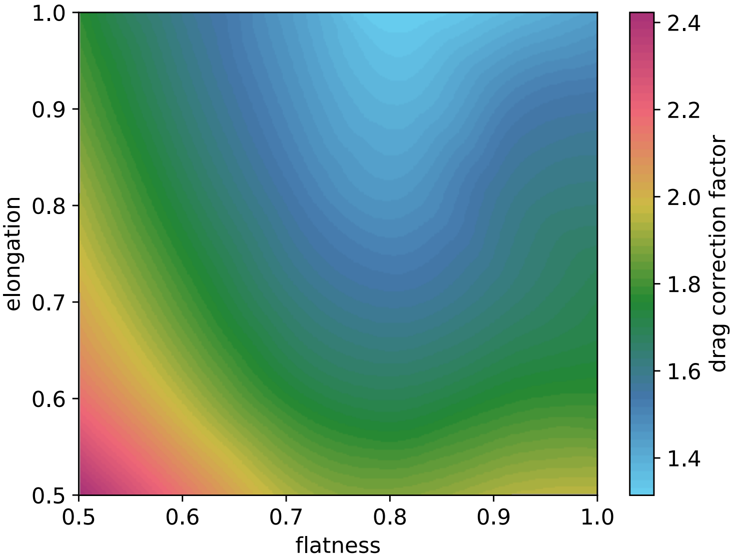

Figure 8. Dependency of the drag correction factor on elongation and flatness.

In most works regarding the drag correlation of non-spherical particles, the particles were labeled by different shape classes, e.g., discs. Since, in this work, the particles were generated from shape parameters, they were not selected according to such a class; however, as applied by Szabó and Domokos [67], different classification systems exist. Those usually depend on the main axis lengths. Zingg [5] proposed 4 classes, namely, discs (27), spheres (109), blades (40) and rods (24). The frequencies of the considered dataset in this investigation are given in parentheses, according to the classification. Another approach was given by Sneed and Folk [6]. They suggested ten shape classes, given as compact (82), compactly platy (21), compactly bladed (4), compactly elongated (14), platy (0), bladed (33), elongated (31), very platy (0), very bladed (5) and very elongated (10). The classification results are also visualised in Figures 9 and 10.

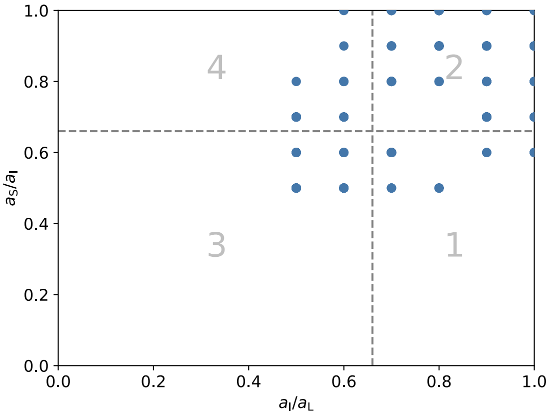

Figure 9. The particles considered in this study are plotted for a shape classification according to Zingg [5]. The four shape classes are 1: discs, 2: spheres, 3: blades and 4: rods.

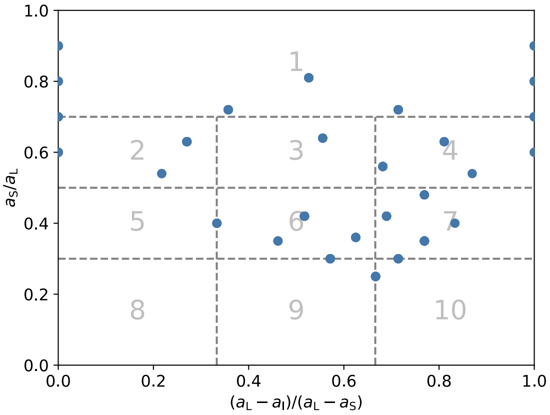

Figure 10. The particles considered in this study are plotted for a shape classification according to Sneed and Folk [6]. They are also classified regarding the compactness, leading to the ten shape classes 1: compact, 2: compactly platy, 3: compactly bladed, 4: compactly elongated, 5: platy, 6: bladed, 7: elongated, 8: very platy, 9: very bladed and 10: very elongated.

Plotting the drag coefficient against the Reynolds number, as depicted in Figure 11, revealed that a differentiation by shape classes, i.e., regarding coefficients defined via the main axes lengths, is sensible. Rods have a significantly higher drag coefficient than spherical particles. Bagheri and Bonadonna [12], therefore, found a good description of the drag coefficient, relying only on the main axes lengths for elongation and flatness and the density ratio, discarding the sphericity. Here, in Figure 11, however, a spread is observable, e.g., for spheres and discs. Further dividing the shape classes into particles with a sphericity higher than 0.8 and the ones below hints that this parameter is able to describe this spread. Therefore, an improved model should rely on both the main axes lengths and the sphericity to cover more aspects of single particle settling.

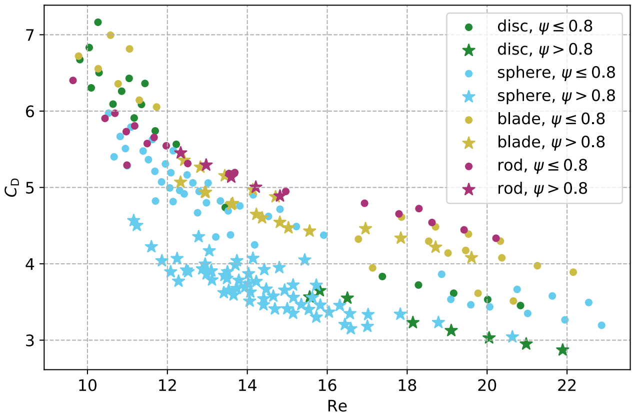

Figure 11. The drag coefficient plotted against the Reynolds number, color with shape classification according to Zingg [5]. A spread is revealed, describable via the sphericity (marker style).

It was furthermore observed that the particles with the 15 highest drag correction factors are labeled as bladed according to Sneed and Folk [6].

5.1.3. Analysis of Exceptions

The particles not reaching a terminal velocity during the simulations were studied separately. Therefore, a logistic regression was applied with a L2-regularisation for a feature space consisting of the shape parameters given in Section 2.2 and the parameters for the construction of the superellipsoids given in Section 2.3 up to the power of three. For the regression, three of the parameters and their powers were considered at a time, with a combination of ξ_2, flatness and convexity yielding the best result of a classification accuracy of 98.5%, i.e., three false negatives. In fact, inspecting the data of the particles not reaching the terminal settling velocity, all have a comparably low flatness of 0.5 or 0.6 and $\xi_2 = 8$ for all of them.

The same analysis was performed for particles which did not reach a stable orientation. However, the highest achieved classification accuracy was 90%, which is insufficient in this context, as 20 particles were still falsely classified, of a total of 25 particles with no stable orientation. The main influencing parameters at this point seem to be ξ_2 and the elongation, as they were part of every model yielding this classification accuracy.

5.2. Regression Analysis

This section covers the regression analyses of the computed data in more depth, e.g., regarding the drag coefficient or the terminal settling velocity. The latter is of interest for a direct correlation, as already mentioned by Haider and Levenspiel [28], since the interdependence between drag coefficient and Reynolds number in the usually presented correlations requires the application of iterative methods for a priori estimations. For the analyses presented here, the additional dataset in Appendix B served as test data for validation of the computed correlations. With the 200 datapoints used for training, the available data were split 18% to 82% into test and training data.

5.2.1. Polynomial Regression Regarding the Drag Coefficient

To evaluate which features might be relevant before the analysis, two approaches were applied. The first one was performing an F-test [62] for a linear regression considering only one independent variable at a time. Since it is a linear regression, predominantly linear relations are detected. The second approach was to calculate the mutual information between two variables [64], which is a measure usually applied in information theory. It is zero only when the variables are strictly independent, and is better in the detection of non-linear dependencies. Both scores were normalized and are depicted for the considered independent variables in Table 3.

Table 3. Normalized results of a F-test and the mutual information for feature selection regarding the drag coefficient.

	a_L	a_I	a_S	ρ_p	E	F	κ_{con}	ψ	$\psi_\perp$	κ_{rnd}	λ_{CSF}	λ_H	λ_{LR}	Re
F_{sample}	1.0	0.33	0.03	0.01	0.12	0.03	0.23	0.18	0.46	0.45	0.07	0.08	0.09	0.36
MI	0.92	0.73	0.65	0.01	0.37	0.12	0.71	0.55	0.74	0.83	0.3	0.51	0.47	1.0

The low F-value, in combination with high *MI*, e.g., for the Reynolds number, suggests the existence of non-linear dependencies for the drag coefficient. Therefore, at least a polynomial regression is required. As already shown in the literature (see Section 2.4), the crosswise sphericity has a higher impact than the normal sphericity. For the actual feature selection, the results depicted in Table 2 have to be taken into account, to minimise effects due to multicollinearity. While this phenomenon does not necessarily harm the reliability of the calculated model, it impacts the numerical stability of the method applied to find the regression coefficients and complicates the evaluation of the significance of a single regression parameter. Therefore, the main axis lengths were not selected for regression, as they are strongly correlated with almost all parameters. Due to the high *MI* score, the Reynolds number was chosen as a parameter for the polynomial regression, together with one parameter from each cluster identified in Table 2. These were the roundness, the elongation and the Hofmann shape entropy, as they yielded the highest F-values and *MI* scores. While the last two parameters showed a correlation, both were selected to capture all effects due to aspect ratio. The impact of this correlation will be monitored in the following.

Due to the non-linear dependencies, second-order polynomials were considered for the regression, including interaction terms. The degree was not further increased, since, for a polynomial of third order, the error in the test data started to increase, indicating overfitting. As the higher-order terms introduced structured multicollinearity, the data were standardized, i.e., mean-centered and divided by the standard deviation. Finally, the regression coefficients were computed, applying a least squares approach with $L2$-regularisation.

For the resulting model, the variance inflation factor was computed as a measure of multicollinearity; the results are depicted in Table 4. Dropping all terms with a *VIF* above 10 leads to

$$\begin{aligned} C_D = &-0.386E - 0.496\kappa_{\text{rnd}} - 0.575\text{Re} + 0.097E\kappa_{\text{rnd}} - 0.322E\text{Re} + 0.0497\kappa_{\text{rnd}}^2 \\ &- 0.128\kappa_{\text{rnd}}\lambda_H + 0.106\kappa_{\text{rnd}}\text{Re} - 0.296\lambda_H\text{Re} + 0.161\text{Re}^2 , \end{aligned} \tag{42}$$

for standardized dependent and independent variables. To apply this model, the data need to be scaled according to the mean values and standard deviations given in the Appendix A. The adjusted coefficient of determination of the found model is $R_a^2 = 0.96$, implying that most of the relevant effects have been captured. Further data of the model performance are depicted in Table 5. Dropping terms with a high *VIF* affected the mean deviation from the simulation data by less than 0.3%.

Table 4. Variance inflation factor for the considered regression variables.

parameter	1	E	κ_{rnd}	λ_H	Re	E^2	$E\kappa_{rnd}$	$E\lambda_H$
VIF	10.15	6.43	6.30	11.49	4.51	12.94	2.62	45.61
parameter	ERe	κ_{rnd}^2	$\kappa_{rnd}\lambda_H$	κ_{rnd}Re	λ_H^2	λ_HRe	Re^2	
VIF	7.90	2.37	5.71	2.72	20.65	8.05	2.84	

Table 5. Performance of the model obtained by polynomial regression on the training and test data, along with errors of models from literature on the training data.

	Error in %		RMSE
	Mean	**Max**	
this work (training data)	2.84	17.46	0.18
this work (test data)	2.65	7.26	0.19
Haider and Levenspiel [28]	17.50	40.13	0.85
Ganser [21]	86.26	98.65	4.05
Leith [20]	84.47	98.64	3.97
Loth [22]	89.33	98.72	4.20
Hölzer and Sommerfeld [23]	23.65	39.16	1.30
Bagheri and Bonadonna [52]	17.70	35.07	0.88
Dioguardi and Mele [26]	26.97	69.03	1.43

Since the models by Leith [20] and Loth [22] focused on the Stokes regime and were used in combination with the formula by Ganser [21], these three approaches had very similar performances. The correlations found by Haider and Levenspiel [28], Hölzer and Sommerfeld [23] and Bagheri and Bonadonna [52] performed far better on the current dataset, with the last one yielding the best results regarding all error measures. The correlation by Dioguardi and Mele [26] performed only slightly worse, despite being based towards a specific dataset for pumice particles. The deviations of the models from the dataset obtained by simulations in this work are similar to the ones reported by Bagheri and Bonadonna [12], who also compared various models regarding data compiled from the literature, analytical expressions and own experiments. This further validates the simulation results. While this investigation considers far more shape parameters, which improves the results, it has to be noted that the small range of Reynolds numbers covered in this investigation might lead to a result that better fits the considered range. Therefore, this model might outperform approaches intended for a larger range of Reynolds numbers due to its higher specialization.

For further investigation of the model's quality, the error was investigated in a QQ-plot [68,69] in Figure 12, depicting the standardized residuals $r = C_{\mathrm{D,sim}} - C_{\mathrm{D,fitted}}$ plotted against the quantiles of a normal distribution. Since the points closely follow the angle bisecting line, the errors can be assumed to be normally distributed, meaning that the relevant effects are captured by the model. In addition, a Tukey–Anscombe plot [70] is printed in Figure 13 for further analysis. As no clear structure is visible for the depicted datapoints, except a slight aggregation on the left side, this supports the assumption that most of the relevant effects were captured by the model. The points are colored by shape classes according to Zingg [5], showing that the existing errors are not related to a specific shape.

The plot is also a first visual approach for an outlier analysis. Points with an absolute standardized residual above three are usually considered to be outliers; this was only the case for particle number 17, with standardized a residual of 7.42. With a value of 2.99, particle 132 can also be considered to be an outlier, while the value was well below 2.4 for all other points. For all particles, the Cook distance [71] was also computed; a point with a value above 0.5 is considered to have a large impact, while values above 1 indicate a model that is not well fitted. The latter is only the case for particle 1, with a value of 1.28. The next highest Cook distances are 0.4 for particle 121 and 0.35 for particle 17. The latter indicates that the single-point influence of the outlier depicted in Figure 13 on the model is limited and might be neglected.

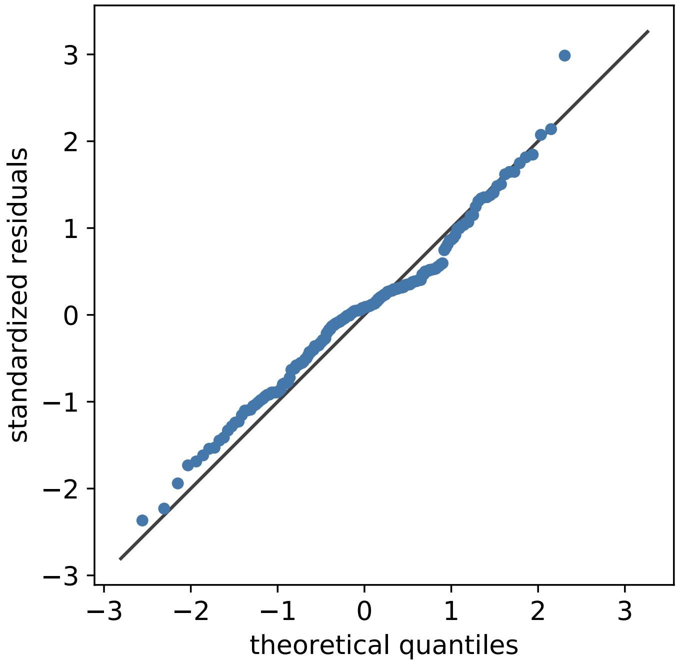

Figure 12. QQ-plot [68,69] of the standardized residuals against the theoretical quantiles of a normal distribution, revealing an approximately normal distributed error.

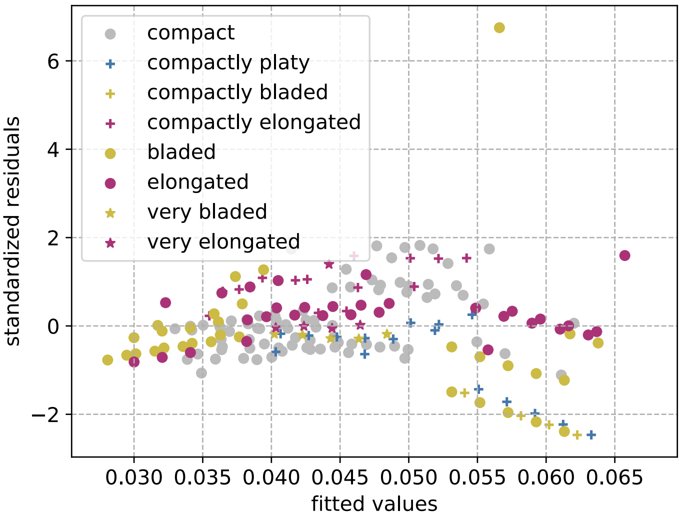

Figure 13. Tukey–Anscombe plot [70] showing the standardized residuals plotted against the fitted values, colored by shape classes according to Zingg [5].

If the regression parameters with a high *VIF* in Table 4 were not dropped, only particle 17 remains, with a high Cook's distance and standardized residual. Inspection of the particle data showed the lowest flatness and sphericity values among all particles, with the combination of both only appearing for particle 17. Since this is the only clear outlier, it indicates that some features of the particle might not be correctly captured during simulations. The particle is also depicted in Figure 1; it is clear that the particle grows thinner the further it gets from its center. Therefore, the most probable source of error is that the resolution was not sufficient to depict the outer regions.

Performing a *t*-test, all regression parameters in the model are relevant on a $\alpha = 0.05$ basis. The resulting t-values are in good accordance with the computed permutation importance *PI*, identifying Re, κ_{rnd}, E and ERe as the most relevant in this order. Except for the lower relative significance of λ_{H}, this is in good accordance with the predictions based on the F-value and *MI* presented in Table 3.

5.2.2. Polynomial Regression Regarding Terminal Settling Velocity

Except for Haider and Levenspiel [28] and Dellino [25], none of the literature considered in this work presented a correlation between shape parameters and terminal settling velocity. Since it would be interesting for a priori estimation of the particle behavior, the dependencies between shape and settling velocity are investigated in this section by regression analysis, similar to Section 5.2.1.

As before, the data and dependent variable were standardized. From the *MI* and F-values in Table 6, it is apparent that the density ratio, roundness and Hofmann shape entropy are the most relevant parameters for regression, considering the correlations found in Table 2. The density ratio is here represented by the particle's density, as the density of the fluid is constant across all simulations. In tests, it was found that adding the sphericity contributes to the quality of the model.

Table 6. Normalized results of a F-test and the mutual information for feature selection regarding the terminal settling velocity.

	ρ_{P}	E	F	κ_{con}	ψ	$\psi_{\perp}$	κ_{rnd}	λ_{CSF}	λ_{H}	λ_{LR}
F_{smaple}	0.76	0.0	0.25	0.06	0.01	0.42	1.0	0.14	0.09	0.07
MI	0.39	0.0	0.0	0.59	0.61	0.52	1.0	0.08	0.29	0.16

Increasing the polynomial degree of the model until the error on the test data increased again yielded a polynomial order of 2 for the regression. Computing the *VIF* for the resulting model showed that the terms $\psi\kappa_{\text{rnd}}$ and κ_{rnd}^2 predominantly introduce multicollinearity, with scores of 25.52 and 12.46, respectively. The elimination of one of these two explanatory variables sufficed; due to the nonlinear dependency on the roundness, the first one was chosen. Further removing the constructed parameter regarding a significance level of $\alpha = 0.05$ leads to the model given in Table 7.

Table 7. Variance inflation factor of the remaining explanatory variables and regression coefficients for the standardized values.

Parameter	ρ_{P}	ψ	κ_{rnd}	λ_{H}	ψ^2	$\psi\lambda_{\text{H}}$	κ_{rnd}^2	$\kappa_{\text{rnd}}\lambda_{\text{H}}$	λ_{H}^2
VIF	1.02	5.23	4.17	4.69	6.83	3.97	3.88	4.30	4.52
coefficient	0.30	−1.23	1.44	−0.45	−0.30	−0.37	−0.34	0.27	0.30

For the remaining model, the *t*-test and permutation importance identified the parameters κ_{rnd}, ψ and κ_{rnd}^2 as the most important. An adjusted coefficient of determination of $R_a^2 = 0.86$ was obtained. The errors on the datasets considered in this work are presented in Table 8, showing good accordance with the simulation data, expect for a single significant outlier in the training data.

Table 8. Performance of the model obtained by polynomial regression on the training and test data, along with errors of the model of Haider and Levenspiel [28] and the one by Dellino [25] on the training data.

	Error in %		**RMSE**
	Mean	**Max**	
this work (training data)	5.50	72.90	0.0037
this work (test data)	4.36	28.52	0.0022
Haider and Levenspiel [28]	57.85	74.22	0.029
Dellino [25]	27.85	53.31	0.016

This artifact was also visible in the QQ-plot [68,69] in Figure 14. Besides a deviation on the left side, the plot shows a predominantly normal distributed error. The Tukey–Anscombe [70] plot (Figure 15), however, indicates that not all effects were captured by the model, as a slightly quadratic behavior of the standardized residuals is recognizable, and a spread on the left hand side is visible. The coloring by the shape classes according to Sneed and Folk [6] suggests a dependency on the ratio of the main axis lengths, as the upper string predominantly consists of elongated particles, while the lower one is composed of compactly platy and (compactly) bladed particles.

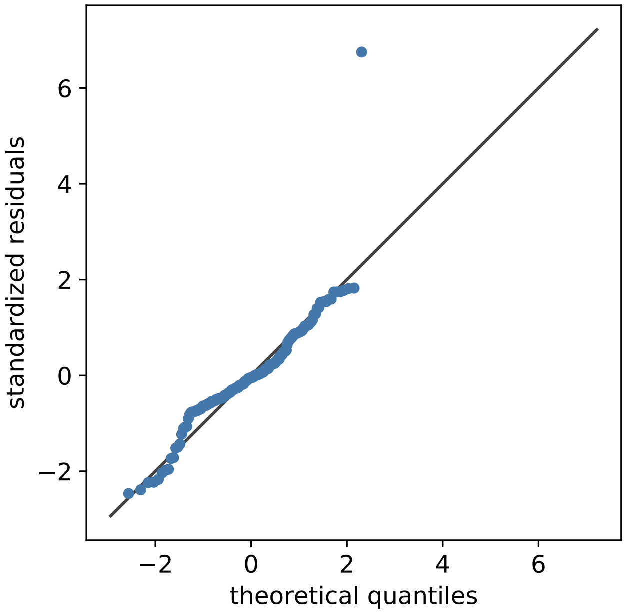

Figure 14. QQ-plot [68,69] of the standardized residuals against the theoretical quantiles of a normal distribution, revealing a predominantly normal distributed error.

The single outlier visible in Figures 14 and 15, with a standardized residual of approximately 6.75, is particle number 17, which has already been discussed in Section 5.2.1. Beside this artifact, no standardized residuals above 2.5 were found. Computing Cook's distance resulted in only two points above 0.25, namely particle 17 with a value of 2.81 and particle 1 with a value of 0.87.

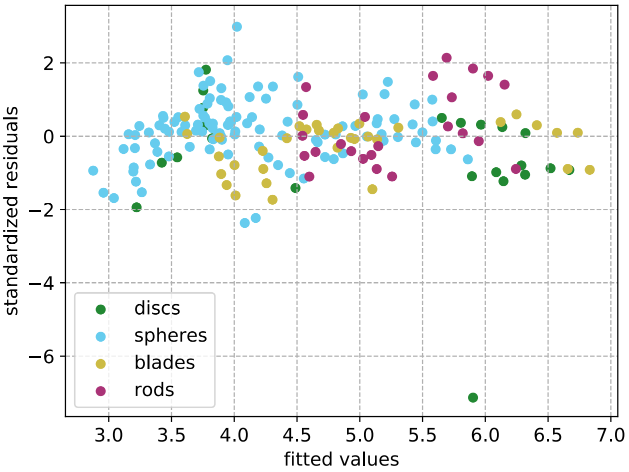

Figure 15. Tukey–Anscombe plot [70] showing the standardized residuals plotted against the fitted values, colored by shape classes according to Sneed and Folk [6].

6. Conclusions

In this work, a constructive way to obtain correlations for the drag coefficient and terminal settling velocity is described, utilizing statistical approaches and measures. It can easily be applied to an enlarged data basis, extending the considered Reynolds numbers. In addition to increasing the number of considered shape parameters, it is also possible to obtain a highly specialized correlation for a considered particle collective. The statistical tools discussed in Section 3.2 allow for a data-driven construction of new models by identifying the most relevant parameters and consideration of interaction terms and also maintaining statistical stability.

By performing a polynomial regression regarding the drag coefficient, also taking interaction terms into account, a model was found which is in good agreement with the data, which is reflected in an adjusted coefficient of determination of $R_a^2 = 0.96$. The mean deviation, considering training and test data, of about 2.75%, is below the uncertainty by the simulation reported by Trunk et al. [34], and outperforms other correlations from the literature on the dataset considered in this study. This might be related to the higher number of considered shape parameters, but also to the higher specialization to the limited range of Reynolds numbers $\mathrm{Re} \in [9.64, 22.86]$. By statistical analysis, the elongation, roundness, Reynolds number and the Hofmann shape entropy were found to be the most relevant.

In addition, a polynomial regression regarding the terminal settling velocity was performed, for which only a few references were found in the literature. The found model yielded an adjusted coefficient of determination of $R_a^2 = 0.86$, relying on the particle density, sphericity, roundness and Hofmann shape entropy as the most relevant parameters. The mean deviation across training and test data was found to be 4.93%, which is approximately a fifth of the other models considered here. An error and outlier analysis also found good agreement between the simulated data and the model.

The considered particle collective was chosen to cover a wide range of equally distributed shape parameters to increase the significance of statistical results. Therefore, superellipsoids were used to describe the particles in numerical simulations. To focus on the influence of shape parameters, the particles are scaled to be equal in volume. Therefore, only a very limited range of Reynolds numbers in the intermediate regime was covered in this investigation. A first inspection showed that particles with a low value in flatness and $\xi_2 = 8$ did not reach their terminal settling velocity in the considered setup. To guarantee that particles reach the terminal settling velocity before reaching the bottom in future works, the domain is to move vertically along with the particle. This would also allow for a shorter domain, compared to the one in this study, thereby reducing the necessary computational effort.

It is, furthermore, possible to extend the described scheme to other setups, considering further effects like Brownian motion or additional external forces, and thereby obtain more specialized correlations.

Author Contributions: Conceptualization, R.T.; Methodology, R.T.; Software, R.T. and M.J.K.; Validation, R.T.; Formal Analysis, R.T. and C.B.; Investigation, R.T.; Resources, M.J.K.; Data Curation, R.T.; Writing—Original Draft Preparation, R.T.; Writing—Review and Editing, R.T. and G.T., M.D. and M.J.K.; Visualization, R.T. and C.B.; Supervision, M.J.K. and H.N.; Project Administration, R.T. and M.J.K.; Funding Acquisition, R.T., M.D. and M.J.K. All authors have read and agreed to the published version of the manuscript.

Funding: This research was funded by the Deutsche Forschungsgemeinschaft (DFG) [grant KR 4259/8-2] within the priority program SPP2045 MehrDimPart "Highly specific and multidimensional fractionation of fine particle systems with technical relevance". The authors also acknowledge support by the Open Access Publishing Fund of the Karlsruhe Institute of Technology (KIT). This work was also supported by grants from the Coordenação de Aperfeiçoamento de Pessoal de Nível Superior (`CAPES`) [`DAAD/CAPES PROBRAL` 88881.198766/2018-01; CAPES-Finance Code 001]-Brazil.

Institutional Review Board Statement: Not applicable.

Informed Consent Statement: Not applicable.

Data Availability Statement: The data presented in this study are available within the article.

Acknowledgments: The authors gratefully acknowledge DUG Technology for providing high-performance computing resources and the Steinbuch Centre for Computing at KIT for providing access to their high performance computing cluster ForHLR II as part of the CPE project.

Conflicts of Interest: The authors declare no conflict of interest.

Abbreviations

The following abbreviations are used in this manuscript:

HLBM	homogenized lattice Boltzmann method
LBM	lattice Boltzmann method
Roman	
a_I	intermediate half-axis
a_L	longest half-axis
a_S	shortest half-axis
A	projected particle surface in direction of motion
A_P	particle surface
C_D	drag coefficient
$C_\mathrm{D,BB}$	drag coefficient according to Bagheri and Bonadonna [52]
$C_\mathrm{D,CG}$	drag coefficient according to Clift and Gauvin [17]
$C_\mathrm{D,DM}$	drag coefficient according to Dioguardi and Mele [26]
$C_\mathrm{D,G}$	drag coefficient according to Ganser [21]
$C_\mathrm{D,HL}$	drag coefficient according to Haider and Levenspiel [28]
$C_\mathrm{D,HS}$	drag coefficient according to Hölzer and Sommerfeld [23]
$C_\mathrm{D,S}$	drag coefficient according to Stokes [15]
$C_\mathrm{D,SN}$	drag coefficient according to Schiller and Naumann [16]
d_Cook	Cook's distance [71]
d_eq	diameter of a volume equivalent sphere

E	elongation
$\boldsymbol{F}_\mathrm{f}$	force acting on the fluid
$\boldsymbol{F}_\mathrm{p}$	force acting on the particle
$\boldsymbol{F}^\mathrm{BG}$	combined buoyancy and gravitational force
$\boldsymbol{F}^\mathrm{D}$	drag force
$\boldsymbol{F}^\mathrm{H}$	hydrodynamic force
F	flatness
F_sample	score of an F-test
g	gravitational acceleration
$\boldsymbol{J}_\mathrm{p}$	moment of inertia
K_N	drag correction factor for the Newton regime
K_S	drag correction factor for the Stokes regime
m_p	particle mass
MI	mutual information
N	resolution related parameter (number of cells per d_eq)
p	pressure
PI	permutation importance
r	residual
R^2	coefficient of determination
R_a^2	adjusted coefficient of determination
Re	Reynolds number
t	time
$\boldsymbol{T}_\mathrm{p}$	torque
T_sample	score of a t-test
$\boldsymbol{u}_\mathrm{f}$	fluid velocity
$u^\mathrm{L}_\mathrm{max}$	maximum lattice velocity in a simulation
u_ts	terminal settling velocity
$u_\mathrm{ts,D}$	terminal settling velocity according to Dellino [25]
$u_\mathrm{ts,HL}$	terminal settling velocity according to Haider and Levenspiel [28]
$u_\mathrm{ts,S}$	terminal settling velocity according to Stokes [15]
$\boldsymbol{u}_\mathrm{p}$	particle velocity
V_p	particle volume
VIF	variance inflation factor
Greek	
δt	temporal discretization parameter
δx	spatial discretization parameter
κ_con	convexity
κ_rnd	roundness
λ_CSF	Corey shape factor [18]
λ_H	Hofmann shape entropy [44]
λ_LR	Le Roux shape factor [46]
ν	kinematic viscosity
ξ_1, ξ_2	exponents determining the shape of a superellipsoid
ρ'	ratio of particle to fluid density
ρ_f	fluid density
ρ_p	particle density
τ	lattice relaxation time
ϕ	circularity
ψ	sphericity
$\psi_\perp$	crosswise sphericity
$\psi_\parallel$	lengthwise sphericity
ω_p	particle angular velocity

Appendix A

Table A1. Data of the particles in the training set.

ID	a_L in m	a_I in m	a_S in m	ξ_1	ξ_2	E	F	ρ_p	κ_con	ψ	$\psi_\perp$	κ_rnd	u_ts	Re	C_D
1	1.47×10^{-4}	1.47×10^{-4}	1.03×10^{-4}	8.0	8.0	1.0	0.7	2360	0.99	0.87	0.96	0.18	3.52×10^{-2}	11.16	4.57
2	2.17×10^{-4}	1.52×10^{-4}	1.21×10^{-4}	2.0	2.0	0.7	0.8	2360	0.95	0.88	0.77	0.15	3.54×10^{-2}	11.23	4.5
3	1.83×10^{-4}	1.65×10^{-4}	1.32×10^{-4}	2.0	2.0	0.9	0.8	2560	0.96	0.91	0.83	0.15	4.10×10^{-2}	12.98	3.87
4	2.08×10^{-4}	1.46×10^{-4}	1.31×10^{-4}	2.0	2.0	0.7	0.9	2660	0.95	0.9	0.83	0.15	4.24×10^{-2}	13.43	3.85
5	2.08×10^{-4}	1.46×10^{-4}	1.31×10^{-4}	2.0	2.0	0.7	0.9	2760	0.95	0.9	0.83	0.15	4.43×10^{-2}	14.03	3.74
6	1.90×10^{-4}	1.52×10^{-4}	1.37×10^{-4}	2.0	2.0	0.8	0.9	2460	0.95	0.9	0.86	0.15	3.94×10^{-2}	12.48	3.92
7	1.90×10^{-4}	1.52×10^{-4}	1.37×10^{-4}	2.0	2.0	0.8	0.9	2560	0.95	0.9	0.86	0.15	4.14×10^{-2}	13.12	3.79
8	1.90×10^{-4}	1.52×10^{-4}	1.37×10^{-4}	2.0	2.0	0.8	0.9	2660	0.95	0.9	0.86	0.15	4.33×10^{-2}	13.74	3.68
9	2.01×10^{-4}	1.41×10^{-4}	1.41×10^{-4}	2.0	2.0	0.7	1.0	2360	0.95	0.9	0.89	0.15	3.74×10^{-2}	11.86	4.04
10	2.01×10^{-4}	1.41×10^{-4}	1.41×10^{-4}	2.0	2.0	0.7	1.0	2460	0.95	0.9	0.89	0.15	3.95×10^{-2}	12.52	3.9
11	2.01×10^{-4}	1.41×10^{-4}	1.41×10^{-4}	2.0	2.0	0.7	1.0	2760	0.95	0.9	0.89	0.15	4.55×10^{-2}	14.41	3.54
12	1.84×10^{-4}	1.47×10^{-4}	1.47×10^{-4}	2.0	2.0	0.8	1.0	2360	0.96	0.91	0.93	0.15	3.81×10^{-2}	12.08	3.89
13	1.84×10^{-4}	1.47×10^{-4}	1.47×10^{-4}	2.0	2.0	0.8	1.0	2560	0.96	0.91	0.93	0.15	4.23×10^{-2}	13.41	3.62
14	1.84×10^{-4}	1.47×10^{-4}	1.47×10^{-4}	2.0	2.0	0.8	1.0	2660	0.96	0.91	0.93	0.15	4.44×10^{-2}	14.06	3.51
15	1.84×10^{-4}	1.47×10^{-4}	1.47×10^{-4}	2.0	2.0	0.8	1.0	2760	0.96	0.91	0.93	0.15	4.63×10^{-2}	14.69	3.41
16	1.70×10^{-4}	1.53×10^{-4}	1.53×10^{-4}	2.0	2.0	0.9	1.0	2360	0.95	0.92	0.96	0.15	3.87×10^{-2}	12.28	3.77
17	2.92×10^{-4}	2.34×10^{-4}	1.17×10^{-4}	2.0	1.0	0.8	0.5	2760	0.91	0.65	0.39	0.09	3.24×10^{-2}	10.26	7.16
18	2.18×10^{-4}	2.18×10^{-4}	1.31×10^{-4}	1.0	2.0	1.0	0.6	2760	0.97	0.87	0.84	0.13	4.91×10^{-2}	15.56	3.57
19	2.23×10^{-4}	2.00×10^{-4}	1.40×10^{-4}	1.0	2.0	0.9	0.7	2360	0.94	0.87	0.88	0.13	4.13×10^{-2}	13.09	3.91
20	2.23×10^{-4}	2.00×10^{-4}	1.40×10^{-4}	1.0	2.0	0.9	0.7	2460	0.94	0.87	0.88	0.13	4.35×10^{-2}	13.79	3.78
21	2.23×10^{-4}	2.00×10^{-4}	1.40×10^{-4}	1.0	2.0	0.9	0.7	2560	0.94	0.87	0.88	0.13	4.57×10^{-2}	14.47	3.67
22	2.23×10^{-4}	2.00×10^{-4}	1.40×10^{-4}	1.0	2.0	0.9	0.7	2660	0.94	0.87	0.89	0.13	4.78×10^{-2}	15.15	3.56
23	2.23×10^{-4}	2.00×10^{-4}	1.40×10^{-4}	1.0	2.0	0.9	0.7	2760	0.94	0.87	0.89	0.13	4.99×10^{-2}	15.83	3.46
24	2.07×10^{-4}	2.07×10^{-4}	1.45×10^{-4}	1.0	2.0	1.0	0.7	2460	0.96	0.88	0.9	0.13	4.40×10^{-2}	13.95	3.7
25	2.07×10^{-4}	2.07×10^{-4}	1.45×10^{-4}	1.0	2.0	1.0	0.7	2560	0.96	0.88	0.9	0.13	4.62×10^{-2}	14.65	3.58
26	2.07×10^{-4}	2.07×10^{-4}	1.45×10^{-4}	1.0	2.0	1.0	0.7	2660	0.96	0.88	0.9	0.13	4.84×10^{-2}	15.35	3.47
27	2.07×10^{-4}	2.07×10^{-4}	1.45×10^{-4}	1.0	2.0	1.0	0.7	2760	0.96	0.88	0.9	0.13	5.06×10^{-2}	16.04	3.37
28	2.13×10^{-4}	1.92×10^{-4}	1.53×10^{-4}	1.0	2.0	0.9	0.8	2460	0.94	0.87	0.85	0.13	4.44×10^{-2}	14.07	3.63
29	1.98×10^{-4}	1.98×10^{-4}	1.59×10^{-4}	1.0	2.0	1.0	0.8	2360	0.97	0.88	1.03	0.13	4.31×10^{-2}	13.66	3.59
30	1.98×10^{-4}	1.98×10^{-4}	1.59×10^{-4}	1.0	2.0	1.0	0.8	2460	0.97	0.88	1.03	0.13	4.54×10^{-2}	14.4	3.46
31	1.98×10^{-4}	1.98×10^{-4}	1.59×10^{-4}	1.0	2.0	1.0	0.8	2560	0.97	0.88	1.03	0.13	4.78×10^{-2}	15.14	3.35
32	1.98×10^{-4}	1.98×10^{-4}	1.59×10^{-4}	1.0	2.0	1.0	0.8	2760	0.97	0.88	1.03	0.13	5.23×10^{-2}	16.59	3.15
33	2.05×10^{-4}	1.84×10^{-4}	1.66×10^{-4}	1.0	2.0	0.9	0.9	2360	0.94	0.87	0.74	0.12	4.13×10^{-2}	13.1	3.91
34	1.91×10^{-4}	1.91×10^{-4}	1.72×10^{-4}	1.0	2.0	1.0	0.9	2360	0.97	0.89	1.06	0.13	4.27×10^{-2}	13.54	3.65
35	1.91×10^{-4}	1.91×10^{-4}	1.72×10^{-4}	1.0	2.0	1.0	0.9	2560	0.97	0.89	1.06	0.13	4.73×10^{-2}	15.0	3.41
36	1.91×10^{-4}	1.91×10^{-4}	1.72×10^{-4}	1.0	2.0	1.0	0.9	2660	0.97	0.89	1.06	0.13	4.96×10^{-2}	15.73	3.3
37	1.91×10^{-4}	1.91×10^{-4}	1.72×10^{-4}	1.0	2.0	1.0	0.9	2760	0.97	0.89	1.06	0.13	5.19×10^{-2}	16.44	3.2
38	1.98×10^{-4}	1.78×10^{-4}	1.78×10^{-4}	1.0	2.0	0.9	1.0	2360	0.95	0.87	0.73	0.12	4.08×10^{-2}	12.95	4.0
39	2.32×10^{-4}	2.32×10^{-4}	2.32×10^{-4}	1.0	1.0	1.0	1.0	2360	1.0	0.89	0.87	0.1	3.66×10^{-2}	11.6	4.22
40	2.32×10^{-4}	2.32×10^{-4}	2.32×10^{-4}	1.0	1.0	1.0	1.0	2460	1.0	0.89	0.87	0.1	3.86×10^{-2}	12.24	4.07
41	2.32×10^{-4}	2.32×10^{-4}	2.32×10^{-4}	1.0	1.0	1.0	1.0	2560	1.0	0.89	0.87	0.1	4.06×10^{-2}	12.87	3.93
42	2.32×10^{-4}	2.32×10^{-4}	2.32×10^{-4}	1.0	1.0	1.0	1.0	2660	1.0	0.89	0.87	0.1	4.26×10^{-2}	13.49	3.81
43	2.31×10^{-4}	2.08×10^{-4}	1.46×10^{-4}	0.9	2.0	0.9	0.7	2760	0.9	0.85	0.92	0.12	5.23×10^{-2}	16.57	3.35
44	2.61×10^{-4}	1.83×10^{-4}	1.46×10^{-4}	0.9	2.0	0.7	0.8	2360	0.89	0.82	0.68	0.11	4.03×10^{-2}	12.78	4.35
45	2.61×10^{-4}	1.83×10^{-4}	1.46×10^{-4}	0.9	2.0	0.7	0.8	2560	0.89	0.82	0.68	0.11	4.46×10^{-2}	14.14	4.07
46	2.61×10^{-4}	1.83×10^{-4}	1.46×10^{-4}	0.9	2.0	0.7	0.8	2660	0.89	0.82	0.68	0.11	4.67×10^{-2}	14.8	3.95
47	2.61×10^{-4}	1.83×10^{-4}	1.46×10^{-4}	0.9	2.0	0.7	0.8	2760	0.89	0.82	0.67	0.11	4.87×10^{-2}	15.44	4.05
48	2.21×10^{-4}	1.99×10^{-4}	1.59×10^{-4}	0.9	2.0	0.9	0.8	2360	0.89	0.85	1.0	0.12	4.26×10^{-2}	13.5	3.9
49	2.21×10^{-4}	1.99×10^{-4}	1.59×10^{-4}	0.9	2.0	0.9	0.8	2460	0.89	0.85	1.0	0.12	4.49×10^{-2}	14.22	3.77
50	2.21×10^{-4}	1.99×10^{-4}	1.59×10^{-4}	0.9	2.0	0.9	0.8	2560	0.89	0.85	1.0	0.12	4.71×10^{-2}	14.93	3.65
51	2.21×10^{-4}	1.99×10^{-4}	1.59×10^{-4}	0.9	2.0	0.9	0.8	2660	0.89	0.85	0.73	0.12	4.93×10^{-2}	15.63	3.56
52	2.21×10^{-4}	1.99×10^{-4}	1.59×10^{-4}	0.9	2.0	0.9	0.8	2760	0.89	0.85	0.73	0.12	5.15×10^{-2}	16.31	3.45
53	2.06×10^{-4}	2.06×10^{-4}	1.65×10^{-4}	0.9	2.0	1.0	0.8	2560	0.89	0.84	1.03	0.12	4.90×10^{-2}	15.54	3.4
54	2.06×10^{-4}	2.06×10^{-4}	1.65×10^{-4}	0.9	2.0	1.0	0.8	2760	0.89	0.84	1.03	0.12	5.36×10^{-2}	17.0	3.18
55	2.30×10^{-4}	1.84×10^{-4}	1.66×10^{-4}	0.9	2.0	0.8	0.9	2360	0.9	0.83	0.67	0.12	4.12×10^{-2}	13.05	4.17
56	2.30×10^{-4}	1.84×10^{-4}	1.66×10^{-4}	0.9	2.0	0.8	0.9	2460	0.9	0.83	0.67	0.12	4.33×10^{-2}	13.74	4.04
57	2.30×10^{-4}	1.84×10^{-4}	1.66×10^{-4}	0.9	2.0	0.8	0.9	2560	0.9	0.83	0.67	0.12	4.55×10^{-2}	14.42	3.92
58	2.30×10^{-4}	1.84×10^{-4}	1.66×10^{-4}	0.9	2.0	0.8	0.9	2760	0.9	0.83	0.68	0.12	4.96×10^{-2}	15.73	3.72
59	2.13×10^{-4}	1.91×10^{-4}	1.72×10^{-4}	0.9	2.0	0.9	0.9	2460	0.9	0.84	0.7	0.12	4.43×10^{-2}	14.03	3.87
60	2.04×10^{-4}	2.04×10^{-4}	1.22×10^{-4}	0.87	8.0	1.0	0.6	2360	0.91	0.81	1.11	0.12	-	-	-

Table A2. Data of the particles in the training set.

ID	a_L in m	a_I in m	a_S in m	ξ_1	ξ_2	E	F	ρ_p	κ_{con}	ψ	$\psi_\perp$	κ_{rnd}	u_{ts}	Re	C_D
61	2.04×10^{-4}	2.04×10^{-4}	1.22×10^{-4}	0.87	8.0	1.0	0.6	2460	0.91	0.81	1.11	0.12	-	-	-
62	2.04×10^{-4}	2.04×10^{-4}	1.22×10^{-4}	0.87	8.0	1.0	0.6	2560	0.91	0.81	1.11	0.12	-	-	-
63	2.04×10^{-4}	2.04×10^{-4}	1.22×10^{-4}	0.87	8.0	1.0	0.6	2660	0.91	0.81	1.11	0.12	-	-	-
64	2.04×10^{-4}	2.04×10^{-4}	1.22×10^{-4}	0.87	8.0	1.0	0.6	2760	0.91	0.81	1.11	0.12	-	-	-
65	1.78×10^{-4}	1.78×10^{-4}	1.60×10^{-4}	0.87	8.0	1.0	0.9	2360	0.93	0.82	0.97	0.13	5.62×10^{-2}	17.83	3.34
66	1.78×10^{-4}	1.78×10^{-4}	1.60×10^{-4}	0.87	8.0	1.0	0.9	2460	0.93	0.82	0.98	0.13	5.93×10^{-2}	18.78	3.23
67	1.78×10^{-4}	1.78×10^{-4}	1.60×10^{-4}	0.87	8.0	1.0	0.9	2660	0.93	0.82	0.99	0.13	6.51×10^{-2}	20.63	3.04
68	2.51×10^{-4}	2.26×10^{-4}	1.36×10^{-4}	0.83	2.0	0.9	0.6	2660	0.84	0.82	0.85	0.11	4.99×10^{-2}	15.81	3.65
69	2.51×10^{-4}	2.26×10^{-4}	1.36×10^{-4}	0.83	2.0	0.9	0.6	2760	0.84	0.82	0.85	0.11	5.21×10^{-2}	16.5	3.55
70	2.38×10^{-4}	2.15×10^{-4}	1.50×10^{-4}	0.83	2.0	0.9	0.7	2760	0.84	0.82	0.95	0.11	5.37×10^{-2}	17.02	3.33
71	2.28×10^{-4}	2.05×10^{-4}	1.64×10^{-4}	0.83	2.0	0.9	0.8	2360	0.84	0.82	0.68	0.11	4.32×10^{-2}	13.7	3.99
72	2.28×10^{-4}	2.05×10^{-4}	1.64×10^{-4}	0.83	2.0	0.9	0.8	2560	0.84	0.82	0.69	0.11	4.78×10^{-2}	15.15	3.72
73	3.94×10^{-4}	2.36×10^{-4}	1.65×10^{-4}	0.83	1.0	0.6	0.7	2360	0.84	0.77	0.57	0.08	3.04×10^{-2}	9.64	6.4
74	3.94×10^{-4}	2.36×10^{-4}	1.65×10^{-4}	0.83	1.0	0.6	0.7	2560	0.84	0.77	0.57	0.08	3.37×10^{-2}	10.69	5.97
75	3.94×10^{-4}	2.36×10^{-4}	1.65×10^{-4}	0.83	1.0	0.6	0.7	2660	0.84	0.77	0.57	0.08	3.53×10^{-2}	11.18	5.81
76	3.94×10^{-4}	2.36×10^{-4}	1.65×10^{-4}	0.83	1.0	0.6	0.7	2760	0.84	0.77	0.57	0.08	3.68×10^{-2}	11.67	5.66
77	3.40×10^{-4}	2.38×10^{-4}	1.90×10^{-4}	0.83	1.0	0.7	0.8	2460	0.84	0.78	0.63	0.08	3.47×10^{-2}	10.99	5.28
78	3.40×10^{-4}	2.38×10^{-4}	1.90×10^{-4}	0.83	1.0	0.7	0.8	2660	0.84	0.78	0.63	0.08	3.80×10^{-2}	12.06	4.99
79	3.62×10^{-4}	2.17×10^{-4}	1.95×10^{-4}	0.83	1.0	0.6	0.9	2460	0.85	0.79	0.67	0.08	3.47×10^{-2}	10.99	5.29
80	3.15×10^{-4}	1.89×10^{-4}	9.45×10^{-5}	0.8	8.0	0.6	0.5	2360	0.84	0.78	0.85	0.12	-	-	-
81	3.15×10^{-4}	1.89×10^{-4}	9.45×10^{-5}	0.8	8.0	0.6	0.5	2660	0.84	0.78	0.87	0.12	6.24×10^{-2}	19.77	3.61
82	3.15×10^{-4}	1.89×10^{-4}	9.45×10^{-5}	0.8	8.0	0.6	0.5	2760	0.84	0.78	0.86	0.12	6.52×10^{-2}	20.66	3.51
83	3.35×10^{-4}	1.67×10^{-4}	1.00×10^{-4}	0.8	8.0	0.5	0.6	2760	0.84	0.78	0.73	0.12	6.00×10^{-2}	19.02	4.14
84	2.67×10^{-4}	1.87×10^{-4}	1.12×10^{-4}	0.8	8.0	0.7	0.6	2360	0.84	0.77	1.02	0.11	5.48×10^{-2}	17.38	3.83
85	2.67×10^{-4}	1.87×10^{-4}	1.12×10^{-4}	0.8	8.0	0.7	0.6	2460	0.84	0.77	0.69	0.11	5.77×10^{-2}	18.28	3.72
86	2.67×10^{-4}	1.87×10^{-4}	1.12×10^{-4}	0.8	8.0	0.7	0.6	2560	0.84	0.77	0.68	0.11	6.05×10^{-2}	19.16	3.61
87	2.67×10^{-4}	1.87×10^{-4}	1.12×10^{-4}	0.8	8.0	0.7	0.6	2660	0.84	0.77	0.68	0.11	6.31×10^{-2}	20.01	3.53
88	2.67×10^{-4}	1.87×10^{-4}	1.12×10^{-4}	0.8	8.0	0.7	0.6	2760	0.84	0.77	0.69	0.11	6.57×10^{-2}	20.84	3.45
89	1.98×10^{-4}	1.78×10^{-4}	1.60×10^{-4}	0.8	8.0	0.9	0.9	2560	0.85	0.77	0.65	0.11	6.18×10^{-2}	19.59	3.46
90	4.02×10^{-4}	2.01×10^{-4}	1.00×10^{-4}	0.8	2.0	0.5	0.5	2460	0.85	0.83	0.68	0.11	3.92×10^{-2}	12.42	5.36
91	3.78×10^{-4}	1.89×10^{-4}	1.13×10^{-4}	0.8	2.0	0.5	0.6	2360	0.84	0.83	0.76	0.11	3.89×10^{-2}	12.33	5.07
92	3.78×10^{-4}	1.89×10^{-4}	1.13×10^{-4}	0.8	2.0	0.5	0.6	2460	0.84	0.83	0.76	0.11	4.08×10^{-2}	12.94	4.94
93	3.78×10^{-4}	1.89×10^{-4}	1.13×10^{-4}	0.8	2.0	0.5	0.6	2560	0.84	0.83	0.76	0.11	4.29×10^{-2}	13.6	4.78
94	3.78×10^{-4}	1.89×10^{-4}	1.13×10^{-4}	0.8	2.0	0.5	0.6	2660	0.84	0.83	0.76	0.11	4.49×10^{-2}	14.23	4.65
95	3.78×10^{-4}	1.89×10^{-4}	1.13×10^{-4}	0.8	2.0	0.5	0.6	2760	0.84	0.83	0.75	0.11	4.67×10^{-2}	14.81	4.54
96	3.63×10^{-4}	1.81×10^{-4}	9.07×10^{-5}	0.77	8.0	0.5	0.5	2360	0.85	0.8	0.85	0.12	-	-	-
97	4.08×10^{-4}	2.45×10^{-4}	1.72×10^{-4}	0.77	1.0	0.6	0.7	2760	0.78	0.77	0.59	0.08	3.78×10^{-2}	11.97	5.55
98	3.39×10^{-4}	2.37×10^{-4}	2.14×10^{-4}	0.77	1.0	0.7	0.9	2360	0.78	0.76	0.59	0.08	3.37×10^{-2}	10.67	5.4
99	3.39×10^{-4}	2.37×10^{-4}	2.14×10^{-4}	0.77	1.0	0.7	0.9	2660	0.78	0.76	0.58	0.08	3.88×10^{-2}	12.31	4.96
100	3.70×10^{-4}	1.85×10^{-4}	9.26×10^{-5}	0.73	8.0	0.5	0.5	2360	0.84	0.8	0.88	0.11	-	-	-
101	3.70×10^{-4}	1.85×10^{-4}	9.26×10^{-5}	0.73	8.0	0.5	0.5	2460	0.84	0.8	0.88	0.11	-	-	-
102	3.70×10^{-4}	1.85×10^{-4}	9.26×10^{-5}	0.73	8.0	0.5	0.5	2560	0.84	0.8	0.88	0.11	-	-	-
103	3.70×10^{-4}	1.85×10^{-4}	9.26×10^{-5}	0.73	8.0	0.5	0.5	2660	0.84	0.8	0.88	0.11	-	-	-
104	2.24×10^{-4}	2.01×10^{-4}	1.41×10^{-4}	0.73	8.0	0.9	0.7	2360	0.78	0.75	0.66	0.11	6.02×10^{-2}	19.09	3.53
105	2.24×10^{-4}	2.01×10^{-4}	1.41×10^{-4}	0.73	8.0	0.9	0.7	2460	0.78	0.75	0.67	0.11	6.33×10^{-2}	20.06	3.44
106	2.24×10^{-4}	2.01×10^{-4}	1.41×10^{-4}	0.73	8.0	0.9	0.7	2560	0.78	0.75	0.68	0.11	6.63×10^{-2}	21.02	3.35
107	2.24×10^{-4}	2.01×10^{-4}	1.41×10^{-4}	0.73	8.0	0.9	0.7	2660	0.78	0.75	0.66	0.11	6.92×10^{-2}	21.95	3.27
108	2.24×10^{-4}	2.01×10^{-4}	1.41×10^{-4}	0.73	8.0	0.9	0.7	2760	0.78	0.75	0.66	0.11	7.21×10^{-2}	22.86	3.19
109	3.70×10^{-4}	2.22×10^{-4}	1.11×10^{-4}	0.73	2.0	0.6	0.5	2360	0.78	0.8	0.73	0.1	4.09×10^{-2}	12.96	4.94
110	3.70×10^{-4}	2.22×10^{-4}	1.11×10^{-4}	0.73	2.0	0.6	0.5	2460	0.78	0.8	0.73	0.1	4.30×10^{-2}	13.63	4.79
111	3.70×10^{-4}	2.22×10^{-4}	1.11×10^{-4}	0.73	2.0	0.6	0.5	2560	0.78	0.8	0.73	0.1	4.53×10^{-2}	14.37	4.6
112	3.70×10^{-4}	2.22×10^{-4}	1.11×10^{-4}	0.73	2.0	0.6	0.5	2660	0.78	0.8	0.73	0.1	4.74×10^{-2}	15.03	4.47
113	3.70×10^{-4}	2.22×10^{-4}	1.11×10^{-4}	0.73	2.0	0.6	0.5	2760	0.78	0.8	0.73	0.1	4.91×10^{-2}	15.56	4.43
114	3.74×10^{-4}	1.87×10^{-4}	1.31×10^{-4}	0.73	2.0	0.5	0.7	2360	0.79	0.8	0.63	0.1	3.89×10^{-2}	12.33	5.45
115	3.74×10^{-4}	1.87×10^{-4}	1.31×10^{-4}	0.73	2.0	0.5	0.7	2460	0.79	0.8	0.63	0.1	4.09×10^{-2}	12.97	5.29
116	3.74×10^{-4}	1.87×10^{-4}	1.31×10^{-4}	0.73	2.0	0.5	0.7	2560	0.79	0.8	0.63	0.1	4.29×10^{-2}	13.6	5.14
117	3.74×10^{-4}	1.87×10^{-4}	1.31×10^{-4}	0.73	2.0	0.5	0.7	2660	0.79	0.8	0.63	0.1	4.48×10^{-2}	14.21	5.0
118	3.74×10^{-4}	1.87×10^{-4}	1.31×10^{-4}	0.73	2.0	0.5	0.7	2760	0.79	0.8	0.63	0.1	4.67×10^{-2}	14.82	4.89
119	3.58×10^{-4}	1.79×10^{-4}	1.43×10^{-4}	0.73	2.0	0.5	0.8	2560	0.79	0.78	0.58	0.1	4.27×10^{-2}	13.54	5.18
120	3.57×10^{-4}	1.78×10^{-4}	1.07×10^{-4}	0.7	8.0	0.5	0.6	2460	0.78	0.76	0.68	0.11	5.63×10^{-2}	17.86	4.61

Table A3. Data of the particles in the training set.

ID	a_L in m	a_I in m	a_S in m	ξ_1	ξ_2	E	F	ρ_p	κ_con	ψ	$\psi_\perp$	κ_rnd	u_ts	Re	C_D
121	3.57×10^{-4}	1.78×10^{-4}	1.07×10^{-4}	0.7	8.0	0.5	0.6	2560	0.78	0.76	0.68	0.11	5.90×10^{-2}	18.71	4.48
122	3.57×10^{-4}	1.78×10^{-4}	1.07×10^{-4}	0.7	8.0	0.5	0.6	2660	0.78	0.76	0.68	0.11	6.16×10^{-2}	19.53	4.39
123	3.57×10^{-4}	1.78×10^{-4}	1.07×10^{-4}	0.7	8.0	0.5	0.6	2760	0.78	0.76	0.68	0.11	6.41×10^{-2}	20.33	4.3
124	3.39×10^{-4}	1.69×10^{-4}	1.19×10^{-4}	0.7	8.0	0.5	0.7	2360	0.79	0.74	0.61	0.1	5.34×10^{-2}	16.93	4.79
125	3.39×10^{-4}	1.69×10^{-4}	1.19×10^{-4}	0.7	8.0	0.5	0.7	2460	0.79	0.74	0.61	0.1	5.61×10^{-2}	17.79	4.65
126	3.39×10^{-4}	1.69×10^{-4}	1.19×10^{-4}	0.7	8.0	0.5	0.7	2560	0.79	0.74	0.61	0.1	5.87×10^{-2}	18.62	4.54
127	3.39×10^{-4}	1.69×10^{-4}	1.19×10^{-4}	0.7	8.0	0.5	0.7	2660	0.79	0.74	0.61	0.1	6.13×10^{-2}	19.42	4.44
128	3.39×10^{-4}	1.69×10^{-4}	1.19×10^{-4}	0.7	8.0	0.5	0.7	2760	0.79	0.74	0.61	0.1	6.38×10^{-2}	20.22	4.33
129	2.37×10^{-4}	1.90×10^{-4}	1.52×10^{-4}	0.7	8.0	0.8	0.8	2360	0.73	0.7	0.61	0.1	5.95×10^{-2}	18.86	3.86
130	2.37×10^{-4}	1.90×10^{-4}	1.52×10^{-4}	0.7	8.0	0.8	0.8	2560	0.73	0.7	0.59	0.1	6.55×10^{-2}	20.75	3.67
131	2.37×10^{-4}	1.90×10^{-4}	1.52×10^{-4}	0.7	8.0	0.8	0.8	2660	0.73	0.7	0.59	0.1	6.82×10^{-2}	21.63	3.58
132	2.37×10^{-4}	1.90×10^{-4}	1.52×10^{-4}	0.7	8.0	0.8	0.8	2760	0.73	0.7	0.59	0.1	7.11×10^{-2}	22.54	3.49
133	4.28×10^{-4}	2.14×10^{-4}	1.07×10^{-4}	0.7	2.0	0.5	0.5	2360	0.78	0.82	0.73	0.1	4.05×10^{-2}	12.83	5.27
134	4.28×10^{-4}	2.14×10^{-4}	1.07×10^{-4}	0.7	2.0	0.5	0.5	2460	0.78	0.82	0.73	0.1	4.24×10^{-2}	13.44	5.15
135	4.28×10^{-4}	2.14×10^{-4}	1.07×10^{-4}	0.7	2.0	0.5	0.5	2560	0.78	0.82	0.73	0.1	4.46×10^{-2}	14.14	4.97
136	4.28×10^{-4}	2.14×10^{-4}	1.07×10^{-4}	0.7	2.0	0.5	0.5	2660	0.78	0.82	0.73	0.1	4.64×10^{-2}	14.71	4.88
137	4.78×10^{-4}	2.87×10^{-4}	1.43×10^{-4}	0.7	1.0	0.6	0.5	2660	0.74	0.73	0.52	0.07	3.34×10^{-2}	10.58	6.99
138	4.78×10^{-4}	2.87×10^{-4}	1.43×10^{-4}	0.7	1.0	0.6	0.5	2760	0.74	0.73	0.52	0.07	3.49×10^{-2}	11.05	6.81
139	4.31×10^{-4}	3.02×10^{-4}	1.51×10^{-4}	0.7	1.0	0.7	0.5	2460	0.74	0.73	0.52	0.07	3.17×10^{-2}	10.04	6.83
140	4.31×10^{-4}	3.02×10^{-4}	1.51×10^{-4}	0.7	1.0	0.7	0.5	2660	0.74	0.73	0.52	0.07	3.48×10^{-2}	11.04	6.43
141	4.31×10^{-4}	3.02×10^{-4}	1.51×10^{-4}	0.7	1.0	0.7	0.5	2760	0.74	0.73	0.53	0.07	3.61×10^{-2}	11.44	6.36
142	3.94×10^{-4}	3.15×10^{-4}	1.58×10^{-4}	0.7	1.0	0.8	0.5	2360	0.73	0.73	0.54	0.07	3.09×10^{-2}	9.81	6.67
143	3.94×10^{-4}	3.15×10^{-4}	1.58×10^{-4}	0.7	1.0	0.8	0.5	2460	0.73	0.73	0.54	0.07	3.25×10^{-2}	10.29	6.5
144	3.94×10^{-4}	3.15×10^{-4}	1.58×10^{-4}	0.7	1.0	0.8	0.5	2560	0.73	0.73	0.54	0.07	3.42×10^{-2}	10.86	6.26
145	3.94×10^{-4}	3.15×10^{-4}	1.58×10^{-4}	0.7	1.0	0.8	0.5	2660	0.73	0.73	0.54	0.07	3.58×10^{-2}	11.35	6.09
146	4.50×10^{-4}	2.70×10^{-4}	1.62×10^{-4}	0.7	1.0	0.6	0.6	2360	0.74	0.75	0.57	0.07	3.08×10^{-2}	9.78	6.72
147	4.50×10^{-4}	2.70×10^{-4}	1.62×10^{-4}	0.7	1.0	0.6	0.6	2460	0.74	0.75	0.56	0.07	3.24×10^{-2}	10.27	6.55
148	4.50×10^{-4}	2.70×10^{-4}	1.62×10^{-4}	0.7	1.0	0.6	0.6	2560	0.74	0.75	0.56	0.07	3.40×10^{-2}	10.77	6.36
149	4.50×10^{-4}	2.70×10^{-4}	1.62×10^{-4}	0.7	1.0	0.6	0.6	2660	0.74	0.75	0.56	0.07	3.56×10^{-2}	11.3	6.14
150	4.50×10^{-4}	2.70×10^{-4}	1.62×10^{-4}	0.7	1.0	0.6	0.6	2760	0.74	0.75	0.57	0.07	3.70×10^{-2}	11.73	6.05
151	4.06×10^{-4}	2.84×10^{-4}	1.70×10^{-4}	0.7	1.0	0.7	0.6	2360	0.73	0.74	0.58	0.07	3.18×10^{-2}	10.09	6.3
152	4.06×10^{-4}	2.84×10^{-4}	1.70×10^{-4}	0.7	1.0	0.7	0.6	2460	0.73	0.74	0.58	0.07	3.36×10^{-2}	10.64	6.09
153	4.06×10^{-4}	2.84×10^{-4}	1.70×10^{-4}	0.7	1.0	0.7	0.6	2560	0.73	0.74	0.58	0.07	3.52×10^{-2}	11.17	5.91
154	4.06×10^{-4}	2.84×10^{-4}	1.70×10^{-4}	0.7	1.0	0.7	0.6	2660	0.73	0.74	0.58	0.07	3.69×10^{-2}	11.7	5.74
155	4.06×10^{-4}	2.84×10^{-4}	1.70×10^{-4}	0.7	1.0	0.7	0.6	2760	0.73	0.74	0.58	0.07	3.86×10^{-2}	12.22	5.56
156	4.08×10^{-4}	2.45×10^{-4}	1.96×10^{-4}	0.7	1.0	0.6	0.8	2360	0.74	0.75	0.6	0.07	3.29×10^{-2}	10.44	5.9
157	4.08×10^{-4}	2.45×10^{-4}	1.96×10^{-4}	0.7	1.0	0.6	0.8	2460	0.74	0.75	0.6	0.07	3.46×10^{-2}	10.97	5.73
158	4.08×10^{-4}	2.45×10^{-4}	1.96×10^{-4}	0.7	1.0	0.6	0.8	2560	0.74	0.75	0.59	0.07	3.63×10^{-2}	11.49	5.57
159	4.08×10^{-4}	2.45×10^{-4}	1.96×10^{-4}	0.7	1.0	0.6	0.8	2760	0.74	0.75	0.59	0.07	3.95×10^{-2}	12.51	5.31
160	3.45×10^{-4}	2.07×10^{-4}	1.03×10^{-4}	0.67	8.0	0.6	0.5	2360	0.73	0.75	0.7	0.1	5.85×10^{-2}	18.54	4.3
161	3.45×10^{-4}	2.07×10^{-4}	1.03×10^{-4}	0.67	8.0	0.6	0.5	2460	0.73	0.75	0.7	0.1	6.14×10^{-2}	19.46	4.18
162	3.45×10^{-4}	2.07×10^{-4}	1.03×10^{-4}	0.67	8.0	0.6	0.5	2560	0.73	0.75	0.7	0.1	6.43×10^{-2}	20.37	4.08
163	3.45×10^{-4}	2.07×10^{-4}	1.03×10^{-4}	0.67	8.0	0.6	0.5	2660	0.73	0.75	0.69	0.1	6.71×10^{-2}	21.26	3.98
164	3.45×10^{-4}	2.07×10^{-4}	1.03×10^{-4}	0.67	8.0	0.6	0.5	2760	0.73	0.75	0.7	0.1	6.99×10^{-2}	22.16	3.89
165	3.48×10^{-4}	1.74×10^{-4}	1.22×10^{-4}	0.67	8.0	0.5	0.7	2460	0.76	0.73	0.6	0.1	5.77×10^{-2}	18.29	4.72
166	3.09×10^{-4}	1.85×10^{-4}	1.85×10^{-4}	0.67	2.0	0.6	1.0	2460	0.69	0.69	0.5	0.08	4.32×10^{-2}	13.69	5.19
167	3.09×10^{-4}	1.85×10^{-4}	1.85×10^{-4}	0.67	2.0	0.6	1.0	2660	0.69	0.69	0.5	0.08	4.72×10^{-2}	14.96	4.95
168	2.79×10^{-4}	1.95×10^{-4}	1.95×10^{-4}	0.67	2.0	0.7	1.0	2460	0.7	0.69	0.52	0.08	4.46×10^{-2}	14.15	4.9
169	2.79×10^{-4}	1.95×10^{-4}	1.95×10^{-4}	0.67	2.0	0.7	1.0	2560	0.7	0.69	0.52	0.08	4.67×10^{-2}	14.82	4.71
170	2.55×10^{-4}	2.04×10^{-4}	2.04×10^{-4}	0.67	2.0	0.8	1.0	2360	0.69	0.7	0.54	0.08	4.36×10^{-2}	13.81	4.76
171	2.55×10^{-4}	2.04×10^{-4}	2.04×10^{-4}	0.67	2.0	0.8	1.0	2460	0.69	0.7	0.54	0.08	4.58×10^{-2}	14.53	4.62
172	2.55×10^{-4}	2.04×10^{-4}	2.04×10^{-4}	0.67	2.0	0.8	1.0	2560	0.69	0.7	0.54	0.08	4.80×10^{-2}	15.23	4.49
173	2.55×10^{-4}	2.04×10^{-4}	2.04×10^{-4}	0.67	2.0	0.8	1.0	2660	0.69	0.7	0.54	0.08	5.02×10^{-2}	15.91	4.37
174	3.28×10^{-4}	3.28×10^{-4}	1.97×10^{-4}	0.67	1.0	1.0	0.6	2760	0.67	0.73	0.65	0.07	4.24×10^{-2}	13.45	4.74
175	2.98×10^{-4}	2.98×10^{-4}	2.39×10^{-4}	0.67	1.0	1.0	0.8	2560	0.68	0.69	0.78	0.07	4.17×10^{-2}	13.21	4.35
176	3.33×10^{-4}	2.66×10^{-4}	2.40×10^{-4}	0.67	1.0	0.8	0.9	2360	0.69	0.7	0.55	0.07	3.45×10^{-2}	10.95	5.51
177	3.33×10^{-4}	2.66×10^{-4}	2.40×10^{-4}	0.67	1.0	0.8	0.9	2460	0.69	0.7	0.55	0.07	3.64×10^{-2}	11.53	5.36
178	3.33×10^{-4}	2.66×10^{-4}	2.40×10^{-4}	0.67	1.0	0.8	0.9	2560	0.69	0.7	0.54	0.07	3.81×10^{-2}	12.09	5.19
179	3.33×10^{-4}	2.66×10^{-4}	2.40×10^{-4}	0.67	1.0	0.8	0.9	2660	0.69	0.7	0.55	0.07	3.99×10^{-2}	12.64	5.06
180	3.08×10^{-4}	2.77×10^{-4}	2.49×10^{-4}	0.67	1.0	0.9	0.9	2460	0.68	0.69	0.55	0.07	3.74×10^{-2}	11.85	5.07

Table A4. Data of the particles in the training set.

ID	a_L in m	a_I in m	a_S in m	ξ_1	ξ_2	E	F	ρ_p	κ_con	ψ	$\psi_\perp$	κ_rnd	u_ts	Re	C_D
181	3.08×10^{-4}	2.77×10^{-4}	2.49×10^{-4}	0.67	1.0	0.9	0.9	2560	0.68	0.69	0.57	0.07	3.92×10^{-2}	12.42	4.92
182	3.08×10^{-4}	2.77×10^{-4}	2.49×10^{-4}	0.67	1.0	0.9	0.9	2660	0.68	0.69	0.56	0.07	4.09×10^{-2}	12.98	4.8
183	3.08×10^{-4}	2.77×10^{-4}	2.49×10^{-4}	0.67	1.0	0.9	0.9	2760	0.68	0.69	0.55	0.07	4.27×10^{-2}	13.52	4.69
184	2.87×10^{-4}	2.87×10^{-4}	2.58×10^{-4}	0.67	1.0	1.0	0.9	2360	0.68	0.68	0.72	0.06	3.69×10^{-2}	11.7	4.82
185	2.87×10^{-4}	2.87×10^{-4}	2.58×10^{-4}	0.67	1.0	1.0	0.9	2660	0.68	0.68	0.83	0.06	4.28×10^{-2}	13.58	4.38
186	2.87×10^{-4}	2.87×10^{-4}	2.58×10^{-4}	0.67	1.0	1.0	0.9	2760	0.68	0.68	0.83	0.06	4.47×10^{-2}	14.18	4.25
187	3.51×10^{-4}	2.46×10^{-4}	2.46×10^{-4}	0.67	1.0	0.7	1.0	2360	0.69	0.69	0.53	0.07	3.32×10^{-2}	10.53	5.97
188	3.51×10^{-4}	2.46×10^{-4}	2.46×10^{-4}	0.67	1.0	0.7	1.0	2460	0.69	0.69	0.53	0.07	3.50×10^{-2}	11.09	5.79
189	3.51×10^{-4}	2.46×10^{-4}	2.46×10^{-4}	0.67	1.0	0.7	1.0	2560	0.69	0.69	0.53	0.07	3.67×10^{-2}	11.62	5.63
190	3.51×10^{-4}	2.46×10^{-4}	2.46×10^{-4}	0.67	1.0	0.7	1.0	2660	0.69	0.69	0.52	0.07	3.83×10^{-2}	12.15	5.48
191	3.21×10^{-4}	2.57×10^{-4}	2.57×10^{-4}	0.67	1.0	0.8	1.0	2360	0.68	0.68	0.53	0.07	3.41×10^{-2}	10.82	5.67
192	3.21×10^{-4}	2.57×10^{-4}	2.57×10^{-4}	0.67	1.0	0.8	1.0	2460	0.68	0.68	0.53	0.07	3.59×10^{-2}	11.39	5.48
193	3.21×10^{-4}	2.57×10^{-4}	2.57×10^{-4}	0.67	1.0	0.8	1.0	2560	0.68	0.68	0.54	0.07	3.77×10^{-2}	11.95	5.31
194	3.21×10^{-4}	2.57×10^{-4}	2.57×10^{-4}	0.67	1.0	0.8	1.0	2660	0.68	0.68	0.53	0.07	3.94×10^{-2}	12.49	5.16
195	3.21×10^{-4}	2.57×10^{-4}	2.57×10^{-4}	0.67	1.0	0.8	1.0	2760	0.68	0.68	0.54	0.07	4.11×10^{-2}	13.02	5.06
196	2.97×10^{-4}	2.67×10^{-4}	2.67×10^{-4}	0.67	1.0	0.9	1.0	2460	0.68	0.68	0.54	0.06	3.69×10^{-2}	11.69	5.21
197	2.97×10^{-4}	2.67×10^{-4}	2.67×10^{-4}	0.67	1.0	0.9	1.0	2660	0.68	0.68	0.56	0.06	4.04×10^{-2}	12.79	4.95
198	2.97×10^{-4}	2.67×10^{-4}	2.67×10^{-4}	0.67	1.0	0.9	1.0	2760	0.68	0.68	0.56	0.06	4.20×10^{-2}	13.33	4.82
199	2.77×10^{-4}	2.77×10^{-4}	2.77×10^{-4}	0.67	1.0	1.0	1.0	2460	0.69	0.67	0.89	0.06	3.83×10^{-2}	12.14	4.81
200	2.77×10^{-4}	2.77×10^{-4}	2.77×10^{-4}	0.67	1.0	1.0	1.0	2560	0.69	0.67	0.89	0.06	4.02×10^{-2}	12.75	4.67

Table A5. Mean values and standard deviations for the parameters relevant to the calculated models.

	E	ρ_p	ψ	κ_rnd	λ_H	Re	C_D	u_ts
mean	0.757	2563.17	0.786	0.101	−0.962	14.380	4.544	0.045
standard deviation	0.166	141.01	0.072	0.026	0.038	3.103	0.970	0.010

Appendix B

Table A6. Data of the particles in the test set.

ID	a_L in m	a_I in m	a_S in m	ξ_1	ξ_2	E	F	ρ_p	κ_con	ψ	$\psi_\perp$	κ_rnd	u_ts	Re	C_D
1	5.39×10^{-4}	2.70×10^{-4}	1.35×10^{-4}	0.7	1.0	0.5	0.5	2460	0.75	0.75	0.51	0.07	2.89×10^{-2}	9.17	8.21
2	4.78×10^{-4}	2.87×10^{-4}	1.43×10^{-4}	0.7	1.0	0.6	0.5	2460	0.74	0.73	0.52	0.07	3.06×10^{-2}	9.71	7.33
3	3.65×10^{-4}	3.28×10^{-4}	1.64×10^{-4}	0.7	1.0	0.9	0.5	2460	0.72	0.73	0.55	0.07	3.32×10^{-2}	10.54	6.21
4	3.40×10^{-4}	3.40×10^{-4}	1.70×10^{-4}	0.7	1.0	1.0	0.5	2460	0.72	0.73	0.56	0.07	3.40×10^{-2}	10.76	5.96
5	5.08×10^{-4}	2.54×10^{-4}	1.52×10^{-4}	0.7	1.0	0.5	0.6	2460	0.76	0.77	0.57	0.08	3.08×10^{-2}	9.75	7.28
6	3.71×10^{-4}	2.97×10^{-4}	1.78×10^{-4}	0.7	1.0	0.8	0.6	2460	0.72	0.74	0.59	0.07	3.45×10^{-2}	10.95	5.75
7	3.43×10^{-4}	3.09×10^{-4}	1.85×10^{-4}	0.7	1.0	0.9	0.6	2460	0.71	0.74	0.61	0.07	3.54×10^{-2}	11.22	5.5
8	3.20×10^{-4}	3.20×10^{-4}	1.92×10^{-4}	0.7	1.0	1.0	0.6	2460	0.71	0.73	0.64	0.07	3.60×10^{-2}	11.4	5.31
9	4.82×10^{-4}	2.41×10^{-4}	1.69×10^{-4}	0.7	1.0	0.5	0.7	2460	0.75	0.77	0.61	0.08	3.24×10^{-2}	10.28	6.53
10	4.27×10^{-4}	2.56×10^{-4}	1.79×10^{-4}	0.7	1.0	0.6	0.7	2460	0.73	0.76	0.62	0.07	3.40×10^{-2}	10.79	5.92
11	3.85×10^{-4}	2.70×10^{-4}	1.89×10^{-4}	0.7	1.0	0.7	0.7	2460	0.72	0.75	0.63	0.07	3.54×10^{-2}	11.22	5.48
12	3.53×10^{-4}	2.82×10^{-4}	1.97×10^{-4}	0.7	1.0	0.8	0.7	2460	0.71	0.74	0.65	0.07	3.64×10^{-2}	11.53	5.19
13	3.26×10^{-4}	2.93×10^{-4}	2.05×10^{-4}	0.7	1.0	0.9	0.7	2460	0.7	0.73	0.67	0.07	3.71×10^{-2}	11.77	4.98
14	3.04×10^{-4}	3.04×10^{-4}	2.13×10^{-4}	0.7	1.0	1.0	0.7	2460	0.7	0.73	0.69	0.07	3.76×10^{-2}	11.93	4.85
15	4.61×10^{-4}	2.31×10^{-4}	1.84×10^{-4}	0.7	1.0	0.5	0.8	2460	0.75	0.77	0.59	0.08	3.28×10^{-2}	10.4	6.37
16	3.69×10^{-4}	2.58×10^{-4}	2.06×10^{-4}	0.7	1.0	0.7	0.8	2460	0.72	0.74	0.61	0.07	3.61×10^{-2}	11.45	5.27
17	3.37×10^{-4}	2.70×10^{-4}	2.16×10^{-4}	0.7	1.0	0.8	0.8	2460	0.71	0.74	0.66	0.07	3.73×10^{-2}	11.83	4.94
18	3.12×10^{-4}	2.81×10^{-4}	2.24×10^{-4}	0.7	1.0	0.9	0.8	2460	0.7	0.72	0.69	0.07	3.83×10^{-2}	12.15	4.67
19	2.91×10^{-4}	2.91×10^{-4}	2.32×10^{-4}	0.7	1.0	1.0	0.8	2460	0.7	0.72	0.75	0.07	3.96×10^{-2}	12.56	4.38
20	4.43×10^{-4}	2.22×10^{-4}	2.00×10^{-4}	0.7	1.0	0.5	0.9	2460	0.75	0.75	0.55	0.07	3.23×10^{-2}	10.24	6.59
21	3.93×10^{-4}	2.36×10^{-4}	2.12×10^{-4}	0.7	1.0	0.6	0.9	2460	0.72	0.74	0.56	0.07	3.39×10^{-2}	10.76	5.96
22	3.54×10^{-4}	2.48×10^{-4}	2.23×10^{-4}	0.7	1.0	0.7	0.9	2460	0.72	0.73	0.57	0.07	3.53×10^{-2}	11.17	5.53
23	2.79×10^{-4}	2.79×10^{-4}	2.51×10^{-4}	0.7	1.0	1.0	0.9	2460	0.71	0.71	0.76	0.07	3.88×10^{-2}	12.31	4.54
24	4.28×10^{-4}	2.14×10^{-4}	2.14×10^{-4}	0.7	1.0	0.5	1.0	2460	0.75	0.73	0.53	0.07	3.22×10^{-2}	10.2	6.62
25	3.79×10^{-4}	2.28×10^{-4}	2.28×10^{-4}	0.7	1.0	0.6	1.0	2460	0.73	0.72	0.54	0.07	3.38×10^{-2}	10.7	6.02
26	4.28×10^{-4}	2.14×10^{-4}	2.14×10^{-4}	0.7	1.0	0.5	1.0	2360	0.75	0.73	0.53	0.07	3.06×10^{-2}	9.7	6.83
27	4.28×10^{-4}	2.14×10^{-4}	2.14×10^{-4}	0.7	1.0	0.5	1.0	2460	0.75	0.73	0.53	0.07	3.22×10^{-2}	10.2	6.62
28	4.28×10^{-4}	2.14×10^{-4}	2.14×10^{-4}	0.7	1.0	0.5	1.0	2560	0.75	0.73	0.53	0.07	3.37×10^{-2}	10.69	6.44
29	4.28×10^{-4}	2.14×10^{-4}	2.14×10^{-4}	0.7	1.0	0.5	1.0	2660	0.75	0.73	0.53	0.07	3.53×10^{-2}	11.18	6.27
30	4.28×10^{-4}	2.14×10^{-4}	2.14×10^{-4}	0.7	1.0	0.5	1.0	2760	0.75	0.73	0.53	0.07	3.68×10^{-2}	11.66	6.11

Table A6. *Cont.*

ID	a_L in m	a_I in m	a_S in m	ξ_1	ξ_2	E	F	ρ_p	κ_{con}	ψ	$\psi_\perp$	κ_{rnd}	u_{ts}	Re	C_D
31	3.79×10^{-4}	2.28×10^{-4}	2.28×10^{-4}	0.7	1.0	0.6	1.0	2360	0.73	0.72	0.53	0.07	3.21×10^{-2}	10.16	6.23
32	3.79×10^{-4}	2.28×10^{-4}	2.28×10^{-4}	0.7	1.0	0.6	1.0	2460	0.73	0.72	0.54	0.07	-	-	-
33	3.79×10^{-4}	2.28×10^{-4}	2.28×10^{-4}	0.7	1.0	0.6	1.0	2560	0.73	0.72	0.53	0.07	3.54×10^{-2}	11.21	5.87
34	3.79×10^{-4}	2.28×10^{-4}	2.28×10^{-4}	0.7	1.0	0.6	1.0	2660	0.73	0.72	0.53	0.07	-	-	-
35	3.79×10^{-4}	2.28×10^{-4}	2.28×10^{-4}	0.7	1.0	0.6	1.0	2760	0.73	0.72	0.53	0.07	-	-	-
36	3.42×10^{-4}	2.40×10^{-4}	2.40×10^{-4}	0.7	1.0	0.7	1.0	2660	0.72	0.71	0.54	0.07	-	-	-
37	3.42×10^{-4}	2.40×10^{-4}	2.40×10^{-4}	0.7	1.0	0.7	1.0	2760	0.72	0.71	0.55	0.07	-	-	-
38	3.13×10^{-4}	2.50×10^{-4}	2.50×10^{-4}	0.7	1.0	0.8	1.0	2560	0.72	0.71	0.56	0.07	3.77×10^{-2}	11.94	5.16
39	2.89×10^{-4}	2.60×10^{-4}	2.60×10^{-4}	0.7	1.0	0.9	1.0	2360	0.72	0.7	0.56	0.07	3.50×10^{-2}	11.09	5.23
40	2.89×10^{-4}	2.60×10^{-4}	2.60×10^{-4}	0.7	1.0	0.9	1.0	2560	0.72	0.7	0.56	0.07	-	-	-
41	2.89×10^{-4}	2.60×10^{-4}	2.60×10^{-4}	0.7	1.0	0.9	1.0	2660	0.72	0.7	0.57	0.07	-	-	-
42	2.70×10^{-4}	2.70×10^{-4}	2.70×10^{-4}	0.7	1.0	1.0	1.0	2360	0.71	0.69	0.71	0.07	-	-	-
43	2.70×10^{-4}	2.70×10^{-4}	2.70×10^{-4}	0.7	1.0	1.0	1.0	2660	0.71	0.69	0.75	0.07	4.20×10^{-2}	13.32	4.42
44	2.70×10^{-4}	2.70×10^{-4}	2.70×10^{-4}	0.7	1.0	1.0	1.0	2760	0.71	0.69	0.76	0.07	4.39×10^{-2}	13.91	4.29

References

1. Fu, X.; Huck, D.; Makein, L.; Armstrong, B.; Willen, U.; Freeman, T. Effect of particle shape and size on flow properties of lactose powders. *Particuology* **2012**, *10*, 203–208. [CrossRef]
2. Kashiwaya, K.; Noumachi, T.; Hiroyoshi, N.; Ito, M.; Tsunekawa, M. Effect of particle shape on hydrocyclone classification. *Powder Technol.* **2012**, *226*, 147–156. [CrossRef]
3. Champion, J.A.; Katare, Y.K.; Mitragotri, S. Particle shape: A new design parameter for micro- and nanoscale drug delivery carriers. *J. Control. Release* **2007**, *121*, 3–9. [CrossRef] [PubMed]
4. Waldschläger, K.; Schüttrumpf, H. Effects of Particle Properties on the Settling and Rise Velocities of Microplastics in Freshwater under Laboratory Conditions. *Environ. Sci. Technol.* **2019**, *53*, 1958–1966. [CrossRef] [PubMed]
5. Zingg, T. Beitrag zur Schotteranalyse. Ph.D. Thesis, ETH, Zürich, Switzerland, 1935.
6. Sneed, E.D.; Folk, R.L. Pebbles in the Lower Colorado River, Texas a Study in Particle Morphogenesis. *J. Geol.* **1958**, *66*, 114–150. [CrossRef]
7. ISO 9276-6:2008(E). *Representation of Results of Particle Size Analysis—Part 6: Descriptive and Quantitative Representation of Particle Shape and Morphology*; Standard; International Organization for Standardization: Geneva, Switzerland, 2008.
8. Hentschel, M.L.; Page, N.W. Selection of Descriptors for Particle Shape Characterization. *Part. Part. Syst. Charact.* **2003**, *20*, 25–38. [CrossRef]
9. Blott, S.J.; Pye, K. Particle shape: A review and new methods of characterization and classification. *Sedimentology* **2008**, *55*, 31–63. [CrossRef]
10. Allen, J.R.L. Chapter 5 Orientation of Particles During Sedimentation: Shape-Fabrics. In *Sedimentary Structures Their Character and Physical Basis Volume I*; Elsevier: Amsterdam, The Netherlands, 1982; Volume 30, pp. 179–235. [CrossRef]
11. Sheikh, M.Z.; Gustavsson, K.; Lopez, D.; Lévêque, E.; Mehlig, B.; Pumir, A.; Naso, A. Importance of fluid inertia for the orientation of spheroids settling in turbulent flow. *J. Fluid Mech.* **2020**, *886*. [CrossRef]
12. Bagheri, G.; Bonadonna, C. On the drag of freely falling non-spherical particles. *Powder Technol.* **2016**, *301*, 526–544. [CrossRef]
13. Komar, P.D.; Reimers, C.E. Grain Shape Effects on Settling Rates. *J. Geol.* **1978**, *86*, 193–209. [CrossRef]
14. Shao, B.; Liu, G.R.; Lin, T.; Xu, G.X.; Yan, X. Rotation and orientation of irregular particles in viscous fluids using the gradient smoothed method (GSM). *Eng. Appl. Comput. Fluid Mech.* **2017**, *11*, 557–575. [CrossRef]
15. Stokes, G.G. On the Effect of Internal Friction of Fluids on the Motion of Pendulums. *Trans. Camb. Philos. Soc.* **1851**, *9*, 8–106. [CrossRef]
16. Schiller, L.; Naumann, A. Über die grundlegenden Berechnungen bei der Schwerkraftaufbereitung. *Z. Des Vereines Dtsch. Ingenieure* **1933**, *77*, 318–320.
17. Clift, R.; Gauvin, W.H. Motion of entrained particles in gas streams. *Can. J. Chem. Eng.* **1971**, *49*, 439–448. [CrossRef]
18. McNown, J.S.; Malaika, J. Effects of particle shape on settling velocity at low Reynolds numbers. *Trans. Am. Geophys. Union* **1950**, *31*, 74. [CrossRef]
19. Sommerfeld, M.; Qadir, Z. Fluid dynamic forces acting on irregular shaped particles: Simulations by the Lattice–Boltzmann method. *Int. J. Multiph. Flow* **2018**, *101*, 212–222. [CrossRef]
20. Leith, D. Drag on Nonspherical Objects. *Aerosol Sci. Technol.* **1987**, *6*, 153–161. [CrossRef]
21. Ganser, G.H. A rational approach to drag prediction of spherical and nonspherical particles. *Powder Technol.* **1993**, *77*, 143–152. [CrossRef]
22. Loth, E. Drag of non-spherical solid particles of regular and irregular shape. *Powder Technol.* **2008**, *182*, 342–353. [CrossRef]
23. Hölzer, A.; Sommerfeld, M. New simple correlation formula for the drag coefficient of non-spherical particles. *Powder Technol.* **2008**, *184*, 361–365. [CrossRef]

24. Tran-Cong, S.; Gay, M.; Michaelides, E.E. Drag coefficients of irregularly shaped particles. *Powder Technol.* **2004**, *139*, 21–32. [CrossRef]
25. Dellino, P.; Mele, D.; Bonasia, R.; Braia, G.; La Volpe, L.; Sulpizio, R. The analysis of the influence of pumice shape on its terminal velocity. *Geophys. Res. Lett.* **2005**, *32*. [CrossRef]
26. Dioguardi, F.; Mele, D. A new shape dependent drag correlation formula for non-spherical rough particles. Experiments and results. *Powder Technol.* **2015**, *277*, 222–230. [CrossRef]
27. Hölzer, A.; Sommerfeld, M. Lattice Boltzmann simulations to determine drag, lift and torque acting on non-spherical particles. *Comput. Fluids* **2009**, *38*, 572–589. [CrossRef]
28. Haider, A.; Levenspiel, O. Drag coefficient and terminal velocity of spherical and nonspherical particles. *Powder Technol.* **1989**, *58*, 63–70. [CrossRef]
29. Henn, T.; Thäter, G.; Dörfler, W.; Nirschl, H.; Krause, M.J. Parallel dilute particulate flow simulations in the human nasal cavity. *Comput. Fluids* **2016**, *124*, 197–207. [CrossRef]
30. Trunk, R.; Henn, T.; Dörfler, W.; Nirschl, H.; Krause, M.J. Inertial dilute particulate fluid flow simulations with an Euler–Euler lattice Boltzmann method. *J. Comput. Sci.* **2016**, *17*, 438–445. [CrossRef]
31. Maier, M.L.; Milles, S.; Schuhmann, S.; Guthausen, G.; Nirschl, H.; Krause, M.J. Fluid flow simulations verified by measurements to investigate adsorption processes in a static mixer. *Comput. Math. Appl.* **2018**, *76*, 2744–2757. [CrossRef]
32. Trunk, R.; Marquardt, J.; Thäter, G.; Nirschl, H.; Krause, M.J. Towards the simulation of arbitrarily shaped 3D particles using a homogenised lattice Boltzmann method. *Comput. Fluids* **2018**, *172*, 621–631. [CrossRef]
33. Krause, M.J.; Klemens, F.; Henn, T.; Trunk, R.; Nirschl, H. Particle flow simulations with homogenised lattice Boltzmann methods. *Particuology* **2017**, *34*, 1–13. [CrossRef]
34. Trunk, R.; Weckerle, T.; Hafen, N.; Thäter, G.; Nirschl, H.; Krause, M.J. Revisiting the Homogenized Lattice Boltzmann Method with Applications on Particulate Flows. *Computation* **2021**, *9*, 11. [CrossRef]
35. Krause, M.J.; Kummerländer, A.; Avis, S.J.; Kusumaatmaja, H.; Dapelo, D.; Klemens, F.; Gaedtke, M.; Hafen, N.; Mink, A.; Trunk, R.; et al. OpenLB—Open source lattice Boltzmann code. *Comput. Math. Appl.* **2020**. [CrossRef]
36. Krause, M.; Avis, S.; Kusumaatmaja, H.; Dapelo, D.; Gaedtke, M.; Hafen, N.; Haußmann, M.; Jeppener-Haltenhoff, J.; Kronberg, L.; Kummerländer, A.; et al. OpenLB Release 1.4: Open Source Lattice Boltzmann Code. *Comput. Math. Appl.* **2020**. [CrossRef]
37. Yow, H.N.; Pitt, M.J.; Salman, A.D. Drag correlations for particles of regular shape. *Adv. Powder Technol.* **2005**, *16*, 363–372. [CrossRef]
38. Dey, S.; Ali, S.Z.; Padhi, E. Terminal fall velocity: The legacy of Stokes from the perspective of fluvial hydraulics. *Proc. R. Soc. A Math. Phys. Eng. Sci.* **2019**, *475*, 20190277. [CrossRef]
39. Bretl, C.; Trunk, R.; Nirschl, H.; Thäter, G.; Dorn, M.; Krause, M.J. Preliminary study of particle settling behaviour by shape parameters via lattice Boltzmann simulations. In *High Performance Computing in Science and Engineering '20*; Nagel, W., Kröner, D., Resch, M., Eds.; Springer: Berlin/Heidelberg, Germany, 2020.
40. Wadell, H. Volume, Shape, and Roundness of Rock Particles. *J. Geol.* **1932**, *40*, 443–451. [CrossRef]
41. Krumbein, W.C. Measurement and Geological Significance of Shape and Roundness of Sedimentary Particles. *SEPM J. Sediment. Res.* **1941**, *11*. [CrossRef]
42. Hayakawa, Y.; Oguchi, T. Evaluation of gravel sphericity and roundness based on surface-area measurement with a laser scanner. *Comput. Geosci.* **2005**, *31*, 735–741. [CrossRef]
43. Dietrich, W.E. Settling velocity of natural particles. *Water Resour. Res.* **1982**, *18*, 1615–1626. [CrossRef]
44. Hofmann, H.J. Grain-shaped indices and isometric graphs. *J. Sediment. Res.* **1994**, *64*, 916–920. [CrossRef]
45. le Roux, J.P. Application of the Hofmann shape entropy to determine the settling velocity of irregular, semi-ellipsoidal grains. *Sediment. Geol.* **2002**, *149*, 237–243. [CrossRef]
46. Le Roux, J. A Hydrodynamic Classification of Grain Shapes. *J. Sediment. Res.* **2004**, *74*, 135–143. [CrossRef]
47. Williams, J.R.; Pentland, A.P. Superquadrics and modal dynamics for discrete elements in interactive design. *Eng. Comput.* **1992**, *9*, 115–127. [CrossRef]
48. Barr, A.H. Superquadrics and Angle-Preserving Transformations. *IEEE Comput. Graph. Appl.* **1981**, *1*, 11–23. 1981. [CrossRef]
49. Wellmann, C.; Lillie, C.; Wriggers, P. A contact detection algorithm for superellipsoids based on the common-normal concept. *Eng. Comput.* **2008**, *25*, 432–442. [CrossRef]
50. Jaklič, A.; Leonardis, A.; Solina, F. Superquadrics and Their Geometric Properties. In *Segmentation and Recovery of Superquadrics*; Springer: Dordrecht, The Netherlands, 2000; pp. 13–39. [CrossRef]
51. Jaklič, A.; Solina, F. Moments of superellipsoids and their application to range image registration. *IEEE Trans. Syst. Man Cybern. Part B (Cybern.)* **2003**, *33*, 648–657. [CrossRef]
52. Bagheri, G.; Bonadonna, C. On the Drag of Freely Falling Non-Spherical Particles. Available online: https://arxiv.org/abs/1810.08787 (accessed on 25 March 2021).
53. Chrust, M.; Bouchet, G.; Dušek, J. Numerical simulation of the dynamics of freely falling discs. *Phys. Fluids* **2013**, *25*, 044102. [CrossRef]
54. Seyed-Ahmadi, A.; Wachs, A. Dynamics and wakes of freely settling and rising cubes. *Phys. Rev. Fluids* **2018**, *4*. physrevfluids.4.074304. [CrossRef]
55. Rahmani, M.; Wachs, A. Free falling and rising of spherical and angular particles. *Phys. Fluids* **2014**, *26*, 083301. [CrossRef]

56. Kupershtokh, A.; Medvedev, D.; Karpov, D. On equations of state in a lattice Boltzmann method. *Comput. Math. Appl.* **2009**, *58*, 965–974. [CrossRef]
57. Wen, B.; Zhang, C.; Tu, Y.; Wang, C.; Fang, H. Galilean invariant fluid–solid interfacial dynamics in lattice Boltzmann simulations. *J. Comput. Phys.* **2014**, *266*, 161–170. [CrossRef]
58. Abraham, F.F. Functional Dependence of Drag Coefficient of a Sphere on Reynolds Number. *Phys. Fluids* **1970**, *13*, 2194. [CrossRef]
59. Krüger, T.; Kusumaatmaja, H.; Kuzmin, A.; Shardt, O.; Silva, G.; Viggen, E.M. *The Lattice Boltzmann Method*; Graduate Texts in Physics; Springer: Cham, Switzerland, 2017. [CrossRef]
60. Young, D.S. *Handbook of Regression Methods*; Chapman and Hall/CRC: Boca Raton, FL, USA, 2017. [CrossRef]
61. Pearson, K. VII. Mathematical contributions to the theory of evolution.—III. Regression, heredity, and panmixia. *Philos. Trans. R. Soc. Lond. Ser. A Contain. Pap. A Math. Phys. Character* **1896**, *187*, 253–318. [CrossRef]
62. Wisniewski, M. Applied Regression Analysis: A Research Tool. *J. Oper. Res. Soc.* **1990**. [CrossRef]
63. Shannon, C.E. A Mathematical Theory of Communication. *Bell Syst. Tech. J.* **1948**, *27*, 379–423. [CrossRef]
64. Kraskov, A.; Stögbauer, H.; Grassberger, P. Estimating mutual information. *Phys. Rev. E* **2004**, *69*. [CrossRef]
65. Breiman, L. Random Forests. *Mach. Learn.* **2001**, *45*, 5–32. [CrossRef]
66. Horowitz, M.; Williamson, C.H.K. The effect of Reynolds number on the dynamics and wakes of freely rising and falling spheres. *J. Fluid Mech.* **2010**, *651*, 251–294. [CrossRef]
67. Szabó, T.; Domokos, G. A new classification system for pebble and crystal shapes based on static equilibrium points. *Cent. Eur. Geol.* **2010**, *53*, 1–19. [CrossRef]
68. Wilk, M.B.; Gnanadesikan, R. Probability plotting methods for the analysis for the analysis of data. *Biometrika* **1968**, *55*, 1–17. [CrossRef]
69. Thode, H.C. *Testing For Normality*; Taylor & Francis: Abingdon, UK, 2002. [CrossRef]
70. Anscombe, F.J.; Tukey, J.W. The Examination and Analysis of Residuals. *Technometrics* **1963**, *5*, 141–160. [CrossRef]
71. Cook, R.D. Detection of Influential Observation in Linear Regression. *Technometrics* **1977**, *19*, 15. [CrossRef]

7 Conclusion and Outlook

This thesis aims to incorporate the particle shape in models regarding the drag and dynamics of particles settling under gravity, by a study based on simulations. Besides the extension, implementation and validation of methods, new approaches are proposed, e.g., for the calculation of exchanged momentum. While various applications of the new method are investigated, new correlations regarding the drag and terminal settling velocity are also obtained. Moreover a constructive way based on statistical measures and methods from machine learning is presented for the creation of such correlations from available data sets, thus yielding a valuable contribution to a data driven design of, e.g., processing machines, in the future.

Extension of Simulation Methods This thesis is mainly concerned with simulations of individual surface-resolved particles. The simulations are based on the homogenized lattice Boltzmann method, first proposed by Krause et al. [71]. Originally described for shapes whose surface and parameters, like the moment of inertia, can be described analytically, the method was extended to depict arbitrary shapes in Chapter 4. This is achieved by applying the parallel axis theorem and utilizing a voxel representation. Furthermore the performance is improved by optimization of the load balancing across the computing cores, by also parallelizing the computation of momentum exchanged between fluid and particles for simulations with multiple objects. Finally the components of the method are revised after a comparative study. Regarding accuracy it is found that the originally applied forcing scheme by Shan and Chen [120] and the adapted version of the momentum exchange method by Ladd [75, 76] perform inferior to the exact difference method [74] for the forcing and momentum exchange algorithm proposed by Wen et al. [147]. Therefore the method is updated to benefit from these schemes.

Newly Developed Simulation Methods Additionally to the extension of methods, a new approach for the calculation of exchanged momentum denoted as *momentum loss algorithm* is proposed. In contrast to other approaches, for which the momentum is calculated via the particle distribution functions close to a no-slip condition at the particle surface, this new method directly calculates the momentum lost by the fluid during the application of the force. Considering the way particles are represented in the HLBM, this approach is a better fit, since objects are not depicted via a no-slip boundary. Due to the latter, an adaption of other approaches calculating the exchanged momentum is often required for HLBM. In other works concomitant to this thesis, the groundwork is performed for further exploitation of the results regarding the link between shape parameters and the experienced drag, as given in Chapter 6. A macroscopic approach for simulations of a large number of entities, relevant on a processing scale, was described and applied by Trunk et al. [138] by considering the particles as a continuum via an advection–diffusion equation. The method extends the Euler–Euler approach by coupling with a turbulence scheme to increase stability for cases with higher flow velocity. In another concomitant publication by Höcker et al. [59], a new LBM approach for the VANS equations is described, accounting for moving objects, and also coupled to a particle simulation by an advection–diffusion approach.

Validation and Application The capability of the new HLBM to depict arbitrary particle shapes is demonstrated in Chapter 4 by presenting the results of simulations of 16 settling realistic limestone particles. The geometry is obtained from computer tomography scans and, as described, processed automatically for the simulations. The comparative study presented in Section 5.4.1 considered various combinations of forcing schemes, i.e., the velocity shift method of Shan and Chen [120], the scheme by Guo et al. [44], and the exact difference method by Kupershtokh [74], with momentum exchange approaches, i.e., the ones by Ladd [75, 76], Wen et al. [147], and Trunk et al. [147]. As mentioned in the last paragraph, the best combination is selected for further validation. Considering the drag of a single settling sphere, it is shown in Section 5.4.1 by comparison to correlations from literature, that the updated method is capable of recovering the correct drag coefficient in the whole intermediate Reynolds number regime. Considering the range from $\mathrm{Re} = 0.24$ to $\mathrm{Re} = 948.67$, the best agreement is found with the correlation proposed by Schiller and Naumann [116], yielding an average error of 7.78%, Furthermore vortex structures as described in literature are observed. Another case is the flow of a neutrally buoyant particle through a pipe. Due to a balance of pressure and friction forces, the particle positions itself in a certain distance to the mid, denoted as tubular pinch effect. It is found in Section 5.4.2 that the updated HLBM is also well suited for this application. Lastly the case of hindered settling is considered for validation. Simulating the settling of 373 up to 1865 spheres, various solid volume fractions are depicted. Comparing to experimentally obtained correlations found in literature, the results are in good agreement, as shown in Section 5.4.3. Also validating the setup for various Reynolds numbers, i.e., $\mathrm{Re} = 0.53$, $\mathrm{Re} = 5.29$, and $\mathrm{Re} = 49.46$, the settling velocities match best with the correlation proposed by Barnea and Mizrahi [8]. Finally a guideline for a sensible parameter selection, regarding accuracy and stability, is presented in Chapter 5.

Newly Developed Models To find a new, improved shape-dependent correlation regarding the drag acting on the particles, the settling of 200 superellipsoids is considered in Chapter 6. Calculating measures from statistics like the Pearson correlation coefficient [103, 152] and the F-value or the mutual information [68] used in information theory, the most relevant shape parameters for a regression analysis are identified. From this set a polynomial up to a desired degree is constructed for a multiple linear regression, also containing interaction terms. To reduce effects due to multicolinearity, terms with a high variance inflation factor are dropped. The optimal degree for the polynomial is evaluated, splitting the data in a training and test set, increasing the degree up to the order for which the error on the test data starts to increase. This is a common approach in the field of machine learning. The obtained models are evaluated regarding the significance of each term, considering the permutation importance [15] and T-values. The whole model is evaluated calculating the adjusted coefficient of determination and mean error. Also an outlier analysis is performed, considering the standardized residuals and Cook's distances. Comparing to literature, the newly calculated models regarding the drag coefficient and terminal settling velocity perform better than every reference on the data calculated by HLBM simulations. Although a splitting in test and training data is performed to prevent overfitting of the model, it is to be noted that most correlations in literature aim to be applicable for a broader range of parameters than considered in this thesis, thereby being possibly outperformed on a narrowed subset. In fact, comparing reference correlations regarding the data they are based on, often a bias in accuracy is observed towards the type of particles given more weight to in the data. It is concluded at this point that the calculation of correlations specific to a particle collective is sensible, as the complexity of the link between particle shape and dynamic particle behaviour can not be reduced to a single general equation without loss of information. Considering the approach given in Section 6.5.2, this is the way, for the reliable determination of such specific correlations.

By this means the aim of this thesis is reached. Not only new correlations for drag and terminal settling velocity regarding various shape parameters in a confined range are presented, but also the most relevant parameters are identified. Rather than a general correlation, a general approach for the creation of such is presented, as the claim of generality of a correlation is often limited by the size and balance of the given data set.

Outlook In the future, the described approach and simulation method can be applied not only to generate correlations regarding a specific particle collective, but also regarding specific process machines and process conditions. In a further concomitant publication, the method was applied for the investigation of settling under conditions in an ultra centrifuge [16]. These studies can be extended to more complex geometries, thereby obtaining or improving guidelines for the design of process machines. To increase the feasibility of the simulations, the performance of the implementation needs to be further improved. Considering that due to recent advances in GPU-computing, for which the LBM is a good fit, significant speedups are achievable. By this means a more general tool for the investigation of particle dynamics in processes can be created by the coupling of several parts. First a large data base is required as a foundation, since the exchange of data between research groups can be tedious and often requires conversion of data to the required format, whereby an open source solution is desired to establish a comprehensive reference and define a uniform format for the data. Such an approach is proposed with the *PARROT* archive by Ditscherlein et al. [36]. From this, sets of particles can be selected and used for simulations to obtain correlations as described in Chapter 6. It is possible to automate the procedure from the selection of particles up to the final correlation. In a further step, the new results can be used for large scale simulations in a processing geometry, applying an Euler approach for the particlesand coupling it with the VANS equations. This allows for a thorough investigation of particle dynamics in processes aiding in the design of machines.

Bibliography

[1] F. F. Abraham. „Functional Dependence of Drag Coefficient of a Sphere on Reynolds Number.“ In: *Physics of Fluids* 13.8 (1970), p. 2194.

[2] C. K. Aidun and J. R. Clausen. „Lattice-Boltzmann Method for Complex Flows.“ In: *Annual Review of Fluid Mechanics* 42.1 (2010), pp. 439–472.

[3] J. Almedeij. „Drag coefficient of flow around a sphere: Matching asymptotically the wide trend.“ In: *Powder Technology* 186.3 (2008), pp. 218–223.

[4] T. B. Anderson and R. Jackson. „Fluid Mechanical Description of Fluidized Beds. Equations of Motion.“ In: *Industrial & Engineering Chemistry Fundamentals* 6.4 (1967), pp. 527–539.

[5] M. J. Andrews and P. J. O'Rourke. „The multiphase particle-in-cell (MP-PIC) method for dense particulate flows.“ In: *International Journal of Multiphase Flow* 22.2 (1996), pp. 379–402.

[6] E. Asylbekov, R. Trunk, M. J. Krause, and H. Nirschl. „Microscale Discrete Element Method Simulation of the Carbon Black Aggregate Fracture Behavior in a Simple Shear Flow.“ In: *Energy Technology* (2021), p. 2000850.

[7] G. Bagheri and C. Bonadonna. „On the drag of freely falling non-spherical particles.“ In: *Powder Technology* 301 (2016), pp. 526–544.

[8] E. Barnea and J. Mizrahi. „A generalized approach to the fluid dynamics of particulate systems.“ In: *The Chemical Engineering Journal* 5.2 (1973), pp. 171–189.

[9] A. B. Basset. „On the motion of a sphere in a viscous liquid.“ In: *Philosophical Transactions of the Royal Society of London. (A.)* 179 (1888), pp. 43–63.

[10] P. L. Bhatnagar, E. P. Gross, and M. Krook. „A Model for Collision Processes in Gases. I. Small Amplitude Processes in Charged and Neutral One-Component Systems." In: *Physical Review* 94.3 (1954), pp. 511–525.

[11] B. Blais and F. Bertrand. „On the use of the method of manufactured solutions for the verification of CFD codes for the volume-averaged Navier–Stokes equations." In: *Computers & Fluids* 114 (2015), pp. 121–129.

[12] B. Blais, J.-M. Tucny, D. Vidal, and F. Bertrand. „A conservative lattice Boltzmann model for the volume-averaged Navier–Stokes equations based on a novel collision operator." In: *Journal of Computational Physics* 294 (2015), pp. 258–273.

[13] S. J. Blott and K. Pye. „Particle shape: a review and new methods of characterization and classification." In: *Sedimentology* 55.1 (2008), pp. 31–63.

[14] A. Brand, L. Allen, M. Altman, M. Hlava, and J. Scott. „Beyond authorship: attribution, contribution, collaboration, and credit." In: *Learned Publishing* 28.2 (2015), pp. 151–155.

[15] L. Breiman. „Random Forests." In: *Machine Learning* 45.1 (2001), pp. 5–32.

[16] C. Bretl, R. Trunk, H. Nirschl, G. Thäter, M. Dorn, and M. J. Krause. „Preliminary study of particle settling behaviour by shape parameters via lattice Boltzmann simulations." In: *High Performance Computing in Science and Engineering '20*. 2020 (accepted).

[17] P. P. Brown and D. F. Lawler. „Sphere Drag and Settling Velocity Revisited." In: *Journal of Environmental Engineering* 129.3 (2003), pp. 222–231.

[18] C. Cercignani. *The Boltzmann Equation and Its Applications*. Springer New York, 1988.

[19] J. A. Champion, Y. K. Katare, and S. Mitragotri. „Particle shape: A new design parameter for micro- and nanoscale drug delivery carriers." In: *Journal of Controlled Release* 121.1–2 (2007), pp. 3–9.

[20] S. Chapman and T. G. Cowling. *The Mathematical Theory of Non-Uniform Gases*. 2nd Edition. Cambridge University Press, 1952.

[21] S. Chen and G. D. Doolen. „Lattice Boltzmann method for fluid flows." In: *Annual Review of Fluid Mechanics* 30.1 (1998), pp. 329–364.

[22] N.-S. Cheng. „Comparison of formulas for drag coefficient and settling velocity of spherical particles." In: *Powder Technology* 189.3 (2009), pp. 395–398.

[23] B. Chopard, J.-L. Falcone, P. Kunzli, L. Veen, and A. Hoekstra. „Multiscale modeling: recent progress and open questions.“ In: *Multiscale and Multidisciplinary Modeling, Experiments and Design* 1.1 (2018), pp. 57–68.

[24] F. Concha and A. Barrientos. „Settling velocities of particulate systems, 3. Power series expansion for the drag coefficient of a sphere and prediction of the settling velocity.“ In: *International Journal of Mineral Processing* 9.2 (1982), pp. 167–172.

[25] E. L. Cussler. *Diffusion: Mass Transfer in Fluid Systems*. 3rd edition. Cambridge University Press, 2009.

[26] D. Dapelo, R. Trunk, M. J. Krause, and J. Bridgeman. „Towards Lattice-Boltzmann modelling of unconfined gas mixing in anaerobic digestion.“ In: *Computers & Fluids* 180 (2019), pp. 11–21.

[27] D. Dapelo, R. Trunk, M. Krause, N. Cassidy, and J. Bridgeman. „The application of Buckingham π theorem to Lattice-Boltzmann modelling of sewage sludge digestion.“ In: *Computers & Fluids* 209 (2020), p. 104632.

[28] N. Deen, M. Van Sint Annaland, M. Van der Hoef, and J. Kuipers. „Review of discrete particle modeling of fluidized beds.“ In: *Chemical Engineering Science* 62.1–2 (2007), pp. 28–44.

[29] F. Delay, P. Ackerer, and C. Danquigny. „Simulating Solute Transport in Porous or Fractured Formations Using Random Walk Particle Tracking: A Review.“ In: *Vadose Zone Journal* 4.2 (2005), pp. 360–379.

[30] P. Dellino, D. Mele, R. Bonasia, G. Braia, L. La Volpe, and R. Sulpizio. „The analysis of the influence of pumice shape on its terminal velocity.“ In: *Geophysical Research Letters* 32.21 (2005).

[31] M. O. Deville and T. B. Gatski. *Mathematical Modeling for Complex Fluids and Flows*. Springer Berlin Heidelberg, 2012.

[32] S. Dey, S. Zeeshan Ali, and E. Padhi. „Terminal fall velocity: the legacy of Stokes from the perspective of fluvial hydraulics.“ In: *Proceedings of the Royal Society A: Mathematical, Physical and Engineering Sciences* 475.2228 (2019), p. 20190277.

[33] W. E. Dietrich. „Settling velocity of natural particles.“ In: *Water Resources Research* 18.6 (1982), pp. 1615–1626.

[34] F. Dioguardi and D. Mele. „A new shape dependent drag correlation formula for non-spherical rough particles. Experiments and results.“ In: *Powder Technology* 277 (2015), pp. 222–230.

[35] R. Ditscherlein, O. Furat, M. de Langlard, J. Martins de Souza e Silva, J. Sygusch, M. Rudolph, T. Leißner, V. Schmidt, and U. A. Peuker. „Multiscale Tomographic Analysis for Micron-Sized Particulate Samples.“ In: *Microscopy and Microanalysis* 26.4 (2020), pp. 676–688.

[36] R. Ditscherlein, E. Löwer, T. Leißner, U. A. Peuker, R. Mehnert, O. Furat, V. Schmidt, R. Trunk, and M. J. Krause. „PARROT - A Pilot Study on the Open Access Provision of Particle Discrete Tomographic Datasets.“ In: *Particle & Particle Systems Characterization* (2021).

[37] K. J. Dong, B. Wang, and A. B. Yu. „Modeling of Particle Flow and Sieving Behavior on a Vibrating Screen: From Discrete Particle Simulation to Process Performance Prediction.“ In: *Industrial & Engineering Chemistry Research* 52.33 (2013), pp. 11333–11343.

[38] H. Enwald, E. Peirano, and A.-E. Almstedt. „Eulerian two-phase flow theory applied to fluidization.“ In: *International Journal of Multiphase Flow* 22 (1996), pp. 21–66.

[39] F. Farivar, H. Zhang, Z. F. Tian, and A. Gupte. „CFD-DEM simulation of fluidization of multisphere- modelled cylindrical particles.“ In: *Powder Technology* 360 (2020), pp. 1017–1027.

[40] C. Feichtinger, S. Donath, H. Köstler, J. Götz, and U. Rüde. „WaLBerla: HPC software design for computational engineering simulations.“ In: *Journal of Computational Science* 2.2 (2011), pp. 105–112.

[41] G. H. Ganser. „A rational approach to drag prediction of spherical and nonspherical particles.“ In: *Powder Technology* 77.2 (1993), pp. 143–152.

[42] J. Garside and M. R. Al-Dibouni. „Velocity-Voidage Relationships for Fluidization and Sedimentation in Solid-Liquid Systems.“ In: *Industrial & Engineering Chemistry Process Design and Development* 16.2 (1977), pp. 206–214.

[43] J. Götz, K. Iglberger, M. Stürmer, and U. Rüde. „Direct Numerical Simulation of Particulate Flows on 294912 Processor Cores.“ In: *2010 ACM/IEEE International Conference for High Performance Computing, Networking, Storage and Analysis* (2010).

[44] Z. Guo, C. Zheng, and B. Shi. „Discrete lattice effects on the forcing term in the lattice Boltzmann method.“ In: *Physical Review E* 65.4 (2002).

[45] Z. Guo and T. S. Zhao. „Lattice Boltzmann model for incompressible flows through porous media.“ In: *Physical Review E* 66.3 (2002).

[46] V. Gupta, S. Beirne, P. N. Nesterenko, and B. Paull. „Investigating the Effect of Column Geometry on Separation Efficiency using 3D Printed Liquid Chromatographic Columns Containing Polymer Monolithic Phases.“ In: *Analytical Chemistry* 90.2 (2018), pp. 1186–1194.

[47] A. Haider and O. Levenspiel. „Drag coefficient and terminal velocity of spherical and nonspherical particles.“ In: *Powder Technology* 58.1 (1989), pp. 63–70.

[48] G. Hammerl and W. A. Wall. „A four-way coupled Euler—Lagrange approach using a variational multiscale method for simulating cavitation.“ In: *Journal of Physics: Conference Series* 656 (2015), p. 012125.

[49] D. Hänel. *Molekulare Gasdynamik*. Springer-Verlag, 2004.

[50] M. Haussmann, N. Hafen, F. Raichle, R. Trunk, H. Nirschl, and M. Krause. „Galilean invariance study on different lattice Boltzmann fluid–solid interface approaches for vortex-induced vibrations.“ In: *Computers & Mathematics with Applications* 80.5 (2020), pp. 671–691.

[51] P. G. W. Hawksley. „Survey of the relative motion of particles and fluids.“ In: *British Journal of Applied Physics* 5.3 (1954), pp. 1–5.

[52] Y. Hayakawa and T. Oguchi. „Evaluation of gravel sphericity and roundness based on surface-area measurement with a laser scanner.“ In: *Computers & Geosciences* 31.6 (2005), pp. 735–741.

[53] L. He, D. K. Tafti, and K. Nagendra. „Evaluation of drag correlations using particle resolved simulations of spheres and ellipsoids in assembly.“ In: *Powder Technology* 313 (2017), pp. 332–343.

[54] Y. He, F. Muller, A. Hassanpour, and A. E. Bayly. „A CPU-GPU cross-platform coupled CFD-DEM approach for complex particle-fluid flows.“ In: *Chemical Engineering Science* 223 (2020), p. 115712.

[55] T. Henn, V. Heuveline, M. J. Krause, and S. Ritterbusch. „Aortic Coarctation Simulation Based on the Lattice Boltzmann Method: Benchmark Results.“ In: *Statistical Atlases and Computational Models of the Heart. Imaging and Modelling Challenges*. 2013, pp. 34–43.

[56] T. Henn, G. Thäter, W. Dörfler, H. Nirschl, and M. J. Krause. „Parallel dilute particulate flow simulations in the human nasal cavity.“ In: *Computers & Fluids* 124 (2016), pp. 197–207.

[57] M. L. Hentschel and N. W. Page. „Selection of Descriptors for Particle Shape Characterization.“ In: *Particle & Particle Systems Characterization* 20.1 (2003), pp. 25–38.

[58] H. Hertz. *Prinzipien der Mechanik*. Springer Berlin Heidelberg, 1972.

[59] S. B. Höcker, R. Trunk, W. Dörfler, and M. J. Krause. „Towards the simulations of inertial dense particulate flows with a volume-averaged lattice Boltzmann method.“ In: *Computers & Fluids* 166 (2018), pp. 152–162.

[60] H. J. Hofmann. „Grain-shaped indices and isometric graphs.“ In: *Journal of Sedimentary Research* 64.4a (1994), pp. 916–920.

[61] A. Hölzer and M. Sommerfeld. „New simple correlation formula for the drag coefficient of non-spherical particles.“ In: *Powder Technology* 184.3 (2008), pp. 361–365.

[62] H.-B. Huang, X.-Y. Lu, and M. C. Sukop. „Numerical study of lattice Boltzmann methods for a convection–diffusion equation coupled with Navier–Stokes equations.“ In: *Journal of Physics A: Mathematical and Theoretical* 44.5 (2011), p. 055001.

[63] R. Jackson. „Locally averaged equations of motion for a mixture of identical spherical particles and a Newtonian fluid.“ In: *Chemical Engineering Science* 52.15 (1997), pp. 2457–2469.

[64] R. Johansson and M. Evertsson. „CFD simulation of a centrifugal air classifier used in the aggregate industry.“ In: *Minerals Engineering* 63 (2014), pp. 149–156.

[65] F. Klemens, B. Förster, M. Dorn, G. Thäter, and M. J. Krause. „Solving fluid flow domain identification problems with adjoint lattice Boltzmann methods.“ In: *Computers & Mathematics with Applications* 79.1 (2020), pp. 17–33.

[66] F. Klemens, S. Schuhmann, R. Balbierer, G. Guthausen, H. Nirschl, G. Thäter, and M. J. Krause. „Noise reduction of flow MRI measurements using a lattice Boltzmann based topology optimisation approach.“ In: *Computers & Fluids* 197 (2020), p. 104391.

[67] F. Klemens, S. Schuhmann, G. Guthausen, G. Thäter, and M. J. Krause. „CFD-MRI: A coupled measurement and simulation approach for accurate fluid flow characterisation and domain identification.“ In: *Computers & Fluids* 166 (2018), pp. 218–224.

[68] A. Kraskov, H. Stögbauer, and P. Grassberger. „Estimating mutual information.“ In: *Physical Review E* 69.6 (2004).

[69] M. J. Krause. „Durch Numerische Simulation zur wissenschaftlichen Erkenntnis.“ In: *Messen und Verstehen in der Wissenschaft*. 2017. Chap. 14, pp. 237–256.

[70] M. J. Krause, A. Kummerländer, S. J. Avis, H. Kusumaatmaja, D. Dapelo, F. Klemens, M. Gaedtke, N. Hafen, A. Mink, R. Trunk, J. E. Marquardt, M.-L. Maier, M. Haussmann, and S. Simonis. „OpenLB—Open source lattice Boltzmann code.“ In: *Computers & Mathematics with Applications* (2020).

[71] M. J. Krause, F. Klemens, T. Henn, R. Trunk, and H. Nirschl. „Particle flow simulations with homogenised lattice Boltzmann methods.“ In: *Particuology* 34 (2017), pp. 1–13.

[72] T. Krüger, H. Kusumaatmaja, A. Kuzmin, O. Shardt, G. Silva, and E. M. Viggen. *The Lattice Boltzmann Method*. Springer International Publishing, 2017.

[73] H. Kruggel-Emden, S. Rickelt, S. Wirtz, and V. Scherer. „A study on the validity of the multi-sphere Discrete Element Method.“ In: *Powder Technology* 188.2 (2008), pp. 153–165.

[74] A. Kupershtokh, D. Medvedev, and D. Karpov. „On equations of state in a lattice Boltzmann method.“ In: *Computers & Mathematics with Applications* 58.5 (2009), pp. 965–974.

[75] A. J. C. Ladd. „Numerical simulations of particulate suspensions via a discretized Boltzmann equation. Part 1. Theoretical foundation.“ In: *Journal of Fluid Mechanics* 271 (1994), pp. 285–309.

[76] A. J. C. Ladd. „Numerical simulations of particulate suspensions via a discretized Boltzmann equation. Part 2. Numerical results.“ In: *Journal of Fluid Mechanics* 271 (1994), pp. 311–339.

[77] C. E. Lapple and C. B. Shepherd. „Calculation of Particle Trajectories.“ In: *Industrial & Engineering Chemistry* 32.5 (1940), pp. 605–617.

[78] J. Latt. „Hydrodynamic Limit of LatticeBoltzmann Equations.“ PhD thesis. University of Geneva, 2007.

[79] J. Latt, B. Chopard, O. Malaspinas, M. Deville, and A. Michler. „Straight velocity boundaries in the lattice Boltzmann method.“ In: *Physical Review E* 77.5 (2008).

[80] K. W. Lee and B. Y. H. Liu. „On the Minimum Efficiency and the Most Penetrating Particle Size for Fibrous Filters.“ In: *Journal of the Air Pollution Control Association* 30.4 (1980), pp. 377–381.

[81] D. Leith. „Drag on Nonspherical Objects.“ In: *Aerosol Science and Technology* 6.2 (1987), pp. 153–161.

[82] X. Liu, J. Gan, W. Zhong, and A. Yu. „Particle shape effects on dynamic behaviors in a spouted bed: CFD-DEM study.“ In: *Powder Technology* 361 (2020), pp. 349–362.

[83] P. Lösch, K. Nikolaus, and S. Antonyuk. „Classification of Fine Particles Using the Hydrodynamic Forces in the Boundary Layer of a Membrane.“ In: *Chemie Ingenieur Technik* 91.11 (2019), pp. 1656–1662.

[84] E. Loth. „Drag of non-spherical solid particles of regular and irregular shape.“ In: *Powder Technology* 182.3 (2008), pp. 342–353.

[85] E. Loth. „Numerical approaches for motion of dispersed particles, droplets and bubbles.“ In: *Progress in Energy and Combustion Science* 26.3 (2000), pp. 161–223.

[86] G. Łukaszewicz and P. Kalita. *Navier–Stokes Equations*. Springer International Publishing, 2016.

[87] M.-L. Maier, R. A. Patel, N. I. Prasianakis, S. V. Churakov, H. Nirschl, and M. J. Krause. „Coupling of multiscale lattice Boltzmann discrete-element method for reactive particle fluid flows.“ In: *Physical Review E* 103.3 (2021).

[88] Y. Manwai. „Analytical solutions to the Navier–Stokes equations.“ In: *Journal of Mathematical Physics* 49.11 (2008), p. 113102.

[89] P. Marchetti, L. Peeva, and A. Livingston. „The Selectivity Challenge in Organic Solvent Nanofiltration: Membrane and Process Solutions.“ In: *Annual Review of Chemical and Biomolecular Engineering* 8.1 (2017), pp. 473–497.

[90] F. Mariani, F. Risi, and C. N. Grimaldi. „Separation efficiency and heat exchange optimization in a cyclone.“ In: *Separation and Purification Technology* 179 (2017), pp. 393–402.

[91] J. E. Marquardt, C.-R. Arlt, R. Trunk, M. Franzreb, and M. J. Krause. „Numerical and experimental examination of the retention of magnetic nanoparticles in magnetic chromatography.“ In: *Computers & Mathematics with Applications* 89 (2021), pp. 34–43.

[92] J. E. McDonald. „The shape and aerodynamics of large raindrops.“ In: *Journal of Meteorology* 11.6 (1954), pp. 478–494.

[93] D. J. McGill and W. W. King. *Engineering Mechanics: An Introduction to Dynamics*. PWS Publishing Company, 1995.

[94] J. S. McNown and J. Malaika. „Effects of particle shape on settling velocity at low Reynolds numbers.“ In: *Transactions, American Geophysical Union* 31.1 (1950), p. 74.

[95] C. J. Meyer and D. A. Deglon. „Particle collision modeling – A review.“ In: *Minerals Engineering* 24.8 (2011), pp. 719–730.

[96] E. E. Michaelides. *Particles, Bubbles and Drops*. World Scientific Publishing, 2006.

[97] A. A. Mohamad. *Lattice Boltzmann Method*. Springer, 2011.

[98] M. Mohrhard, G. Thäter, J. Bludau, B. Horvat, and M. J. Krause. „Auto-vectorization friendly parallel lattice Boltzmann streaming scheme for direct addressing.“ In: *Computers & Fluids* 181 (2019), pp. 1–7.

[99] F. Moukalled, L. Mangani, and M. Darwish. *The Finite Volume Method in Computational Fluid Dynamics*. Springer International Publishing, 2016.

[100] J. M. Nitsche and G. K. Batchelor. „Break-up of a falling drop containing dispersed particles.“ In: *Journal of Fluid Mechanics* 340 (1997), pp. 161–175.

[101] D. Oliver. „The sedimentation of suspensions of closely-sized spherical particles.“ In: *Chemical Engineering Science* 15.3–4 (1961), pp. 230–242.

[102] C. W. Oseen. „Über die Stokessche Formel und über eine verwandte Aufgabe in der Hydrodynamik.“ In: *Arkiv for mathematik, astronomi och fysik* 6.29 (1910).

[103] K. Pearson. „VII. Mathematical contributions to the theory of evolution.—III. Regression, heredity, and panmixia.“ In: *Philosophical Transactions of the Royal Society of London. Series A, Containing Papers of a Mathematical or Physical Character* 187 (1896), pp. 253–318.

[104] C. Peng, Y. Teng, B. Hwang, Z. Guo, and L.-P. Wang. „Implementation issues and benchmarking of lattice Boltzmann method for moving rigid particle simulations in a viscous flow.“ In: *Computers & Mathematics with Applications* 72.2 (2016), pp. 349–374.

[105] G. R. Pesch, M. Lorenz, S. Sachdev, S. Salameh, F. Du, M. Baune, P. E. Boukany, and J. Thöming. „Bridging the scales in high-throughput dielectrophoretic (bio-)particle separation in porous media.“ In: *Scientific Reports* 8.1 (2018).

[106] C. S. Peskin. „The immersed boundary method.“ In: *Acta Numerica* 11 (2002), pp. 479–517.

[107] F. Podczeck. „A shape factor to assess the shape of particles using image analysis.“ In: *Powder Technology* 93.1 (1997), pp. 47–53.

[108] P. Pourghahramani and E. Forssberg. „Review of applied particle shape descriptors and produced particle shapes in grinding environments. Part I: particle shape descriptors.“ In: *Mineral Processing and Extractive Metallurgy Review* 26.2 (2005), pp. 145–166.

[109] C. Rettinger and U. Rüde. „A comparative study of fluid-particle coupling methods for fully resolved lattice Boltzmann simulations.“ In: *Computers & Fluids* 154 (2017), pp. 74–89.

[110] F. Rhein, F. Scholl, and H. Nirschl. „Magnetic seeded filtration for the separation of fine polymer particles from dilute suspensions: Microplastics.“ In: *Chemical Engineering Science* 207 (2019), pp. 1278–1287.

[111] J. Richardson and W. Zaki. „Sedimentation and fluidisation: Part I.“ In: *Chemical Engineering Research and Design* 75 (1954), pp. 82–100.

[112] J. Richardson and W. Zaki. „The sedimentation of a suspension of uniform spheres under conditions of viscous flow.“ In: *Chemical Engineering Science* 3.2 (1954), pp. 65–73.

[113] J. P. le Roux. „Application of the Hofmann shape entropy to determine the settling velocity of irregular, semi-ellipsoidal grains.“ In: *Sedimentary Geology* 149.4 (2002), pp. 237–243.

[114] W. W. Rubey. „Settling velocity of gravel, sand, and silt particles.“ In: *American Journal of Science* s5-25.148 (1933), pp. 325–338.

[115] M. Saidi, M. Rismanian, M. Monjezi, M. Zendehbad, and S. Fatehiboroujeni. „Comparison between Lagrangian and Eulerian approaches in predicting motion of micron-sized particles in laminar flows.“ In: *Atmospheric Environment* 89 (2014), pp. 199–206.

[116] L. Schiller and A. Naumann. „Über die grundlegenden Berechnungen bei der Schwerkraftaufbereitung.“ In: *Zeitschrift des Vereines Deutscher Ingenieure* 77 (1933), pp. 318–320.

[117] M. Schönherr, K. Kucher, M. Geier, M. Stiebler, S. Freudiger, and M. Krafczyk. „Multi-thread implementations of the lattice Boltzmann method on non-uniform grids for CPUs and GPUs.“ In: *Computers & Mathematics with Applications* 61.12 (2011), pp. 3730–3743.

[118] R. Scotti, L. Wahba, M. Crippa, M. D’Arienzo, R. Donetti, N. Santo, and F. Morazzoni. „Rubber–silica nanocomposites obtained by in situ sol–gel method: particle shape influence on the filler–filler and filler–rubber interactions.“ In: *Soft Matter* 8.7 (2012), p. 2131.

[119] C. Semprebon, T. Krüger, and H. Kusumaatmaja. „Ternary free-energy lattice Boltzmann model with tunable surface tensions and contact angles.“ In: *Physical Review E* 93.3 (2016), p. 03305.

[120] X. Shan and H. Chen. „Lattice Boltzmann model for simulating flows with multiple phases and components.“ In: *Physical Review E* 47.3 (1993), pp. 1815–1819.

[121] A. V. Shcheprov. „Analytical solutions of Navier-Stokes equations for axisymmetric and plane flows of a viscous incompressible fluid.“ In: *Doklady Physics* 49.2 (2004), pp. 127–131.

[122] S. R. Singiresu. *The Finite Element Method in Engineering*. Vol. six. Butterworth-Heinemann, 2018.

[123] P. A. Skordos. „Initial and boundary conditions for the lattice Boltzmann method.“ In: *Physical Review E* 48.6 (1993), pp. 4823–4842.

[124] E. D. Sneed and R. L. Folk. „Pebbles in the Lower Colorado River, Texas a Study in Particle Morphogenesis.“ In: *The Journal of Geology* 66.2 (1958), pp. 114–150.

[125] M. Sommerfeld and Z. Qadir. „Fluid dynamic forces acting on irregular shaped particles: Simulations by the Lattice–Boltzmann method.“ In: *International Journal of Multiphase Flow* 101 (2018), pp. 212–222.

[126] F. Song, W. Wang, and J. Li. „A lattice Boltzmann method for particle-fluid two-phase flow.“ In: *Chemical Engineering Science* 102 (2013), pp. 442–450.

[127] H. H. Steinour. „Rate of sedimentation.Nonflocculated Suspensions of Uniform Spheres.“ In: *Industrial & Engineering Chemistry* 36.7 (1944), pp. 618–624.

[128] G. G. Stokes. „On the Effect of Internal Friction of Fluids on the Motion of Pendulums.“ In: *Transaction of the Cambridge Philosophical Society* 9 (2 1851), pp. 8–106.

[129] D. Su and W. M. Yan. „Prediction of 3D size and shape descriptors of irregular granular particles from projected 2D images.“ In: *Acta Geotechnica* 15.6 (2020), pp. 1533–1555.

[130] S. Succi. *The Lattice Boltzmann Equation: For Fluid Dynamics and Beyond*. OUP Oxford, 2013.

[131] S. Succi, R. Benzi, and F. Higuera. „The lattice Boltzmann equation: A new tool for computational fluid-dynamics.“ In: *Physica D: Nonlinear Phenomena* 47.1–2 (1991), pp. 219–230.

[132] S. Suga. „Numerical Schemes Obtained from Lattice Boltzmann Equations for Advection Diffusion Equations.“ In: *International Journal of Modern Physics C* 17.11 (2006), pp. 1563–1577.

[133] L. Sun, H. Qiu, C. Wu, J. Niu, and B. X. Hu. „A review of applications of fractional advection–dispersion equations for anomalous solute transport in surface and subsurface water.“ In: *WIREs Water* 7.4 (2020).

[134] S. Tenneti, R. Garg, and S. Subramaniam. „Drag law for monodisperse gas–solid systems using particle-resolved direct numerical simulation of flow past fixed assemblies of spheres.“ In: *International Journal of Multiphase Flow* 37.9 (2011), pp. 1072–1092.

[135] P. J. Thomas. „On the influence of the Basset history force on the motion of a particle through a fluid.“ In: *Physics of Fluids A: Fluid Dynamics* 4.9 (1992), pp. 2090–2093.

[136] R. Trunk, C. Bretl, G. Thäter, H. Nirschl, M. Dorn, and M. J. Krause. „A Study on Shape-Dependent Settling of Single Particles with Equal Volume Using Surface Resolved Simulations.“ In: *Computation* 9.4 (2021), p. 40.

[137] R. Trunk, T. Weckerle, N. Hafen, G. Thäter, H. Nirschl, and M. J. Krause. „Revisiting the Homogenized Lattice Boltzmann Method with Applications on Particulate Flows.“ In: *Computation* 9.2 (2021), p. 11.

[138] R. Trunk, T. Henn, W. Dörfler, H. Nirschl, and M. J. Krause. „Inertial dilute particulate fluid flow simulations with an Euler–Euler lattice Boltzmann method.“ In: *Journal of Computational Science* 17 (2016), pp. 438–445.

[139] R. Trunk, J. Marquardt, G. Thäter, H. Nirschl, and M. J. Krause. „Towards the simulation of arbitrarily shaped 3D particles using a homogenised lattice Boltzmann method.“ In: *Computers & Fluids* 172 (2018), pp. 621–631.

[140] R. Turton and O. Levenspiel. „A short note on the drag correlation for spheres.“ In: *Powder Technology* 47.1 (1986), pp. 83–86.

[141] M. Uhlmann. „An immersed boundary method with direct forcing for the simulation of particulate flows.“ In: *Journal of Computational Physics* 209.2 (2005), pp. 448–476.

[142] V. Vand. „Viscosity of Solutions and Suspensions. I. Theory.“ In: *The Journal of Physical and Colloid Chemistry* 52.2 (1948), pp. 277–299.

[143] T. F. de Vasconcelos, B. Sapoval, J. S. Andrade, J. B. Grotberg, Y. Hu, and M. Filoche. „Particle capture into the lung made simple?“ In: *Journal of Applied Physiology* 110.6 (2011), pp. 1664–1673.

[144] H. Versteeg and W. Malalasekera. *An Introduction to Computational Fluid Dynamics: The Finite Volume Method*. 2nd rev. edition. Pearson Education, 2007.

[145] H. Wadell. „Volume, Shape, and Roundness of Rock Particles." In: *The Journal of Geology* 40.5 (1932), pp. 443–451.

[146] K. Waldschläger and H. Schüttrumpf. „Effects of Particle Properties on the Settling and Rise Velocities of Microplastics in Freshwater under Laboratory Conditions." In: *Environmental Science & Technology* 53.4 (2019), pp. 1958–1966.

[147] B. Wen, C. Zhang, Y. Tu, C. Wang, and H. Fang. „Galilean invariant fluid–solid interfacial dynamics in lattice Boltzmann simulations." In: *Journal of Computational Physics* 266 (2014), pp. 161–170.

[148] S. Whitaker. *The Method of Volume Averaging*. Springer Netherlands, 1999.

[149] M. Winkler, H. Sonner, M. Gleiss, and H. Nirschl. „Fractionation of ultrafine particles: Evaluation of separation efficiency by UV–vis spectroscopy." In: *Chemical Engineering Science* 213 (2020), p. 115374.

[150] D. A. Wolf-Gladrow. *Lattice Gas Cellular Automata and Lattice Boltzmann Models*. Springer, 2000.

[151] Y. Yamamoto, F. Hisataka, and S. Harada. „Numerical simulation of concentration interface in stratified suspension: Continuum–particle transition." In: *International Journal of Multiphase Flow* 73 (2015), pp. 71–79.

[152] D. S. Young. *Handbook of Regression Methods*. Chapman and Hall/CRC, 2017.

[153] Z. Yuan, F. Li, P. Zhang, and B. Chen. „Description of shape characteristics through Fourier and wavelet analysis." In: *Chinese Journal of Aeronautics* 27.1 (2014), pp. 160–168.

[154] J. Zhang, L. Wang, and J. Ouyang. „Lattice Boltzmann model for the volume-averaged Navier-Stokes equations." In: *EPL (Europhysics Letters)* 107.2 (2014), p. 20001.

[155] Z. Zhang and Q. Chen. „Comparison of the Eulerian and Lagrangian methods for predicting particle transport in enclosed spaces." In: *Atmospheric Environment* 41.25 (2007), pp. 5236–5248.

[156] Z. Y. Zhou, S. B. Kuang, K. W. Chu, and A. B. Yu. „Discrete particle simulation of particle–fluid flow: model formulations and their applicability." In: *Journal of Fluid Mechanics* 661 (2010), pp. 482–510.

[157] H. Zhu, Z. Zhou, R. Yang, and A. Yu. „Discrete particle simulation of particulate systems: A review of major applications and findings." In: *Chemical Engineering Science* 63.23 (2008), pp. 5728–5770.

[158] H. Zhu, Z. Zhou, R. Yang, and A. Yu. „Discrete particle simulation of particulate systems: Theoretical developments.“ In: *Chemical Engineering Science* 62.13 (2007), pp. 3378–3396.

[159] T. Zingg. „Beitrag zur Schotteranalyse.“ in: Schweizerische mineralogische und petrographische Mitteilungen, Vol. 15, pp.39–140, No. 849, Ref.: Niggli, P. ; Korref.: Burri, C. PhD thesis. ETH, 1935.

[160] Q. Zou and X. He. „On pressure and velocity boundary conditions for the lattice Boltzmann BGK model.“ In: *Physics of Fluids* 9.6 (1997), pp. 1591–1598.

Appendix

A List of Publications

Peer-Reviewed Journal Publications

- **R. Trunk**, T. Henn, W. Dörfler, H. Nirschl, M. J. Krause. Inertial dilute particulate fluid flow simulations with an Euler–Euler lattice Boltzmann method. *Journal of Computational Science*, 17.2 (2016).

- M. J. Krause, F. Klemens, T. Henn, **R. Trunk**, H. Nirschl. Particle Flow Simulations with Homogenised Lattice Boltzmann Methods. *Particuology*, 34 (2017).

- **R. Trunk**, J. Marquardt, G. Thäter, H. Nirschl, M. J. Krause. Towards the Simulation of arbitrarily shaped 3D particles using a homogenised lattice Boltzmann method. *Computers & Fluids*, 172 (2018).

- S. B. Höcker, **R. Trunk**, W. Dörfler, M. J. Krause. Towards the simulations of inertial dense particulate flows with a volume-averaged lattice Boltzmann method. *Computers & Fluids*, 166 (2018).

- D. Dapelo, **R. Trunk**, M. J. Krause, J. Bridgeman. Towards Lattice-Boltzmann modelling of unconfined gas mixing in anaerobic digestion. *Computers & Fluids*, 180 (2018).

- M. Haussmann, N. Hafen, F. Raichle, **R. Trunk**, H. Nirschl, M. J. Krause. Galilean invariance study on different lattice Boltzmann fluid–solid interface approaches for vortex-induced vibrations. *Computers & Mathematics with Applications*, 80.5 (2020).

- D. Dapelo, **R. Trunk**, M. J. Krause, N. Cassidy, J. Bridgeman. The application of Buckingham π theorem to Lattice-Boltzmann modelling of sewage sludge digestion. *Computers & Fluids*, 209 (2020).

- M. J. Krause, A. Kummerländer, S. J. Avise, H. Kusumaatmaja, D. Dapelo, F. Klemens, M. Gaedtke, N. Hafen, A. Mink, **R. Trunk**, J. E. Marquardt, M.-L. Maier, M. Haussmann, S. Simonis. OpenLB—Open source lattice Boltzmann code. *Computers & Mathematics with Applications*, 81 (2021).

- E. Asylbekov, **R. Trunk**, M. J. Krause, H. Nirschl. Microscale DEM Simulation of the Carbon Black Aggregate Fracture Behavior in a Simple Shear Flow. *Special Issue of Energy Technology*, (2021).

- J. E. Marquardt, C.-R. Arlt, **R. Trunk**, M. Franzreb, M. J. Krause. Numerical and Experimental Examination of the Retention of Magnetic Nanoparticles in Magnetic Chromatography. *Computers and Mathematics with Applications*, 89 (2021).

- **R. Trunk**, T. Weckerle, N. Hafen, G. Thäter, H. Nirschl, M. J. Krause. Revisiting the Homogenized Lattice Boltzmann Method with Applications on Particulate Flows. *Computation* 9.2 (2021).

- **R. Trunk**, C. Bretl, G. Thäter, H. Nirschl, M. Dorn, M. J. Krause. A Study on Shape-Dependent Settling of Single Particles with Equal Volume Using Surface Resolved Simulations. *Computation* 9.40 (2021).

- R. Ditscherlein, E. Löwer, T. Leißner, U. A. Peuker, R. Mehnert, O. Furat, V. Schmidt, **R. Trunk**, M. J. Krause. PARROT - A Pilot Study on the Open Access Provision of Particle Discrete Tomographic Datasets. *Particle & Particle Systems Characterization* 2021 (submitted)

Peer-Reviewed Proceedings

- C. Bretl, **R. Trunk**, H. Nirschl, G. Thäter, M. Dorn, M. J. Krause. Preliminary study of particle settling behaviour by shape parameters via lattice Boltzmann simulations. *High Performance Computing in Science and Engineering 2020*, Article accepted (2020).

Talks

- **R. Trunk**, T. Henn, H. Nirschl, M. J. Krause. Inertial Dilute Particulate Fluid Flow Simulations with an Euler-Euler Lattice Boltzmann Method for Cross Flow Filtration. *Jahrestreffen der ProcessNet-Fachgruppen Agglomerations- und Schüttguttechnik, Mehrphasenströmungen und Computational Fluid Dynamics*, Bingen, Germany (2015).

- **R. Trunk**, T. Henn, M. J. Krause. Approaches to the Simulation of Particle-Laden Flows with OpenLB. *25th International Conference on Discrete Simulation of Fluid Dynamics (DSFD)*, Shenzhen, China (2016).

- **R. Trunk**. Mehrkomponentenströmungen mit OpenLB. *Kurs: Simulation Partikelbeladener Strömungen*, Karlsruhe, Germany (2016)

- **R. Trunk**, M.-L. Maier, T. Henn. LBM and Particles. *SpringSchool: Lattice Boltzmann Methods with OpenLB Software Lab*, Hammamet, Tunis (2017).

- M. J. Krause, F. Klemens, T. Henn, **R. Trunk**, H. Nirschl. A Homogenized Lattice Boltzmann Method for the Simulation of Arbitrary-shaped 3D Particle in a Fluid Flow. *The 3rd International Conference on Numerical Methods in Multiphase Flows (ICNMMF-III)*, Tokyo, Japan (2017).

- **R. Trunk**, J. Marquardt, H. Nirschl, M. J. Krause. Simulation of Arbitrary 3D Objects Using the Homogenised Lattice Boltzmann Method. *26th International Conference on Discrete Simulation of Fluid Dynamics (DSFD)*, Erlangen, Germany (2017).

- **R. Trunk**, M.-L. Maier. Particulate flows. *SpringSchool: Lattice Boltzmann Methods with OpenLB Software Lab*, Karlsruhe, Germany (2018).

- **R. Trunk**. Mehrkomponentenströmungen mit OpenLB. *Kurs: Simulation Partikelbeladener Strömungen*, Karlsruhe, Germany (2018)

- **R. Trunk**, M.-L. Maier. Particulate flows. *SpringSchool: Lattice Boltzmann Methods with OpenLB Software Lab*, Mannheim, Germany (2019).

- **R. Trunk**, H. Nirschl, M. J. Krause. The Influence of Shape on the Settling of Particles Simulated with a Homogenised Lattice Boltzmann Approach. *PARTEC: International Congress on Particle Technology*, Nürnberg, Germany (2019).

- **R. Trunk**, H. Nirschl, M. J. Krause. Studying the Settling Behaviour of Arbitrarily Shaped Particles with a Homogenised Lattice Boltzmann Approach.

16th International Conference for Mesoscopic Methods in Engineering and Science (ICMMES), Edinburgh, UK (2019).

- **R. Trunk**, S. Simonis, M. J. Krause. Particulate flows and Boundary Conditions for LBM. *LBM Workshop with OpenLB Software Lab*, Porto Alegre, Brazil (2019)

- **R. Trunk**, J. Marquardt, S. Reinecke. Particulate flows. *SpringSchool: Lattice Boltzmann Methods with OpenLB Software Lab*, Berlin, Germany (2020).

- **R. Trunk**, C. Bretl, H. Nirschl, M. J. Krause. Study of the Effect of Various Particle Shape Parameter on the Settling Behaviour. *29th International Conference on Discrete Simulation of Fluid Dynamics (DSFD)*, Viterbo (online), Italy (2020).

Posters

- M. J. Krause, **R. Trunk**. OpenLB: An Open Source Library for Parallel Lattice Boltzmann Fluid Flow Simulations. *HELIX 2015: Fluid-Structure Interactions and Vortex Dynamics in Aerodynamics*, Hyères, France (2015).

- **R. Trunk**, M. J. Krause. Zweiskalenansatz zur Simulation von mehrdimensionaler Fraktionierung in Feinpartikelsystemen. *Begutachtungskolloquium* "*MehrDimPart*" Frankfurt, Germany (2017)

- **R. Trunk**, M. J. Krause. Modellierung und Simulation von mehrdimensionaler Fraktionierung in Feinpartikelsystemen und deren Anwendung. *Begutachtungskolloquium* "*MehrDimPart*" Frankfurt, Germany (2020)

- **R. Trunk**, C. Bretl , A. Kummerländer, M. J. Krause. Modellierung und Simulation mehrdimensionaler Fraktionierung in Feinpartikelsystemen und deren Anwendung. *HLRS Results- & Review Workshop* Stuttgart (online), Germany (2020).

B List of OpenLB Test and Application Cases

The following table lists the presented test cases and the related commit hashes in the OpenLB git repository on the master branch.

Name	description	commit hash	case folder in `apps/robin/`
Flow around a cylinder	Section 4.4.2	6a584deb	`valid_HLBM3D_drag`
Sedimentation of a sphere	Section 4.4.3	faff5ebd	`mordantPinton`
Sedimentation of 15 limestone particle	Section 4.4.4	4ea4aaca	`sed3Darbitrary`
Settling sphere (ten Cate)	Section 5.4.1	389d8bdf	`cate`
Settling sphere (correlation)	Section 5.4.1	58576b66	`dragCorrel`
Tubular Pinch Effect	Section 5.4.2	56f10c33	`silver`
Hindered Settling	Section 5.4.3	7e84edba	`zaki`
Settling superellipsoids	Section 6.4	c8cc8712	`hlbm_shape_study_single`